

**Modulation of the Intrinsic Properties of Alzheimer's
Amyloid Beta Peptide with Nanosurfaces and
Chemical Modifications: A Computational Approach**

Thesis Submitted to AcSIR for the Award of the Degree of
DOCTOR OF PHILOSOPHY
in Chemical Sciences



By

Mr. Asis Kumar Jana

Registration Number: 10CC11A26003

**Under the guidance of
Dr. Neelanjana Sengupta**

**Physical Chemistry Division
CSIR- National Chemical Laboratory,
Pune - 411008, India**

May 2016



राष्ट्रीय रासायनिक प्रयोगशाला
(वैज्ञानिक तथा औद्योगिक अनुसंधान परिषद)
डॉ. होमी भाभा रोड, पुणे - 411 008. भारत
NATIONAL CHEMICAL LABORATORY
(Council of Scientific & Industrial Research)
Dr. Homi Bhabha Road, Pune - 411008. India



Certificate

This is to certify that the work incorporated in this Ph.D. thesis entitled *Modulation of the Intrinsic Properties of Alzheimer's Amyloid Beta Peptide with Nanosurfaces and Chemical Modifications: A Computational Approach* submitted by **Mr. Asis Kumar Jana** to Academy of Scientific and Innovative Research (AcSIR) in fulfillment of the requirements for the award of the Degree of *Doctor of Philosophy in Chemical Sciences*, embodies original research work under my supervision. I further certify that this work has not been submitted to any other University or Institution in part or full for the award of any degree or diploma. Research material obtained from other sources has been duly acknowledged in the thesis. Any text, illustration, table etc., used in the thesis from other sources, have been duly cited and acknowledged.

Asis Kumar Jana

(Student)

Dr. Neelanjana Sengupta

(Supervisor)

Date:

Place: Pune

Communications Channels
+91 20 25902000
+91 20 25893300
+91 20 25893400

Fax +91 20 25902601 (Director)
+91 20 25902660 (Admin.)
+91 20 25902639 (Business Development)

URL : www.ncl-india.org

Declaration

I hereby declare that the thesis entitled “*Modulation of the Intrinsic Properties of Alzheimer’s Amyloid Beta Peptide with Nanosurfaces and Chemical Modifications: A Computational Approach*” submitted for the degree of *Doctor of Philosophy in Chemical Sciences* to the Academy of Scientific & Innovative Research (AcSIR), has been carried out by me at the Physical and Materials Chemistry Division of CSIR-National Chemical Laboratory, Pune under the guidance of *Dr. Neelanjana Sengupta*. Such material as has been obtained by other sources has been duly acknowledged in this thesis. The work is original and has not been submitted in part or full by me for any other degree or diploma to any other Institution or University.

Date:
CSIR-National Chemical Laboratory,
Pune - 411008

Research Student
Mr. Asis Kumar Jana

Dedicated to

My Beloved Parents

and

AratiMa

Acknowledgements

During my PhD tenure at CSIR-National chemical laboratory, I have been supported, inspired and accompanied by many people like scientists, friends, non-academic staffs etc. It gives me great privilege to take this opportunity to express my heartfelt gratitude for all of them.

*First of all, I would like to thank my teacher and research advisor **Dr. Neelanjana Sengupta** for excellent guidance, incessant encouragement and positive criticism in every respect at all phases of research career. I consider myself extremely fortunate to have a supervisor who not only guided me how to do research and think independently but also taught me discipline, professionalism and shown unique ways to reach goals. I must say, without her help it was not possible for me to complete my research work in time. I am thankful to UGC for awarding junior and senior research fellowship.*

I owe a special debt to Dr. Mahesh J. Kulkarni and Dr. Ruchi Anand (IIT, Bombay) and their research groups especially to Sneha Bansode, Kedar and Hussain (IIT, Bombay) for giving me the opportunity to extend computational support in their experimental studies and enriching scientific discussions. I would like to pay special thanks to Dr. Bishwajit Maiti (Banaras Hindu University) for his support regarding quantum calculations.

I owe to thank Dr. Sarika Maitra Bhattacharyya, Dr. T. G. Ajithkumar, Dr. Kumar Vanka, Dr. Durba Sengupta and Dr. Kavita Joshi who taught me during my course work in NCL. I also thank Dr. Srabanti Chaudhury (IISER, Pune) for appearing my UGC upgradation seminar. I thank Prof. Ashwini Nangia, Director, NCL, Dr. Vijaymohanan, Dr. P. A. Joy, Head, Division of Physical Chemistry and Dr. Anil Kumar (Former HoDs, Physical Chemistry Division) for giving me the opportunity to perform research work in NCL, Pune and providing all necessary facilities and infrastructures. Among the non-academic staffs I am thankful to Ms. Purnima Kolhe, Ms. Deepa Puranik, Ms. Vaishali Suryawansi and others from SAC office for their help and support for various documentations during my PhD. I am also thankful to Parag and Rahul for their kind help in cluster management. Special thanks to my teachers who guided me in

my school and graduation because of whom I learnt a lot.

I thank my labmates Savan, Jaya and Sneha for their help. Especially I am very thankful to my roommate Anjani Dubey and closest friend Ashok Kumar who encouraged and supported me in every stages of my research career. I am grateful to Turbasu Sengupta for generously helping me to make schematic pictures and presentations and overcoming technical problems. Sincere thanks to Deepak Kumar, Sushma, Santhi Vardhan, Devadutta, Sabadi, Dar Manzoor, Sadhu Sir, Sharath, Tushar, Laxmiprasad, Bishnu, Yadagiri, Krunal, Xavier, Rakesh, Brijesh, Kundan, Jugal and Yuvraj for their constant support and help. I am also thankful to Mrityunjay Tiwari for his help during quantum calculations.

My heartfelt thanks and appreciation to my parents for their unending support and sacrifices they have made in raising me to this level. I would also specially thank 'Aratima' for her love and care that she had showered upon me since my childhood days. I want to acknowledge my mashi 'Kalpana' for her love and care.

Final respects and thanks to "God Almighty" for his enormous love and blessings.

Asis Kumar Jana

Contents

Abstract	vi
Abbreviations	x
List of Publications	xii
1. General Introduction	
1.1. Protein Folding	3
1.2. Intrinsically Disordered Proteins	5
1.2.1. The A β Peptide	7
1.2.2. A β Self-Assembly	10
1.2.3. Influence of Nanomaterials on A β Aggregation	12
1.3. Motivation and Outline of Thesis	13
1.4. References	14
2. Molecular Dynamics Simulations: A Brief Overview	
2.1. Molecular Dynamics for Macromolecular Systems	22
2.2. Atomistic Force Fields	22
2.3. Equations of Motion	25
2.4. Thermodynamic State Control	26
2.4.1. Temperature Control	27
2.4.2. Pressure Control	28
2.5. Periodic Boundary Conditions	29
2.6. References	31

3. Adsorption Mechanism and Collapse Propensities of the Full-Length, Monomeric Aβ₁₋₄₂ on the Surface of a Single-Walled Carbon Nanotube: A Molecular Dynamics Simulation Study	
3.1. Introduction	35
3.2. Materials and Methods	38
3.2.1. Setup of Peptide-SWCNT Complexes	38
3.2.2. MD Simulations and Free Energy Calculations	39
3.3. Results and Discussion	40
3.3.1. Peptide Adsorption on the SWCNT Surface	40
3.3.2. Peptide-Nanotube Interaction Energies	43
3.3.3. Propensity of Peptide Collapse	45
3.4. Conclusion	48
3.5. References	49
4. Critical Roles of Key Domains in Complete Adsorption of Aβ Peptide on Single-Walled Carbon Nanotubes: Insights with Point Mutations and MD Simulations.	
4.1. Introduction	55
4.2. Materials and Methods	58
4.2.1. System Setups	58
4.2.2. MD Simulations	59
4.2.3. Adaptive Biasing Force Calculations	59
4.3. Results	60
4.3.1. Effect of F19I and F19Y Mutations on Peptide's Intrinsic Collapse and Adsorption on SWCNT Surface	60
4.3.1.1. Effect of F19I and F19Y Mutations on	60

	Monomeric Compactification	
4.3.1.2.	Complete Adsorption on SWCNT: Role of N-terminal Domains	64
4.3.1.3.	Competition Between the Collapse and the Adsorption Processes	68
4.3.1.4.	Decoupling the Roles of Hydrophobicity and π - π Stacking in the Adsorption Process	69
4.3.2.	Effect of F19A Mutations on Peptide's Intrinsic Collapse and Adsorption on SWCNT Surface	72
4.3.2.1.	Effect of F19A Mutation on Free Peptide Collapse	72
4.3.2.2.	Propensity for SWCNT Adsorption	74
4.3.2.3.	Post Adsorption Peptide Collapse in NT2A	76
4.3.2.4.	Enhanced Movement on Nanotube Surface Arising from Weakened Tethering of HP1 in NT2A	78
4.3.2.5.	Dewetting Effects in Free and Surface Induced Collapse	81
4.4.	Discussion and Conclusion	83
4.5.	References	85
5.	Competition between Aβ Self-Association and Adsorption on the Hydrophobic SWCNT Surface: A Molecular Dynamics Study	
5.1.	Introduction	91
5.2.	Methods	92
5.2.1.	General Simulation Protocol	92
5.2.2.	Principal Component Analysis (PCA)	93

5.2.3.	A β Monomer	93
5.2.4.	Adaptive Biasing Force (ABF) Free Energy Calculations	94
5.3.	Results and Discussion	95
5.3.1.	Spontaneous Small Oligomeric Assembly	95
5.3.2.	SWCNT Surface Adsorption Competes with Inherent Self-Assembly	96
5.3.3.	Growth Potential of Oligomers Immobilized on the Nanosurface	98
5.4.	Summary and Conclusion	100
5.5.	References	101
6.	Unraveling Origins of the Heterogeneous Curvature Dependence of Polypeptide Interactions with Carbon Nanostructures	
6.1.	Introduction	108
6.2.	Methods	110
6.2.1.	MD Simulations	110
6.2.2.	Trajectory Analyses	112
6.2.3.	DFT Methods	113
6.3.	Results	115
6.3.1.	Surface Curvature Dependence of Protein Adsorption	115
6.3.2.	Curvature Dependence of Binding Free Energy	118
6.3.3.	Insights from DFT Calculations	119
6.3.4.	Interaction of Aromatic Residues with CNS	120
6.3.5.	Interaction of Non-polar Aliphatic Residues with CNS	123

6.3.6.	Interaction of Polar Residues with CNS	126
6.3.7.	Interaction of Acidic and Basic Residues with CNS	128
6.4.	Discussion	130
6.4.1.	Dispersion	130
6.4.2.	Molecular Orbital Picture	131
6.4.3.	Molecular Electrostatic Potential Map	132
6.5.	Summary and Conclusions	134
6.6.	References	135
7.	Glycation Induces Conformational Changes in Amyloid-β Peptide and Enhances its Aggregation Propensity: Molecular Insights	
7.1.	Introduction	142
7.2.	Methods	144
7.2.1.	Experimental Methods	144
7.2.2.	Computational Methods	145
7.3.	Results and Discussion	148
7.3.1.	Glycation Promotes A β Aggregation	148
7.3.2.	Early Oligomerization	149
7.3.3.	Glycation Strengthens Inter-Protein Association	154
7.3.4.	Intra- and Intermolecular Salt Bridging Propensities	156
7.3.5.	Effect of Glycation on Preformed Protofibrils	158
7.4.	Conclusions	162
7.5.	References	163
	Copyrights and Permissions	168

Abstract

Alzheimer's disease (AD), a progressive neurodegenerative disorder characterized by the presence of insoluble protein aggregates in the neuronal synapses of the brain, is considered a major health problem in ageing populations. According to the widely accepted 'amyloid hypothesis', self-assembly of the intrinsically disordered 39-42 residue Amyloid beta ($A\beta$) protein in the synaptic, extracellular regions of the brain is the central event triggering the disease's progression. The large conformational heterogeneity and rapid aggregation propensity of $A\beta$ in purely aqueous environment limits the ability of standard experimental methods to adequately elicit the mechanism of its self-assembly. In this respect, the advent of advanced computational resources is a powerful tool to unravel the thermodynamic and structural details of the underlying pathways.

Emerging research suggests that carbon nanomaterials can play important roles in biotechnology, and that their interactions with proteins may form the basis for novel therapeutic development. Particularly, specific carbon nanomaterials have been reported to inhibit protein self-assembly and amyloid formation. In this dissertation, we have used fully atomistic molecular dynamics (MD) simulations in conjunction with suitable free energy calculations to investigate the conformational changes and the early self-assembly pathways of the $A\beta$ peptide, and modulation of these pathways in presence of carbon based nanomaterials. Our silico studies provide direct evidence that the $A\beta$ sequence is capable of dramatically altering its interfacial behavior in presence of the single-walled carbon nanotube (SWCNT) surface; these insights may have important bearing upon the design of molecules and surfaces for disrupting intrinsic $A\beta$ behavior. In addition, the role of surface curvature of carbon nanomaterials on protein adsorption processes have been elicited in detail using atomistic MD and high level quantum calculations. Further, investigations on the effects of nonenzymatic glycation on the structural, self-assembly and aggregation propensities of the $A\beta$ peptide have been studied; our computer simulation results are corroborated with detailed biophysical assays. The thesis is organized into seven chapters as follows:

Chapter 1

This chapter introduces the concept of protein folding, with an overview of the factors that guide the folding process. Intrinsically disordered proteins are introduced, and the association between the inherent lack of a natively folded state and the higher propensity to self-assemble is briefly discussed.

Chapter 2

An overview of atomistic molecular dynamics (MD) simulations, the basis for the bulk of the research carried out, is presented. This includes a description of atomistic force field parameters, numerical integration algorithms for trajectory generation, control of thermodynamic states and periodic boundary conditions.

Chapter 3

We have investigated the interactions of the full-length monomeric A β peptide with a SWCNT of small diameter. Starting with peptide-nanotube complexes that delineate the interactions of different segments of the peptide, we find rapid convergence in the peptide's adsorption behavior on the surface, thereby losing its natural propensity to collapse. The adsorption phenomena are initiated by interactions arising from the HP1, and consolidated by those arising from the N-terminal residues.

Chapter 4

We have investigated the mechanistic overlap between the A β compactification and its adsorption on the SWCNT surface, while decoupling the roles of hydrophobicity and aromaticity *via* point mutations. The peptide's intrinsic collapse propensity in aqueous environment is reduced by altering hydrophobicity, but not the aromatic character, of the HP1. Conversely, peptide's adsorption propensity on the SWCNT is severely diminished, when either the hydrophobicity or the aromatic character in HP1 is reduced. Interestingly, peptide undergoes collapse after complete adsorption on the surface by sharply reducing hydrophobic and aromatic character of the HP1. The weakened tethering of HP1 on the surface allow its greater translational movement along the surface, thereby facilitating interactions with the C-terminal domain of the peptide that lead to collapse of the peptide. These insights may be leveraged for designing molecular surfaces for disrupting intrinsic A β behavior.

Chapter 5

We evaluate the adsorption behavior of small A β oligomers on the surface of a SWCNT of high curvature. While the intrinsic self-assembly propensity of A β is markedly hindered by adsorption, the oligomeric units show high degrees of surface immobilization. Immobilized complexes are capable of oligomeric growth, but with a shifted monomer–oligomer equilibrium compared to the free states. The results provide an important basis for further investigations in the design of new effective therapeutics for preventing AD progression.

Chapter 6

We address the origins of the curvature dependence of polypeptide adsorption on carbon nanomaterial surfaces (CN), a phenomenon bearing an acute influence upon the behavior and activity of CN–protein conjugates. Our benchmark molecular dynamics (MD) simulations demonstrate that protein adsorption is strongest on the concave CN surface, weakest on the convex surface, and intermediary on the planar surface, in agreement with recent experimental reports. For a better revelation of interaction, we performed high-level quantum chemical (QM) calculations with amino acid analogs (AAA) representing their five prominent classes, and convex, concave and planar CN fragments. Interestingly, our study revealed that the interaction trends of the high-level QM calculations were captured well by the empirical force field. The findings in this study have important bearing upon the design of carbon based bio-nanomaterials.

Chapter 7

We have investigated the effect of glycation into the process of early A β self-assembly using computer simulations in conjunction with experimental studies. Detailed biophysical assays establish that glycation decreases the lag phase of A β nucleation and accelerates fibril formation, while enhancing the overall β -sheet content and aggregate size. Fully atomistic MD simulations are exploited to obtain direct molecular insights into the process of early A β self-assembly in the presence and absence of glycated Lysine residues. Simulation results reveal that the enhanced interactions originate, in large part, due to markedly stronger, as well as new, inter-monomer salt bridging propensities in the glycated variety. Interestingly, these conformational and energetic effects are broadly

reflected in preformed protofibrillar forms of A β small oligomers modified with glycation. Our studies provide a basis for further mechanistic studies and therapeutic endeavors that could potentially result in novel ways of combating AGE related AD progression.

Abbreviations

AD	Alzheimer's Disease
A β	Amyloid beta
APP	Amyloid Precursor Protein
CHC	Central Hydrophobic Core
CHARMM	Chemistry at HARvard Macromolecular Mechanics
DFT	Density Functional Theory
DNA	Deoxyribonucleic acid
MM-GBSA	Molecular Mechanics-Genaralized Born Surface Area
HFIP	Hexafluroisopropanol
QM/MM	Quantum and Molecular Mechanics
H-bond	Hydrogen bond
IDP	Intrinsically Disordered Protein
LJ	Lennard-Jones
LBD	Lewy Body Disorder
MSD	Mean Square Displacements
MD	Molecular Dynamics
MM	Molecular Mechanics
QM	Quantum Mechanical
MC	Monte Carlo
NAMD	Nanoscale Molecular Dynamics
NMR	Nuclear Magnetic Resonance
PME	Particle Mesh Ewald
PCA	Principle Component Analysis
PDB	Protein Data Bank
RDFs	Radial Distribution Functions

R _g	Radius of Gyration
RMSD	Root Mean Squared Deviation
RMSF	Root Mean Squared Fluctuation
SASA	Solvent Accessible Surface Area
CNT	Carbon Nanotube
SWCNT	Single-Walled Carbon Nanotube
VMD	Visual Molecular Dynamics
HOMO	Highest Occupied Molecular Orbital
LUMO	Lowest Unoccupied Molecular Orbital
ABF	Adaptive Biasing Force
AGEs	Advanced Glycation End Products
RAGE	Receptors for Advanced Glycation End products
ThT	ThioflavinT
CD	Circular Dichroism
ssNMR	Solid-State Nuclear Magnetic Resonance
cPCA	Cartesian Principle Component Analysis
CML	Carboxymethyl Lysine
CN	Carbon Nanomaterial
AAA	Amino Acid Analogs
PCs	Principal Components
MWCNT	Multi-Walled Carbon Nanotube
vdW	van der Waals
WT	Wild Type Variant
PMF	Potential of Mean Force
AFM	Atomic Force Microscopy
MESP	Molecular Electrostatic Potential Maps
CNS	Carbon Nanomaterial Surface

List of Publications

1. **Asis K. Jana** and Neelanjana Sengupta. Adsorption Mechanism and Collapse Propensities of the Full-Length, Monomeric A β ₁₋₄₂ on the Surface of a Single-Walled Carbon Nanotube: A Molecular Dynamics Simulation Study. *Biophysical Journal*, **2012**, *102*, 1889–1896.
2. **Asis K. Jana**, Jaya C. Jose and Neelanjana Sengupta. Critical Roles of Key Domains in Complete Adsorption of A β Peptide on Single-Walled Carbon Nanotubes: Insights with Point Mutations and MD Simulations. *Physical Chemistry Chemical Physics*, **2013**, *15*, 837–844.
3. **Asis K. Jana** and Neelanjana Sengupta. Surface Induced Collapse of A β ₁₋₄₂ with the F19A Replacement Following Adsorption on a Single Walled Carbon Nanotube. *Biophysical Chemistry*, **2013**, *184*, 108–115.
4. Sneha B. Bansode, **Asis K. Jana**, Kedar B. Batkulwar, Shrikant D. Warkad, Rakesh S. Joshi, Neelanjana Sengupta and Mahesh J. Kulkarni. Molecular Investigations of Protriptyline as a Multi-Target Directed Ligand in Alzheimer's Disease. *PLOS ONE*, **2014**, *9*, e105196.
5. **Asis K. Jana** and Neelanjana Sengupta. A β Self-Association and Adsorption on a Hydrophobic Nanosurface: Competitive Effects and the Detection of Small Oligomers via Electrical Response. *Soft Matter*, **2015**, *11*, 269-279.
6. Sneha B. Bansode, Kedar B. Batkulwar, Shrikant D. Warkad, **Asis K. Jana**, Neelanjana Sengupta and Mahesh J. Kulkarni. Tolbutamide Induces Conformational Change and Promotes Albumin Glycation. *RSC Advances*, **2015**, *5*, 40070-40075.
7. **Asis K. Jana**, Mrityunjay Tiwari, Kumar Vanka and Neelanjana Sengupta. Unraveling Origins of the Heterogeneous Curvature Dependence of Polypeptide Interactions with Carbon Nanostructures. *Physical Chemistry Chemical Physics*, **2016**, *18*, 5910-5924.
8. **Asis K. Jana**, Kedar B. Batkulwar, Mahesh J. Kulkarni and Neelanjana Sengupta. Glycation Induces Conformational Changes in Amyloid- β Peptide and Enhances its Aggregation Propensity: Molecular Insights. (Under revision)

9. Kedar B. Batkulwar, **Asis K. Jana**, Rashmi K. Godbale, Neelanjana Sengupta and Mahesh J. Kulkarni. Hydralazine Prevents Amyloid beta (A β) Aggregation, Glycation and Ameliorates A β ₁₋₄₂ Induced Neurotoxicity. (Submitted)

Chapter – 1

General Introduction

Abstract

The physical process by which an unfolded polypeptide folds into its characteristic and functional three-dimensional structure at physiological conditions is known as ‘protein folding’. Failure of a protein to fold correctly into a functional native form, or ‘protein misfolding,’ may lead to physiological malfunctioning within living organisms. However, there exists a class of some proteins that are ‘intrinsically disordered’ at physiological conditions, and are therefore not associated with any uniquely folded state. This class of proteins is known as ‘intrinsically disordered proteins’ (IDPs). The absence of a stable native state can make an IDP very prone to misfolding and self-assembly, and can further seed intractable aggregates within cells or in extracellular space. The formation of insoluble aggregates within tissues, in the brain, heart and spleen leads to disorders including Alzheimer’s disease, spongiform encephalopathies and type II diabetes, respectively. The discovery of physico-chemical methods to prevent self-assembly of IDPs are therefore intricately associated with therapeutics for such diseases. Recently, carbon based nanomaterials have been found to interact with biological molecules, and their applicability and usage in biology and medicine is increasingly being considered. Interestingly, recent studies show that carbon based nanomaterials can directly influence the natural characteristics of amyloidogenic proteins as well as the rate of their assembly. However, understanding the mechanistic aspects of the influence of carbon nanoparticles on IDPs remains a key challenge. Therefore, detailed studies on carbon based nanomaterials with amyloidogenic proteins are necessitated, as this may open up new therapeutic advances for several proteopathic diseases.

1.1 Protein Folding

The mechanisms by which disordered polypeptide chains organize themselves into specific three-dimensional structures within relatively short time scales have begun to emerge in the last few decades.¹ Recent years have seen a revolution in experimental and computational techniques that can give near atomic-level description of the protein folding process in physiological media. In a cell, proteins are slowly biosynthesized within the ribosome, and the process of protein folding in some cases is co-translational,² i.e it starts before the completion of full protein synthesis. Other proteins undergo the major part of their folding in the cytoplasm after release from the ribosome.³ In the early 1960s, classic experiments conducted by Christian B. Anfinsen and co-workers on renaturation of denatured ribonuclease showed that folding is a reversible process, leading to an assumption that the completely folded protein exists in its global free energy minima.⁴ Soon afterward, in the late 1960s, Cyrus Levinthal recognized that due to the very large number of possible conformations of an unfolded polypeptide chain, it is impossible for a protein to attain its correctly folded native state within a biologically relevant time period by systematically sampling all the possible conformations.⁵ Levinthal hypothesized that protein folding must occur through specific ‘folding pathways’. However, several key questions remained. Particularly, is there a single pathway or multiple parallel routes by which an unfolded polypeptide folds to the native state? Further, how can one describe the protein folding landscape connecting the unfolded and folded state?

Thereafter, a very exciting approach the ‘folding funnel’ model based on the energy landscape theory emerged, which provided a quantitative description of the protein conformational space.⁶⁻¹⁰ In this model, protein folding can be regarded as going down the funnel-like energy landscape through multiple parallel routes from the large number of non-native conformations towards the native state around the bottom of the funnel.^{6, 8, 11} The bottom of the funnel represents the native state of the protein.^{6, 8, 11} The funnel-like free energy landscape of protein folding is shown in Figure 1.1. In the energy landscape, the horizontal axis represents the conformational degrees of freedom of the protein and the vertical axis is a measure of the free energy. Local free energy minima represent the transient kinetic traps. A huge number of the unfolded conformations are located at the upper surface of the funnel and possess higher conformational entropy, whereas only one unique native conformation with a global free energy minimum is located at the narrowest part of the

funnel, and has the lowest conformational entropy.

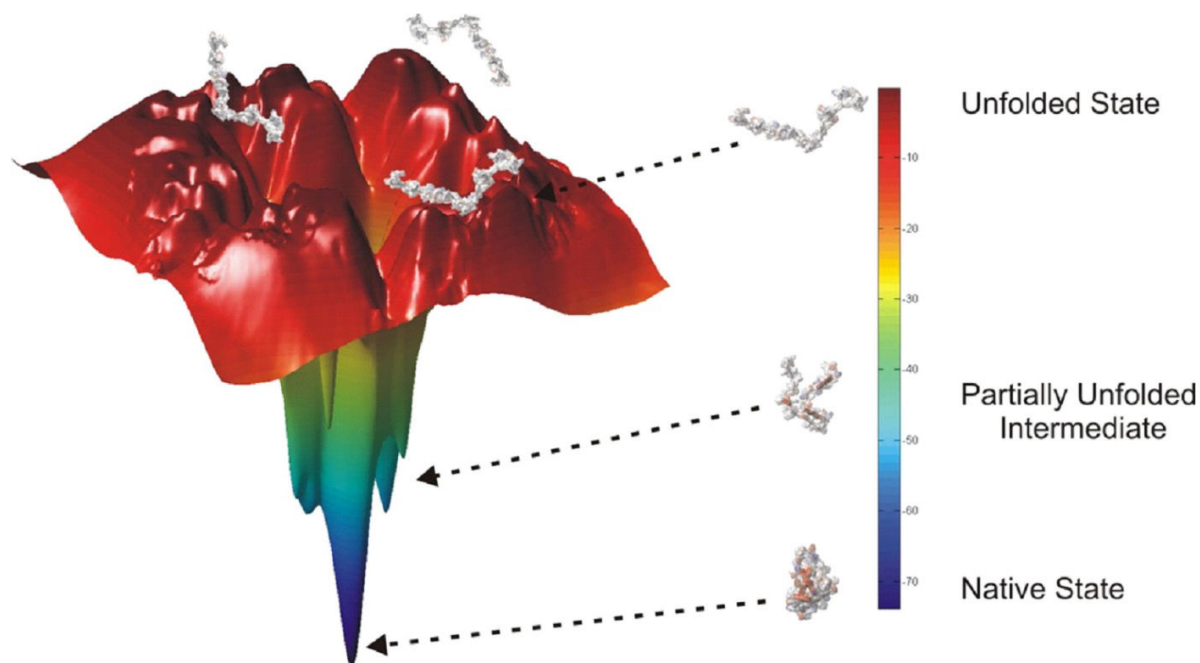


Figure 1.1: Schematic representation of a protein folding free-energy landscape. The bottom of the funnel represents the native state having lower free energy, whereas the unfolded state locate at the upper surface of the funnel having higher free energy values. Reproduced from Ref. 13 with permission from Nature publishing group.

The protein energy landscape, representing the change in a protein's energetics with its conformation, is largely depend on its amino acid sequence. The energy landscape is rugged, characterized by the presence of numerous local free energy minima.^{12, 13} An incompletely folded protein exists as heterogeneous conformations, and transient trapping in the local energy minima slow down the protein folding pathways. A Plethora of computational and theoretical studies, particularly using simulation techniques, have been performed to understand the protein folding pathway.^{14, 15} The results suggest that the random fluctuations of the unfolded polypeptide chain allow different segments of a protein to come close to or interact with each other.^{11, 14, 15} Once the key residues interact with each other or a native contact is formed, the rest of the structure evolves rapidly to generate the native state. On the other hand, if these native-like contacts are not formed, the unfolded protein can not reach to the native fold. Although the essential elements that drive the folding process are not yet clear, the hydrophobic effect and the inter-residue hydrogen bonding are thought to be predominant factors in triggering the folding pathway.^{16, 17} Conformational entropy loss during folding is compensated by the gain in enthalpy as more native contacts are formed.^{9, 11}

1.2 Intrinsically Disordered Proteins

Many proteins are noted to perform critical cellular functions, including transcription, translation, cell signaling and cell cycle control without possessing unique, three-dimensional native state structures.^{18, 19} Such proteins are highly abundant in nature, particularly in eukaryotes, and are generally termed as ‘intrinsically disordered proteins’ (IDPs) or ‘natively unfolded proteins’.^{18, 19} The discovery of IDPs clearly contradicts the traditional “protein structure-function” paradigm by demonstrating that the lack of perfectly folded compact three-dimensional structure does not preclude proteins from being biologically functional.²⁰ These proteins generally exist within highly dynamic and heterogeneous ensembles of rapidly interconverting conformations.²¹

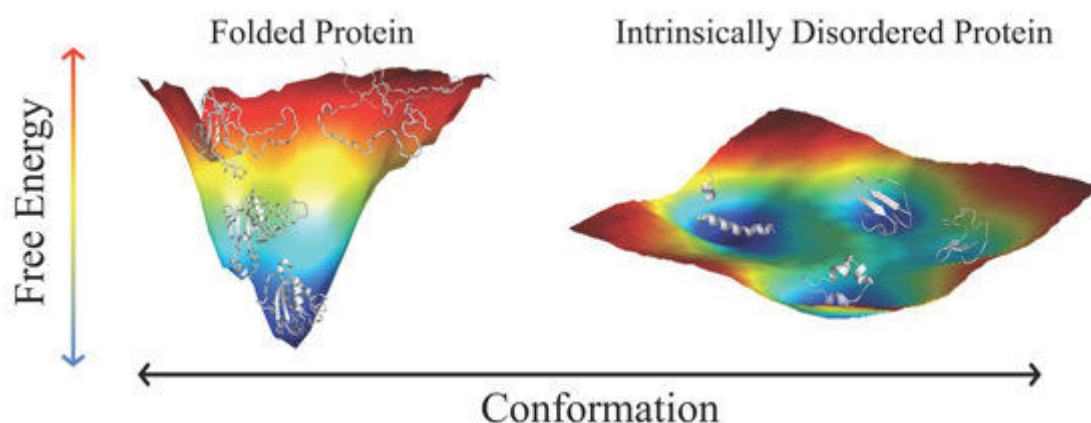


Figure 1.2: Schematic representation of energy landscape of folded protein and IDP. Reproduced from Ref. 23, distributed as open access under *Creative Commons Attribution License (CC BY)*.

IDPs are significantly different from the ordered globular proteins at the level of their amino acid contents and sequences.²² The difference of IDPs from the folded proteins can also be easily understood from their energy landscapes (shown in Figure 1.2). Unlike globular proteins, a typical IDP has a relatively flat energy landscape with a large number of equivalent local minima, separated by small energy barriers.²³ Rapid conformational transitions between the local minima enables an IDP to sample a large number of structurally dissimilar conformations. Thus, secondary structure populations and long range contacts in IDPs are very transient, and the overall structural propensities of IDPs are sensitive to the environmental conditions.²¹ Importantly, the inherent conformational disorder makes it very difficult to determine the ensemble average structure of IDPs using classic experimental methods such as Nuclear Magnetic Resonance (NMR) and X-ray diffraction techniques.^{23, 24}

No.	Diseases	Associated IDP	Number of residues	Native structure of IDP
1.	Alzheimer's disease	Amyloid beta (A β)	39-43	Natively unfolded
2.	Congophilic angiopathy	A β	39-43	Natively unfolded
3.	Spongiform encephalopathies	Prion protein	253	Natively unfolded (residues 1-120) and α -helical (121-230)
4.	Type II diabetes	Amylin	37	Natively unfolded
5.	Cardiovascular disease	Hirudin	65	N-terminal domain (1-39) folded and C-terminal domain (40-65) disordered
6.	Huntington's disease	Huntingtin with polyglutamine extension	3144	Largely natively unfolded
7.	Parkinson's disease	α -Synuclein	140	Natively unfolded
8.	Lewy Body Dementia	α -Synuclein	140	Natively unfolded
9.	Multiple system atrophy	α -Synuclein	140	Natively unfolded
10.	Pick's disease	Tau protein	352-441	Natively unfolded
11.	Fronto-temporal dementias	Tau protein	352-441	Natively unfolded

Table 1.1. List of diseases and the IDPs associated with the diseases. The number of residues and native structure of IDPs are also presented for comparison.

Since IDPs play central roles in a multitude of biological processes, and therefore it is not surprising that some of them are related to the pathogenesis of human diseases.^{25, 26} Some of these diseases and their corresponding IDPs are listed in Table 1.1. These diseases are often

termed as ‘protein conformational diseases’ as they are pathologically characterized by the conformational change and misfolding of IDPs leading to the formation of insoluble aggregates. Though the primary sequence of these IDPs vary significantly from one another, their similar cross- β sheet fibrillar aggregates suggests a common self-assembly pathway.²⁷ Probing the physico-chemical nature of their primary sequences and their association in self-assembly and fibril formation may reveal key interactions that need to be disrupted for preventing aggregation. This information can then be utilized to direct the design of new effective therapeutics.

1.2.1 The A β Peptide

Among the known neurodegenerative diseases, Alzheimer’s disease (AD) is the most common form of old-age related dementia. It accounts for more than 60% of the dementia cases worldwide and affects over 35 million people.²⁸ It is a chronic neurological disorder that affects the parts of the brain that are important for memory, thought and language.²⁹ There is no cure for this disease, which worsens as it progresses, and eventually leads to death. AD was first described by German psychiatrist and neuropathologist Alois Alzheimer in 1906.³⁰

Although the exact causes of AD remain unknown, current research indicates that this disease is strongly associated with the presence of insoluble plaques and tangles, comprised mainly of insoluble deposits of the amyloid beta (A β) peptide and the tau protein, respectively, in the hippocampus and cortex of the human brain.³⁰ Numerous hypotheses have attempted to explain the etiology of AD. According to the widely accepted *amyloid cascade hypothesis*, self-assembly of 39-43 residue A β peptide into insoluble aggregates is the key causative factor responsible for the onset of AD.²⁹ Interestingly, emerging research suggests that the disordered and soluble oligomers of A β may be the more neurotoxic species than the insoluble aggregates.³¹

The A β peptide is produced from the ~700 residue amyloid precursor protein (APP), a transmembrane protein by sequential endoproteolytic cleavage, catalyzed by β - and γ -secretases (shown in Figure 1.3).³² Variable cleavage by secretase enzymes generates A β peptides of various lengths, with the 42 residue variant A β ₁₋₄₂, being the most neurotoxic.^{33, 34} A number of mutations in APP near the β and γ secretase cleavage sites promote more production of A β .³⁵ In addition to this, there are six pathogenic mutations in A β at amino

acid positions 21 through 23: the Flemish A21G mutation, Arctic E22G mutation, Dutch E22Q mutation, Italian E22K mutation, Osaka E22 Δ mutation and Iowa D23N mutation.³⁶ These mutations change the inherent nature of A β peptide, and both *in vivo* and *in vitro* studies have found that except the Flemish mutation, the aggregation propensities of Arctic, Dutch, Italian and Iowa mutants are higher compared to pure-A β ₄₂.³⁷⁻⁴⁰ Prior to enzymatic cleavage and within APP, the A β sequence is thought to be primarily of helical conformation, and undergo conformational transitions to predominantly beta sheet forms after release into aqueous cytoplasm.^{41, 42}

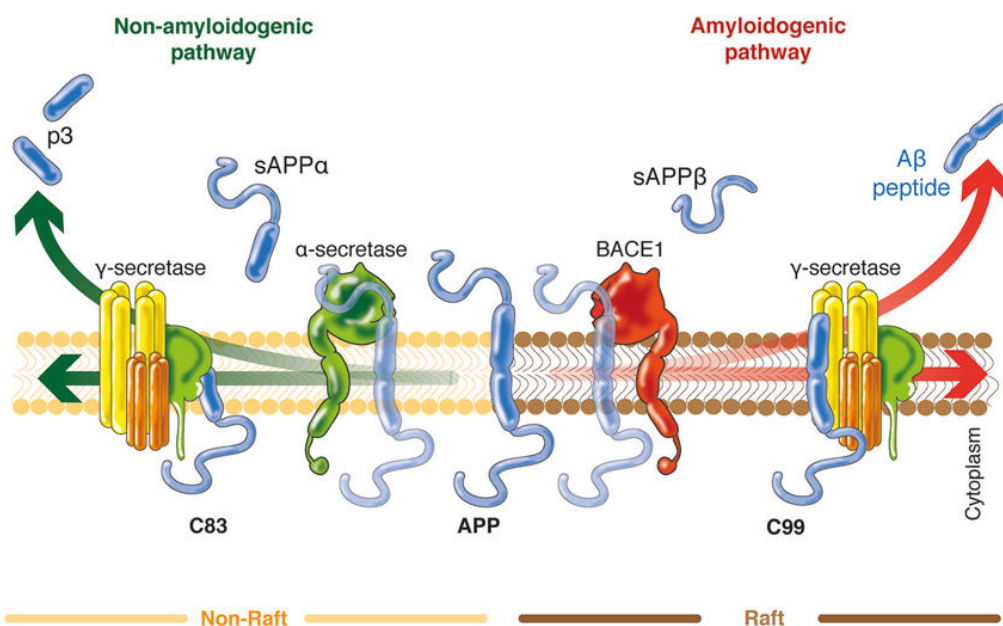


Figure 1.3: Schematic representation of A β production from proteolytic cleavage of amyloid precursor protein. Reproduced from Ref. 32, distributed as open access under *Creative Commons Attribution License (CC BY)*.

Experimentally determining the monomeric and oligomeric structures of A β in aqueous solution is not a very straightforward process due to the very rapid aggregation of A β in water.⁴³ However, some experimental evidences indicate the important key regions of A β in the aggregation process. Solution NMR studies implicate the β -strand propensities in the Central hydrophobic core (CHC; L₁₇VFFA₂₁) and C-terminal region (G₂₉AIIGLMVGGVVIA₄₂) in A β ₁₋₄₂.⁴⁴ Circular dichroism (CD) spectra study further suggest a significant overall β -sheet content in the monomers.⁴⁵ Due to limitations of experimental techniques, several research groups have turned to theoretical simulations to thoroughly investigate the structural properties of A β monomers.⁴⁶⁻⁴⁸ Several simulation studies using different force fields and different sampling techniques revealed that the A β monomer is

mostly disordered in aqueous media, but possesses some extent of β -sheet propensities in particular in the CHC and C-terminal regions.^{49, 50} Greater β -sheet propensity in $A\beta$ is associated with higher aggregation propensity, compared to the peptide conformations with α -helical and random coil conformations.^{51, 52} This antiparallel β -hairpin conformation is characterized by a hydrophilic turn flanked by β -sheet forming regions composed of the CHC and the C-terminal region at both ends. Interestingly, emerging research suggests that this β -hairpin structure can accelerate the fibril formation by reducing the lag phase of amyloid formation, and has been considered to be a common motif in the self-assembly processes of other disease-causing IDPs such as the prion protein and the human islet amyloid polypeptide.^{53, 54} A schematic representation of aggregation pathway of $A\beta$ is shown in Figure 1.4.

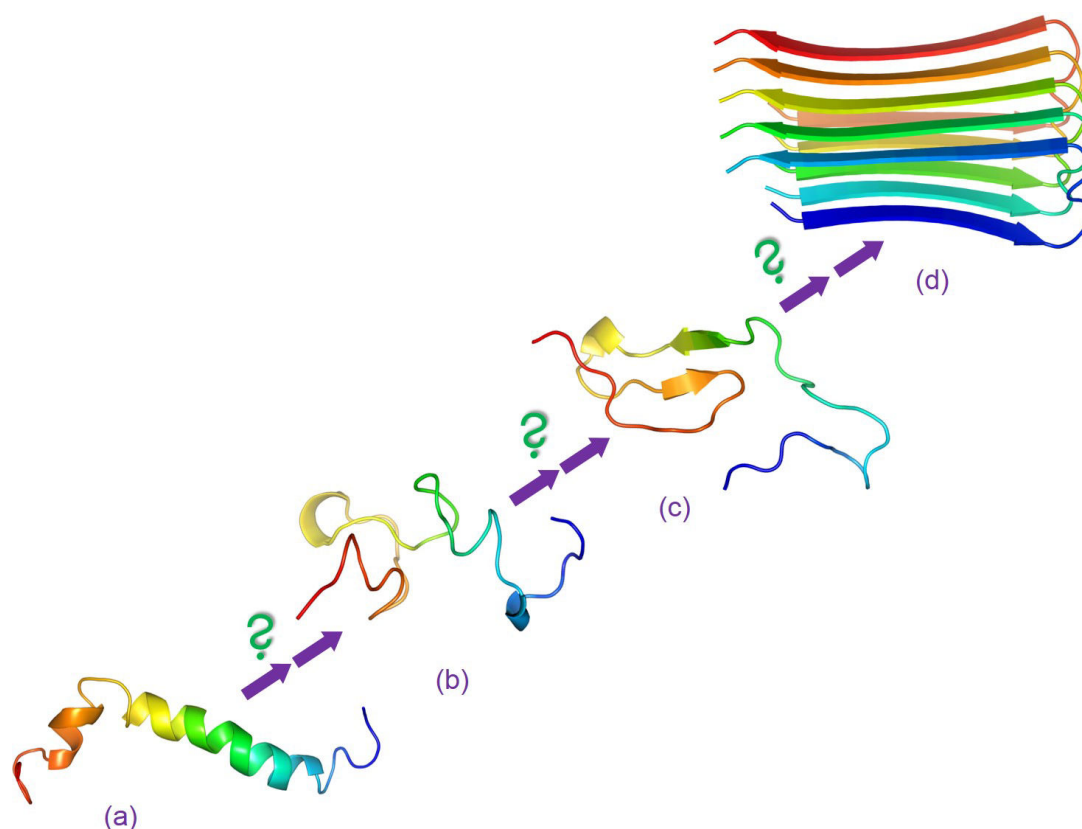


Figure 1.4: Schematic representation of aggregation pathway of $A\beta$. Largely helical conformation of $A\beta_{1-42}$ monomer (a) is taken from solution NMR study of $A\beta_{1-42}$ in hexafluoro-2-propanol and water mixture,⁴³ this and other related structures have been considered analogous to that of freshly cleaved peptide upon release from APP into aqueous cytoplasm.^{42, 55} $A\beta$ structures in (b) and (c) represent the $A\beta$ monomeric structure ensemble in aqueous environment, which are structurally similar with formerly reported experimental and simulation data.^{44, 56} $A\beta$ fibrillar structure (d) is taken from Luhrs et al.⁵⁷

1.2.2 A β Self-Assembly

A β aggregation pathway involves a cascade of events including misfolding, conformation changes and intermolecular interactions that drive the disordered monomers to amyloid fibril formation. Amyloid fibrils are generally characterized by highly organized and insoluble protein aggregates with cross- β sheet structural motif.⁵⁸ Diameter of these fibrils range within 70 to 120 Å, and have a length of 1 μ m.⁵⁹ Interestingly, emerging research suggest that hydrophobic interactions between the side-chains and backbone hydrogen bonding are two major driving forces that stabilize the fibrillar structures. The A β aggregation pathway can be triggered by several physical and chemical factors like changes in ionic strength, temperature, pH, oxidative stress, interactions with metal ions and lipid molecules, etc.^{11, 14, 60}

Although the exact mechanism of A β aggregate formation is still under debate, several studies suggest that A β aggregate formation occurs through a nucleation-dependent polymerization process.⁶¹⁻⁶³ On the basis of kinetic experimental studies, A β fibril formation is believed to follow a two stage process: a nucleation (lag) phase, and a fibril elongation (growth) phase.^{61, 64} During the nucleation stage, unstructured A β monomers assemble reversibly one by one or in groups and form nuclei. This step is thermodynamically unfavorable and is considered as a rate limiting step. Once the critical size is reached, the further addition of a monomer to the nuclei is thermodynamically favoured and the nuclei quickly form protofibrils, which can further elongate to form stable fibrils by the addition of incoming monomer to the protofibril.

The mechanistic details of A β fibrillar growth have been the subject of numerous experimental and computational studies.⁶⁵⁻⁶⁸ Kinetic studies proposed a two step “dock-lock” growth mechanism⁶⁹: incoming A β monomers first reversibly bind (“dock”) to the fibril ends, and after making initial fibrillar contacts in irreversible locking step, they undergo structural rearrangements to adopt β -strand conformation. Kinetic studies also showed that for A β ₁₋₄₂, the docking step is 10⁴ times faster than locking step.⁶⁷ To understand the atomic details, several simulation studies have been performed.^{65, 66, 70} Simulation results revealed that the CHC domain exhibits strong propensity for initial fibrillar contacts compared to the other regions, suggesting key roles of this segment in driving initial fibril elongation.⁶⁵ Simulation studies also revealed that when the CHC of incoming monomer forms initial contacts with the fibrillar surface, it tends to form β -hairpin conformations involving antiparallel contacts between the CHC and C-terminal region.⁶⁵ This finding suggests direct

evidence that β -hairpin A β monomeric structures are on-pathway intermediates during the fibril elongation stage.⁶⁵ Interestingly, a growing number of *in vivo* and *in vitro* studies suggest that the process of A β aggregation is significantly affected by various post-translational modifications such as phosphorylation, pyroglutamination, glycation etc.^{71, 72} Post-translational modifications of A β enhances its aggregation propensity and cytotoxicity and can serve as a template for enhanced aggregation.

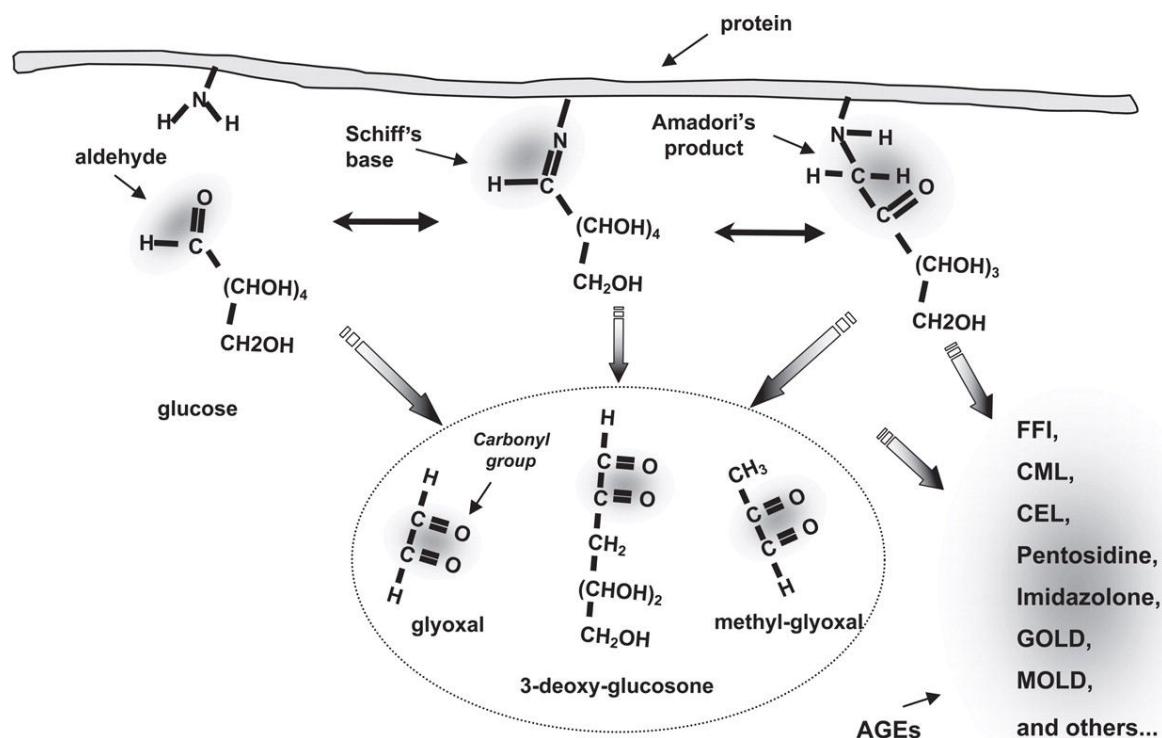


Figure 1.5: A schematic representation of possible pathways for AGEs formation. Reproduced from Ref. 78 with permission from Oxford University Press.

Of the several post-translational modifications possible, the nonenzymatic process of glycation has been implicated as one of the major determining factors involved in the enhancement of A β self-assembly and fibrillogenesis.^{73, 74} Clinical and epidemiological studies indicate diabetes as one of the major risk factor for developing AD⁷⁵⁻⁷⁷, and the AD brain shows higher concentration of Advanced Glycation End products (or AGEs) and the Receptors for Advanced Glycation End Products (RAGEs) similar to diabetes. AGEs are formed by the Maillard chemical process, which refers to a series of parallel and sequential non-enzymatic reactions involving carbonyl group of reducing sugars or reactive dicarbonyls like methyl glyoxal or glyoxal, and free amino acid residues, especially N- ϵ -amino group of Lysine and Arginine.^{78, 79} A schematic representation of possible pathways for AGEs

formation is shown in Figure 1.5. The amino acids Lysine and Arginine can be variously modified with AGEs.⁷⁹ N(6)-Carboxy methyl lysine is one of the major AGE structure reported so far.⁸⁰ AGE formation leads to several types of cellular damage including abnormal protein structure-function, inflammation, oxidative stress and RAGE activation.⁸¹⁻⁸³ Importantly, recent research studies suggest that glycation of A β results in distinctly faster rates of fibril formation along with greater β -sheet propensities and larger aggregate sizes.^{74,84} Despite its emerging relevance in AD progression, the underlying molecular mechanism that potentially affects fibril formation in glycated A β has not been known till date.

1.2.3 Influence of Nanomaterials on A β Aggregation

Nanoparticles are materials whose dimensions lie in the range of 1-100 nm, and owing to their small size, are characterized by a very large surface to volume ratio.⁸⁵ Owing to their ultra-small size and large surface to volume ratio, these particles exhibit unique and distinct physico-chemical properties, which are not seen in the bulk form of the corresponding materials. Some characteristics attributed to nanomaterials are high aspect ratio and surface area, high mechanical strength, ultralight weight, exceptional thermal conductivity, which make them suitable for many novel applications in optical and electronic devices.^{86, 87} Further, nanomaterials have unique abilities to interact with and influence the behavior of biological systems.^{88, 89} Importantly, they have been noted to easily enter almost all parts of the body, including the human brain.⁹⁰ Interaction of nanoparticles with living organisms have opened up several applications in medicine and diagnostics,⁸⁹ including biomolecular sensors,⁹¹ therapeutics⁹² and drug delivery,⁹³ although several issues pertaining to their cytotoxicity and potential side effects need to be suitably addressed.^{94, 95}

One of the potential therapeutic and diagnostic applications of nanomaterials and nanoparticles is to harness their effect on protein aggregation process and thereby combat the progression of neurodegenerative proteopathies. Emerging research demonstrates that nanoparticles can play differential roles on IDP self-assembly pathways.⁹⁶⁻⁹⁹ Broadly speaking, the large surface area of nanoparticles enhance their protein adsorption capacity, leading to surface localization of the protein, and reducing energetic barriers for protein aggregation. However localization of a protein may also block active sites essential for fibril formation. So, there is a critical balance between the effect of nanoparticles on the protein aggregation, either as an accelerative or inhibitory effect, depending on the material's physico-chemical properties, concentration, temperature or pH of the solution, etc.^{98, 100} Linse

and co-authors have observed that various kinds of nanoparticles, such as uncharged copolymeric N-isopropyl acrylamide (NIPAM) nanoparticles, cerium oxide particles and quantum dots increase the probability of critical nucleus formation of the human protein β -microglobulin associated with dialysis-related amyloidosis; thereafter, the fibrillation proceeds rapidly.¹⁰¹ Several studies have also reported that gold and hydrophilic TiO₂ nanoparticles can accelerate the rates of A β fibril formation.¹⁰²⁻¹⁰⁴ Interestingly, one striking observation is that commercial polystyrene nanoparticles with amino modification shows a dual effect on the A β fibrillation process.⁹⁸ Depending on the nanoparticle concentration, A β aggregation is accelerated by reducing the lag phase at lower particle concentration, while at higher particle concentration, the aggregation process is reduced by increasing the lag phase.

It is noteworthy here that emerging research suggests possible inhibitory actions of some key nanomaterials on the protein aggregation process.¹⁰⁵⁻¹⁰⁸ Particularly, various kinds of carbon based nanoparticles such as fullerene (C₆₀), graphene oxide, single-walled carbon nanotubes (SWCNTs) can have strong inhibitory influence on A β fibrillation.^{105, 107, 109} Kim and Lee first showed that 1,2-(dimethoxymethano) fullerene decreases the A β aggregation process by preferentially binding to the K₁₆LVFF₂₀ segment of the A β peptide.¹⁰⁵ Simulation study showed that fullerene can destabilize the A β fibrillar structure by disrupting the intra- and inter-molecular salt-bridges in the turn region of the protein.¹¹⁰ Further, fullerene can also entrap free radicals and reduce their life-time;¹¹¹ this property has been considered to make fullerene a potential candidate for AD therapeutic designs. Further study show that the A β ₂₅₋₃₅ segment forms β -barrel in the presence of the hydrophobic SWCNT surface and therefore may hinder further self-assembly.¹⁰⁶ Mahmoudi *et. al.* recently found that graphene oxide strongly, inhibits the A β aggregation by increasing the lag phase of A β fibrillation through the peptide's adsorption on the surface.¹⁰⁷ These data clearly suggest a role for carbon based nanoparticles as modulators of A β aggregation process.

1.3 Motivation and Outline of Thesis

As discussed thus far, self-assembly and aggregation of the A β peptide, produced from proteolytic cleavage of the large, transmembrane precursor protein (APP) in predominantly aqueous media, is considered a key causative factor in the onset and progression of the neurodegenerative Alzheimer's disease (AD). A prerequisite for the development of suitable therapeutics for preventing or halting the progression of this debilitating disease is a complete understanding of the mechanistic aspects of A β self-assembly, including the

pathways leading to the nucleation and further growth and the roles therein of specific residues and regions within the A β sequence. While a lot of details emerge from recent experimental efforts, the molecular aspects that underlie the self-assembly process have remained elusive, in large part due to the rapid *in vitro* aggregation of the peptide in aqueous solution. Such experimental limitations are beginning to be overcome with extensive computer simulations that are capable of providing a ‘bottoms-up’ picture that, in addition to structural and molecular aspects, can provide details of the interplay amongst the various thermodynamic factors.

A detailed, molecular-level understanding of the processes of A β self-assembly and aggregation should immensely aid the search for suitable molecular interventions to the formation of toxic assemblies associated with AD. Carbon nanomaterials have recently emerged as unique materials capable of strongly interacting with and influencing biomolecular behavior. Importantly, their significant influence on the A β segmental aggregates suggest that they may potentially be of importance in the design of AD therapeutics. However, this requires molecular level studies of how such materials can modulate the intrinsic characteristics of the monomeric and multimeric forms of the A β peptide. This thesis presents detailed mechanistic studies, with fully atomistic molecular dynamics (MD) simulations, of how an important form of these materials, namely single-walled carbon nanotubes (SWCNTs) of high curvature, interacts with and adsorbs the full-length A β peptide, and further modulates the energetics of its self-assembly. The role of the surface curvature of carbon materials in influencing the interactions is further elicited in detail. In addition, the role of a post-translational modification, namely that of glycation, in influencing the energetics of A β self-assembly is studied in conjunction with experimental data.

1.4 References

1. M. Vendruscolo, J. Zurdo, C. E. MacPhee and C. M. Dobson, *Phil. Trans. R. Soc. Lond.*, 2003, **361**, 1205-1222.
2. B. Hardesty and G. Kramer, *Prog. Nucleic Acid Res. Mol. Biol.*, 2000, **66**, 41-66.
3. B. Bukau and A. L. Horwich, *Cell*, 1998, **92**, 351-366.
4. C. B. Anfinsen, E. Haber, M. Sela and F. White, *Proc. Natl. Acad. Sci.*, 1961, **47**, 1309-1314.

5. C. Levinthal, *J. Chim. Phys.*, 1968, **65**, 44-45.
6. P. G. Wolynes, J. N. Onuchic and D. Thirumalai, *Science*, 1995, **267**, 1619-1619.
7. H. Frauenfelder, S. G. Sligar and P. G. Wolynes, *Science*, 1991, **254**, 1598-1603.
8. K. A. Dill and H. S. Chan, *Nat. Struct. Biol.*, 1997, **4**, 10-19.
9. J. D. Bryngelson, J. N. Onuchic, N. D. Socci and P. G. Wolynes, *Proteins: Struct. Funct. Bioinf.*, 1995, **21**, 167-195.
10. D. Wales, *Energy landscapes: Applications to clusters, biomolecules and glasses*, Cambridge University Press, Cambridge, 2003.
11. C. M. Dobson, *Nature*, 2003, **426**, 884-890.
12. S. S. Plotkin, J. Wang and P. G. Wolynes, *Phys. Rev. E*, 1996, **53**, 6271.
13. A. Quintas, *OA Biochemistry*, 2013, **1**, 1-8.
14. C. M. Dobson, *Trends Biochem. Sci.*, 1999, **24**, 329-332.
15. D. Thirumalai and G. Reddy, *Nat. Chem.*, 2011, **3**, 910-911.
16. K. A. Dill, *Biochemistry*, 1990, **29**, 7133-7155.
17. H. Li, C. Tang and N. S. Wingreen, *Phys. Rev. Lett.*, 1997, **79**, 765.
18. P. Tompa, *Trend Biochem. Sci.*, 2012, **37**, 509-516.
19. V. N. Uversky, C. J. Oldfield and A. K. Dunker, *Annu. Rev. Biophys.*, 2008, **37**, 215-246.
20. P. Tompa, *FEBS Lett.*, 2005, **579**, 3346-3354.
21. S. Kosol, S. Contreras-Martos, C. Cedeño and P. Tompa, *Molecules*, 2013, **18**, 10802-10828.
22. P. Romero, Z. Obradovic, X. Li, E. C. Garner, C. J. Brown and A. K. Dunker, *Proteins: Struct. Funct. Bioinf.*, 2001, **42**, 38-48.
23. V. M. Burger, T. Gurry and C. M. Stultz, *Polymers*, 2014, **6**, 2684-2719.
24. M. R. Jensen and M. Blackledge, *Proc. Natl. Acad. Sci.*, 2014, **111**, E1557-E1558.
25. V. N. Uversky, C. J. Oldfield and A. K. Dunker, *Annu. Rev. Biophys.*, 2008, **37**, 215-246.
26. V. N. Uversky, *Front. Aging Neurosci.*, 2015, **7**.
27. M. Sunde, L. C. Serpell, M. Bartlam, P. E. Fraser, M. B. Pepys and C. C. F. Blake, *J. Mol. Biol.*, 1997, **273**, 729.

28. I. W. Hamley, *Chem. Rev.*, 2012, **112**, 5147-5192.
29. J. Hardy and D. J. Selkoe, *Science*, 2002, **297**, 353.
30. M. Graeber, S. Kösel, R. Egensperger, R. Banati, U. Müller, K. Bise, P. Hoff, H. Möller, K. Fujisawa and P. Mehraein, *Neurogenetics*, 1997, **1**, 73-80.
31. C. Haass and D. J. Selkoe, *Nat. Rev. Mol. Cell Biol.*, 2007, **8**, 101-112.
32. J. M. Zolezzi, S. Bastías-Candia, M. J. Santos and N. C. Inestrosa, *Front. Aging Neurosci.*, 2014, **6**.
33. M. Q. Liao, Y. J. Tzeng, L. Y. X. Chang, H. B. Huang, T. H. Lin, C. L. Chyan and Y. C. Chen, *FEBS Lett.*, 2007, **581**, 1161-1165.
34. O. Bugiani, *Neurol. Sci.*, 2011, **32**, 1241-1247.
35. P. H. St George-Hyslop, *Biol. Psychiatry*, 2000, **47**, 183-199.
36. M. Goedert and M. G. Spillantini, *Science*, 2006, **314**, 777-781.
37. N. L. Fawzi, K. L. Kohlstedt, Y. Okabe and T. Head-Gordon, *Biophys. J.*, 2008, **94**, 2007-2016.
38. L. M. Luheshi, G. G. Tartaglia, A.-C. Brorsson, A. P. Pawar, I. E. Watson, F. Chiti, M. Vendruscolo, D. A. Lomas, C. M. Dobson and D. C. Crowther, *PLoS Biol.*, 2007, **5**, e290.
39. M. G. Krone, A. Baumketner, S. L. Bernstein, T. Wyttenbach, N. D. Lazo, D. B. Teplow, M. T. Bowers and J.-E. Shea, *J. Mol. Biol.*, 2008, **381**, 221-228.
40. D. M. Walsh, A. Lomakin, G. B. Benedek, M. M. Condron and D. B. Teplow, *J. Biol. Chem.*, 1997, **272**, 22364-22372.
41. D. B. Teplow, *Amyloid*, 1998, **5**, 121-142.
42. Y. Xu, J. Shen, X. Luo, W. Zhu, K. Chen, J. Ma and H. Jiang, *Proc. Natl. Acad. Sci. U.S.A.*, 2005, **102**, 5403-5407.
43. T. Simona, E. Veronica, V. Paolo, A. J. v. N. Nico, M. J. J. B. Alexandre, G. Remo, T. Teodorico, A. T. Piero and P. Delia, *ChemBioChem*, 2006, **7**, 257-267.
44. L. Hou, H. Shao, Y. Zhang, H. Li, N. K. Menon, E. B. Neuhaus, J. M. Brewer, I.-J. L. Byeon, D. G. Ray, M. P. Vitek, T. Iwashita, R. A. Makula, A. B. Przybyla and M. G. Zagorski, *J. Am. Chem. Soc.*, 2004, **126**, 1992-2005.
45. K. Ono, M. M. Condron and D. B. Teplow, *Proc. Natl. Acad. Sci.*, 2009, **106**, 14745-14750.
46. D. J. Rosenman, C. R. Connors, W. Chen, C. Wang and A. E. García, *J. Mol. Biol.*, 2013, **425**, 3338-3359.
47. Y.-S. Lin, G. R. Bowman, K. A. Beauchamp and V. S. Pande, *Biophys. J.*, 2012, **102**,

- 315-324.
48. A. Baumketner and J.-E. Shea, *J. Mol. Biol.*, 2007, **366**, 275-285.
 49. S. Côté, P. Derreumaux and N. Mousseau, *J. Chem. Theory Comput.*, 2011, **7**, 2584-2592.
 50. N. G. Sgourakis, Y. Yan, S. A. McCallum, C. Wang and A. E. Garcia, *J. Mol. Biol.*, 2007, **368**, 1448-1457.
 51. M. G. Zagorski and C. J. Barrow, *Biochemistry*, 1992, **31**, 5621-5631.
 52. D. Burdick, B. Soreghan, M. Kwon, J. Kosmoski, M. Knauer, A. Henschen, J. Yates, C. Cotman and C. Glabe, *J. Biol. Chem.*, 1992, **267**, 546-554.
 53. Q. Qiao, G. R. Bowman and X. Huang, *J. Am. Chem. Soc.*, 2013, **135**, 16092-16101.
 54. M. Grabenauer, C. Wu, P. Soto, J.-E. Shea and M. T. Bowers, *J. Am. Chem. Soc.*, 2010, **132**, 532-539.
 55. C. Lee and S. Ham, *J. Comput. Chem.*, 2010, **32**, 349-355.
 56. D. J. Rosenman, C. Wang and A. E. Garcia, *J. Phys. Chem. B*, 2015, **120**, 259-277.
 57. T. Lührs, C. Ritter, M. Adrian, D. Riek-Loher, B. Bohrmann, H. Döbeli, D. Schubert and R. Riek, *Proc. Natl. Acad. Sci. U.S.A.*, 2005, **102**, 17342-17347.
 58. K. A. Ball, A. H. Phillips, P. S. Nerenberg, N. L. Fawzi, D. E. Wemmer and T. Head-Gordon, *Biochemistry*, 2011, **50**, 7612-7628.
 59. C. K. Hall, *AIChE J.*, 2008, **54**, 1956-1962.
 60. T. R. Jahn and S. E. Radford, *FEBS J.*, 2005, **272**, 5962-5970.
 61. J. D. Harper and P. T. Lansbury Jr, *Annu. Rev. Biochem.*, 1997, **66**, 385-407.
 62. H. Naiki and F. Gejyo, *Methods Enzymol.*, 1999, **309**, 305-318.
 63. S. Kumar and J. Walter, *Aging (Albany NY)*, 2011, **3**, 803-812.
 64. S. Burgold, S. Filser, M. M. Dorostkar, B. Schmidt and J. Herms, *Acta Neuropathol. Commun.*, 2014, **2**, 1.
 65. W. Han and K. Schulten, *J. Am. Chem. Soc.*, 2014, **136**, 12450-12460.
 66. E. P. O'ÄöBrien, Y. Okamoto, J. E. Straub, B. R. Brooks and D. Thirumalai, *J. Phys. Chem. B*, 2009, **113**, 14421-14430.
 67. W. Qiang, K. Kelley and R. Tycko, *J. Am. Chem. Soc.*, 2013, **135**, 6860-6871.
 68. T. Ban, K. Yamaguchi and Y. Goto, *Acc. Chem. Res.*, 2006, **39**, 663-670.
 69. W. P. Esler, E. R. Stimson, J. M. Jennings, H. V. Vinters, J. R. Ghilardi, J. P. Lee, P.

- W. Mantyh and J. E. Maggio, *Biochemistry*, 2000, **39**, 6288-6295.
70. G. Reddy, J. E. Straub and D. Thirumalai, *Proc. Natl. Acad. Sci.*, 2009, **106**, 11948-11953.
71. D. J. Selkoe, *J. Biol. Chem.*, 1996, **271**, 18295-18298.
72. C. S. Atwood, R. N. Martins, M. A. Smith and G. Perry, *Peptides*, 2002, **23**, 1343-1350.
73. A. Lapolla, D. Fedele and P. Traldi, *Clin. Chim. Acta*, 2005, **357**, 236-250.
74. X. Li, L. Du, X. Cheng, X. Jiang, Y. Zhang, B. Lv, R. Liu, J. Wang and X. Zhou, *Cell Death Dis.*, 2013, **4**, e673.
75. J. Götz, L. Ittner and Y.-A. Lim, *Cell. Mol. Life Sci.*, 2009, **66**, 1321-1325.
76. Y. Yang and W. Song, *Neuroscience*, 2013, **250**, 140-150.
77. L. Li and C. Hölscher, *Brain Res. Rev.*, 2007, **56**, 384-402.
78. G. Basta, A. M. Schmidt and R. De Caterina, *Cardiovasc. Res.*, 2004, **63**, 582-592.
79. R. Singh, A. Barden, T. Mori and L. Beilin, *Diabetologia*, 2001, **44**, 129-146.
80. S. Reddy, J. Bichler, K. J. Wells-Knecht, S. R. Thorpe and J. W. Baynes, *Biochemistry*, 1995, **34**, 10872-10878.
81. K. B. Batkulwar, S. B. Bansode, G. V. Patil, R. K. Godbole, R. S. Kazi, S. Chinnathambi, D. Shanmugam and M. J. Kulkarni, *Proteomics*, 2015, **15**, 245-259.
82. S. Lovestone and U. Smith, *Proc. Natl. Acad. Sci.*, 2014, **111**, 4743-4744.
83. A. S. Charonis and E. C. Tsilibary, *Diabetes*, 1992, **41**, 49-51.
84. B. Kuhla, H. J. LÜTH, D. Haferburg, K. Boeck, T. Arendt and G. Münch, *Ann. N. Y. Acad. Sci.*, 2005, **1043**, 211-216.
85. H. S. Sharma, S. Hussain, J. Schlager, S. F. Ali and A. Sharma, *Acta Neurochir. Suppl.*, 2010, **106**, 359-364.
86. A. N. Shipway, E. Katz and I. Willner, *Chem. Phys. Chem.*, 2000, **1**, 18-52.
87. F. E. Kruis, H. Fissan and A. Peled, *J. Aerosol Sci.*, 1998, **29**, 511-535.
88. Y. Wenrong, P. Thordarson, J. J. Gooding, S. P. Ringer and F. Braet, *Nanotechnology*, 2007, **18**, 412001.
89. L. Lacerda, A. Bianco, M. Prato and K. Kostarelos, *Adv. Drug Deliv. Rev.*, 2006, **58**, 1460-1470.
90. J. M. Koziara, P. R. Lockman, D. D. Allen and R. J. Mumper, *J. Pharm. Res.*, 2003, **20**, 1772-1778.

91. B. Luan and R. Zhou, *J. Phys. Chem. Lett.*, 2012, **3**, 2337-2341.
92. A. Bianco, K. Kostarelos and M. Prato, *Curr. Opin. Chem. Biol.*, 2005, **9**, 674-679.
93. A. A. Bhirde, V. Patel, J. Gavard, G. Zhang, A. A. Sousa, A. Masedunskas, R. D. Leapman, R. Weigert, J. S. Gutkind and J. F. Rusling, *ACS Nano*, 2009, **3**, 307-316.
94. K. Kostarelos, *Nat. Biotechnol.*, 2008, **26**, 774-776.
95. G. Zuo, Q. Huang, G. Wei, R. Zhou and H. Fang, *ACS Nano*, 2010, **4**, 7508-7514.
96. M. Mahmoudi, H. R. Kalhor, S. Laurent and I. Lynch, *Nanoscale*, 2013, **5**, 2570-2588.
97. R. Vácha, S. Linse and M. Lund, *J. Am. Chem. Soc.*, 2014, **136**, 11776-11782.
98. C. Cabaleiro-Lago, F. Quinlan-Pluck, I. Lynch, K. A. Dawson and S. Linse, *ACS Chem. Neurosci.*, 2010, **1**, 279-287.
99. C. Cabaleiro-Lago, I. Lynch, K. A. Dawson and S. Linse, *Langmuir*, 2009, **26**, 3453-3461.
100. A. A. Shemetov, I. Nabiev and A. Sukhanova, *ACS Nano*, 2012, **6**, 4585-4602.
101. S. Linse, C. Cabaleiro-Lago, W.-F. Xue, I. Lynch, S. Lindman, E. Thulin, S. E. Radford and K. A. Dawson, *Proc. Natl. Acad. Sci.*, 2007, **104**, 8691-8696.
102. J. Jose and N. Sengupta, *Eur. Biophys. J.*, 2013, **42**, 487-494.
103. W.-h. Wu, X. Sun, Y.-p. Yu, J. Hu, L. Zhao, Q. Liu, Y.-f. Zhao and Y.-m. Li, *Biochem. Biophys. Res. Commun.*, 2008, **373**, 315-318.
104. Q. Ma, G. Wei and X. Yang, *Nanoscale*, 2013, **5**, 10397-10403.
105. J. E. Kim and M. Lee, *Biochem. Biophys. Res. Commun.*, 2003, **303**, 576-579.
106. Z. Fu, Y. Luo, P. Derreumaux and G. Wei, *Biophys. J.*, 2009, **97**, 1795-1803.
107. M. Mahmoudi, O. Akhavan, M. Ghavami, F. Rezaee and S. M. A. Ghiasi, *Nanoscale*, 2012, **4**, 7322-7325.
108. A. V. Ghule, K. M. Kathir, T. K. S. Kumar, S.-H. Tzing, J.-Y. Chang, C. Yu and Y.-C. Ling, *Carbon*, 2007, **45**, 1586-1589.
109. H. Li, Y. Luo, P. Derreumaux and G. Wei, *Biophys. J.*, 2011, **101**, 2267-2276.
110. S. A. Andujar, F. Lugli, S. Hofinger, R. D. Enriz and F. Zerbetto, *Phys. Chem. Chem. Phys.*, 2012, **14**, 8599-8607.
111. P. KRUsrc, E. Wasserman, P. Keizer and I. Morton, *Science*, 1991, **254**, 1183-1185.

Chapter – 2

Molecular Dynamics Simulations: A Brief Overview

Abstract

Computational and theoretical models are well accepted research methodologies for understanding the physics and chemistry of complex molecular systems. Quantum chemical calculations are invariably associated with the electrons of many body systems and can provide insights into properties that depend upon the electronic distribution of the systems; however, these methods are severely limiting in the sizes of the systems that can be studied. Conversely, molecular mechanics models calculate the properties of systems by invoking the Born-Oppenheimer approximation, by considering only nuclear motions and ignoring the electronic motions within individual atoms. Due to this approximation, molecular mechanics models are applicable in studies of large molecular systems, such as those associated with biomolecules and their complexes. Of these methods, molecular dynamics (MD) simulation is considered as one of the most appropriate computational techniques, that can provide deep insights into the structural, dynamical and thermodynamic properties of complex macromolecular systems. This method essentially involves describing the many-body interactions within a system with empirical potentials, followed by evaluation of the force and numerical integration of the classical equations of motion for each constituent particle. With rapidly increasing computational power, MD simulations can be effectively used for providing molecular mechanisms of intricate biological processes such as protein folding and misfolding, protein aggregation, effect of solvent on protein dynamics, interaction of protein with nucleic acids, lipid dynamics and mechanisms of enzymatic actions. Further, this method is capable of complementing experimental studies over a fairly wide range of time and length scales. Additionally, it also provides a valuable protocol for research in other fields such as nanotechnology, polymer science and atmospheric chemistry. As the key motivation of this dissertation is to understand the self-assembly pathways of the intrinsically disordered A β and effect of carbon nanoparticles on A β aggregation, we have extensively used the atomistic MD simulation technique for the work presented. A brief overview of the MD simulation protocol is presented in this chapter.

2.1 Molecular Dynamics for Macromolecular Systems

Molecular dynamics (MD) simulations techniques involve sampling of the phase space of a complex system in terms of the position and momentum (velocity) of the constituting particles. The temporal evolution of these quantities, often referred to as the ‘trajectory’ of the system, can then be processed using the principles of statistical mechanics to yield valuable insights into the system’s behaviour. The positional coordinates and velocities of the particles are obtained by invoking Newton’s second law of motion, wherein the force acting upon a particle at a given point of time equals the product of its mass and acceleration. The force on each particle, i , is derived as the negative gradient of a potential U_i imposed on it by interactions from the rest of the system, through the relationship,

$$\vec{F}_i = -\nabla U_i \quad (2.1.1)$$

For complex biomolecular systems whose sizes often exceed thousands of atoms and whose characteristics evolve within the microsecond time regimes, the interaction potentials of the constituent atoms are typically described empirically, and often designated as *force fields*.¹ For systems not exceeding a few hundred atoms in size, the interactions may be obtained from underlying quantum chemical calculations, and are often referred to as *ab initio force fields*.² Conversely, for systems of increased complexities whose sizes exceed hundreds of nanometers and dynamical timescales exceeds the microsecond time regime, the interaction potentials are often described with *coarse grained potentials*, wherein a group of atoms is treated as a single particle.^{3, 4} The structural, dynamical and thermodynamic aspects of systems involving small and medium sized biomolecules are most aptly described with described atomistic potentials, and have been used in the bulk of the research presented in this dissertation. The subsequent sections present an overview of the primary protocols involved in generating MD simulation trajectories for such systems.

2.2 Atomistic Force Fields

The basic functional form of the potential energy in classical MD simulation includes various bonded and non-bonded terms.¹ The functional form of total potential energy, U , for an N atom system, can be specified by the following equation,

$$U \equiv \sum_{\text{bonds}} k_b (b - b_0)^2 + \sum_{\text{angles}} k_\theta (\theta - \theta_0)^2 + \sum_{\text{dihedrals}} \sum_{n=1}^N k_\varphi^{(n)} [1 + \cos(n\varphi - \delta)] + \sum_{\text{impropers}} k_\omega (\omega - \omega_0)^2$$

$$+ \sum_{j=i+1}^N \sum_{l=1}^N 4 \varepsilon_{ij} \left[\left(\frac{\sigma_{ij}}{r_{ij}} \right)^{12} - \left(\frac{\sigma_{ij}}{r_{ij}} \right)^6 \right] + \sum_{j=i+1}^N \sum_{l=1}^N \frac{q_i q_j}{4 \pi \varepsilon_0 r_{ij}} \quad (2.2.1)$$

A schematic representation of different potential functions used in the empirical force field is shown in Figure 2.1. The first four terms in eqn (2.2.1) arise due to the atoms that are covalently linked with each other and are known as the *bonded interaction potentials*. The fifth term is the contribution due to the long-range electrostatic interactions, and the last term represents short-range dispersion interactions; they are collectively known as the *non-bonded interaction potentials*. The first term arises due to the change in energy during stretching of a bond from the equilibrium bond length; here, b_0 is the equilibrium bond distance, whereas k_b is the force constant. The second term gives total energy deviation due to angle bending from the equilibrium angle represented by θ_0 ; k_θ represents the force constant. The first two terms in eqn (2.2.1) are modelled by a harmonic potential and Hooke's law of simple massless spring are used to describe both these functions. The third term in eqn (2.2.1) represents the torsional potential (dihedral term) between four consecutive bonded atoms associated with the rotational motion of the bonds and is modelled using a periodic function. Here, k_φ represents rotational energy barrier height; the cosine function gives the periodicity of the torsional potential; φ represents the torsional angle; and δ is the phase factor of the torsional potential where the potential passes through a minima; n is the multiplicity whose value represents the number of minima during a 360° rotation of a bond. The fourth term in eqn (2.2.1) is the improper torsion potential, used to maintain planarity in molecular structures and the stereochemistry of chiral centres, and modelled using a harmonic potential. Unlike the torsional angle, the fourth atom in the improper torsional angle is not consecutively bonded to the first three atoms, but the central atom is bonded to the remaining three atoms. For this potential, k_ω and ω_0 represent the improper torsional force constant and equilibrium improper torsional angle, respectively. The force constants of the intramolecular potential (bonded potential) are usually obtained from a combination of the vibrational analysis of experimental and quantum calculations.⁵

The first term in the non-bonded interaction potential in eqn (2.2.1) is the short-ranged van der Waals interaction energy between atoms arising due to dipole-dipole interactions, dipole-induced dipole interaction and the interaction between instantaneously induced dipoles (London dispersion forces). In an empirical force field, van der Waals interaction potential between any pair of atoms, indexed i and j , separated by interatomic distance r_{ij} is typically modelled using the Lennard-Jones potential or the 6-12 potential, as,

$$V_{LJ(i,j)} = \varepsilon_{ij} \left[\left(\frac{R_{min}}{r_{ij}} \right)^{12} - 2 \left(\frac{R_{min}}{r_{ij}} \right)^6 \right] \quad (2.2.2)$$

$$R_{min} = 2^{1/6} \sigma_{ij} \quad (2.2.3)$$

ε_{ij} , σ_{ij} , and R_{min} represent depth of the potential wall, collision diameter and location of the potential minima respectively. The Lennard-Jones potential has two terms: an attractive term that varies with r_{ij}^{-6} and a repulsive term that varies with r_{ij}^{-12} . At shorter separation distance ($r_{ij} < R_{min}$) the interaction energy becomes repulsive and at very large distance the interaction tends to zero. Due to the short-ranged nature of van der Waals interactions, the inter-atomic potential calculation is usually truncated after a certain distance (cut-off distance) for reducing the computational cost. The interaction between all pairs of atoms is assumed to be zero beyond the cut-off.

The second term in non-bonded interaction potential, i.e. the last term in eqn (2.2.1), is the long-ranged electrostatic energy, which has a major contribution to the non-bonded interaction potential. The electrostatic energy between any pair of atoms (i and j), having partial charges q_i and q_j respectively, separated by interatomic distance r_{ij} is calculated using Coulomb's law and ε_0 represents the permittivity constant. Because of the long-ranged nature of the electrostatic interaction, simple truncation methods using cut-off distance are not useful to handle the long-ranged forces. More comprehensive algorithms such as the Ewald summation method⁶, reaction field and image charge method⁷, cell multiple method^{8, 9} etc have been developed for proper treatment of long-ranged forces. Of these several methods, we have performed simulations using Ewald summation method, developed by Ewald as implemented in CHARMM force field.^{5, 10} Applying this method, the summation of interaction energies is divided into two summations: a short-range contribution calculated in real space and a long-range contribution calculated in Fourier space.

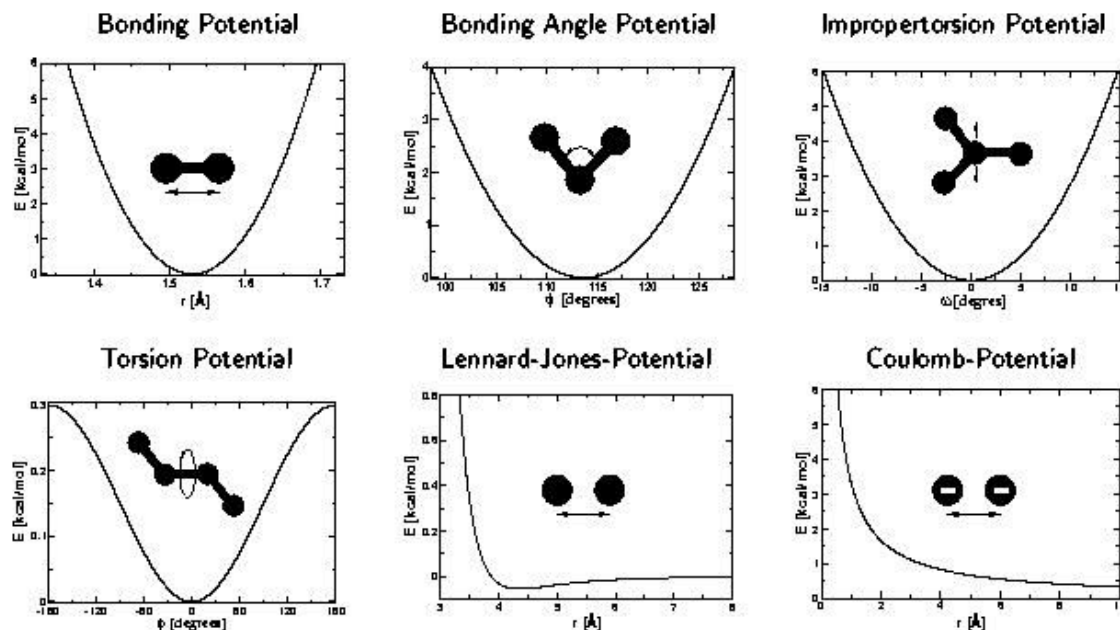


Figure 2.1: A schematic representation of different potential functions used in the empirical force field.

2.3 Equations of Motion

As stated earlier, MD simulations invoke Newton's second law of motion to obtain trajectories of the constituent particles of the system of interest. Newton's second law of motion for a particle can be expressed as,

$$\vec{F}_i = \vec{a}_i = m_i \frac{d\vec{v}_i}{dt} = m_i \frac{d^2\vec{r}_i}{dt^2} \quad (2.3.1)$$

Here, \vec{F}_i is the force acting on the particle and m_i is the mass of i^{th} particle. The acceleration \vec{a}_i is the time derivative of particle velocity \vec{v}_i , and the second time derivative of the positional coordinate \vec{r}_i .

Thus, combining eqn 2.1.1 and eqn 2.3.1,

$$\vec{a}_i = \frac{\vec{F}_i}{m_i} = -\frac{(\nabla U_i)}{m_i} \quad (2.3.2)$$

It is not possible to analytically solve eqn. (2.3.2) for a many body system, and therefore the solutions are obtained by integrating the set of 'n' equations numerically. There are several algorithms such as velocity Verlet algorithm¹¹, leap-frog algorithm¹² and Beeman's algorithm¹³ that are optimized for integrating these equations numerically and generating a system's trajectory. Of these methods, the velocity Verlet algorithm is used extensively in

simulation packages such as NAMD¹⁴, AMBER¹⁵ and GROMACS¹⁶⁻¹⁸, and its underlying protocol is described below.

The position of an atom i at a time $(t + \delta t)$ (with timestep δt) using Taylor's series expansion can be written in terms of the position and velocity at the earlier time t as,

$$\vec{r}_i(t + \delta t) = \vec{r}_i(t) + \delta t \cdot \vec{v}_i(t) + \frac{\delta t^2}{2m_i} \vec{f}_i(t) \quad (2.3.3)$$

Here, $r_i(t)$ and $v_i(t)$ are the position and velocity of the i^{th} particle at time t respectively. Velocity of the particle at a time $(t + \delta t)$ can be written as,

$$\vec{v}_i(t + \delta t) = \vec{v}_i(t) + \frac{\delta t}{2m_i} [\vec{f}_i(t) + \vec{f}_i(t + \delta t)] \quad (2.3.4)$$

From the above equation, the position at time $(t + 2\delta t)$ can be obtained. It is useful to point out that initial velocities of the particles are a requirement for carrying out simulations using the velocity Verlet algorithm. The initial velocities can either be assigned from the system's temperature according to the Maxwell-Boltzmann velocity distribution function, or from those obtained at the end of an earlier simulation. It is further important to note that the timestep δt is chosen such that it is smaller than the time period of fastest atomic motion present in the system. Bond vibrations are the fastest atomic motions in complex biomolecular system, and their time periods are usually range within few femtoseconds (10^{-15} s). Consequently, δt should not exceed more than 2 fs in a typical atomistic MD simulation. For obtaining better computational speed and sampling, multiple time step algorithms, which separate out slow, medium and fast atomic motions present in the system and incorporate different timesteps for each kind of motion, are sometime used in MD simulations.¹⁹

2.4 Thermodynamic State Control

Conformational ensembles generated by the numerical integration of Newton's equation of motion correspond to the *microcanonical ensemble*, where energy (E), volume (V) and number of particle (N) in the system are fixed. However, most of the experimental studies are performed under conditions of constant temperature (T) or pressure (P), or both, and therefore to obtain results synchronized with experiments, simulations are often performed under isothermal (constant T) or isobaric (constant P) conditions. Additionally, the study of processes where the number of particles of the system is not constant, such as adsorption of gases upon surfaces or phase equilibria in liquids, necessitates simulations under conditions of constant chemical potential (μ) for the system. Since constant temperature and pressure

(*NPT*), or constant temperature and volume (*NVT*) with fixed number of particles (N) simulations have been used to obtain all results presented in the remaining chapters, the following discussion is limited to the methods of temperature and pressure control.

2.4.1 Temperature Control

According to the *equipartition theorem*, at thermal equilibrium, the average kinetic energy of a system is directly proportional to the temperature of the system. The average kinetic energy (K.E.) of a system can be written as,

$$\langle K.E \rangle = \frac{1}{2} N_f k_B T \quad (2.4.1.1)$$

Here, N_f represents the total number of degrees of freedom in the system, and k_B and T represent the Boltzmann's constant and absolute temperature of the system, respectively. The total kinetic energy of a system is equal to the summation of the kinetic energies of individual particles. So, the temperature of a system can be expressed as,

$$T = \sum_{i=1}^N \frac{m_i v_i^2}{k_B N_f} \quad (2.4.1.2)$$

Here, m_i and v_i represent the mass and the magnitude of velocity of the i^{th} particle in the system, and N represents the total number of particles in the system. From the above expression, it appears that in order to maintain the temperature of system, one must have to control the magnitudes of the velocities of the constituent particles in the system. This can be achieved simply by intermittently scaling the velocity of individual particles proportionally, such as by multiplying the velocity by the factor $\sqrt{T_f / T_i}$, where T_f is the desired temperature and T_i is the current temperature of the system obtained from the kinetic energy. An alternative method to modify the temperature of the system through particle velocities is to assign the velocities of constituent particles periodically to newer values from the Maxwell-Boltzmann velocity distribution at the target temperature. Both these methods are simple and effective, but suffer from a disadvantage that the inherent dynamical properties of an *NVE* ensemble are changed.

For these reasons, more advanced techniques have been developed for running simulations under isothermal conditions. One such method uses Langevin dynamics and the stochastic collision method.²⁰ In this method, temperature control can be achieved by

choosing a particle randomly at specific intervals and assigning it a new velocity according to the Maxwell-Boltzmann velocity distribution at the desired temperature. This is similar to the system being coupled with a heat bath that randomly emits ‘thermal particles’ that periodically bombard the system. The Newton’s equation of motion for the particles in the entire system is modified due to random collisions and can thus be expressed as,

$$f_i - \gamma_i \frac{dr_i}{dt} + R_i = m_i \frac{d^2 r_i}{dt^2} \quad (2.4.1.3)$$

Here, γ_i and R_i represent the frictional constant and additional random force respectively. Between each of these random collisions, the system samples at constant energy conditions. Conversely, one of the potential drawbacks in using this method is that the system cannot generate smooth trajectories.

Another method of temperature control is an extended system method which was originally introduced by Nosé and was further developed by Hoover.^{21, 22} In this method, the system is coupled to an isothermal reservoir which is considered as a ‘fictitious mass’ with an additional degrees of freedom. The magnitude of the ‘fictitious mass’ determines the strength of coupling between the system and the reservoir, and hence controls the energy flow between the reservoir and the system. The Nosé-Hoover thermostat is considered as one of the most appropriate and efficient techniques for running simulations under isothermal conditions.

2.4.2 Pressure Control

MD simulations are frequently carried out at constant pressure in order to mimic experimental conditions. In order to maintain constant pressure, the simulated system is usually coupled to a ‘pressure bath’, analogous to temperature coupling.²⁰ Various algorithms have been developed for controlling the pressure of the system. In the weak coupling method developed by Berendsen *et. al.*, volume is treated as an additional dynamical variable, but the equation that describes the volume evolution is first order and the degree of coupling to the external pressure bath is followed by volume fluctuations.²³ The weak coupling method has the major disadvantage that it does not generate trajectories in any meaningful ensemble and hence, the average and fluctuation in any observed quantity cannot be used realistically.

In the Langevin piston algorithm, the piston degrees of freedom are formulated by a Langevin equation,²⁴ where partial damping is applied to the motion of the piston. The resultant equations of motion of the system can be expressed as,

$$\frac{dr_i}{dt} = \frac{p_i}{m_i} + \frac{1}{3V} \frac{dV}{dt} r_i \quad (2.4.2.1)$$

$$\frac{dp_i}{dt} = f_i - \frac{1}{3V} \frac{dV}{dt} p_i \quad (2.4.2.2)$$

$$\frac{d^2V}{dt^2} = \frac{1}{W} [P(t) - P_{ext}] - \gamma \frac{dV}{dt} + R(t) \quad (2.4.2.3)$$

In the above equation, $P(t)$ and P_{ext} are the instantaneous pressure and the applied pressure respectively; V is the volume of the system; W is the piston mass; γ is the Langevin collision frequency; and m_i , r_i , p_i and f_i represent mass, position, momentum and force acting on the i^{th} particle respectively. $R(t)$ is the magnitude of a random force obtained from a Gaussian distribution. The mean value of $R(t)$ is zero and its variance can be written as,

$$\langle R(0)R(t) \rangle = \frac{2\gamma k_B T \delta(t)}{W} \quad (2.4.2.4)$$

where, k_B is the Boltzmann constant. The previous extended system method can be obtained for $\gamma = 0$. The instantaneous pressure of the system at any given time (t) can be written as:

$$P(t) = \frac{1}{3V} \left(2K.E. + \sum_i f_i r_i \right) \quad (2.4.2.5)$$

Here, $K.E.$ represents instantaneous kinetic energy of the system, and the second summation represents the system's internal virial.

2.5 Periodic Boundary Conditions

In MD simulations, periodic boundary conditions are usually employed to avoid artifacts arising due to the boundary and finite size effects.¹ Periodic boundary conditions are incorporated to replicate bulk-like conditions, thereby enabling simulations to reproduce various macroscopic properties using a relatively small number of particles. Essentially, a finite size system is made infinite by replicating the central simulation box throughout 3-dimensional space to form an infinite lattice.¹ This is systematically depicted in Figure 2.2, where the shaded box represents the central simulation cell, and the surrounding boxes are the periodic images of the central cell. Using this technique, particles in the simulation box experience forces as if they were in bulk fluid. During a simulation run, whenever a particle leaves (enters) the simulation cell, its image enters (leaves) it with exactly the same velocity from the opposite direction, such that the total number of particle in the central simulation cell remains constant. Due to periodic boundary conditions, each particle in the simulation cell not only interacts with other particles within the cell, but also interacts with their images

in adjoining image cells. As a result, the number of interactions between atom pairs increase rapidly. This can be avoided by using *minimum image criterion*.¹ According to this convention, forces are calculated such that each atom interacts only with the nearest neighbor (closest image) of the remaining particles in the system.¹

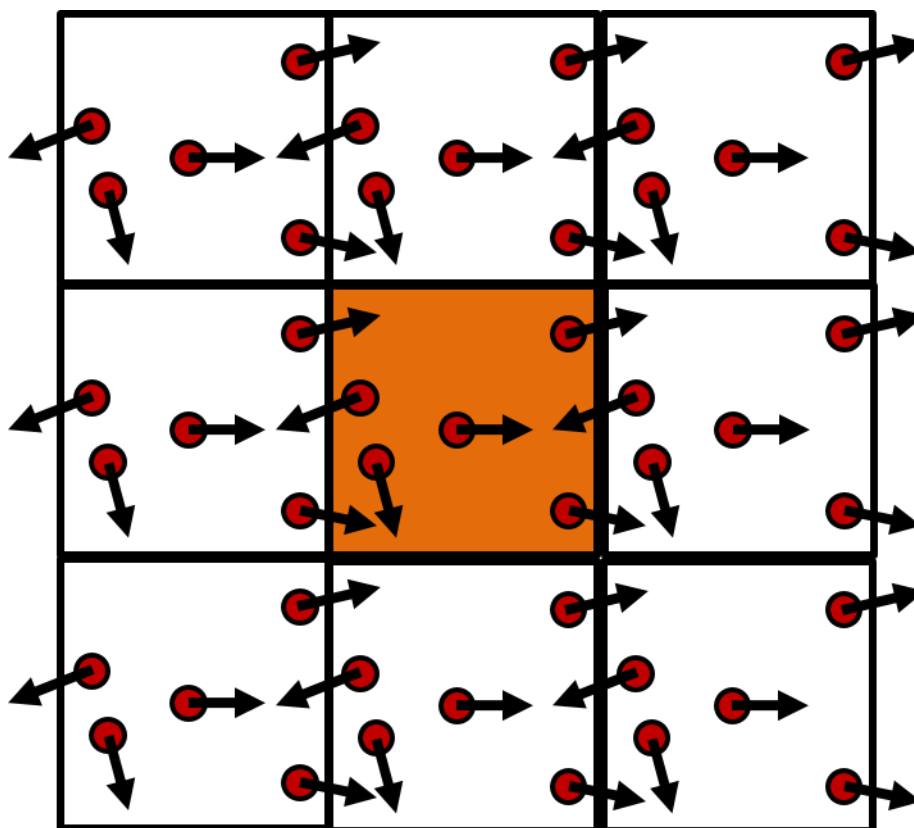


Figure 2.2: Pictorial representation of periodic boundary condition. Particles are shown as red circles, and the arrows indicate their directions of motion. The central simulation box is highlighted in orange. A particle leaving a simulation cell enters an adjoining cell from the opposite direction.

When a simulation performed with periodic boundary conditions is processed, the inter-particle distance should be calculated keeping the minimum image convention in mind. In the case of an orthorhombic simulation cell whose cell basis vectors along the x -, y - and z -directions are of lengths $cella$, $cellb$, and $cellc$ respectively, the distance Δr between two particles at positions (x_i, y_i, z_i) and (x_j, y_j, z_j) should be re-calculated as,

$$\Delta r = \sqrt{\Delta x_{ij}^2 + \Delta y_{ij}^2 + \Delta z_{ij}^2} \quad 2.5.1$$

where,

$$\Delta x_{ij} = (x_j - x_i) - cella * \left[\text{round} \left(\frac{x_j - x_i}{cella} \right) \right] \quad 2.5.2$$

$$\Delta y_{ij} = (y_j - y_i) - cellb * \left[\text{round} \left(\frac{y_j - y_i}{cellb} \right) \right] \quad 2.5.3$$

$$\Delta z_{ij} = (z_j - z_i) - cellc * \left[\text{round} \left(\frac{z_j - z_i}{cellc} \right) \right] \quad 2.5.4$$

In the expressions above, the function $\text{round}(\alpha)$ yields the nearest integral value of the real number argument, α .

2.6 References

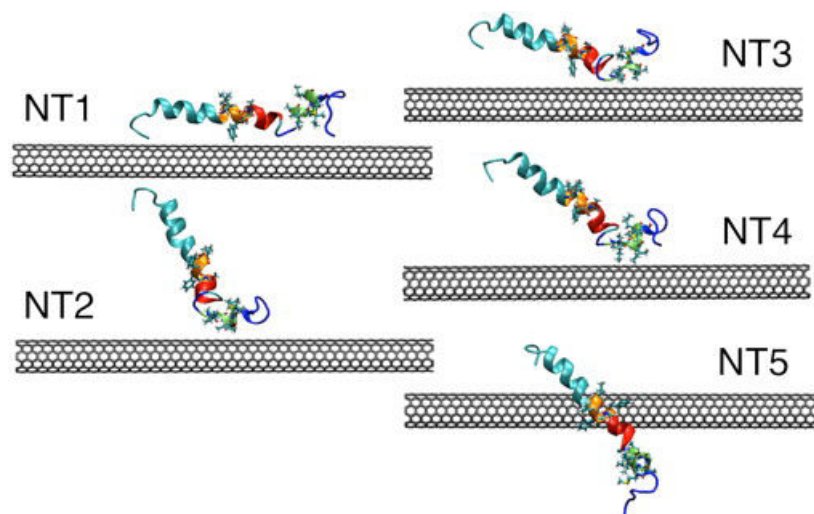
1. R. L. Andrew, *Molecular Modelling Principles and Applications*. Pearson Education Ltd., 2nd edition, 2001.
2. P. Carloni, U. Rothlisberger and M. Parrinello, *Acc. Chem. Res.*, 2002, **35**, 455-464.
3. W. Noid, *J. Chem. Phys.*, 2013, **139**, 090901.
4. A. Voegler Smith and C. K. Hall, *Proteins: Struct. Funct. Bioinf.*, 2001, **44**, 344-360.
5. A. D. MacKerell, D. Bashford, Bellott, R. L. Dunbrack, J. D. Evanseck, M. J. Field, S. Fischer, J. Gao, H. Guo, S. Ha, D. Joseph-McCarthy, L. Kuchnir, K. Kuczera, F. T. K. Lau, C. Mattos, S. Michnick, T. Ngo, D. T. Nguyen, B. Prodhom, W. E. Reiher, B. Roux, M. Schlenkrich, J. C. Smith, R. Stote, J. Straub, M. Watanabe, J. Wiórkiewicz-Kuczera, D. Yin and M. Karplus, *J. Phys. Chem. B*, 1998, **102**, 3586-3616.
6. U. Essmann, L. Perera, M. L. Berkowitz, T. Darden, H. Lee and L. G. Pedersen, *J. Chem. Phys.*, 1995, **103**, 8577-8593.
7. H. L. Friedman, *Mol. Phys.*, 1975, **29**, 1533-1543.
8. L. Greengard and V. Rokhlin, *J. Comput. Phys.*, 1987, **73**, 325-348.
9. H.-Q. Ding, N. Karasawa and W. A. Goddard, *Chem. Phys. Lett.*, 1992, **196**, 6-10.
10. A. D. Mackerell, M. Feig and C. L. Brooks, *J. Comput. Chem.*, 2004, **25**, 1400-1415.
11. W. C. Swope, H. C. Andersen, P. H. Berens and K. R. Wilson, *J. Chem. Phys.*, 1982, **76**, 637-649.
12. R. W. Hockney, *METHODS Comput. Phys.*, Hampton, Va., 1970, **9**, 136.
13. D. Beeman, *J. Comput. Phys.*, 1976, **20**, 130-139.
14. L. KalÈ, R. Skeel, M. Bhandarkar, R. Brunner, A. Gursoy, N. Krawetz, J. Phillips, A.

-
- Shinozaki, K. Varadarajan and K. Schulten, *J. Comput. Phys.*, 1999, **151**, 283-312.
15. R. Salomon - Ferrer, D. A. Case and R. C. Walker, *WIRES Comput. Mol. Sci.*, 2013, **3**, 198-210.
 16. B. Hess, C. Kutzner, D. van der Spoel and E. Lindahl, *J. Chem. Theory Comput.*, 2008, **4**, 435-447.
 17. E. Lindahl, B. Hess and D. Van Der Spoel, *J. Mol. Model.*, 2001, **7**, 306-317.
 18. H. J. Berendsen, D. van der Spoel and R. van Drunen, *Comput. Phys. Commun.*, 1995, **91**, 43-56.
 19. M. Tuckerman, B. J. Berne and G. J. Martyna, *J. Chem. Phys.*, 1992, **97**, 1990-2001.
 20. H. C. Andersen, *J. Chem. Phys.*, 1980, **72**, 2384-2393.
 21. S. Nosé, *Mol. Phys.*, 1984, **52**, 255-268.
 22. W. G. Hoover, *Phys. Rev. A*, 1985, **31**, 1695.
 23. H. J. Berendsen, J. v. Postma, W. F. van Gunsteren, A. DiNola and J. Haak, *J. Chem. Phys.*, 1984, **81**, 3684-3690.
 24. S. E. Feller, Y. Zhang, R. W. Pastor and B. R. Brooks, *J. Chem. Phys.*, 1995, **103**, 4613-4621.

Chapter – 3

Adsorption Mechanism and Collapse Propensities of the Full-Length, Monomeric A β ₁₋₄₂ on the Surface of a Single-Walled Carbon Nanotube: A Molecular Dynamics Simulation Study

Abstract



Though nanomaterials such as carbon nanotubes have gained recent attention in biology and medicine, there are few studies at the single-molecule level that explore their interactions with disease causing proteins. Using atomistic molecular dynamics simulations, we

have investigated the interactions of the monomeric $A\beta_{1-42}$ peptide with a single walled carbon nanotube of small diameter. Starting with peptide-nanotube complexes that delineate the interactions of different segments of the peptide, we find rapid convergence in the peptide's adsorption behavior on the nanotube surface, manifested in its arrested movement, the convergence of peptide-nanotube contact areas and approach distances, and in increased peptide 'wrapping' around the nanotube. In systems where the N-terminal domain is initially distal from nanotube, the adsorption phenomena are initiated by interactions arising from the central hydrophobic core, and precipitated by those arising from the N-terminal residues. Our simulations and free energy calculations together demonstrate that the presence of the nanotube increases the energetic favorability of the 'open' state. We note that the observation of peptide localization could be leveraged for site-specific drug delivery, while the decreased propensity of collapse appears promising for altering kinetics of the peptide's self-assembly.

3.1 Introduction

According to the Amyloid hypothesis, self-assembly of the 39-42 residue Amyloid beta (A β) peptide into insoluble aggregates is associated with the onset of the dreaded Alzheimer's disease (AD).¹ The A β peptide is created from exact proteolysis of the amyloidogenic sequence within the amyloid precursor protein (APP). Though the production rates of the 42-residue peptide are about 8 times lower than the 40-residue form, it has greater propensity to oligomerize and aggregate and is associated with far greater neurotoxic effects.^{2, 3} There is evidence that the peptide's self-assembly is influenced by mutations, changes in the solvent environment, and thermodynamics conditions.⁴⁻⁷ Interestingly, a number of emerging studies suggest that the soluble, oligomeric intermediates could be more toxic than the insoluble aggregates.^{3, 8, 9}

Structural and computational studies indicate that residues belonging to three contiguous regions within the A β peptide play prominent roles in its self-assembly: the 'central hydrophobic core' spanning the residues L₁₇VFFA₂₁,^{5, 10, 11} the 'turn' region spanning V₂₄GSN₂₇,^{12, 13} and a second, C-terminal hydrophobic domain thought to span a subset of the residues G₂₉AIIGLMVGGVVIA₄₂.^{5, 10} The importance of these regions and the interplay of their dynamics has been demonstrated by several experimental and computational studies.^{5, 11, 14, 15} Self-assembly of the peptide includes a number of key steps that involve the interplay of enthalpic (favoring association) and entropic (favoring dissociation) effects, and at optimal thermodynamic conditions result in the formation of insoluble fibrils, wherein the two strands of the peptide separated by the turn region form a collapsed, hairpin like structure.^{11, 14}

Interactions between the peptide's hydrophobic domains leading to its collapse is thus considered one of the key steps in A β self-assembly, whether into soluble oligomers or into insoluble aggregates.^{5, 15} Efforts to interfere with or de-stabilize the self-assembly of the peptide have included approaches that impose external perturbations to the physico-chemical behavior of these domains. Since the central hydrophobic core is thought to play a key role in the adhesion of peptide units, it had been suggested that fibrillar extension could be prevented with the binding of small peptides or ligands to this patch.¹¹ It has been shown that potential AD drug candidates preferentially interact with and stabilize the central hydrophobic core of the peptide, and perhaps work by preventing conformational changes that could lead to

amyloid formation.¹⁶ Interestingly, a very recent study points out the inverse correlation between the strength of ligand binding to this core and the aggregation rate.¹⁷

The convergence of many unique properties in carbon nanotubes (CNTs) (such as ordered structure; high aspect ratio and surface area; ultralight weight; high mechanical strength; etc) has opened up several avenues of their applicability.¹⁸⁻²⁰ Particularly in biology, CNTs are currently being considered for usage in biomolecular sensors and in biomedical devices,^{21, 22} as well as in therapeutics, either for direct interaction with disease-causing biomolecules²³ or for site-specific drug delivery.²⁴ Such potential applications have necessitated detailed studies of CNT interactions with peptides, proteins, sugars, membrane lipids and nucleic acids, and in fact, a number of recent studies demonstrate interesting structural, conformational and functional changes in biological molecules adsorbed on CNT surfaces.²⁵⁻²⁹ Molecular dynamics (MD) simulations have demonstrated how single-walled carbon nanotubes (SWCNTs) induce curvature increases in biomolecules around them, leading to the observation of biomolecular ‘wrapping’ around nanotubes.²⁵⁻²⁸ SWCNTs have also been shown to interfere with backbone hydrogen bonding of helical peptides, and the dimensions of the SWCNT has been shown to have an effect on the interaction propensities.^{25, 26, 30-32}

Experimentally, it has been shown that CNTs (and related nanoparticles such as fullerenes) affect protein aggregation kinetics.³³ This is noteworthy in light of a number of earlier studies that have implicated π - π stacking of aromatic residues in peptide self-assembly,³⁴⁻³⁶ and as inhibition of amyloid formation has oftentimes been attributed to the interference by drug molecules to the interactions between aromatic sidechains of nearby peptide units.^{37, 38} Conversely, very recent experimental work involving mutations of Phe19 and Phe20 of A β ₁₋₄₂ with aliphatic sidechains such as Leu and Ile show that aggregation propensities remain unchanged (or even enhanced).^{39, 40} Interestingly, substitution of the aromatic residues with Valine causes a decreased stability of the aggregates.⁴⁰ Detailed simulation studies have already shown that oligomeric A β fragments belonging the second hydrophobic domain (G₂₅SNKGAIIGLM₃₅) form barrel-like structures on SWCNTs surfaces and can hinder further self-assembly.⁴¹ However, as noted in that study, details of SWCNT interactions with other important regions of the peptide (such as the central hydrophobic core and the C-terminal hydrophobic tail) require further investigations.

The body of research discussed above suggests that CNTs could significantly affect the intrinsic behavior of disease causing peptides. However, barring a few insightful studies that describe the interaction mechanisms between CNTs and such peptide candidates,^{29, 33, 40} this area of research remains largely unexplored. As mentioned earlier, CNTs can be used either directly as site-specific drug-delivery agents, or as entities that modulate the conformational landscape of amyloidogenic proteins, thus interfering with self-assembly and amyloid formation. We report in this article, results obtained with fully atomistic molecular dynamics (MD) simulations of the full-length, A β ₁₋₄₂ peptide (PDB code: 1Z0Q) in proximity to SWCNTs in aqueous environment. We have carried out a total of nine simulations of 80 ns each, with five different relative orientations of the peptide's central hydrophobic core and the second, C-terminal hydrophobic domain with the SWCNT. The five configurations differ in their initial peptide-SWCNT contact areas, as well as distances of the important hydrophobic regions from the SWCNT; the contact area was initially the least (greatest) and the distance from the central hydrophobic core was the greatest (least) when the second (first) helical region was placed parallel to the SWCNT. Further, a control simulation of the same trajectory length has been generated for the pure peptide in absence of SWCNT.

We find that the central hydrophobic region and the first 16 residues at the N-terminus play an important role in influencing the interactions with the SWCNT. Though these regions are distal to the nanotube in two of the setups, the interaction strength is such that there is rapid convergence in the peptide-SWCNT distance and contact areas with the values obtained with the other setups. For all simulations, there is a manifold increase in the peptide-SWCNT contact area within tens of nanoseconds, resulting in similar 'wrapping' propensities around the SWCNT. Our adaptive biasing force (ABF) based calculations of the free energies as a function of the distance between centers of mass of the A β strands (the 'collapse distance'), performed with the setups where the SWCNT is parallel to either of the hydrophobic domains, demonstrates that the presence of SWCNTs hinders the propensity of peptide collapse. This is corroborated by the converged, high distance of collapse obtained with all the simulation trajectories. We discuss the implications of peptide localization and adsorption, and the thermodynamic favorability of the 'open' relative to the 'closed' states in the presence of SWCNT, in the development of methods to prevent self-assembly of A β peptides.

3.2 Materials and Methods

3.2.1 Setup of Peptide-SWCNT Complexes

We have considered an armchair (6,6), single-walled carbon nanotube (SWCNTs) of length 99.5 Å, radius 4.1 Å, containing 984 carbon atoms. The SWCNT coordinates were obtained using the VMD package.⁴² To avoid artifacts that may arise due to edge effects, periodic boundary conditions were used to create infinitely long SWCNTs parallel to the x-axis; this approach has been adopted in recent simulation studies.²⁵ The coordinates for the A β ₁₋₄₂ peptide were obtained from the PDB database (PDB code 1Z0Q).⁷ These coordinates, obtained with solution NMR studies in a 3:7 mixture of hexafluoro-2-propanol and water, correspond to a largely helical form of the monomeric peptide. The structure consists of a long N-terminal helix (S₈GYEVHHQKLVFFAEDVG₂₅) and a shorter, C-terminal helix (K₂₈GAIIGLMVGG₃₈), separated by a 2-residue turn (S₂₆N₂₇). In our first system (referred henceforth as NT1), the SWCNT axis is made parallel to the vector joining the C α atoms of the 8th and the 25th residues. In our second system, (referred henceforth as NT2), the SWCNT axis is made parallel to the vector joining the C α atoms of the 28th and the 38th residues. Three more systems (referred henceforth as NT3, NT4 and NT5) were created with either helical domain oriented at 30° or 45° relative to the SWCNT. In all the setups, the SWCNT axis is set at exactly 12.6 Å away from the center of mass of the closest helix; thus, the SWCNT surface is, in all cases, 8.5 Å away from the respective center of mass. The initial setups are depicted in Figure 3.1. The relative orientations of the two helices with the SWCNT in each setup, the distances and angles of the two helical domains relative to the SWCNT, are provided in Table 3.1. Throughout the simulations and the free energy calculations, the SWCNTs were held fixed at its setup position with a constant harmonic force with a force constant 2 kcal mol⁻¹. The A β ₁₋₄₂ peptide is characterized by the presence of two important hydrophobic regions, which have been referred throughout this paper as ‘HP1’ and ‘HP2’. The central hydrophobic core, comprising of residues 17 to 21 (LVFFA), has been referred to as ‘HP1’. Of the C-terminal residues, the importance of residues 30 to 35 (A₃₀IIGLM₃₅) has often been discussed.^{3, 16, 43} We refer to the residue stretch from 30 to 35 as ‘HP2’. A control simulation for the peptide was also performed. The NH₃⁺ and COO⁻ groups were added to the N- and C- termini, respectively of the peptide in all six setups, and each system was solvated with the TIP3P water model.⁴⁴ Three sodium counter ions were added to neutralize each system.

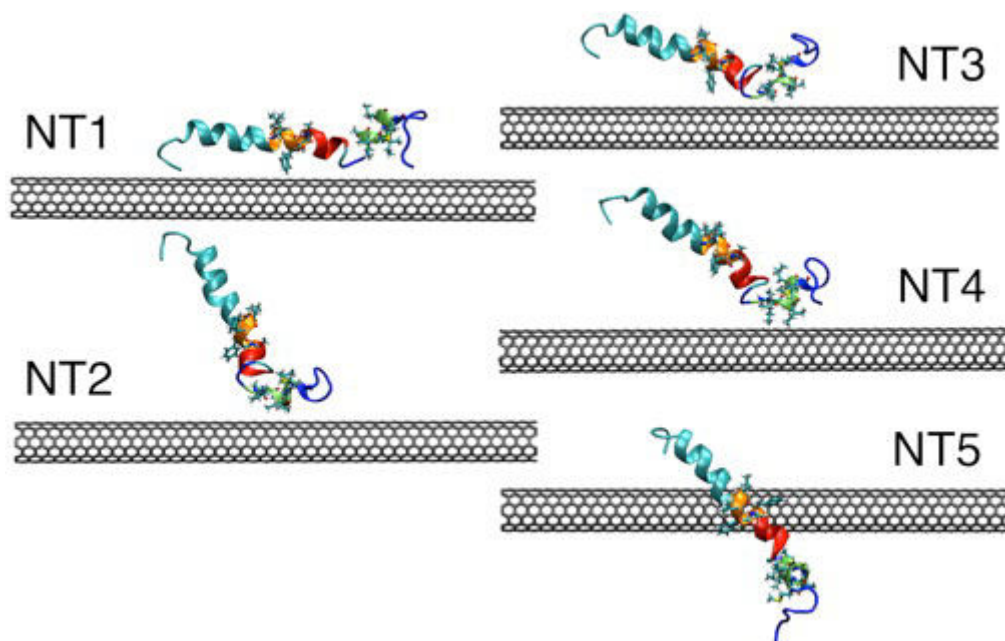


Figure 3.1. Setups of the $A\beta_{1-42}$ peptide-SWCNT complex. Segments $L_{17}VFFAEDVGS_{26}$ and $K_{28}GAIIGLMVGGVVIA_{42}$ are shown in red-orange and blue-green, respectively. $L_{17}VFFA_{21}$ (the central hydrophobic core ‘HP1’) lies at one end to the first patch and is highlighted in orange, and $A_{30}IIGLM_{35}$ (‘HP2’) lies within the second patch and is highlighted in green. The sidechains of these segments are shown in line representation.

System	θ_1 (°)	θ_2 (°)	d_1 (Å)	d_2 (Å)	CA (Å ²)
NT1	0.0	53.0	8.5	9.5	517.3
NT2	62.7	0.0	24.7	8.5	181.4
NT3	16.7	45.0	12.8	8.5	256.4
NT4	32.8	30.0	17.2	8.5	227.8
NT5	45.0	86.6	8.5	19.3	245.6

Table 3.1. Details of the five peptide-SWCNT configurations used in the study. The angles (in degrees) made by the helices 1 and 2 with the SWCNT axis are θ_1 and θ_2 , respectively. The center of mass distance (in Å) between helix 1 and the SWCNT is d_1 ; the center of mass distance (in Å) between helix 2 and the SWCNT is d_2 . The initial contact area (in Å²) between the peptide and SWCNT is denoted as CA.

3.2.2 MD Simulations and Free Energy Calculations

MD simulations were performed with NAMD2.7 simulation package⁴⁵ and visualizations were made using the VMD tool.⁴² The CHARMM22 all-atom force field with the CMAP correction was used.^{46, 47} Bond lengths involving hydrogen atoms were held fixed using the SHAKE algorithm.⁴⁸ Energy minimization, using the conjugate gradient technique was first

performed for 10 000 steps on all the systems. Following this, simulations were carried out in the isothermal-isobaric (NPT) ensemble. Three independent trajectories of 80 ns duration were generated for the NT1 and NT2 simulations, and one each for NT3, NT4, NT5 and the free peptide. Thus, the total simulation data for the peptide-nanotube complex was for 720 ns. A constant temperature of 310 K was maintained using Langevin dynamics with a collision frequency of 1 ps^{-1} , and a 1 atmosphere pressure was maintained using the Langevin piston Nose-Hoover method.^{49, 50} A timestep of 2 fs was used. Three-dimensional orthorhombic periodic boundary conditions were employed. Electrostatic interactions were calculated with the particle mesh Ewald (PME) method.⁵¹ The cutoff distance for non-bonded interactions were set to 12 Å with a smoothing function employed from 10.5 Å.

The Adaptive Biasing Force (ABF) method, as implemented in the NAMD2.7 package, was used to calculate the free energy profiles of the NT1 and NT2 systems, as well as for the pure peptide.^{52, 53} Unlike the umbrella sampling technique, this method for calculating the potential of mean force (PMF) requires no prior knowledge of the free energy surface, and has been used in a number of recent studies to probe conformational changes in biomolecular systems, using a variety of spatial reaction coordinates.⁵⁴⁻⁵⁶ In our calculations, the center of mass distance of the residue segments $L_{17}VFFAEDVGS_{26}$ and $K_{28}GAIIGLMVGGVVIA_{42}$ was taken as the reaction coordinate to characterize the peptide's collapse. This distance, ' $d_{collapse}$ ', spanned a separation of 8 to 21 Å, which was divided into 52 "windows", each 0.25 Å wide. The free energy profiles used for comparing barrier heights converged over a period of at least 18 ns. The total sampling time for the NT1 and NT2 systems was 180 ns and 198 ns respectively, while it was 130 ns for the pure peptide.

3.3 Results and Discussion

3.3.1 Peptide Adsorption on the SWCNT Surface

It has been observed that amphiphilic peptides have a distinctive tendency to adsorb around the rigid hydrophobic surface of high curvature provided by CNTs. For the 42 residue A β peptide with relatively long, contiguous hydrophobic regions, the contact area with the SWCNT can be used as a quantitative measure for characterizing the extent of adsorption on to the nanotube. For our simulation trajectories, we have estimated this value by the method specified in recent reports,^{25, 26} as half the difference between the sum of the solvent accessible surface areas of the peptide and the SWCNT, and that of the peptide-SWCNT

complex. A probe of 1.8 Å diameter is used to calculate the individual solvent accessible surface areas of the peptide, SWCNT, and the complexes.

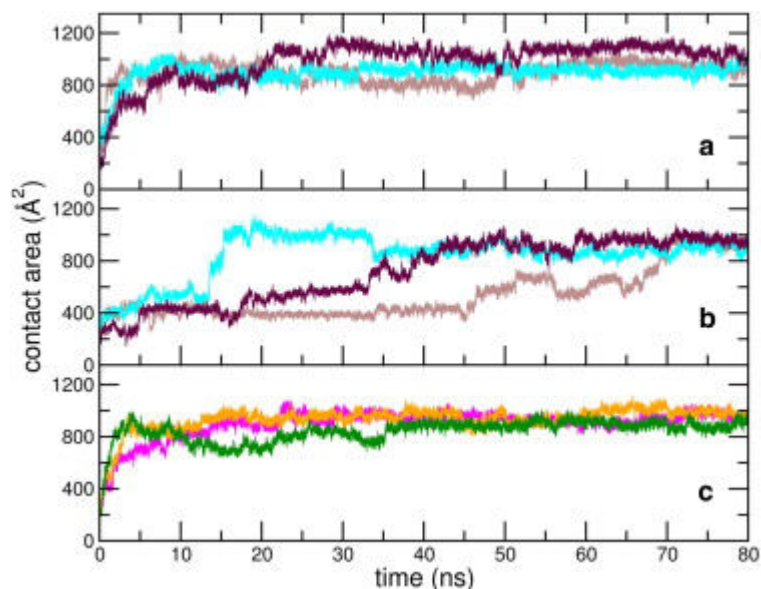


Figure 3.2. Evolution of peptide-SWCNT contact area over *a)* three NT1 trajectories, *b)* three NT2 trajectories, *c)* NT3 (in green), NT4 (in magenta) and NT5 (in orange) trajectories.

We show in Figure 3.2, temporal evolution of the full peptide-SWCNT contact area for the nine peptide-SWCNT simulations. Despite initial differences in dynamics in the early stages, all the peptide-SWCNT simulations show marked increase in the contact area; the final values attained are in the vicinity of 900 Å². For the NT1, NT3, NT4 and NT5 simulations, the contact areas rise rapidly and attain saturation values within a few tens of nanoseconds. But the inspection of each individual NT2 plots show that there is near convergence with the value (~ 900 Å²) occurring at ~ 70 , 42 and 15ns.

In Figure 3.3, we have plotted the evolution of the mean radial distance of the centers of mass of HP1 and HP2 from the SWCNT surface for the NT1 and NT2 trajectories (see Fig 3.4 for plots of the other systems). The radial distance between HP1 and the nanotube converges for all systems by the end of the simulations. For the HP2 patch the corresponding changes are minor, and the radial distance from the nanotube remains largely constant for all trajectories. We note that for systems with low initial contact areas (NT2 and NT4), the decrease in the approach distance of HP1 to the nanotube *precedes* the increase in the peptide-SWCNT contact area. Thus, it appears that the adsorption mechanism first involves an approaching closeness of the SWCNT with the central hydrophobic core. The eventual convergence of the radial distances and the contact areas suggest that the initial relative

configuration between the peptide and the SWCNT is of minor importance in the adsorption mechanism.

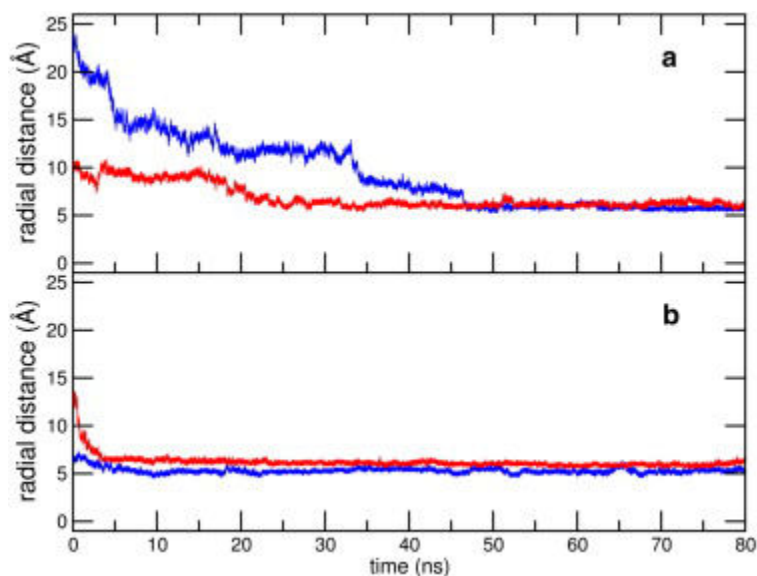


Figure 3.3. Time evolution of the radial distance of SWCNT and with *a)* HP1 and *b)* HP2 segments of $A\beta_{1-42}$ for the NT1 (in red) and NT2 (in blue) setups, averaged over three trajectories each.

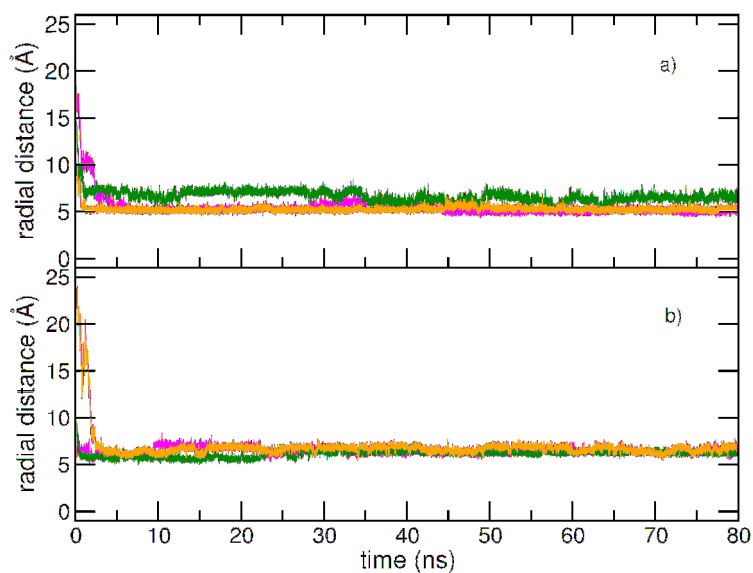


Figure 3.4. Radial distance of the centers of mass of *a)* segment HP1 and, *b)* segment HP2, from the SWCNT surface, for the NT3 (*green*), NT4 (*magenta*) and NT5 (*orange*) simulation trajectories.

3.3.2 Peptide-Nanotube Interaction Energies

It is known that hydrophobic interactions are the dominant forces behind peptide and protein adsorption on fullerene balls, pristine graphene sheets and CNTs.^{25, 30, 33} The different initial geometries used in our study are meant to delineate interactions of the important parts of the A β ₁₋₄₂ peptide with the SWCNT; however, we observe strong convergence in the peptide behavior in these systems within a few tens of nanoseconds. For understanding the differential contributions of the principle hydrophobic regions in the A β ₁₋₄₂ peptide in the observed adsorption mechanism, we have calculated for all the trajectories, the self, non-bonded energy of the peptide; the peptide's interaction energies with the SWCNT; and interaction energies of important hydrophobic regions of the peptide with the SWCNT.

We show, in Figure 3.5a, the total non-bonded energy of the peptide over the peptide-nanotube complexes, as well as for the control simulation of the pure peptide; data for NT1 and NT2 are averaged over three trajectories each. This energy is higher overall when in proximity to the SWCNT. Towards the end of the simulations, the total non-bonded energy of the peptide, averaged over all nine simulations with the SWCNT, is lesser than that of the pure peptide by ~ 105 kcal mol⁻¹. Not surprisingly, the peptide's *bonded* self-energy (the sum total of bond, angle, dihedral and improper components) displays no significant differences amongst any of the simulated trajectories (data not shown). It is thus obvious that interactions with the SWCNT are responsible for the decreased stability of the peptide. In Figure 3.5b, we show evolutions of interaction energy of the nanotube with the full peptide. This interaction is found to stabilize rapidly for all, except the NT2 trajectories. Towards the end of the simulations, however, we find clear convergence in the interactions, irrespective of the initial configurations. The mean peptide-SWCNT interaction in the last 10 ns is $-128.8 (\pm 11.2)$ kcal mol⁻¹.

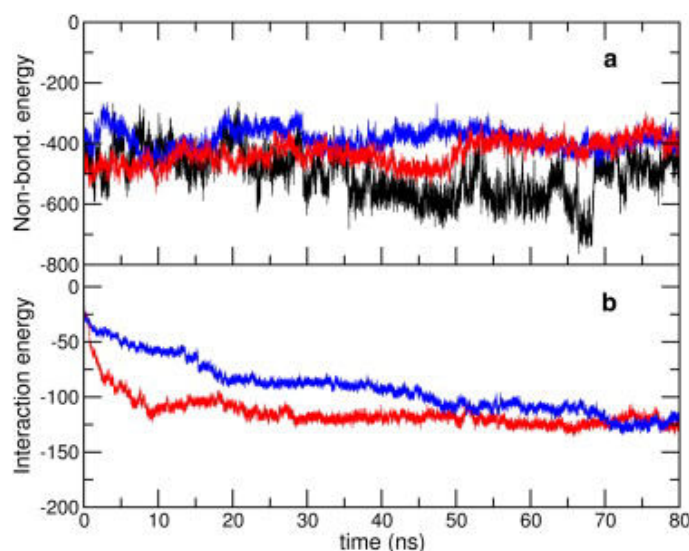


Figure 3.5. *a)* Total non-bonded energy of the full peptide along the control (in black), NT1 (in red) and NT2 (in blue) simulation trajectories. *b)* Total interaction energy of the full peptide and the SWCNT along the NT1 (in red) and NT2 (in blue) simulation trajectories. Energy units used are kcal mol⁻¹. The data for NT1 and NT2 have been averaged over the three independent trajectories each.

To understand the role of key regions in the peptide's adsorption on the SWCNT, we have calculated the interaction energies of the N-terminal segment (residues 1 to 16), HP1 and HP2 with the SWCNT, for all the nine peptide-SWCNT trajectories. As seen from plots of these interactions in Figures 3.6 and 3.7, corresponding interactions obtained from different trajectories converge toward the end of the simulations. Averaged over all trajectories, between 70 and 80 ns, the interaction with the N-terminal residues is $-55.0 (\pm 7.8)$ kcal mol⁻¹; with the HP1 segment is $-17.1 (\pm 3.1)$ kcal mol⁻¹; and with the HP2 segment is $-16.2 (\pm 2.6)$ kcal mol⁻¹. For the NT2 simulations, we observe an interesting correlation between the interaction strengths and the peptide's adsorption on the SWCNT surface. First, we observe an onset in the interaction strength with the HP1 domain and a concurrent sharp drop in the distance from the SWCNT. This is followed by a more substantial increase in the interaction strength with the N-terminal domain, and the attainment of saturation values of the peptide-nanotube contact area. This reiterates the role of HP1 in initiating the adsorption process, whose interactions with the SWCNT appear to initiate the adsorption process by bringing the N-terminal domain closer to the nanotube.

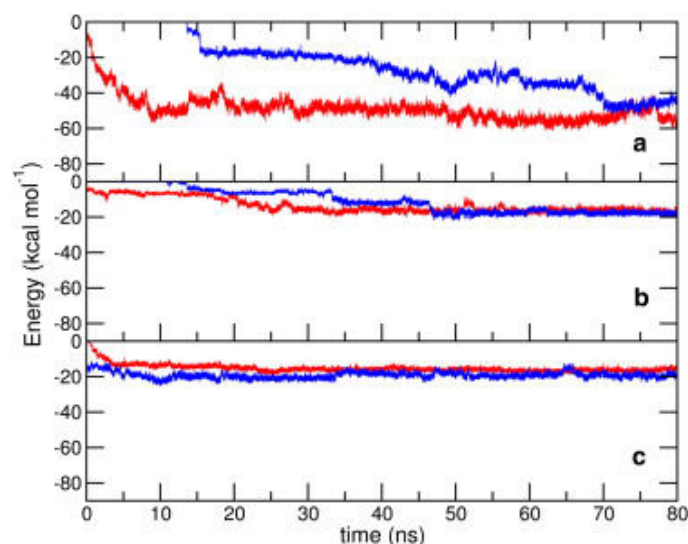


Figure 3.6. Time evolution of interaction energies of the SWCNT with *a*) residues 1-16, *b*) HP1 and *c*) HP2 segments of the peptide in the NT1 (in red) and NT2 (in blue) setups, averaged over three independent trajectories each.

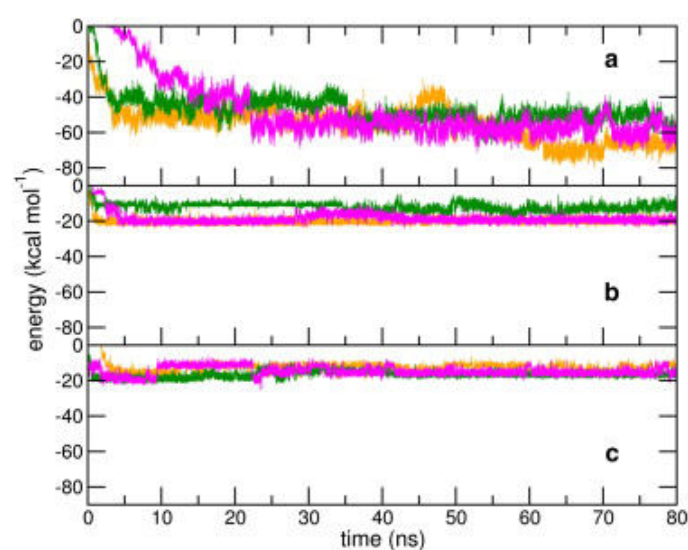


Figure 3.7. Time evolution of interaction energies of the SWCNT with *a*) residues 1-16, *b*) HP1 and *c*) HP2 segments of the peptide in the NT3 (in green), NT4 (in magenta) and NT5 (in orange) setups.

3.3.3 Propensity of Peptide Collapse

A key step in the self-assembly of the A β peptide in a primarily aqueous environment either into oligomers or into insoluble aggregates, is the formation of collapsed units of the monomeric form. This collapse is thought to be largely due to the strong hydrophobic interactions of the central hydrophobic core, and the hydrophobic patches near the peptide's

C-terminus.^{10, 12, 15} Therefore, devising methods in which the propensity for peptide collapse is decreased can lead to effective ways of preventing A β self-assembly and amyloidogenesis. As mentioned earlier, we have chosen the center of mass distance ' $d_{collapse}$ ' between the contiguous sequences L₁₇VFFAEDVGS₂₆ and K₂₈GAIIGLMVGGVVIA₄₂ of the A β ₁₋₄₂ for comparing the free energy changes due to peptide collapse; this has been done for the peptide-SWCNT systems with the largest and the smallest initial contact areas (ie. NT1 and NT2), and the pure peptide. The first sequence contains the central hydrophobic core and the greater part of the first helix of the 1Z0Q structure, and the second sequence contains the main C-terminal hydrophobic sequence. It is to be noted that the collapse (opening) of the peptide will effectively bring these patches closer (farther away), and therefore the separation between their centers of mass can be considered as an effective metric to probe loop closure propensity of the monomeric A β .

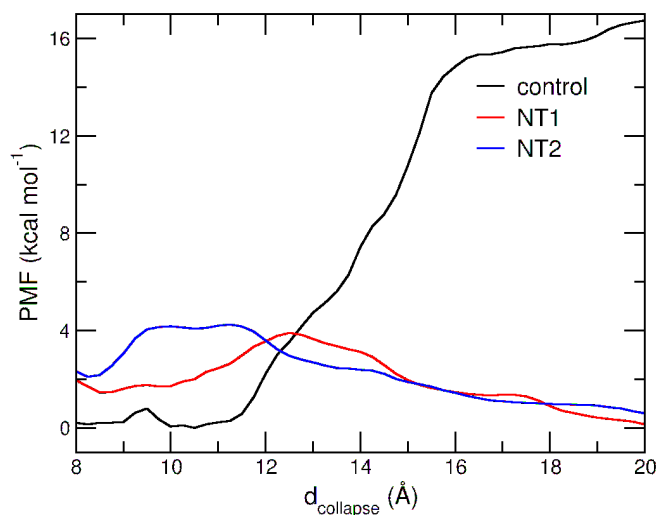


Figure 3.8. Free energy profiles along $d_{collapse}$ for the control, NT1 and NT2 setups obtained with ABF calculations.

In Figure 3.8, we show the PMF profiles obtained with the three setups mentioned above. (Details pertaining to the PMF calculation and the order parameter involved are provided in the *Methods* section). For the peptide monomer in the purely aqueous environment, there is a clear propensity for the patches to come together, or to ‘collapse’, and the energetic cost of maintaining the ‘open’ state is (more than) ~ 15 kcal mol⁻¹. In the presence of the SWCNT, there is a striking decrease in the energetic cost of maintaining the ‘open’ states, which are energetically more favorable compared to the ‘closed’ states. The PMF profiles indicate the appearance of a barrier between the two states, and considering the initial $d_{collapse}$ value of 16.7 Å, a marked propensity for the ‘open’ states. From estimates of

the peptide-nanotube contact area, we ascertained that the peptide remains in the vicinity of the SWCNT after a transient time during the course of the ABF calculation.

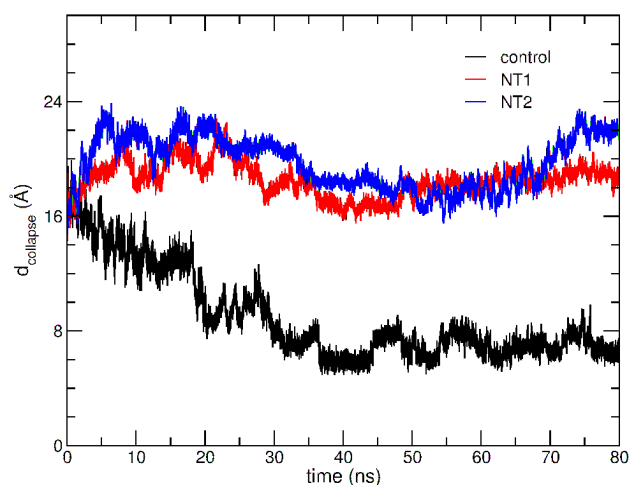


Figure 3.9. Time evolution of $d_{collapse}$ for the control, NT1 and NT2 trajectories. Data for NT1 and NT2 have been averaged over three independent trajectories.

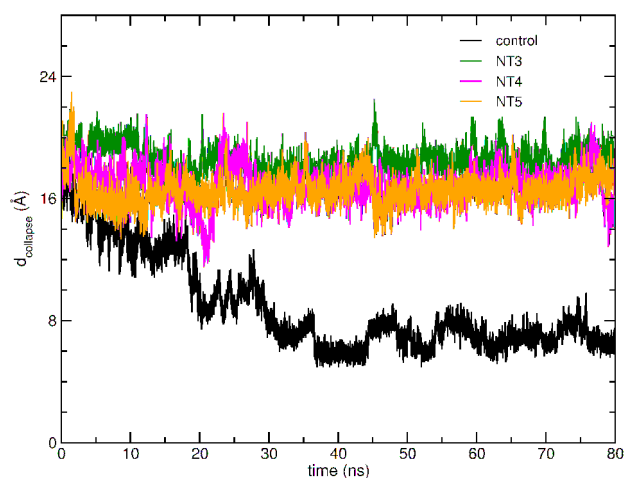


Figure 3.10. Time evolution of $d_{collapse}$ for the control, NT3, NT4 and NT5 trajectories.

Shown in Figure 3.9 are plots of $d_{collapse}$ obtained from the canonical MD simulation trajectories of the free peptide, and the NT1 and NT2 systems; corresponding data for NT3, NT4 and NT5 are shown in Figure 3.10. For the peptide in NT1 through NT5, $d_{collapse}$, for the last 40 ns is $17.8 (\pm 1.4)$ Å. On the other hand, the average value over the last 40 ns of the free peptide trajectory is $6.9 (\pm 0.8)$ Å, representing a decrease by 58.7% over the initial value. We mention here that three other independent 50 ns simulations of the same peptide coordinates in a purely aqueous environment, performed at 300 K, show a consistent decrease in $d_{collapse}$;

the average value of 8.2 Å (or a decrease of about 51%) at the end of the 50 ns simulations reiterates the spontaneity of collapse of the peptide when placed in a purely aqueous environment (data not shown). The presence of the SWCNT thus acts to disrupt the spontaneity of the collapse process.

3.4 Conclusion

In this article, we have presented the results of our investigations on the effects of a SWCNT on the full length, monomeric A β ₁₋₄₂ peptide. Five different initial configurations of the peptide and the SWCNT, with differences in the distances of and the angles made by the nanotube with key domains, as well as in the initial peptide-nanotube contact area, have been used. Compared with the pure monomeric peptide, we find significant changes in the behavior of the peptide when in proximity to the nanotube. We observe that peptide diffusion is largely arrested in the presence of the SWCNT, resulting in an overall localization of the peptide in its vicinity. The structural stability of the peptide is decreased; and the change in the peptide's non-bonded energy approximately equivalent to the interaction strength of the peptide with the SWCNT. The adsorption is independent of the initial peptide-nanotube configuration, as indicated by the converged values of the contact area obtained from all trajectories.

Our studies show that the peptide's collapse propensity is markedly reduced in the presence of the SWCNT. Adaptive biasing force based free energy calculations using two representative peptide-SWCNT setups indicate that the 'open' state should be largely populated at physiological temperatures. Preliminary analyses show that interactions of the HP1 segment with HP2 are hindered due to the onset of interactions with the nanotube. Further studies will be required to unravel in detail, the competition between interactions that lead to spontaneous collapse of the free peptide, with interactions arising due to the nanotube that act to prevent the collapse.

We propose that some of the observations from this study, and other computational studies of SWCNT interactions with the A β peptide fragments,⁴⁴ may be leveraged as means to disrupt A β aggregation in aqueous environment. As mentioned previously, in recent years, CNTs are being considered for applications such as site-directed drug delivery and gene therapy. In the case of the A β peptide, the observance of peptide localization near the SWCNT could thus be advantageous as it could increase the specificity of drug delivery

mechanisms. Importantly, the inhibition of peptide collapse suggests that SWCNTs could be a powerful agent for prevention of the peptide's self-assembly.

It is necessary, however, to keep in mind some of the current limitations and challenges that need to be met. Firstly, CNTs of very large dimensions can be highly cytotoxic (as they are capable of deforming the walls of living cells).⁵⁷ Thus, only CNTs of limited sizes may be used in actual, cell-based studies. Further, we know that pristine CNTs are insoluble in water.²¹ However, recent experimental work shows that suitably functionalized CNTs have vastly increased solubilities,^{58, 59} and several approaches for increasing the dispersion of CNTs in soluble media with non-covalent functionalization also exist.^{27, 60}

Further studies of the A β peptide with such suitably functionalized SWCNTs that retain sufficient hydrophobic surface area for the peptide's adsorption will be required; this may require finding optimal aspect ratios of the nanotubes. Lastly, this study has been performed with the monomeric form of the A β ₁₋₄₂ peptide, and the present approach may only work *before* the formation of insoluble aggregates, or even soluble oligomers and protofibrils. Detailed studies probing the competition between adsorption of a free monomeric on to a SWCNT surface and its propensity for deposition on the edge of a protofibril would be required; it needs to be determined whether or not the strength of the interactions with the SWCNT is sufficient to overcome the enthalpy of protofibrillar elongation.

3.5 References

1. J. Hardy and D. J. Selkoe, *Science*, 2002, **297**, 353-356.
2. O. Bugiani, *Neurol. Sci.*, 2011, **32**, 1241-1247.
3. M. Q. Liao, Y. J. Tzeng, L. Y. X. Chang, H. B. Huang, T. H. Lin, C. L. Chyan and Y. C. Chen, *FEBS Lett.*, 2007, **581**, 1161-1165.
4. N. Demeester, C. Mertens, H. Caster, M. Goethals, J. Vandekerckhove, M. Rosseneu and C. Labeur, *Eur. J. Neurosci.*, 2001, **13**, 2015-2024.
5. J. Khandogin and C. L. Brooks, *Proc. Natl. Acad. Sci.*, 2007, **104**, 16880-16885.
6. O. Crescenzi, S. Tomaselli, R. Guerrini, S. Salvadori, A. M. D'Ursi, P. A. Temussi and D. Picone, *Eur. J. Biochem.*, 2002, **269**, 5642-5648.
7. T. Simona, E. Veronica, V. Paolo, A. J. v. N. Nico, M. J. J. B. Alexandre, G. Remo,

- T. Teodorico, A. T. Piero and P. Delia, *ChemBioChem*, 2006, **7**, 257-267.
8. C. Haass and D. J. Selkoe, *Nat. Rev. Mol. Cell Biol.*, 2007, **8**, 101-112.
9. R. Cappai and K. Barnham, *Neurochem. Res.*, 2008, **33**, 526-532.
10. S. L. Bernstein, T. Wyttenbach, A. Baumketner, J.-E. Shea, G. Bitan, D. B. Teplow and M. T. Bowers, *J. Am. Chem. Soc.*, 2005, **127**, 2075-2084.
11. T. Lührs, C. Ritter, M. Adrian, D. Riek-Loher, B. Bohrmann, H. Döbeli, D. Schubert and R. Riek, *Proc. Natl. Acad. Sci. U.S.A.*, 2005, **102**, 17342-17347.
12. A. Baumketner and J.-E. Shea, *J. Mol. Biol.*, 2007, **366**, 275-285.
13. L. Triguero, R. Singh and R. Prabhakar, *J. Phys. Chem. B*, 2008, **112**, 7123-7131.
14. A. T. Petkova, Y. Ishii, J. J. Balbach, O. N. Antzutkin, R. D. Leapman, F. Delaglio and R. Tycko, *Proc. Natl. Acad. Sci. U.S.A.*, 2002, **99**, 16742-16747.
15. C. Lee and S. Ham, *J. Comput. Chem.*, 2010, **32**, 349-355.
16. J. Li, R. Liu, K. S. Lam, L.-W. Jin and Y. Duan, *Biophys. J.*, 2011, **100**, 1076-1082.
17. M. H. Viet, S. T. Ngo, N. S. Lam and M. S. Li, *J. Phys. Chem. B*, 2011, **115**, 7433-7466.
18. M. Mattson, R. Haddon and A. Rao, *J. Mol. Neurosci.*, 2000, **14**, 175-182.
19. L. P. Zanello, B. Zhao, H. Hu and R. C. Haddon, *Nano Lett.*, 2006, **6**, 562-567.
20. X. Shi, B. Sitharaman, Q. P. Pham, F. Liang, K. Wu, W. Edward Billups, L. J. Wilson and A. G. Mikos, *Biomaterials*, 2007, **28**, 4078-4090.
21. L. Lacerda, A. Bianco, M. Prato and K. Kostarelos, *Adv. Drug Deliv. Rev.*, 2006, **58**, 1460-1470.
22. A. Bianco, J. Hoebeke, S. Godefroy, O. Chaloin, D. Pantarotto, J.-P. Briand, S. Muller, M. Prato and C. D. Partidos, *J. Am. Chem. Soc.*, 2004, **127**, 58-59.
23. Y. Wenrong, P. Thordarson, J. J. Gooding, S. P. Ringer and F. Braet, *Nanotechnology*, 2007, **18**, 412001.
24. V. V. Chaban, T. I. Savchenko, S. M. Kovalenko and O. V. Prezhdo, *J. Phys. Chem. B*, 2010, **114**, 13481-13486.
25. C.-c. Chiu, G. R. Dieckmann and S. O. Nielsen, *J. Phys. Chem. B*, 2008, **112**, 16326-16333.
26. K. Balamurugan, R. Gopalakrishnan, S. S. Raman and V. Subramanian, *J. Phys. Chem. B*, 2010, **114**, 14048-14058.

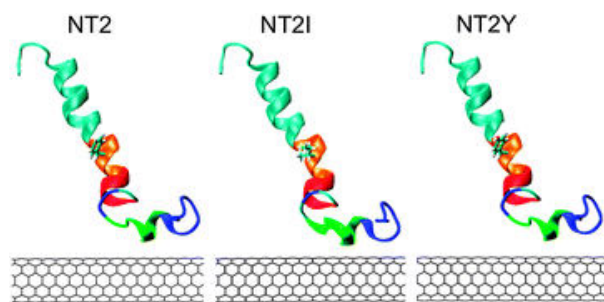
27. Y. Liu, C. Chipot, X. Shao and W. Cai, *J. Phys. Chem. C*, 2011, **115**, 1851-1856.
28. R. R. Johnson, B. J. Rego, A. T. C. Johnson and M. L. Klein, *J. Phys. Chem. B*, 2009, **113**, 11589-11593.
29. A. Hirano, K. Uda, Y. Maeda, T. Akasaka and K. Shiraki, *Langmuir*, 2010, **26**, 17256-17259.
30. K. Balamurugan, E. R. A. Singam and V. Subramanian, *J. Phys. Chem. C*, 2011, **115**, 8886-8892.
31. E. J. Sorin and V. S. Pande, *J. Am. Chem. Soc.*, 2006, **128**, 6316-6317.
32. Y. Kang, Q. Wang, Y.-C. Liu, J.-W. Shen and T. Wu, *J. Phys. Chem. B*, 2010, **114**, 2869-2875.
33. J. E. Kim and M. Lee, *Biochem. Biophys. Res. Commun.*, 2003, **303**, 576-579.
34. C. D. Tatko and M. L. Waters, *J. Am. Chem. Soc.*, 2002, **124**, 9372-9373.
35. S. M. Tracz, A. Abedini, M. Driscoll and D. P. Raleigh, *Biochemistry*, 2004, **43**, 15901-15908.
36. G. W. Platt, K. E. Routledge, S. W. Homans and S. E. Radford, *J. Mol. Biol.*, 2008, **378**, 251-263.
37. Y. Porat, A. Abramowitz and E. Gazit, *Chem. Biol. Drug Des.*, 2006, **67**, 27-37.
38. R. Scherzer-Attali, R. Pellarin, M. Convertino, A. Frydman-Marom, N. Egoz-Matia, S. Peled, M. Levy-Sakin, D. E. Shalev, A. Caflisch, E. Gazit and D. Segal, *PLoS ONE*, 2010, **5**, e11101.
39. A. H. Armstrong, J. Chen, A. F. McKoy and M. H. Hecht, *Biochemistry*, 2011, **50**, 4058-4067.
40. F. T. Senguen, T. M. Doran, E. A. Anderson and B. L. Nilsson, *Mol. Biosyst.*, 2011, **7**, 497-510.
41. Z. Fu, Y. Luo, P. Derreumaux and G. Wei, *Biophys. J.*, 2009, **97**, 1795-1803.
42. W. Humphrey, A. Dalke and K. Schulten, *J. Mol. Graph.*, 1996, **14**, 33-38.
43. S. J. Hamodrakas, C. Liappa and V. A. Iconomidou, *Int. J. Biol. Macromol.*, 2007, **41**, 295-300.
44. W. L. Jorgensen, J. Chandrasekhar, J. D. Madura, R. W. Impey and M. L. Klein, *J. Chem. Phys.*, 1983, **79**, 926-935.
45. L. KalÈ, R. Skeel, M. Bhandarkar, R. Brunner, A. Gursoy, N. Krawetz, J. Phillips, A. Shinozaki, K. Varadarajan and K. Schulten, *J. Comput. Phys.*, 1999, **151**, 283-312.

46. A. D. MacKerell, D. Bashford, Bellott, R. L. Dunbrack, J. D. Evanseck, M. J. Field, S. Fischer, J. Gao, H. Guo, S. Ha, D. Joseph-McCarthy, L. Kuchnir, K. Kuczera, F. T. K. Lau, C. Mattos, S. Michnick, T. Ngo, D. T. Nguyen, B. Prodhom, W. E. Reiher, B. Roux, M. Schlenkrich, J. C. Smith, R. Stote, J. Straub, M. Watanabe, J. Wiórkiewicz-Kuczera, D. Yin and M. Karplus, *J. Phys. Chem. B*, 1998, **102**, 3586-3616.
47. A. D. Mackerell, M. Feig and C. L. Brooks, *J. Comput. Chem.*, 2004, **25**, 1400-1415.
48. J.-P. Ryckaert, G. Ciccotti and H. J. C. Berendsen, *J. Comput. Phys.*, 1977, **23**, 327-341.
49. S. E. Feller, Y. Zhang, R. W. Pastor and B. R. Brooks, *J. Chem. Phys.*, 1995, **103**, 4613-4621.
50. G. J. Martyna, D. J. Tobias and M. L. Klein, *J. Chem. Phys.*, 1994, **101**, 4177-4189.
51. U. Essmann, L. Perera, M. L. Berkowitz, T. Darden, H. Lee and L. G. Pedersen, *J. Chem. Phys.*, 1995, **103**, 8577-8593.
52. E. Darve, D. Rodriguez-Gomez and A. Pohorille, *J. Chem. Phys.*, 2008, **128**, 144120-144133.
53. J. r. Héning, G. Fiorin, C. Chipot and M. L. Klein, *J. Chem. Theory Comput.*, 2009, **6**, 35-47.
54. L. Jean, Chiu F. Lee and David J. Vaux, *Biophys. J.*, 2012, **102**, 1154-1162.
55. J. Gumbart, C. Chipot and K. Schulten, *J. Am. Chem. Soc.*, 2011, **133**, 7602-7607.
56. C. Wei and A. Pohorille, *J. Phys. Chem. B*, 2011, **115**, 3681-3688.
57. K. Kostarelos, *Nat. Biotechnol.*, 2008, **26**, 774-776.
58. C. A. Dyke and J. M. Tour, *Chem. – A Euro. J.*, 2004, **10**, 812-817.
59. C. A. Dyke and J. M. Tour, *J. Phys. Chem. A*, 2004, **108**, 11151-11159.
60. L. Vaisman, H. D. Wagner and G. Marom, *Adv. Colloid Interface Sci.*, 2006, **128-130**, 37-46.

Chapter – 4

**Critical Roles of Key Domains in Complete Adsorption of A β
Peptide on Single-Walled Carbon Nanotubes: Insight with Point
Mutations and MD simulations**

Abstract



Owing to the influence of nanomaterials on biomacromolecular behavior, their potential applications are rapidly gaining attention. Based on atomistic molecular dynamics simulation studies we have recently reported that the full-length A β peptide, whose self-

assembly is associated with Alzheimer's disease, adsorbs rapidly on single-walled carbon nanotubes, thereby losing its natural propensity to collapse. Here, we investigate the mechanistic overlap between the peptide's compactification and its adsorption, while decoupling the roles of hydrophobicity and aromaticity *via* point mutations. The collapse mechanism is correlated with interactions between the central hydrophobic core and the peptide's C-terminal domain, which are almost exactly compensated by interactions arising from the nanotube after complete adsorption. Adsorption is initiated by HP1 and consolidated by strong interactions arising from the N-terminal domain. Altering the hydrophobicity, but not the aromatic character, of the central residue in HP1 decreases the collapse probability. On the other hand, the adsorption propensity is dramatically reduced when either the hydrophobicity or the aromatic character in HP1 is compromised. The hydrophobicity of HP1 is responsible for dewetting transitions that facilitate its initial interactions with the nanotube, which then lead to very favorable interactions with the nanotube. We also report here the effects of sharply reducing both aromatic and hydrophobic character within the peptide's central hydrophobic core on its free and surface behavior. Interestingly, in such an altered peptide, complete surface adsorption is found to induce, rather than prevent, the adsorbed peptide's collapse. The weakened surface interactions of the central hydrophobic core allow its greater translational mobility on the surface, thereby facilitating interactions that lead to compaction. Both the adsorption and the subsequent collapse are accompanied by a loss of surface hydration in the modified peptide. We further find that such a two-step dewetting leads to hydration levels comparable to that obtained after compaction of the free peptide. These insights may be leveraged for designing molecular surfaces for disrupting intrinsic A β behavior.

4.1 Introduction

The 39-42 residue Amyloid beta ($A\beta$) is produced from exact proteolytic cleavage of the amyloidogenic sequence within the much larger (~ 70 kDa) membrane embedded precursor protein (APP).^{1, 2} Within APP, the $A\beta$ sequence is thought to be primarily of helical conformation, and to undergo conformational transitions to predominantly beta sheet forms after release into aqueous cytoplasm.^{3, 4} The sequence is highly prone to misfolding, self-assembly and aggregation, the physiological triggers of which are beginning to be unraveled via a variety of experimental, theoretical and computational studies.⁵⁻¹¹ Computational studies are especially useful as the high aggregation propensity of monomeric $A\beta$ monomer makes it difficult to experimentally follow the self-assembly pathways in purely aqueous environment.¹² The amyloid hypothesis contends that the aggregation of $A\beta$ into insoluble, fibrillar aggregates marks the onset of the neurodegenerative Alzheimer's disease (AD).¹³ In recent years, however, emerging studies have implicated the role of the peptide's soluble, oligomeric forms in neurotoxicity and dementia.^{14, 15} In any case, it appears that hindering the self-assembly pathways of the peptide could be a crucial strategy to counter the onset of AD. Thus, recent experimental and computational studies have been directed towards finding novel physico-chemical processes that may potentially inhibit self-assembly of the $A\beta$ monomer or destabilize its oligomeric or pre-aggregated fibrillar forms.¹⁶⁻²³

NMR studies indicate that in fully aqueous environment, monomeric $A\beta$ attains compact conformations.²⁴⁻²⁶ The peptide's strong propensity to collapse has also been described by computational studies of $A\beta$ segments,²⁷⁻²⁹ as well as of those of the full-length peptide.^{22, 26, 30} The compactification occurs due to interactions between the peptide's central hydrophobic core and regions belonging to its C-terminal domain.^{24-26, 30, 31} The collapse and subsequent structural realignment has generally been considered to constitute early steps of the peptide self-assembly.^{25, 26} Emerging studies, however, indicate that the solvation thermodynamics plays important roles in the initial dimerization process.^{10, 32} Nevertheless, monomers constituting the multimeric and the aggregated forms of $A\beta$ are compact, and preventing the compactification of the peptide monomer in aqueous environment could be an important way with which to hinder or prevent self-assembly.

Carbon-based nanomaterials such as fullerene, graphene, and single- and multi-walled carbon nanotubes have recently been found to interact with and influence biological

molecules and assemblies such as peptides and proteins,^{16, 33-37} nucleic acids,^{38, 39} polysaccharides⁴⁰ and lipid membranes.⁴¹⁻⁴³ Their applicability and usage in biology and medicine is increasingly being considered, although an array of issues related to their solubility and cellular toxicity remain to be suitably addressed.⁴⁴⁻⁴⁶ Nevertheless, their strong influence on biological systems necessitates a deep understanding of the nature of their interactions, and recently, molecular dynamics (MD) simulations have been utilized extensively to unravel these interactions at the ‘single-molecule’ level. Interestingly, simulations show that these nanomaterials can directly influence the natural characteristics of amyloidogenic proteins²² as well as their assemblies,^{20, 21, 47} thereby generating interest in their potential applications as amyloid pathway blockers or amyloid destabilizers. This is supported by a growing number of experiments that describe perturbations to intrinsic amyloidogenic properties of A β in presence of these materials.^{16, 48, 49}

We have shown very recently with atomistic molecular dynamics (MD) simulations that monomeric A β spontaneously adsorbs on the hydrophobic surface of a single-walled carbon nanotube (SWCNT) within tens of nanoseconds.²² This phenomenon was observed irrespective of the initial peptide-nanotube orientation. Importantly, we found that the presence of the SWCNT surface drastically disrupted the intrinsic collapse propensities of the monomeric peptide, and increased the thermodynamic favorability of the ‘open’ states at physiological temperatures. We found that the key hydrophobic domains of the peptide, L₁₇VFFA₂₁ (the central hydrophobic core, or ‘HP1’) and A₃₀IIGLMV₃₅ (or ‘HP2’) interact strongly with the nanotube. Interestingly, in the peptide-nanotube complexes where the N-terminal region was initially distal from the nanotube, it was seen that HP1 played a key role in initiating the interaction of the nanotube, resulting in complete adsorption. We noted a two-fold manner in which the results could be plausibly utilized: the reduced propensity to collapse could potentially block the amyloidogenic pathway, while the peptide’s localization on the SWCNT surface could be leveraged for site-specific drug delivery.

The phenomena observed in the previous study open up interesting and important mechanistic questions. The simulations suggest that the phenomena of peptide collapse and adsorption on the nanotube are mutually exclusive. Thus, the details of the mechanistic overlap between the collapse and the adsorption phenomena, or the manner in which the interactions with the nanotube interfere with those between the important domains need to be understood with clarity. If the interactions responsible for the two have low overlap, a pre-

collapsed monomer may still adsorb on the nanotube, or collapse can occur after adsorption. Strong affinity between the HP1 domain and the nanotube irrespective of initial orientation suggests that π - π stacking interactions could be playing critical roles in the adsorption process. We point out that while probing these non-covalent interactions can be computationally challenging, a number of recent studies have successfully used MD approaches to qualitatively rank and compare phenomena involving interactions between aromatic moieties (ie. π - π stacking) under varying conditions.^{50, 51} Interestingly, comparisons with quantum mechanical and MD simulation based calculations for amino acid analogues demonstrate that MD approaches are capable of reflecting the energetic trends of interactions involving π - π stacking.⁵²

In an attempt to answer the important questions that emerge from the last study, we have systematically mutated the aromatic residue that takes up the central position in HP1 (Phe19) with a residue of comparable hydrophobicity (Ile), a residue of lower hydrophobicity but of similar aromatic character (Tyr) and a residue of very lower hydrophobicity (Ala). Independently run MD trajectories of the peptide with these mutations lend mechanistic insight not only into the intrinsic behavior of the peptide monomer in water, but also that in complex with the SWCNT. The hydrophobic character of HP1 is essential for bringing about the peptide's complete collapse. Further, HP1 is found to initiate complete adsorption of the peptide on the SWCNT. The behavior of the mutated peptide-SWCNT complexes demonstrate that the adequate balance of hydrophobic and aromatic character within HP1 is necessary for bringing about strong adsorption. The loss of hydrophobic character results in screening effects by solvent water molecules, while the loss in aromatic character in the central residue weakens the overall interaction strength with the nanotube, possibly by diminishing the π - π stacking propensity. Interestingly, in sharp contrast with our previous observations, the nanotube surface induced, rather than prevented, the compaction of the peptide in the event of complete adsorption of the F19A altered peptide. Adaptive biasing force (ABF) based free energy calculations performed on the pre-adsorbed F19A peptide corroborate the thermodynamic favorability of the peptide collapse. The weaker surface interactions allow a greater degree of lateral movement of HP1 on the nanotube surface, effectively facilitating interaction with the C-terminal domain and inducing marked compaction. The dewetting resulting from the post-adsorption collapse of F19A is comparable to that resulting from spontaneous collapse on the unmutated peptide. Our studies directly demonstrate the critical dependence of observed surface and biophysical

characteristics of the $A\beta$ sequence on the overall chemical nature of its key domains. The insights gained may have important ramifications in the design of molecular surfaces for disrupting intrinsic $A\beta$ behavior.

4.2. Materials and Methods

4.2.1 System Setups

Coordinates for the full-length $A\beta_{1-42}$ peptide, taken from the PDB database (PDB ID: 1Z0Q) were reported via solution NMR in the 3:7 mixture of hexafluoro-2-propanol and water, an environment considered to be similar to that of the lipid phase of membranes.¹² We mention here that the pathway in pure water, of this, and other similar structures have been considered analogous to that of enzymatically cleaved $A\beta$ upon release into aqueous cytoplasm.^{4,12,30} A single-walled carbon nanotube (SWCNT) of (6,6) chirality, 4.1 Å radius and 99.5 Å length, was generated with the VMD package.⁵³ The setup for the NT2 configuration, described in detail ref. 22, was used in this study for the unmutated and the mutated peptide-nanotube complexes. This configuration had the least initial peptide-nanotube contact area amongst the five complexes studied in ref. 22; the total adsorption was found to be independent of the initial setup. In the NT2 setup, the SWCNT axis was held parallel to the x-axis and to the C-terminal domain. The SWCNT was fixed at the setup position with harmonic forces. To avoid artifacts arising due to edge effects, infinitely long SWCNTs were created using periodic boundary conditions.³³ The NH_3^+ and COO^- groups were added to the peptide's N- and C-termini, respectively, and three Na^+ counterions were added to neutralize the system. The peptide-nanotube complex was solvated with about 9500 water molecules, using the TIP3P water model.⁵⁴ The pure, unmutated peptide (referred in the remaining text as F19) was similarly setup for simulation without the nanotube, with about 9400 water molecules.

The mutated peptide-nanotube complexes were obtained by replacing the Phe residue at position 19 of the peptide in the NT2 setup with a residue of Ile (an aliphatic residue), Tyr (an aromatic residue) and Ala (a smaller aliphatic residue) to yield, respectively, the NT2I, the NT2Y and the NT2A systems. The Fauchere-Pliska scale, derived from partitioning of the N-acetyl-amino-acids in octanol/water, reports the hydrophobicity indices (π_R) of Phe, Ile, Tyr and Ala as 1.79, 1.80, 0.96 and 0.31 respectively.⁵⁵ Similarly, replacement of Phe19 in the pure peptide yielded the mutated peptide systems, F19I, F19Y and F19A respectively.

4.2.2 MD Simulations

As earlier, MD simulations were performed with the NAMD2.7 simulation tool,⁵⁶ with the CHARMM22 all-atom force field including the CMAP corrections.^{57, 58} Bonds including hydrogen atoms were held fixed with SHAKE.⁵⁹ Energy minimizations were performed initially on all systems with conjugate gradient minimization, followed by simulations in the isothermal-isobaric ensemble. A temperature of 310 K was maintained using Langevin dynamics, using collision frequency of 1 ps⁻¹. A pressure of 1 atmosphere was maintained with the Langevin piston Nosé-Hoover algorithm.⁶⁰ The simulation timestep was 2 fs, and three-dimensional orthorhombic periodic boundary conditions were applied. Electrostatic interactions were calculated with particle-mesh Ewald.⁶¹ The cutoff for non-bonded interactions was 12 Å, with smoothing started from 10.5 Å.

4.2.3 Adaptive Biasing Force Calculations

To characterize the energetic favorability of collapse of the F19A peptide adsorbed on the SWCNT surface, the potential of mean force (PMF) was calculated with the adaptive biasing force (ABF) method as implemented in the NAMD package was used.^{62, 63} As earlier, the center of mass distance between the segments L₁₇VFFAEDVGS₂₆ and K₂₈GAIIGLMVGGVVIA₄₂ (or ' $d_{collapse}$ ') was chosen as the reaction coordinate to describe peptide compactification.²² Initial coordinates were taken from a snapshot obtained just after the peptide had reached saturated $A_{contact}$ value. The ABF method is a thermodynamic integration formalism wherein the average force acting along a particular reaction coordinate (say ζ) is used to estimate the bias required for overcoming local barriers in the free energy iso-surface. With a single dimensional surface, the gradient of the free energy A is calculated from the average force exerted on ζ , *ie.*,

$$\frac{dA(\zeta)}{d\zeta} = -\langle F_{\zeta} \rangle_{\zeta}$$

F_{ζ} accumulated in small bins over the range of interest is used to estimate the biasing force required to overcome local free energy barriers.

In this study, $d_{collapse}$ ranged from 8 to 21 Å and was divided into 52 windows, each 0.25 Å wide. Unbiased sampling was obtained for 500 steps before estimation and application of the bias in order to avoid non-equilibrium effects. The ABF simulations were

carried out for more than 200 ns, and the free energy profile reported converged over a period of 50 ns. The maximum extent of error for the free energy calculation was estimated using the methodology proposed by Rodriguez-Gomez.^{64,65}

4.3 Results

4.3.1 Effect of F19I and F19Y Mutations on Peptide's Intrinsic Collapse and Adsorption on SWCNT Surface

4.3.1.1 Effect of F19I and F19Y Mutations on Monomeric Compactification

As mentioned earlier, the $A\beta$ monomer is characterized by a strong propensity to form compact structures in water, and this process has been considered to be an early step in the peptide's self-assembly pathway. We have earlier characterized the compactness of the full-length $A\beta$ peptide by the metric ' $d_{collapse}$ ', the center of mass distance between the contiguous N- and C-terminal sequences, L₁₇VFFAEDVGS₂₆ and K₂₈GAIIGLMVGGVVI₄₂.²² This distance has an initial value of 16.7 Å in the 1Z0Q structure. In Figure 4.1, we plot for a representative F19 trajectory, the temporal evolution of the peptide's radius of gyration (R_g); the $d_{collapse}$ value; the interaction energy between the HP1 and HP2 (E_1); and the interaction energy between HP1 and the full C-terminal segment K₂₈GAIIGLMVGGVVI₄₁ (E_2). Data for representative trajectories of the F19I and the F19Y systems are provided in Figure 4.2, Figure 4.3 and Figure 4.4.

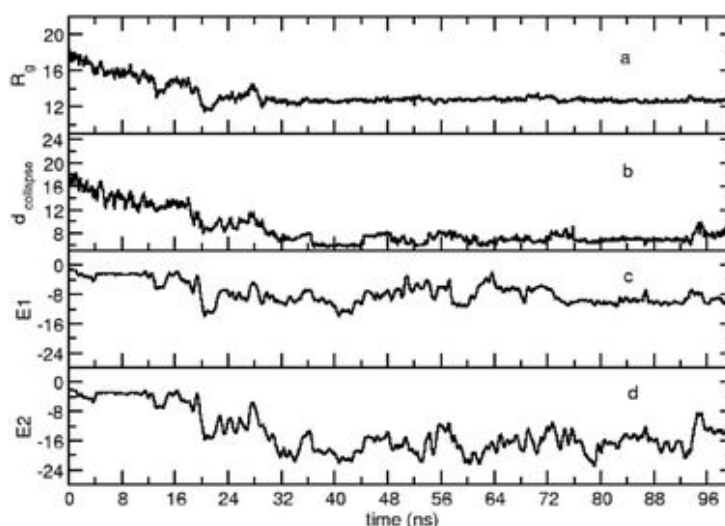


Figure 4.1. Evolution of *a*) peptide radius of gyration, R_g (in Å); *b*) $d_{collapse}$ (in Å); *c*) interaction energy E_1 (in kcal mol⁻¹); *d*) interaction energy E_2 (kcal mol⁻¹), along a sample F19 trajectory. See text for details.

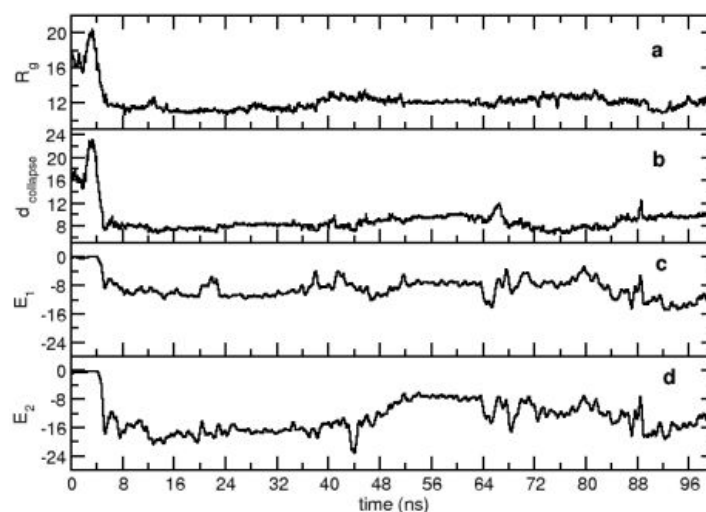


Figure 4.2. Evolution of *a*) peptide radius of gyration, R_g (in Å); *b*) $d_{collapse}$ (in Å); *c*) interaction energy E_1 (in kcal mol⁻¹); *d*) interaction energy E_2 (kcal mol⁻¹), along an F19I trajectory.

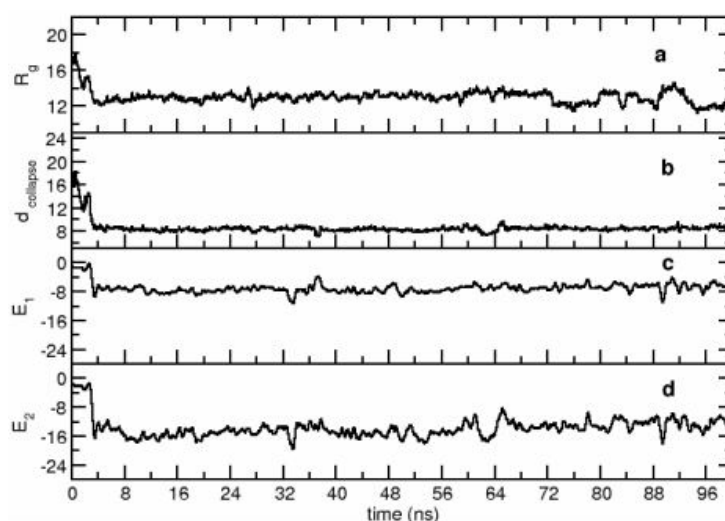


Figure 4.3. Evolution of *a*) peptide radius of gyration, R_g (in Å); *b*) $d_{collapse}$ (in Å); *c*) interaction energy E_1 (in kcal mol⁻¹); *d*) interaction energy E_2 (kcal mol⁻¹), along a collapsing F19Y trajectory.

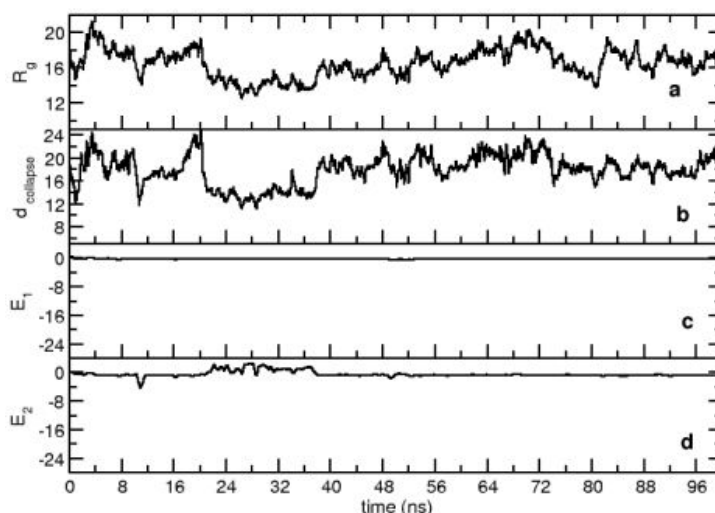


Figure 4.4. Evolution of *a*) peptide radius of gyration, R_g (in Å); *b*) $d_{collapse}$ (in Å); *c*) interaction energy E_1 (in kcal mol⁻¹); *d*) interaction energy E_2 (kcal mol⁻¹), along a non-collapsing F19Y trajectory.

The plots show that the temporal pattern of R_g is well correlated with that of $d_{collapse}$. For example, in the F19 system shown, the gradual drop in R_g within the first 20 ns of the simulation time is commensurate with decreasing $d_{collapse}$ over the same time. This data confirms that $d_{collapse}$ is an appropriate metric for depicting the degree of the peptide's compactness. Furthermore, we observe a strong temporal correlation of $d_{collapse}$ with E_1 and E_2 . Interestingly, E_1 is found to constitute a large fraction of the total interaction of HP1 with the full C-terminus, showing that interactions between HP1 and HP2 are one of the key factors that lend stability to the peptide's compact form. In Figure 4.5, we depict the distributions of $d_{collapse}$ values obtained by combining data from the last 10 ns of the simulation trajectories, for the F19, F19I and the F19Y systems. The distributions indicate that the propensity for $d_{collapse}$ to significantly decrease from the initial value is pronounced in the F19 and the F19I systems, whereas there is a significant population of 'open' states in F19Y, with a mean $d_{collapse}$ value of 18.2 Å over the last 10 ns. Thus, lowering the effective hydrophobicity of the central hydrophobic core can affect the collapse propensity. Henceforth, we shall refer to a simulated peptide to have attained collapse if $d_{collapse}$ decreases by at least 30% within the final 10 ns of the simulation. All the simulated trajectories of F19 and F19I attain the collapsed, or the 'closed' state, whereas one of the F19Y trajectories remains in the 'open' state.

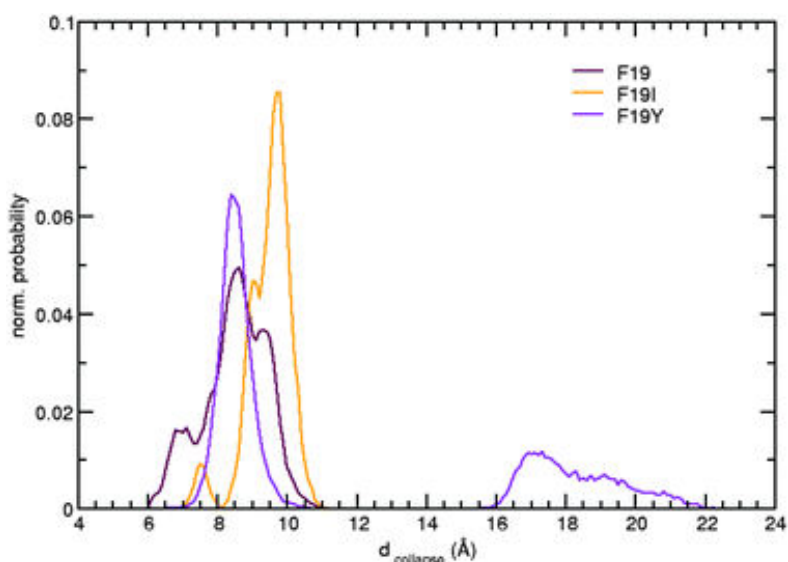


Figure 4.5. Normalized distributions of $d_{collapse}$ obtained from the last 10 ns of the free peptide simulations. Data for F19, F19I and F19Y are shown in maroon, orange and purple, respectively.

The results discussed highlight the important role played by the hydrophobic domain HP1 in bringing about spontaneous compactness in the $A\beta$ monomer, in agreement with earlier reports. Small alterations to this domain may alter the rate of compactification. In Table 4.1, we have listed the mean values of $d_{collapse}$ during the final 10 ns of simulation along with the mean values of the interactions E_1 and E_2 for the native and the mutated systems. Toward the end of the 100 ns simulation, the final values of $d_{collapse}$ and R_g are found to be progressively higher in going from the unmutated peptide, to F19I and F19Y; the interactions E_1 and E_2 follow the trend in reverse. The trends qualitatively follow the hydrophobicity of residue 19 as reported by the scale of Pliska and Fauchere,⁵⁵ thereby reiterating the importance of the HP1 hydrophobicity domain in bringing about the peptide's collapse. Interestingly, it has been observed experimentally that the aggregation kinetics of $A\beta$ remains unchanged with the F19I mutation, but is distinctly lowered with the F19Y mutation.⁶⁶ While this reflects the importance of the HP1 domain in $A\beta$ aggregation, in light of the data discussed above, it is also plausible that this reflects a relationship between monomeric compactness and later stages of self-assembly.

System	π_r	E_1	E_2	d_{collapse}
F19	1.79	- 10.1 (2.8)	-17.4 (4.4)	8.3 (0.9)
F19I	1.80	- 7.4 (4.6)	-13.2 (3.5)	9.4 (0.6)
F19Y	0.96	- 4.4 (3.4)	-9.0 (6.3)	11.7 (4.7)

Table 4.1. Mean values of the interactions E_1 and E_2 (in kcal mol⁻¹), and d_{collapse} (in Å), averaged over the last 10 ns of all simulated trajectories of F19, F19I and F19Y systems. π_r represents the hydrophobicity of residue 19, from the scale of Fauchere-Pliska (ref 55).

4.3.1.2 Complete Adsorption on SWCNT: Role of N-terminal Domains

We have recently demonstrated that the $A\beta$ monomer completely adsorbs on the curved, hydrophobic surface of SWCNTs within tens of nanoseconds, irrespective of the initial orientation of the nanotube relative to the peptide. We had noted that when the N-terminus was initially distal from the nanotube, complete adsorption of the peptide was dependent on the sequential adsorption of the HP1 and first 16 residues of the N-terminal domain on the nanotube surface. Here, we closely scrutinize this phenomenon, and examine how alterations to Phe19, the central residue of the HP1 domain, may affect the overall adsorption propensities. Specifically, we have sought to understand whether the overall hydrophobic character of HP1, or the presence of the aromatic Phe residues, or both, is the key determinant in its strong interaction with the nanotube.

In Figure 4.6, we present evolution of the total peptide-nanotube contact area (based on the calculation method described in ref. 22), averaged at each time point over values obtained from four simulated trajectories each of NT2, NT2I and NT2Y. As in the previous study, we consider the peptide to have fully adsorbed on the nanotube if a total contact area of about 900 Å² is achieved. These data show that complete adsorption within the simulated timescale was achieved only for the NT2 system; altering either the aromatic character (as in NT2I), or the hydrophobicity (as in NT2Y) of the central residue in HP1 significantly reduced the adsorption propensity. While the peptide in all four NT2 trajectories adsorbed completely on the nanotube, the peptide in only two of the NT2I, and in two of the NT2Y trajectories underwent complete adsorption within the final 10 ns. In Figure 4.7, we have shown the evolution of the contact areas of key domains of the peptide with the nanotube for

a representative NT2 trajectory, and for a representative fully adsorbing trajectory of NT2I and NT2Y; evolution of the contact areas for a representative partially adsorbing trajectory is shown in Figure 4.8. In Table 4.2, we list the mean contact areas obtained over the final 10 ns for the complete adsorbing and the partially adsorbing cases. For the fully adsorbing cases, N-terminal and the HP1 domains together contribute between 59 to 64% of the total contact area. For the partially adsorbing cases, however, these values are small (about 14% for NT2I) or negligible (for NT2Y). On the other hand, the contact area of the C-terminal domains $A_{30}IIGLM_{35}$, and $V_{36}GGVVI_{41}$ do not show marked differences between the fully and the partially adsorbing trajectories. We point out that the contact areas with these domains are similar to those obtained with the other four initial orientations of peptide and nanotube (see ref. 22). Therefore, total adsorption of the peptide is contingent upon stable adsorption of the N-terminal and the HP1 domains. The higher propensity of the N-terminal domains to interact with the nanotube compared to the C-terminal domains could be due to the presence of a large number of residues that can potentially participate in π - π stacking and π -cation interactions.^{52, 67}

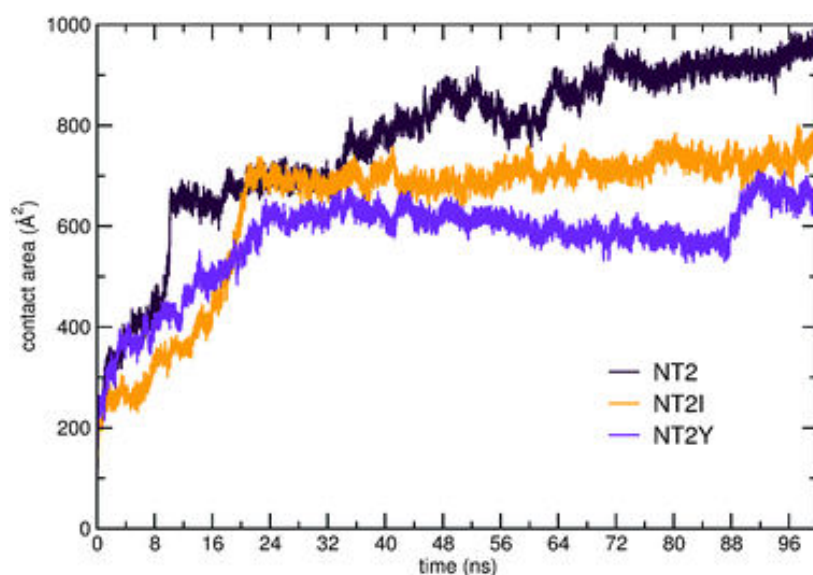


Figure 4.6. Evolution of the total peptide-SWCNT contact area in NT2 (maroon), NT2I (orange), and NT2Y (purple) systems, averaged over four simulated trajectories at every time point.

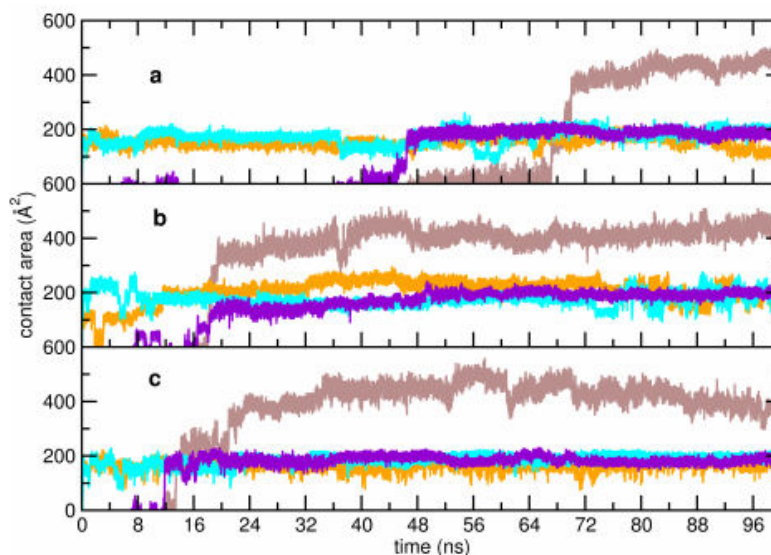


Figure 4.7. Evolution of the contact area of key domains for representative fully adsorbing trajectories of *a)* NT2, *b)* NT2I, *c)* NT2Y. Contact area of HP1 is in purple; residues 1 to 16 in light brown; HP2 in orange; residues 36 to 41 in cyan.

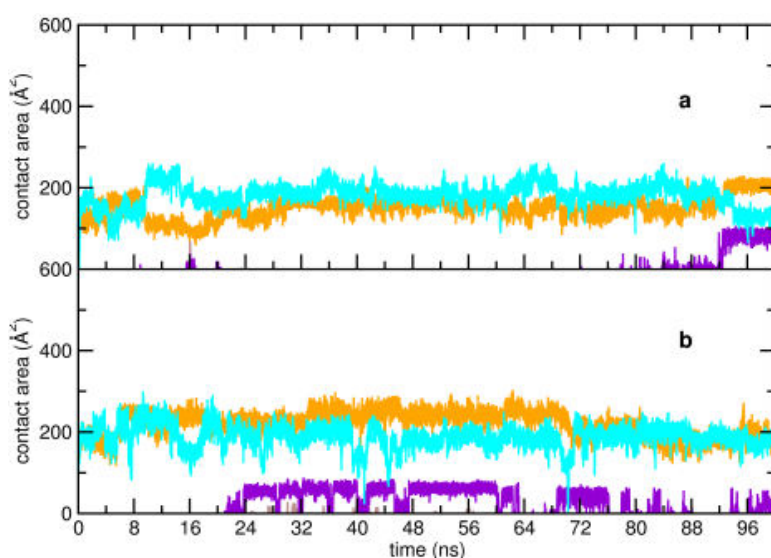


Figure 4.8. Evolution of the contact area of key domains for representative partially adsorbing trajectories of *a)* NT2I, *b)* NT2Y. Contact area of HP1 is in purple; residues 1 to 16 in light brown; HP2 in orange; residues 36 to 41 in cyan.

We note that for the fully adsorbing cases, the adsorption of the N-terminal domain ($D_1AEFRHDSGYEVHHQK_{16}$) on the nanotube is preceded by the adsorption of the HP1. This is reiterated by examining the evolution of the interaction energies of these segments with the nanotube (see Figure 4.9); attainment of ~ -15 kcal mol⁻¹ in the HP1-SWCNT interaction energy causes an initial rapid drop in the interaction of the N-terminal domain to at least ~ -30 kcal mol⁻¹, and an eventual decrease in the latter to at least ~ -50 kcal mol⁻¹. For

the latter part of the trajectories, the interaction strength of HP1 with the SWCNT is nearly the same in the adsorbed cases, regardless of the residue at position 19. Conversely, the trajectories of NT2I and NT2Y that do not completely adsorb on the SWCNT, we find that the interaction strength of the HP1 domain with the SWCNT does not exceed $-7.0 \text{ kcal mol}^{-1}$, and consequently, does not lead to the adsorption of the N-terminal domain.

System	Total	1-16	HP1	30-35	36-41
NT2	935.6 (52.7)	423.4 (66.9)	179.5 (18.5)	171.2 (50.4)	168.2 (29.3)
NT2I _a	963.6 (55.0)	405.5 (40.8)	159.0 (44.3)	219.1 (24.0)	165.4 (39.8)
NT2Y _a	936.4 (45.1)	379.5 (26.6)	184.9 (13.2)	178.9 (19.2)	218.6 (24.7)
NT2I _{na}	511.4 (26.3)	0.0 (0.0)	75.1 (28.7)	138.0 (59.1)	156.4 (24.6)
NT2Y _{na}	390.6 (116.4)	0.0 (0.0)	2.7 (8.9)	174.7 (18.8)	167.0 (24.0)

Table 4.2. Mean values of the contact area with the SWCNT (in \AA^2) of key domains, over the simulated adsorbing (NT2; NT2I_a; NT2Y_a) and the partially adsorbing (NT2I_{na}; NT2Y_{na}) trajectories.

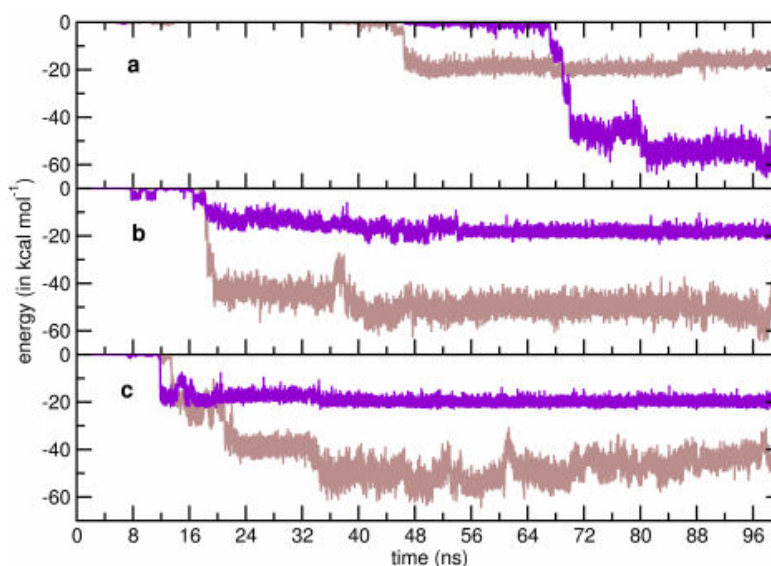


Figure 4.9. Evolution of the interaction energy with the SWCNT, of HP1 (in purple) and residues 1 to 16 (in light brown), for the representative fully adsorbing trajectories of *a)* NT2, *b)* NT2I, *c)* NT2Y.

4.3.1.3 Competition Between the Collapse and the Adsorption Processes

Our earlier study had shown that complete adsorption of the unmutated A β monomer on the SWCNT walls was accompanied by its clear preference for the ‘open’ state. We have demonstrated here that the HP1 domain plays important roles both in the collapse, and in initiating complete peptide adsorption on the nanotube. In this section, we examine the mechanistic reasons that cause the adsorption and the collapse processes to be mutually exclusive. In Table 4.3, we have compared the mean values of E_2 in pure protein with its value in the corresponding protein-nanotube complexes, as well as the strength of the HP1-SWCNT interactions (E_3) in the complexes; the data is considered over the last 10 ns of the simulation trajectories. For the unmutated peptide, the E_2 in the pure peptide matches the corresponding E_3 value almost exactly. The near cancellation of the interactions that lead to collapse, by those arising from the nanotube, results in complete prevention of the unmutated peptide’s collapse in the NT2 systems; the value of E_2 in the peptide-nanotube complex is negligible.

System	E_2	E_3
F19	-17.4 (4.4)	-
NT2	-0.7 (0.8)	-17.0 (2.6)
F19I	-13.2 (3.5)	-
NT2I	-1.1 (1.0)	-10.5 (5.2)
F19Y	-9.0 (6.3)	-
NT2Y	-0.2 (0.3)	-9.6 (9.5)

Table 4.3. Comparison of the mean values of the interactions E_2 and E_3 (in kcal mol⁻¹), averaged over the last 10 ns of all simulated trajectories, for the pure peptide and the peptide-nanotube complexes. Standard deviations are provided within braces. See text for details.

As pointed out previously, the strength of E_2 is relatively weakened with the decrease in hydrophobicity in the central residue of HP1. As seen from Table 4.3, the interaction strength E_3 also progressively weakens from NT2 to NT2I and NT2Y. The mean value of E_2 in the pure, mutated peptide matches the E_3 value in the corresponding complex well, and as in the unmutated case, results in very small values of E_2 in the peptide-nanotube complexes. It is to be kept in mind that unlike in NT2, the probability of complete adsorption is less than 1.0 in the NT2I and the NT2Y cases. In Table 4.4, we report the mean E_2 and E_3 and values obtained separately for the last 10 ns of the adsorbing trajectories of NT2I and NT2Y.

Interestingly, for the adsorbing trajectories, the mean E_3 is stronger in NT2Y than in NT2I by ~ 5 kcal mol⁻¹, and close to the corresponding value in NT2. (As discussed later, interactions from the solvent water leads to the screening of favorable π - π stacking interactions in NT2Y).

System	E_2	E_3
NT2I _a	- 1.5 (1.3)	- 14.0 (4.9)
NT2Y _a	- 0.1 (0.2)	-19.0 (2.0)
NT2I _{na}	- 0.7 (0.2)	- 7.1 (2.8)
NT2Y _{na}	- 0.2 (0.3)	- 0.2 (0.5)

Table 4.4. Mean values of the interactions E_2 and E_3 (in kcal mol⁻¹), averaged over the last 10 ns of the fully adsorbing (NT2I_a; NT2Y_a) and the partially adsorbing (NT2I_{na}; NT2Y_{na}) mutated peptide-nanotube complexes trajectories. Standard deviations are provided within braces.

The mean E_2 and E_3 and values for the last 10 ns of the partially adsorbing trajectories are given in Table 4.4. Unlike in unmutated NT2, the peptide in both sets of partially adsorbing mutated complexes fail to collapse; this is reflected in negligible values of the interaction strength E_2 . In order to understand why this is so for NT2I, we recall that the interaction between the nanotube and the HP2 domain is highly favorable,²² which is reflected in the high HP2-nanotube contact area. This interaction tethers the C-terminus, and does not allow it to interact with the HP1, which, in the absence of aromatic Phe19, is held on to the nanotube with the reduced interaction strength of about -7 kcal mol⁻¹. On the other hand, the failure of the peptide to form the compact states in the partially adsorbing NT2Y is a reflection of the diminished collapse propensity of the peptide with the F19Y mutation. Unlike NT2I, the E_3 value in the partially adsorbing NT2Y cases is very small. As discussed in the next section, solvent waters play a role in screening HP1 with the Tyr mutation, and acts to hinder the collapse and the adsorption processes.

4.3.1.4 Decoupling the Roles of Hydrophobicity and π - π Stacking in the Adsorption Process

The behavior of free peptide shows that the hydrophobicity of HP1 is critically important for the collapse process. On the other hand, the HP1 initiated complete peptide adsorption on the

SWCNT is compromised when either the hydrophobicity or the aromatic character of its central residue is reduced. Interestingly, we saw in the last section that if complete adsorption succeeds in an NT2Y system, the interaction strength of HP1 with the nanotube is comparable to that found in the unmutated peptide-nanotube complex. This data strongly suggests that the interplay of HP1 hydrophobicity and π - π interactions with the nanotube is critical for affecting complete adsorption.

We point out here that Tyr has been implicated in strong protein-carbon nanotube interactions,⁶⁸ and the binding affinity of Tyr could even be marginally higher than that of Phe.³⁴ In that light, the overall lowered adsorption propensity of NT2Y compared to NT2 (despite comparable interaction strengths after adsorption) appears anomalous. To resolve this apparent inconsistency, we first note that hydroxyl group of Tyr makes it markedly more polar than Phe. Computational studies show that the side-chain analog of Tyr has significantly lower solvation free energy compared to Ile and Phe.^{69, 70} Thus, it is plausible that the solvent is responsible for screening critical hydrophobic interactions arising from the HP1 domain in the NT2Y systems, thereby contributing to its decreased adsorption propensity.

In Figure 4.10, we depict the evolution of the number of water molecules within a 3.0 Å solvation layer of the HP1 domain in completely adsorbing peptides in sample NT2, NT2I and NT2Y trajectories (adsorbing completely at 70, 20 and 15 ns, respectively; see Figure 4.7). For comparison, corresponding data for sample non-adsorbing trajectories have also been depicted. We find that the adsorption is accompanied by a loss in the number of waters (or a ‘dewetting’) around the HP1 domain. For an estimate of the energetic effects arising from the loss in solvation, we also compare, normalized distributions of the total interaction energy of HP1 with the solvation waters for 2 ns before and after the HP1 initiated complete adsorption. We first note that the single Tyr mutation results in nearly doubling the energetic favorability of the total HP1-solvent interaction; the Ile mutation does not noticeably disturb this interaction strength. In each of the peptide-nanotube complexes, complete adsorption and the commensurate dewetting is reflected in a shift, on the average, of the HP1-solvent interactions to higher values. In Table 4.5, we list the mean solvation number and the mean value of HP1-solvent interactions before and after adsorption. We note that while the magnitude of dewetting in NT2Y is similar to that of NT2 and NT2I, the average shift in the solvent interaction due to adsorption is marginally higher.

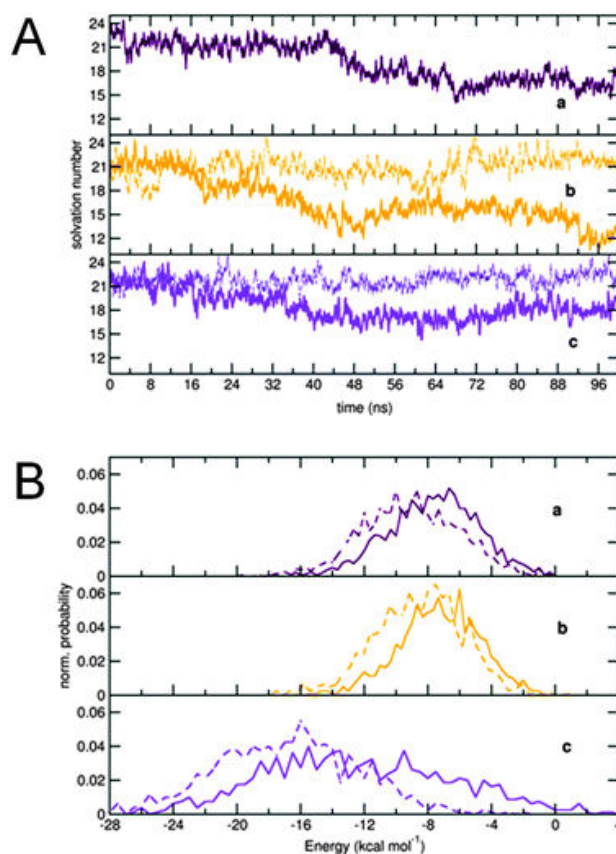


Figure 4.10. (A) Evolution of the solvation number around the HP1 domain for sample trajectories of *a)* NT2, *b)* NT2I, *c)* NT2Y systems. Data for fully and partially adsorbing trajectories are shown in solid and in broken lines, respectively. (B) Normalized distributions of the total HP1-solvent interaction energy for the adsorbing *a)* NT2, *b)* NT2I, *c)* NT2Y systems. Distributions before and after adsorption are shown in broken and in solid lines, respectively.

System	W_b	E_b	W_a	E_a
NT2	21.7 (3.9)	- 9.4 (3.1)	15.2 (3.4)	- 7.8 (2.9)
NT2I	21.1 (3.8)	- 8.8 (2.8)	15.6 (4.7)	- 7.4 (2.5)
NT2Y	21.7 (3.5)	- 17.0 (4.5)	18.6 (3.5)	- 13.0 (5.8)

Table 4.5. The mean solvation number around HP1 (W_b) and the mean solvent interaction strength (E_b) 2 ns before adsorption; and the mean solvation number around HP1 (W_a) and the mean solvent interaction strength (E_a) 2 ns after adsorption. Energy units are kcal mol⁻¹. Standard deviations are provided within braces.

The replacement of Phe19 with the more polar Tyr causes the HP1 domain to be highly shielded by solvent interactions. Unlike in the NT2 and in the NT2I systems, where the magnitude of solvent interactions is lower than the HP1-nanotube interaction strength, the solvent interactions in NT2Y nearly match the potential interactions arising from the nanotube. Thus, the probability of overcoming the solvation barrier is severely reduced in the case of NT2Y, leading to decreased probability of interaction of the HP1 domain with the nanotube, and consequently, decreased probability of complete adsorption. However, once the barrier presented by the solvent is overcome, the aromaticity of the Tyr residues initiate strong interactions with the nanotube that are comparable to that found in the unmutated peptide. On the other hand, the solvent barrier is overcome much more easily by the systems with the Ile mutation; however, as seen earlier, the loss of an aromatic residue results in overall weaker interaction with the nanotube. The natural sequence of HP1, containing the two hydrophobic Phe residues, therefore has the correct balance of hydrophobic and aromatic character that is critical for HP1 to initiate complete adsorption with the nanotube.

4.3.2 Effect of F19A Mutations on Peptide's Intrinsic Collapse and Adsorption on SWCNT Surface

4.3.2.1 Effect of F19A Mutation on Free Peptide Collapse

The $A\beta$ monomer displays a strong propensity to form collapsed states in water that can potentially nucleate and initiate heterogeneous self-assembly pathways. As in our previous studies, we monitor the compaction of the peptide *via* the value of ' $d_{collapse}$ ', the center of mass distance between the N-terminal ($L_{17}VXFAEDVGS_{26}$) and C-terminal ($K_{28}GAIIGLMVGGVVIA_{42}$) domains, with the 'X' at position 19 representing the modification. We have demonstrated earlier that $d_{collapse}$ is temporally well correlated with E_1 , the interaction strength between HP1 and HP2, and that E_1 provides the major component of E_2 , the interaction between HP1 and the full C-terminal domain. We mention here that interaction strength between two groups includes the sum of the non-bonded (electrostatic and van der Waals) interaction energies. Collapse was taken to have occurred if $d_{collapse}$ decreased by 30% or more from the original value of 16.7 Å. To understand the effect of the F19 mutation on this essential self-assembly step, we first depict the normalized probabilities of $d_{collapse}$ values obtained during the last 10 ns of the simulated F19A trajectories in Figure 4.11 a. The plot describes two distinct groups of 'collapsing' and 'non-collapsing' structures. The mean $d_{collapse}$ of 9.6 (± 0.3) Å of the former group is comparable to that of the mean value

obtained for the pure, unmutated peptide, while the mean value of $17.0 (\pm 1.2)$ Å for the latter group represents structures that remain significantly more ‘open’ at the end of the simulations. In Figure 4.11 b, we have depicted evolution of the peptide’s radius of gyration (R_g) with that of $d_{collapse}$, E_1 and E_2 for representative ‘collapsing’ and ‘non-collapsing’ trajectories. In Table 4.6, we have compared the mean values of R_g , $d_{collapse}$, E_1 and E_2 , as well as the probability of peptide collapse obtained from the F19A simulations and the previously reported simulations of the unmutated peptide. We had shown earlier that while the F19I appeared to have no significant effect on the collapse probability of the peptide in water, the F19Y mutation diminished this probability by 33%. In F19A system, only one out of the three simulated F19A trajectories is found to achieve collapse. We note here that the interactions E_1 and E_2 for the collapsing F19A trajectory are marginally weaker than the corresponding values obtained in the unmutated peptide. This data shows that the effective hydrophobicity of the HP1 domain is requisite for the efficient collapse kinetics of the nascent $A\beta$ monomer in aqueous environment.

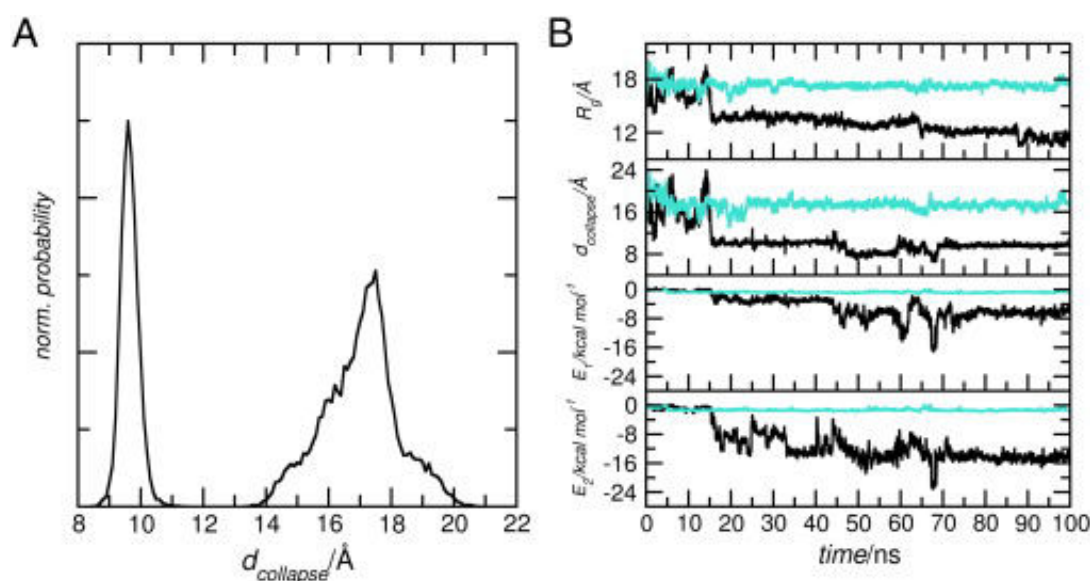


Figure 4.11. A) Normalized distributions of $d_{collapse}$ (in Å) value obtained from the last 10 ns of the simulated free F19A peptide. B) Evolution of peptide radius of gyration, R_g (in Å), $d_{collapse}$ (in Å), and the interactions E_1 and E_2 (in kcal mol⁻¹) over the simulation time, for a sample collapsing (in black) and non-collapsing (in cyan) free F19A peptide.

System	R_g	$d_{collapse}$	E_1	E_2
F19	12.1 (0.5)	8.3 (0.9)	-10.1 (2.8)	-17.4 (4.4)
F19A	15.0 (2.7)	14.5 (3.6)	-2.9 (2.7)	-6.1 (6.2)

Table 4.6. Comparison of mean values of R_g (in Å), $d_{collapse}$ (in Å), E_1 (in kcal mol⁻¹) and E_2 (in kcal mol⁻¹) over the last 10 ns of free F19A and unmutated simulations. Standard deviations are provided in braces.

4.3.2.2 Propensity for SWCNT Adsorption

We next investigate the combined effect of decreased aromatic character and reduced effective hydrophobicity in HP1 on the peptide's adsorption propensity on the SWCNT. The peptide-nanotube contact area, or $A_{contact}$, calculated as described in the previous studies was used to monitor adsorption. As in our previous studies, the peptide is considered to have fully adsorbed on the SWCNT if a minimum $A_{contact}$ of 800.0 Å² is achieved. From our earlier extensive simulations, we found that the unmutated peptide compulsorily adsorbs on the surface of the SWCNT placed in its vicinity within tens of nanoseconds irrespective of the initial peptide-nanotube orientation. In comparison, replacement of Phe19 with either Ile or Tyr caused a marked decrease in the overall adsorption propensity. However, in each case, an adsorption event resulted in prevention of the peptide's collapse. We further noted that the adsorption of the N-terminal domain, which was essential for attainment of the saturated $A_{contact}$ value, was dependent on the prior interaction of HP1 with the SWCNT. In Table 4.7, we report the mean $A_{contact}$ and $d_{collapse}$ values obtained over the last 10 ns of the NT2A simulations, along with the mean interaction strength of the nanotube with the full peptide, the HP1 domain, and the C-terminal region. For comparison, we have also reported corresponding mean values obtained from the previous simulations of unmutated peptide-SWCNT complex. As indicated by the difference in $A_{contact}$ value, the F19A mutation results in a 26% decrease in the mean adsorption propensity. Further, the mean $d_{collapse}$ value is 27% lower compared to the unmutated peptide-SWCNT complex within the simulated timescales.

System	A_{contact}	d_{collapse}	E_{3a}	E_{3b}	E_{3c}
NT2	935.6 (52.7)	19.05 (5.0)	-130.0 (8.5)	-17.0 (2.6)	-37.8 (7.4)
NT2A	691.6 (176.3)	13.9 (2.6)	-96.0 (23.4)	-8.0 (5.6)	-39.5 (3.8)

Table 4.7. Comparison of the mean A_{contact} , d_{collapse} , full peptide-nanotube interaction (E_{3a}), HP1-nanotube interaction (E_{3b}), C-terminal domain-nanotube interaction (E_{3c}) obtained over last 10 ns of all the simulated NT2A and NT2 trajectories. Standard deviations are provided in braces. Energies are in kcal mol⁻¹ unit.

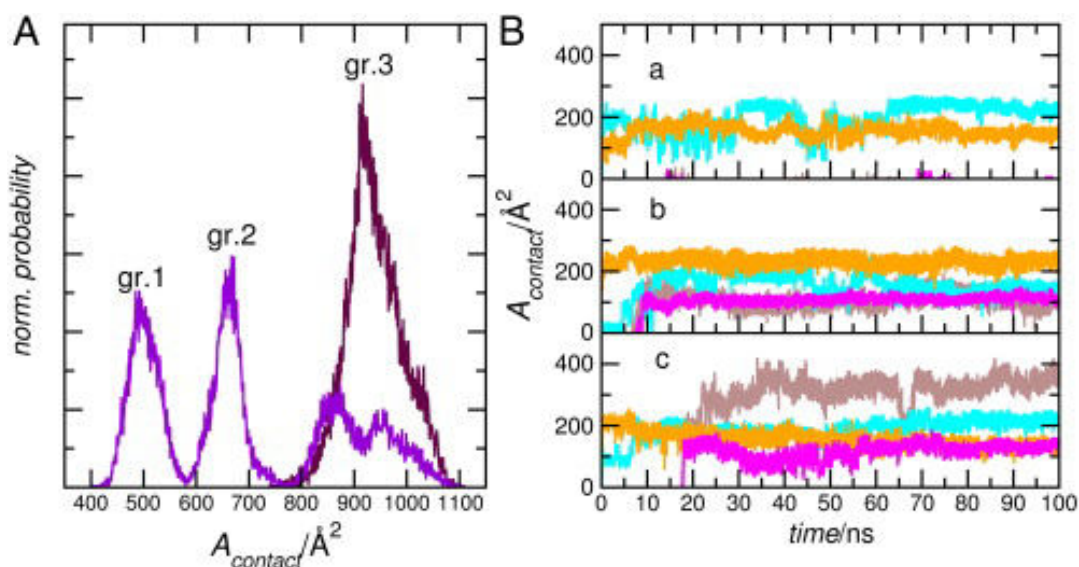


Figure 4.12. A) Normalized distribution of A_{contact} values obtained from the last 10 ns of the simulated NT2A systems (in violet) compared to the NT2 systems (in maroon), and B) evolution of nanotube contact area of key domains for representative trajectories belonging to a) gr. 1, b) gr. 2, and c) gr. 3. See text for details. Contact area with HP1 is in magenta; with residues 1 to 16 in light brown; with residues 30 to 35 in orange; and with residues 36 to 41 in cyan.

Out of our six simulations of the NT2A complex, the peptide was found to adsorb on the SWCNT surface in only two, indicating a lower probability of complete adsorption compared to the systems studied earlier. In Figure 4.12, we depict normalized distributions of the value of A_{contact} obtained by combining data from the last 10 ns of all the simulated trajectories; for comparison, the corresponding distribution from NT2 has also been shown. The data indicates the presence of three distinct groups, which we denote here as groups 1, 2

and 3, with mean $A_{contact}$ values of $500.5 (\pm 28.8) \text{ \AA}^2$, $660.0 (\pm 29.1) \text{ \AA}^2$ and $889 (\pm 60.3) \text{ \AA}^2$. In the same figure, we also show temporal evolution of the contact area of the key domains (N-terminal domain; HP1; HP2 and C-terminal domain) with the SWCNT over sample trajectories corresponding to each of the three groups.

System	$A_{contact}$	1-16	HP1	30-41	$d_{collapse}$
NT2	935.6 (52.7)	423.4 (66.9)	179.5 (18.5)	312.6 (30.5)	19.05 (5.0)
gr.1	500.5 (28.8)	0.0	50.4 (30.0)	315.4 (25.4)	16.4 (1.3)
gr.2	660.0 (29.1)	173.0 (81.4)	97.2 (25.4)	325.0 (17.8)	14.1 (1.3)
gr.3	889.0 (60.3)	392.1 (55.0)	147.44 (23.01)	313.5 (16.5)	11.2 (2.2)

Table 4.8. Mean values of the contact area with the SWCNT (in \AA^2) of key domains, and $d_{collapse}$ (in \AA) obtained from last 10 ns of all NT2 systems, gr. 1, gr. 2, and gr. 3.

In Table 4.8, we have reported the mean $A_{contact}$ and $d_{collapse}$ of the different domains for the three groups obtained over the final 10 ns of the simulations along with the mean contact area of the key domains. For comparison, earlier data corresponding to the NT2 system has also been presented. As earlier, we find that stable adsorption of the HP1 domain is a prior requisite for complete N-terminal adsorption of the peptide; the latter provides a large fraction of the $A_{contact}$ corresponding to complete adsorption. However, we note that in the case of group 2, the HP1-SWCNT interaction yields only partial N-terminal adsorption on the nanotube. Interestingly, unlike the previous systems studied, we find that the complete adsorption of the F19A system on the SWCNT gives rise to a low value of $d_{collapse}$. While this value is marginally higher than that corresponding to collapse of the free peptide (native or mutated), it is 41% less than the mean $d_{collapse}$ attained at the end of the NT2 simulation (we underscore here that in the earlier systems studies, complete adsorption was shown to erase the natural collapse propensity). This unexpected behavior has been examined in greater details in subsequent sections.

4.3.2.3 Post Adsorption Peptide Collapse in NT2A

We introspect the phenomenon of post-adsorption collapse observed in the NT2A systems. In Figure 4.13, we present plots of $A_{contact}$ and $d_{collapse}$ as a function of simulation time for the trajectories that are found to completely adsorb within the simulated timescale. The saturation in $A_{contact}$ is followed by a lag period (of $\sim 30\text{-}40$ ns duration), after which the peptide is found

to dramatically compactify by attaining a $d_{collapse}$ of 11.2 Å. However, the lowered adsorption probability yielded just two completely adsorbed trajectories, and therefore it remained to be unequivocally determined whether the collapse observed upon F19A adsorption is indeed surface induced. To this end, we present the PMF profile calculated *via* ABF as described earlier in Figure 4.14, with the complex achieved just after attaining saturated $A_{contact}$ ($d_{collapse}$ of 17.0 Å) as the starting conformation. The free energy data indicates a downhill transition to the ‘closed’ states for the peptide. The highest probability is found in the vicinity of a $d_{collapse}$ value of 10.75 Å, which is very close to the mean $d_{collapse}$ value of the fully adsorbed peptide obtained through unbiased sampling of the NT2A systems. In contrast, the ‘open’ states (corresponding to $d_{collapse}$ values greater than the original value of 16.7 Å) of the adsorbed peptide correspond to high free energy values and thus the probability of sampling those states are low. It is easily seen that for the complex studied, there is an energetically favorable downhill transition to the ‘closed’ states from the starting $d_{collapse}$ value. This is in contrast to unmutated NT2 system, in which the free energy profile over $d_{collapse}$ describes a downhill transition to the ‘open’ states.²² We note, however, that the surface induced collapse is marginally weaker compared to the free peptide collapse.

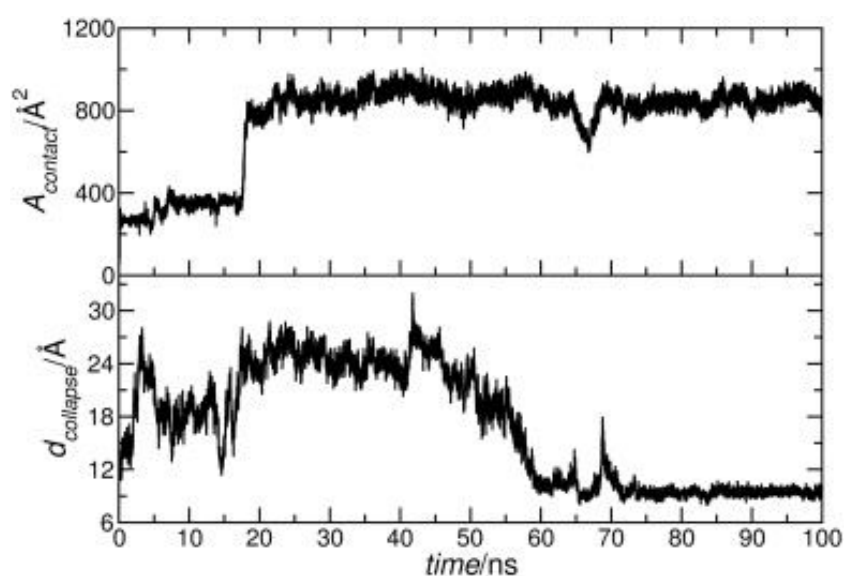


Figure 4.13. Evolution of $A_{contact}$ (in upper panel) and $d_{collapse}$ (in lower panel) over simulation time for a sample, fully adsorbing NT2A trajectory.

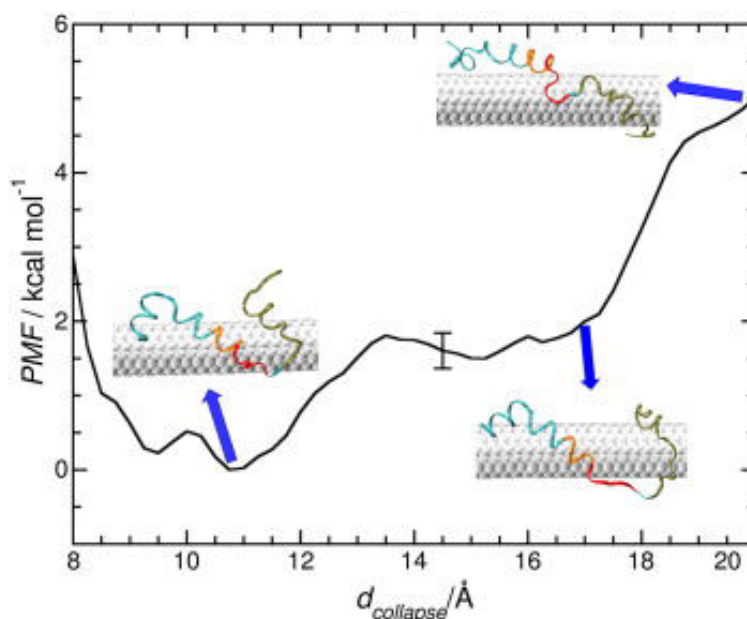


Figure 4.14. The free energy profile along $d_{collapse}$ for the peptide in a completely adsorbed NT2A trajectory obtained with ABF calculations. Snapshots of the adsorbed peptide-SWCNT complex corresponding $d_{collapse}$ values of 11.0 Å, 17.0 Å and 20.0 Å along the profile are shown.

4.3.2.4 Enhanced Movement on Nanotube Surface Arising from Weakened Tethering of HP1 in NT2A

For mechanistic insights into the role played by the SWCNT in facilitating collapse of the fully adsorbed peptide in NT2A, we begin by re-examining the mean interaction strengths of different domains with the nanotube surface. In the case of the fully adsorbed NT2A, we note that a large part of the difference in overall peptide-nanotube interaction (in comparison with NT2) is accounted for by the weakened interaction of HP1 with the nanotube. In Figure 4.15, we have compared distributions of the HP1-nanotube contact area for 20 ns after adsorption, between the NT2A (fully adsorbing) and the NT2 systems. The mean HP1-nanotube contact area values for the two systems are $147.4 (\pm 23.0)$ and $179.5 (\pm 18.5)$ Å², respectively. In the same figure, we also depict evolution of the radial distance of the center of mass of HP1 from the nanotube for these systems. The sharp drop in the radial distances are indicative of HP1 localization on the nanotube surface following complete adsorption. This data, along with the lower mean contact area and the distinctly broader HP1-nanotube contact area distribution, indicate that the peptide in NT2A is less stably adsorbed and weakly tethered to the nanotube surface. We do not notice any meaningful differences in interaction of the nanotube with the C-terminal domain.

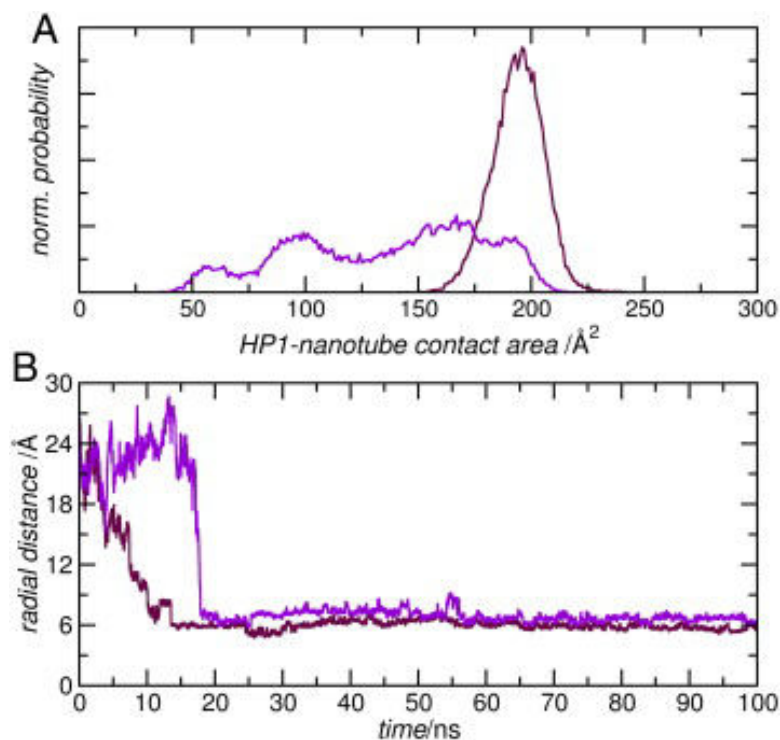


Figure 4.15. a) Comparison of the HP1-nanotube contact area distribution, calculated for 20 ns after adsorption, between the fully adsorbing NT2A (in violet) and the unmutated NT2 (in black) systems, and b) comparison of the evolution of the radial distance of the HP1 domain's center of mass from the nanotube surface, for a sample fully adsorbing NT2A (in violet) trajectory and NT2 trajectory (in black).

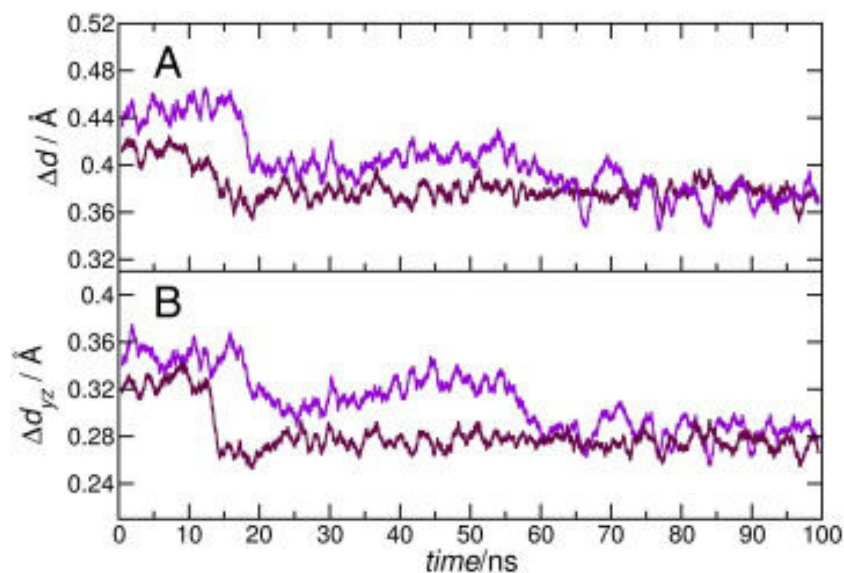


Figure 4.16. a) The distances (Δd) moved by the HP1 center of mass between consecutive steps as function of simulation time, for representative fully adsorbing NT2A (in violet) and NT2 (in black) trajectories, and b) evolution of the component Δd_{yz} over the simulation time.

To directly compare the extent of domain mobility on the nanotube surface in the two cases, we depict in Figure 4.16, the distances (Δd) moved by the HP1 domain center of mass between consecutive frames (*ie.* every picosecond), as a function of simulation time for representative NT2A and NT2 trajectories. Although the adsorption event in both cases are marked by diminished movement of this domain, its weakened tethering allows it to have greater translational mobility on the surface in the NT2A complex compared to NT2. However, the C-terminal tethering combined with the ‘hairpin’-like conformation of the peptide restricts its mobility parallel to the nanotube axis (*ie.* along the x-axis). Thus, the Δd is well correlated with the transverse movement on the nanotube surface (*ie.* with Δd_{yz}), as shown in the same figure. Corresponding data for the C-terminal domains show no clear differences in the extent of movements in NT2 and NT2A (see Figure 4.17). The ‘restricted random walk’ of the HP1 domain in the adsorbed NT2A system dramatically increases its likelihood of coming within approach distance of HP2 and the C-terminal domains. Thus, after a post-adsorption lag phase (corresponding to an ‘open’ state with higher $d_{collapse}$ value), strong interactions between HP1 and the C-terminal two domains result in compaction of the peptide.

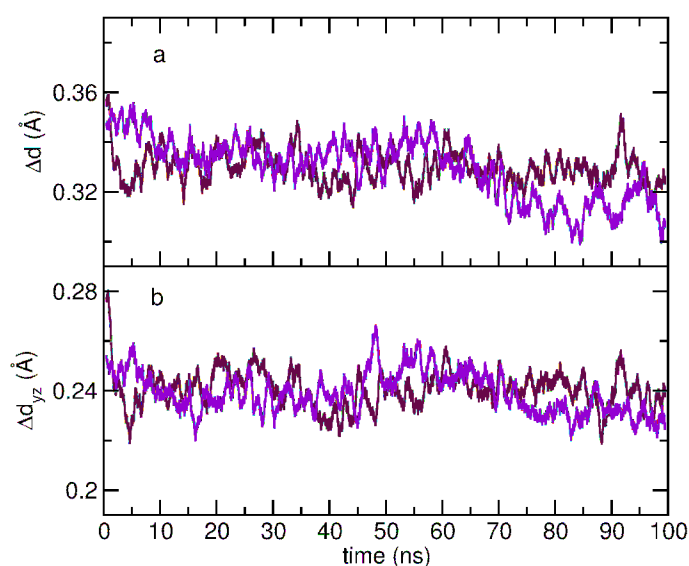


Figure 4.17. a) The distance (Δd) moved by the C terminal domain center of mass between consecutive steps as a function of simulation time, for representative fully adsorbing NT2A (violet) and NT2 (maroon) trajectories, and b) evolution of the component Δd_{yz} over the simulation time.

4.3.2.5 Dewetting Effects in Free and Surface Induced Collapse

We have earlier shown that peptide adsorption on the surface is accompanied by a distinct dewetting transition at the HP1 domain in NT2, NT2I and NT2Y systems. Here, we examine the dewetting due to complete peptide adsorption, and that induced by the subsequent collapse in NT2A. In Figure 4.18, we present comparisons of the radial distribution functions (RDFs) of water oxygen around the terminal carbon atoms of HP1 domains F19A (collapsing) and NT2A (adsorbing) trajectories, before and after collapse for the former, and before and after adsorption and after collapse for the latter. Corresponding data for the F19 and NT2 systems is shown in Figure 4.19. We first note that in the unmutated systems, the drop in the height of the first solvation peak located at 3.7 Å, is nearly due to collapse (of the free system) and due to SWCNT adsorption, and further, this is comparable due to the dewetting from collapse of the free F19A peptide. With the Ala mutation, however, full peptide adsorption does not result in complete dewetting as seen from the larger first solvation peak of the terminal carbons of HP1 post adsorption. Interestingly, the collapse transition following the adsorption brings a distinct lowering in the first solvation peak and eventually makes it comparable to that obtained from the free collapse. Thus, the event of complete peptide adsorption in NT2A, the reduced degree of peptide solvation is achieved via a ‘two-step’ dewetting involving the peptide’s collapse. This is also evidenced by comparing the hydration number within 3.0 Å of the heavy atoms of HP1. The hydration numbers in F19A are slightly lower despite the lower hydrophobicity of Ala compared to Phe; this is due to the lower van Der Waals volume of Ala.⁷¹ In Figure 4.20, we have compared evolutions of the number of surface waters around HP1 for a sample NT2A (adsorbing) trajectory. We note here that recent studies have demonstrated the importance of surface hydration in the self-assembly thermodynamics of $A\beta$. The net entropic gain due to expulsion of surface waters during peptide compaction and during monomeric association and the consequential energetic favorability have been elaborated.³² It is plausible therefore that the second dewetting transition in NT2A contributes to the thermodynamic favorability of collapse in the adsorbed peptide. We note here that compared to the unmutated peptide, the peptide in (adsorbing) NT2A complex is relatively more stabilized due to the post-adsorption collapse (see Table 4.9). Further detailed studies will be required to directly validate the role played surface waters in the observed phenomena.

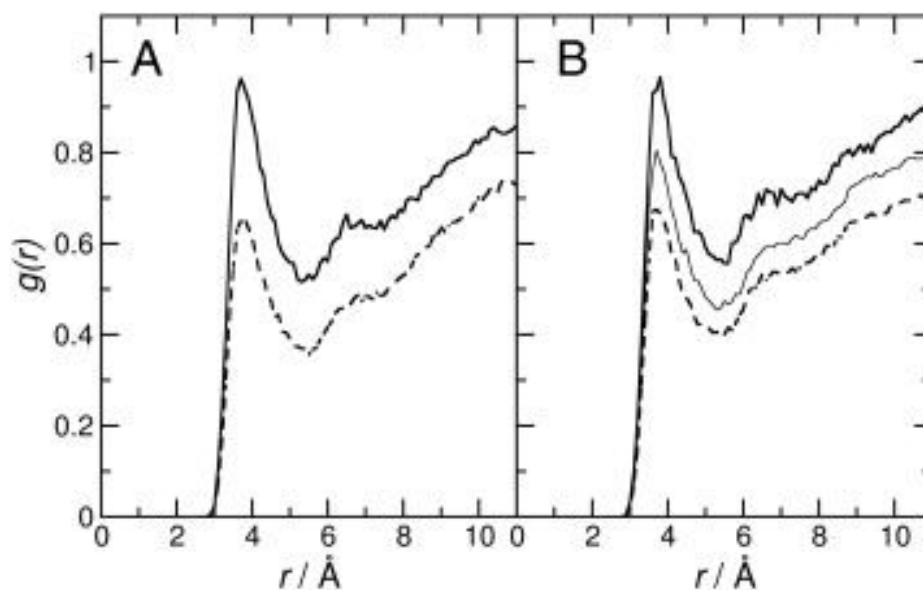


Figure 4.18. Radial distribution functions (RDFs) of water oxygens around the terminal carbons of the HP1 domain obtained from a) collapsing F19A free peptide simulation, b) fully adsorbing NT2A simulation. The RDFs are over the initial 10 ns in both (solid thick line), 10 ns after adsorption in NT2A (solid thin line), and 10 ns after collapse (broken line).

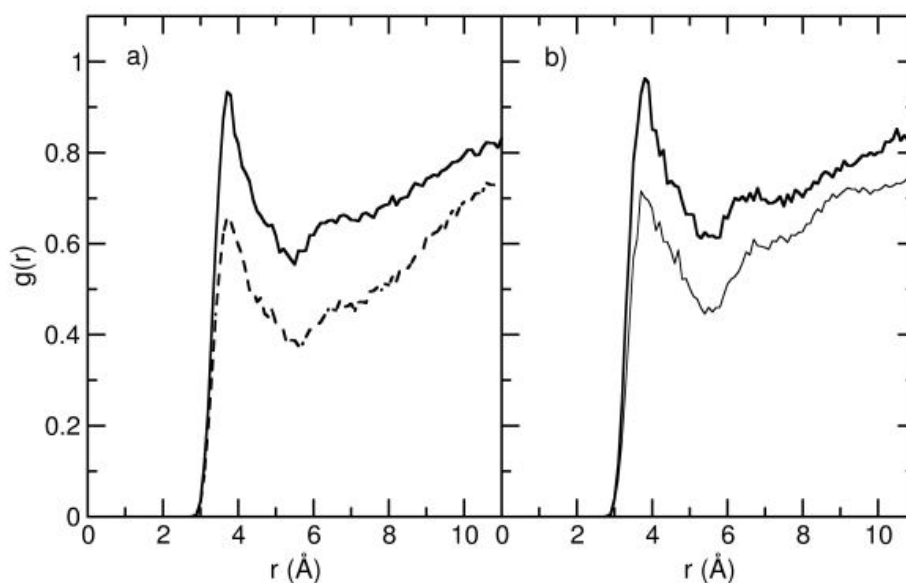


Figure 4.19. Radial distribution functions (RDFs) of water oxygens around the terminal carbons of the HP1 domain obtained from a) F19 free peptide simulation, b) NT2 simulation. The RDFs are over the initial 10 ns in both (solid thick line), 10 ns after adsorption in NT2 (solid thin line), and 10 ns after collapse (broken line) in F19.

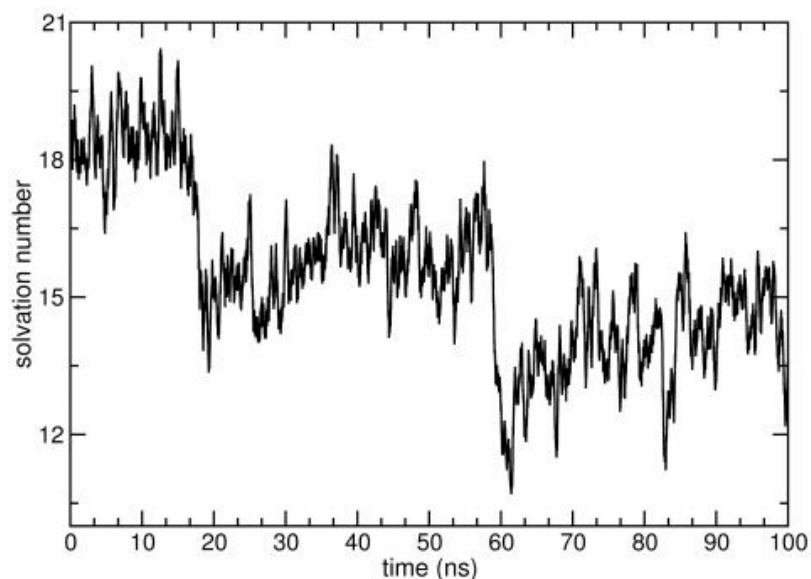


Figure 4.20. Evolution of the solvation number around the HP1 domain for representative fully adsorbing NT2A system.

System	E_i	E_a	E_c
NT2	-420.0 (50.0)	-368.2 (44.1)	-
NT2A	-418.0 (46.2)	-380.0 (40.0)	-479.0 (50.0)

Table 4.9. Initial internal energy of peptide (E_i) compared to after adsorption (E_a), and after collapse (E_c), for the peptide in the NT2A (fully adsorbing) and NT2 systems. Data is averaged over 10 ns

4.4. Discussion and Conclusion

In this paper, we have examined the mechanistic overlap between the collapse of the $A\beta_{1-42}$ monomer and its adsorption on SWCNTs observed with atomistic molecular dynamics simulations. Alteration to a key domain, the central hydrophobic core (HP1), via single-point mutations allows us to decouple the roles of hydrophobicity and the aromaticity in these normally spontaneous processes. The collapse is mainly caused by the strong interactions of HP1 with residues belonging to the C-terminal domain and its probability remains unaffected by substituting the central aromatic residue of HP1, Phe19, with a non-aromatic residue of comparable size and hydrophobicity. It is to be noted here that the C-terminal domain does not possess any residues capable of π - π stacking interactions. We are currently investigating how alterations to the aromatic character of HP1 can affect the collapse process, as well as the conformational heterogeneity of the ‘closed’ state. The interactions arising between the

nanotube with the HP1 directly interfere with the strand-strand interactions, and thereby prevent the collapse of the peptide. Alteration to either the overall aromaticity or the overall hydrophobicity of HP1 is found to dramatically reduce the propensity of adsorption on a SWCNT, indicating that both aspects are required for maintaining efficient adsorption kinetics. In the event of full adsorption, HP1 is found to interact most strongly with the SWCNT when it contains an aromatic residue at position 19. Solvent waters are found to initially screen the HP1 domain when a polar amino acid is present, and full adsorption is contingent upon this domain surpassing the solvent barrier and interacting completely with the nanotube.

Interestingly, the simultaneous reduction in both hydrophobic and aromatic character within HP1 domain dramatically reduces the propensity for complete peptide adsorption and the propensity for free collapse. Compared to the natural sequence where there is 100% adsorption, only two out of six F19A altered peptide-SWCNT complexes are found to fully adsorb within the simulated timescales. The incomplete interaction of the HP1 domain is found to hinder the complete N-terminal interaction. The mutual exclusivity of collapse and complete adsorption observed earlier is found to be absent in the case of the F19A system. On the contrary, complete peptide adsorption is necessarily followed by peptide compaction on the surface; this is corroborated with free energy calculations. Weakened tethering of HP1 results in its ‘restricted random walk’ on the surface, thereby facilitating its interaction with the hydrophobic C-terminal domains.

Our results reinforce the importance of the HP1 domain in the intrinsic behavior of full-length $A\beta$. While there has been some recent debate, it is generally believed that the compactification of the peptide is necessary for initiating the self-assembly process. Since the interactions of SWCNTs with the HP1 domain directly interfere with the peptide’s intrinsic collapse, it is plausible that targeting this domain with carbon nanotubes may offer a strategy to prevent the peptide self-assembly. Further, targeting this domain with chemical moieties that can potentially participate in π - π stacking could yield more efficient blockers to the amyloid pathway compared to those moieties whose interactions with the domain are only propelled by hydrophobic interactions.

Lastly, as we have discussed earlier,²² the localization of the peptides on the carbon nanotubes may be used for site-specific drug delivery.^{22, 72} In this light, we point out that previous studies have reported the first 16 residues of the N-terminal domain to be a

disordered region and to have relatively less important roles in structural aspects of amyloid fibrils.⁷³ However, our study shows that this domain contributes to a high fraction of the nanotube contact area. Strategies that employ suitable functionalization of the carbon nanotubes that further strengthen interactions with this domain while exploiting the synergistic adsorptions of HP1 and this domain, may be used for more efficient drug-delivery purposes.

References

1. C. Haass, M. G. Schlossmacher, A. Y. Hung, C. Vigo-Pelfrey, A. Mellon, B. L. Ostaszewski, I. Lieberburg, E. H. Koo, D. Schenk, D. B. Teplow and D. J. Selkoe, *Nature*, 1992, **359**, 322-325.
2. J. Kang, H.-G. Lemaire, A. Unterbeck, J. M. Salbaum, C. L. Masters, K.-H. Grzeschik, G. Multhaup, K. Beyreuther and B. Muller-Hill, *Nature*, 1987, **325**, 733-736.
3. D. B. Teplow, *Amyloid*, 1998, **5**, 121-142.
4. Y. Xu, J. Shen, X. Luo, W. Zhu, K. Chen, J. Ma and H. Jiang, *Proc. Natl. Acad. Sci. U.S.A.*, 2005, **102**, 5403-5407.
5. Y. Fezoui and D. B. Teplow, *J. Biol. Chem.*, 2002, **277**, 36948-36954.
6. M. M. Pallitto and R. M. Murphy, *Biophys. J.*, 2001, **81**, 1805-1822.
7. S. L. Bernstein, N. F. Dupuis, N. D. Lazo, T. Wyttenbach, M. M. Condrón, G. Bitan, D. B. Teplow, J.-E. Shea, B. T. Ruotolo, C. V. Robinson and M. T. Bowers, *Nat. Chem.*, 2009, **1**, 326-331.
8. M. F. Masman, U. L. M. Eisel, I. G. Csizmadia, B. Penke, R. D. Enriz, S. J. Marrink and P. G. M. Luiten, *J. Phys. Chem. B*, 2009.
9. M. Ahmed, J. Davis, D. Aucoin, T. Sato, S. Ahuja, S. Aimoto, J. I. Elliott, W. E. Van Nostrand and S. O. Smith, *Nat. Struct. Mol. Biol.*, 2010, **17**, 561-567.
10. S.-H. Chong and S. Ham, *Phys. Chem. Chem. Phys.*, 2012, **14**, 1573-1575.
11. Y. Miller, B. Ma and R. Nussinov, *Proc. Natl. Acad. Sci.*, 2010, **107**, 9490-9495.
12. T. Simona, E. Veronica, V. Paolo, A. J. v. N. Nico, M. J. J. B. Alexandre, G. Remo, T. Teodorico, A. T. Piero and P. Delia, *ChemBioChem*, 2006, **7**, 257-267.
13. J. Hardy and D. J. Selkoe, *Science*, 2002, **297**, 353.
14. C. Haass and D. J. Selkoe, *Nat. Rev. Mol. Cell Biol.*, 2007, **8**, 101-112.

15. R. Cappai and K. Barnham, *Neurochem. Res.*, 2008, **33**, 526-532.
16. J. E. Kim and M. Lee, *Biochem. Biophys. Res. Commun.*, 2003, **303**, 576-579.
17. B. Sahoo, S. Nag, P. Sengupta and S. Maiti, *Biophys. J.*, 2009, **97**, 1454-1460.
18. M. H. Viet, S. T. Ngo, N. S. Lam and M. S. Li, *J. Phys. Chem. B*, 2011, **115**, 7433-7466.
19. J. Li, R. Liu, K. S. Lam, L.-W. Jin and Y. Duan, *Biophys. J.*, 2011, **100**, 1076-1082.
20. Z. Fu, Y. Luo, P. Derreumaux and G. Wei, *Biophys. J.*, 2009, **97**, 1795-1803.
21. H. Li, Y. Luo, P. Derreumaux and G. Wei, *Biophys. J.*, 2011, **101**, 2267-2276.
22. A. K. Jana and N. Sengupta, *Biophys. J.*, 2012, **102**, 1889-1896.
23. Y. Chebaro, P. Jiang, T. Zang, Y. Mu, P. H. Nguyen, N. Mousseau and P. Derreumaux, *J. Phys. Chem. B*, 2012, **116**, 8412-8422.
24. A. T. Petkova, Y. Ishii, J. J. Balbach, O. N. Antzutkin, R. D. Leapman, F. Delaglio and R. Tycko, *Proc. Natl. Acad. Sci. U.S.A.*, 2002, **99**, 16742-16747.
25. S. Zhang, K. Iwata, M. J. Lachenmann, J. W. Peng, S. Li, E. R. Stimson, Y. a. Lu, A. M. Felix, J. E. Maggio and J. P. Lee, *J. Struct. Biol.*, 2000, **130**, 130-141.
26. S. L. Bernstein, T. Wyttenbach, A. Baumketner, J.-E. Shea, G. Bitan, D. B. Teplow and M. T. Bowers, *J. Am. Chem. Soc.*, 2005, **127**, 2075-2084.
27. A. Baumketner and J.-E. Shea, *J. Mol. Biol.*, 2007, **366**, 275-285.
28. G. Wei and J.-E. Shea, *Biophys. J.*, 2006, **91**, 1638-1647.
29. J. Khandogin and C. L. Brooks, *Proc. Natl. Acad. Sci.*, 2007, **104**, 16880-16885.
30. C. Lee and S. Ham, *J. Comput. Chem.*, 2010, **32**, 349-355.
31. N. G. Sgourakis, Y. Yan, S. A. McCallum, C. Wang and A. E. Garcia, *J. Mol. Biol.*, 2007, **368**, 1448-1457.
32. S.-H. Chong and S. Ham, *Proc. Natl. Acad. Sci.*, 2012, **109**, 7636-7641.
33. C.-c. Chiu, G. R. Dieckmann and S. O. Nielsen, *J. Phys. Chem. B*, 2008, **112**, 16326-16333.
34. S. M. Tomásio and T. R. Walsh, *J. Phys. Chem. C*, 2009, **113**, 8778-8785.
35. R. R. Johnson, B. J. Rego, A. T. C. Johnson and M. L. Klein, *J. Phys. Chem. B*, 2009, **113**, 11589-11593.

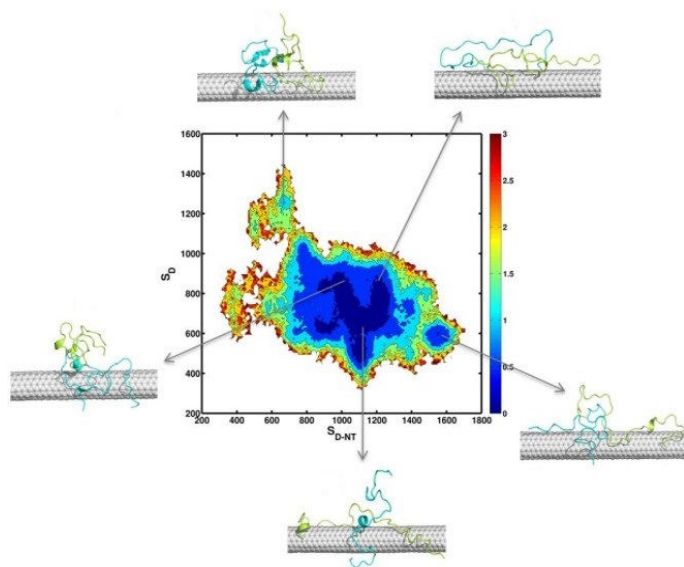
36. C.-c. Chiu, M. C. Maher, G. R. Dieckmann and S. O. Nielsen, *ACS Nano*, 2010, **4**, 2539-2546.
37. Y. Kang, Q. Wang, Y.-C. Liu, J.-W. Shen and T. Wu, *J. Phys. Chem. B*, 2010, **114**, 2869-2875.
38. R. R. Johnson, A. Kohlmeyer, A. T. C. Johnson and M. L. Klein, *Nano Lett.*, 2009, **9**, 537-541.
39. D. Roxbury, A. Jagota and J. Mittal, *J. Am. Chem. Soc.*, 2011, **133**, 13545-13550.
40. Y. Liu, C. Chipot, X. Shao and W. Cai, *J. Phys. Chem. C*, 2011, **115**, 1851-1856.
41. A. Hirano, K. Uda, Y. Maeda, T. Akasaka and K. Shiraki, *Langmuir*, 2010, **26**, 17256-17259.
42. S. Kraszewski, M. Tarek and C. Ramseyer, *ACS Nano*, 2011, **5**, 8571-8578.
43. X. Li, Y. Shi, B. Miao and Y. Zhao, *J. Phys. Chem. B*, 2012, **116**, 5391-5397.
44. L. Lacerda, A. Bianco, M. Prato and K. Kostarelos, *Adv. Drug Deliv. Rev.*, 2006, **58**, 1460-1470.
45. K. Kostarelos, *Nat. Biotechnol.*, 2008, **26**, 774-776.
46. C. A. Dyke and J. M. Tour, *Chem.–Eur. J.*, 2004, **10**, 812-817.
47. S. A. Andujar, F. Lugli, S. Hofinger, R. D. Enriz and F. Zerbetto, *Phys. Chem. Chem. Phys.*, 2012, **14**, 8599-8607.
48. M. Mahmoudi, O. Akhavan, M. Ghavami, F. Rezaee and S. M. A. Ghiasi, *Nanoscale*, 2012, **4**, 7322-7325.
49. A. Nazem and G. A. Mansoori, *J. Alzheimer's Dis.*, 2008, **13**, 199-223.
50. C. Ge, J. Du, L. Zhao, L. Wang, Y. Liu, D. Li, Y. Yang, R. Zhou, Y. Zhao, Z. Chai and C. Chen, *Proc. Natl. Acad. Sci.*, 2011, **108**, 16968-16973.
51. G. Zuo, X. Zhou, Q. Huang, H. Fang and R. Zhou, *J. Phys. Chem. C*, 2012, **115**, 23323-23328.
52. Z. Yang, Z. Wang, X. Tian, P. Xiu and R. Zhou, *J. Chem. Phys.*, 2012, **136**, 025103-025110.
53. W. Humphrey, A. Dalke and K. Schulten, *J. Mol. Graphics*, 1996, **14**, 33-38.
54. W. L. Jorgensen, J. Chandrasekhar, J. D. Madura, R. W. Impey and M. L. Klein, *J. Chem. Phys.*, 1983, **79**, 926-935.
55. J. L. Fauchere and V. Pliska, *Eur. J. Med. Chem.*, 1983, **18**, 379-375.

56. L. KalÈ, R. Skeel, M. Bhandarkar, R. Brunner, A. Gursoy, N. Krawetz, J. Phillips, A. Shinozaki, K. Varadarajan and K. Schulten, *J. Comput. Phys.*, 1999, **151**, 283-312.
57. A. D. Mackerell, M. Feig and C. L. Brooks, *J. Comput. Chem.*, 2004, **25**, 1400-1415.
58. A. D. MacKerell, D. Bashford, Bellott, R. L. Dunbrack, J. D. Evanseck, M. J. Field, S. Fischer, J. Gao, H. Guo, S. Ha, D. Joseph-McCarthy, L. Kuchnir, K. Kuczera, F. T. K. Lau, C. Mattos, S. Michnick, T. Ngo, D. T. Nguyen, B. Prodhom, W. E. Reiher, B. Roux, M. Schlenkrich, J. C. Smith, R. Stote, J. Straub, M. Watanabe, J. Wiórkiewicz-Kuczera, D. Yin and M. Karplus, *J. Phys. Chem. B*, 1998, **102**, 3586-3616.
59. J.-P. Ryckaert, G. Ciccotti and H. J. C. Berendsen, *J. Comput. Phys.*, 1977, **23**, 327-341.
60. S. E. Feller, Y. Zhang, R. W. Pastor and B. R. Brooks, *J. Chem. Phys.*, 1995, **103**, 4613-4621.
61. U. Essmann, L. Perera, M. L. Berkowitz, T. Darden, H. Lee and L. G. Pedersen, *J. Chem. Phys.*, 1995, **103**, 8577-8593.
62. E. Darve, D. Rodriguez-Gomez and A. Pohorille, *J. Chem. Phys.*, 2008, **128**, 144120-144113.
63. J. Héning, G. Fiorin, C. Chipot and M. L. Klein, *J. Chem. Theory Comput.*, 2010, **6**, 35-47.
64. D. Rodriguez-Gomez, E. Darve and A. Pohorille, *J. Chem. Phys.*, 2004, **120**, 3563-3578.
65. J. Héning and C. Chipot, *J. Chem. Phys.*, 2004, **121**, 2904-2914.
66. N. S. de Groot, F. X. Aviles, J. Vendrell and S. Ventura, *FEBS J.*, 2006, **273**, 658-668.
67. D. Nepal and K. E. Geckeler, *Small*, 2007, **3**, 1259-1265.
68. G. Zuo, W. Gu, H. Fang and R. Zhou, *J. Phys. Chem. C*, 2011, **115**, 12322-12328.
69. J. Chang, A. M. Lenhoff and S. I. Sandler, *J. Phys. Chem. B*, 2007, **111**, 2098-2106.
70. M. R. Shirts and V. S. Pande, *J. Chem. Phys.*, 2005, **122**, 134508-134513.
71. T. E. Creighton, ed., *Proteins: Structure and Molecular Properties*, 2nd Ed., 1993.
72. V. V. Chaban, T. I. Savchenko, S. M. Kovalenko and O. V. Prezhdo, *J. Phys. Chem. B*, 2010, **114**, 13481-13486.
73. T. Lührs, C. Ritter, M. Adrian, D. Riek-Loher, B. Bohrmann, H. Döbeli, D. Schubert and R. Riek, *Proc. Natl. Acad. Sci. U.S.A.*, 2005, **102**, 17342-17347.

Chapter – 5

**Competition between A β Self-association and Adsorption on the
Hydrophobic SWCNT Surface: A Molecular Dynamics Study**

Abstract



Treatment of Alzheimer's disease (AD) is impeded by the lack of effective therapeutics. Small, soluble A β globulomers play a major role in AD neurotoxicity. We evaluate the adsorption behavior of small A β oligomers on the surface of a single walled carbon nanotube of high curvature. While the intrinsic self-assembly propensity of A β is markedly hindered by adsorption, the oligomeric units show high degrees of surface immobilization. Immobilized complexes are capable of oligomeric growth, but with a shifted monomer–oligomer equilibrium compared to the free states. The results provide a important basis for further investigations in the design of new effective therapeutics for preventing AD progression.

5.1 Introduction

The profound influence of nanomaterials on the behavior of intrinsically disordered proteins (IDPs) has come to the fore recently.¹⁻³ IDPs defy the classic protein structure-function paradigm in biology.⁴ Importantly, their inherent resistance to adopt natively folded forms can be compensated by their high tendency to form self-assembled units, which are often associated with the onset of debilitating neurodegenerative diseases.^{5, 6} Key insights into IDP self-assembly pathways have emerged over the last decade from a combination of advanced experimental, theoretical and computational approaches.⁷⁻¹³ It is believed that the underlying physico-chemical basis of nanomaterial influence on IDP assembly could be harnessed for potential therapeutic and diagnostic applications in combating these debilitating proteopathies.^{1, 14-16}

The 4 kDa Amyloid beta (A β) peptide, often considered a paradigm for studying IDP self-assembly, is associated with familial as well as sporadic Alzheimer's disease (AD).¹⁷ AD has no cure yet, and its prognosis is worsened by a lack of early diagnostic methods. A β assembly can be described as a nucleation dependent process wherein the formation of a critical nucleus triggers higher ordered growth characterized by the appearance of insoluble amyloid fibrils.^{18, 19} It is noteworthy, however, that recent research implicates soluble small oligomers of A β , rather than its fibrillar aggregates, in AD neurotoxicity.²⁰⁻²² A detailed molecular picture of the early oligomeric self-assembly pathway is therefore necessary to design effective AD therapeutics. But the tendency of the A β monomer to aggregate very rapidly in water hinders experiments designed to probe mechanistic aspects of the assembly pathways.^{23, 24} However, structural information on the monomeric and various self-assembled forms has been obtained via NMR methods.²⁵ In this respect, computational and theoretical methods have been indispensable in the development of mechanistic models for the A β aggregation process and in unraveling roles of key domains within the peptide sequence.^{7, 18, 26-28}

Non-covalent interactions arising from various nanomaterials could be harnessed for modulating the intrinsic self-assembly characteristics of A β . Interactions of A β with polymeric, gold, or TiO₂ nanoparticles may potentially enhance fibrillation rates, as suggested by a growing body of *in vitro* research.²⁹⁻³² Conversely, carbon nanomaterials such as fullerene, carbon nanotubes and graphene oxide have been shown to strongly influence

conformational properties in A β units, destabilize A β protofibrils, and reduce the size of the aggregates in a concentration dependent manner.³³⁻³⁷ Kim and Lee first showed that 1,2-(dimethoxymethano) fullerene specifically binds to KLVFF region of A β protein, thereby suppressing A β aggregation.³⁸ More recently, Andujar *et al.* found that fullerene (C₆₀) can preferentially bind to the turn region of pentameric A β and destabilize the intramolecular and intermolecular salt bridges.³⁶ Mahmoudi *et al.* have recently reported that graphene oxide can increase lag phase of A β fibrillation process through adsorption of A β monomers.³⁹ Li *et al.* found that single walled carbon nanotubes (SWCNT) inhibits destabilizes β -sheet aggregates by hydrophobic and π - π stacking interaction.³⁵ We have recently described the mechanistic aspects of full-length A β monomeric adsorption on a SWCNT.^{33, 34, 40}

Motivated by the need for suitable AD therapeutics, we herein investigate the self-assembly and adsorption behavior of the full-length A β ₁₋₄₂ peptide on the curved surface of a SWCNT. We point out that while significant insights have been gained from studies of smaller A β fragments, key differences in behavior exist between segmental forms and the full length peptide.⁴¹ Interestingly, the A β ₁₋₄₂ form displays stronger aggregation properties and neurotoxic effects than even the A β ₁₋₄₀ form.⁴² We have earlier described the spontaneous adsorption of monomeric A β ₁₋₄₂ on the SWCNT surface,^{33, 34, 40} while other studies report its thermodynamic favorability to assemble into dimeric units.^{43, 44} Herein, we find that while the propensity of A β to self-associate is hindered noticeably in the presence of the SWCNT, the interactions arising from the surface are insufficient to fully dissociate the individual monomeric units. Our Adaptive Biasing Force (ABF) based free energy calculations show that while the SWCNT surface can cause a small shift in the monomer-oligomer equilibrium, the surface adsorbed states are remarkably capable of oligomeric growth. The implications of our observations may be leveraged for further studies aimed to design potential therapeutics for preventing AD progression.

5.2. Methods

5.2.1 General Simulation Protocol

All simulations were performed with the NAMD simulation package.⁴⁵ The CHARMM22 force field with the CMAP correction^{46, 47} was used for all the simulations. The solvent molecules were modeled with TIP3P water,⁴⁸ and requisite counterions added to obtain charge neutral systems. The simulation box was rectangular with a minimum distance of 15

Å between any atom and a box side, three-dimensional orthorhombic periodic boundary conditions applied. Each system was first energy minimized for 10 000 steps with the conjugate gradient method. Simulations were conducted with a 2 fs timestep in the isothermal-isobaric (NPT) ensemble. Constant temperature was maintained with Langevin dynamics at a collision frequency of 1 ps^{-1} , and a pressure of 1 atm maintained with the Nosé-Hoover method.^{49, 50} Electrostatic interactions were calculated with particle-mesh Ewald⁵¹ and SHAKE⁵² was used to constrain bonds involving hydrogen atoms. The cutoff for non-bonded interactions was set to 12 Å, with smoothing started from 10.5 Å.

5.2.2 Principle Component Analysis (PCA)

Assemblies of IDPs such as A β are characterized by large degrees of conformational and interaction heterogeneity.^{17, 43, 53} Cartesian Principle Component Analysis (PCA), a useful clustering technique in biomolecular simulations,⁵⁴ was used as implemented in the CARMA package⁵⁵ to identify the key conformations and interaction modes within the simulated ensembles. After removing translational and rotational degrees of freedom, distributions of the first three principal components (PCs) using a root mean squared deviation (RMSD) cutoff of 2.4 Å. The ensembles were projected on to the free energy landscape of the first (PC1) and second (PC2) principle components, and representative conformations selected from the first and second most populated clusters in this landscape.

5.2.3 A β Monomer

The solution state NMR structure of A β_{1-42} peptide, obtained in a 70:30 mixture of water and hexafluoro-2-propanol, (PDB: 1Z0Q)⁵⁶ was heated at 373 K in the gas phase to generate random coil configurations. Ten of these structures were then independently simulated in explicit water at 310 K for at least 150 ns, generating a cumulative simulation data of over 1.6 μs . The array of A β conformations were subjected to PCA and structures from the two most populated clusters, shown in Figures 5.1a and b, were selected. The structural propensities of these conformations, presented in Figure 5.1c and d, are remarkably similar to full-length A β conformations reported to populate the peptide's ensemble in water.^{57, 58} 6 ns simulations of the representative conformations were performed, and ^{15}N and $^{13}\text{C}_\alpha$ chemical shifts calculated with the SHIFTS program⁵⁹ were compared with corresponding experimental data.²⁵ Residue-wise correlation plots between the experimental and calculated

chemical shifts, and values of the Pearson Correlation Coefficients (R) are presented in Figures 5.1e to h.

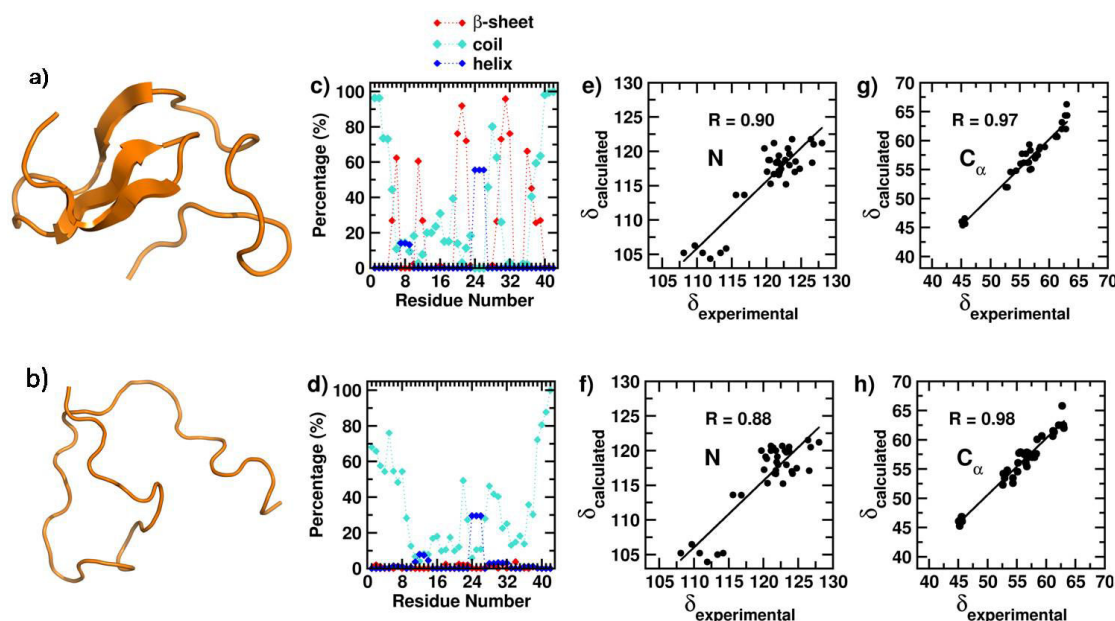


Figure 5.1. a), b) Snapshots of representative monomer conformations used in this study ; c), d) corresponding residue-wise secondary structure propensity. For the conformation in a), correlation of the average ^{15}N and $^{13}\text{C}_\alpha$ NMR chemical shifts with corresponding experimental values are shown in e) and g); the data for the conformation in b) are shown in f) and h). Linear regressions of the calculated ($\delta_{\text{calculated}}$) and the experimental ($\delta_{\text{experimental}}$) chemical shifts are provided with the Pearson Correlation Coefficients (R).

5.2.4 Adaptive Biasing Force (ABF) Free Energy Calculations

Potential of mean force (PMF) calculations were carried out with the Adaptive Biasing Force (ABF) method^{60, 61} as implemented in the NAMD package. ABF is a thermodynamic integration method in which the mean force acting along a reaction coordinate ' σ ' is used to estimate local barriers in the energy surface. The gradient of the free energy is obtained from the average force F_σ as,

$$\frac{dA(\sigma)}{d\sigma} = -\langle F_\sigma \rangle_\sigma \quad (5.1)$$

F_σ is accumulated over small bins within the desired range of σ . Here, the reaction coordinate used, the distance d_{in} (see *Results*), was varied from 6 to 24 Å. Three 6 Å segments were used with each segment was divided into 24 bins of 0.25 Å width, and ABF calculations carried out independently in each segment. To avoid non-equilibrium effects, unbiased sampling was

carried out for 500 steps prior to application of bias. The standard deviations were obtained from the system forces using the method formulated by Rodriguez-Gomez.^{62, 63} The ABF simulations within each segment were carried out for 650 ns, with convergence obtained over at least 200 ns.

5.3. Results and Discussion

5.3.1 Spontaneous Small Oligomeric Assembly

We begin first by investigating the spontaneity of small oligomerisation in the full length A β . As described in Methods, an ensemble of dimeric structures amounting to a cumulative simulation time of 1.5 μ s was obtained from independent trajectories started by placing two monomeric units at 33 Å apart at varying relative orientations. Stable dimeric conformations were selected via principle component analysis (PCA), and the trimeric ensemble obtained by placing a third A β monomer at center of mass distances of 33 Å at varying orientations and generating 1.5 μ s of cumulative simulation data. In Figures 5.2a and c, we depict temporal evolution of the total inter-monomer interactions for the dimer (E_{1-2}) and the trimer (E_{1-2-3}) averaged over multiple simulation trajectories. The marked strengthening of the interactions within a few tens of nanoseconds highlights the spontaneity of early oligomeric assembly of A β , in agreement with earlier reports.^{43, 44} The mean values of E_{1-2} and E_{1-2-3} over the last 10 ns of the simulation trajectories are -224.6 (\pm 65.0) and -364.1 (\pm 72.1) kcal mol⁻¹, respectively. In Figures 5.2b and d, we describe the ensemble of conformations projected into the landscape of the first (PC1) and second (PC2) principle components, and present snapshots of the representative conformations of the first and second most populated clusters in this landscape. The representative conformations were further used for simulations of oligomer-SWCNT interactions studies described in the remainder of the paper.

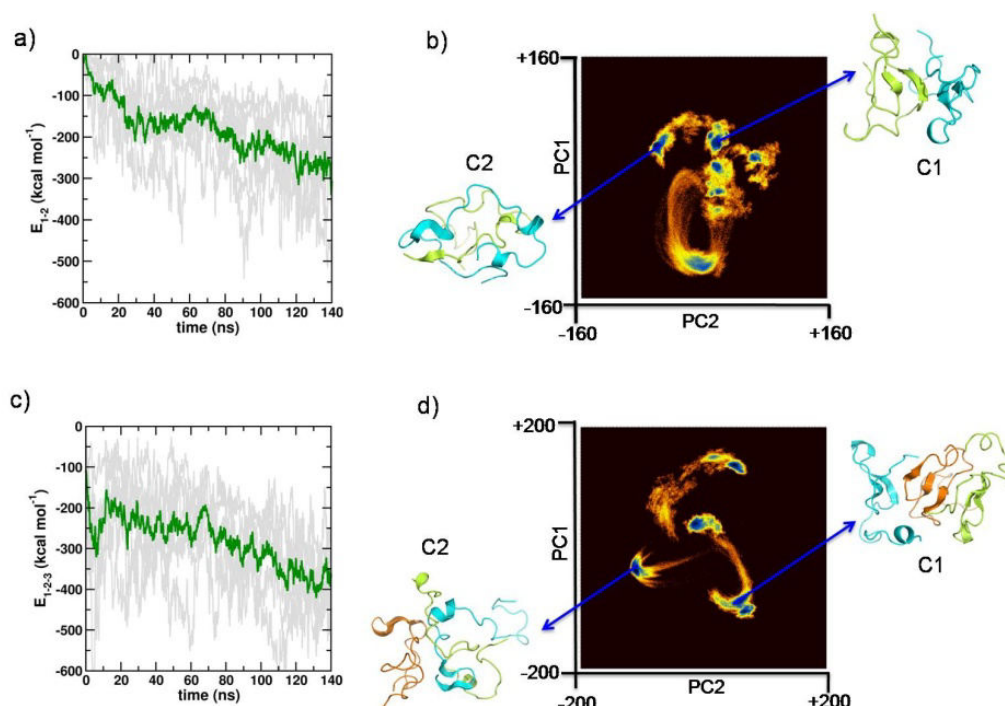


Figure 5.2. Time evolution of the total inter-monomer interaction energies in a) dimerizing simulations (E_{1-2}) and c) trimerizing simulations (E_{1-2-3}). Evolutions over individual trajectories are depicted in gray, and the mean over multiple trajectories in *green*. Free energy landscape as a function of the first (PC1) and second (PC2) principal components for the b) dimer ensemble, and d) the trimer ensemble. Representative snapshots of the first and the second most populated clusters are depicted as C1 and C2, respectively.

5.3.2 SWCNT Surface Adsorption Competes with Inherent Self-Assembly

We have earlier described the (enthalpic) factors that lead to spontaneous adsorption of $A\beta_{1-42}$ on the outer surface of a SWCNT.^{33, 34} We herein investigate whether the interactions arising from the SWCNT can compensate for the strong enthalpy driven self-assembly of the $A\beta$ monomer. Representative dimeric conformations (from clusters C1 and C2) were placed in the vicinity of the curved outer surface of a SWCNT of (6,6) chirality, at center of mass distances from the SWCNT varying between 15 and 20 Å. Six independent trajectories, amounting to a cumulative simulation time of 1.2 μ s, were generated. Evolution of E_{1-2} , and that of E_{D-NT} , the interaction of SWCNT with the dimer complex, was monitored; these are shown for a sample trajectory in Figure 5.3a. The mean values of E_{1-2} and E_{D-NT} obtained from over last 10 ns of all trajectories were $-119.1 (\pm 41.9)$ and $-160.3 (\pm 32.6)$ kcal mol⁻¹, respectively, showing that the nanotube offsets the inter-monomer binding strength of the dimer complex by nearly 50%. For a better understanding of the interplay between the competing $A\beta$ propensities of assembly and adsorption, we obtain probability distributions, $p(S_{D-NT}, S_D)$, of the inter-monomer (S_D) and the dimer-SWCNT (S_{D-NT}) contact areas from

the simulated data. The contact area calculation has been described in previous studies.^{33, 64} The probabilities were converted to the free energy landscape (see Figure 5.3b) using $F(S_{D-NT}, S_D) = -k_B T \ln(p/p_{\max})$, where k_B , T and p_{\max} are the Boltzmann's constant, absolute temperature and the maximum probability, respectively. The shallow minimum (marked 'A') corresponds to early conformations in the simulation trajectories while the deeper minima (containing 'B', 'C' and 'D') correspond to states obtained after full adsorption. The landscape is also characterized by another deep minimum (marked 'E') with a much narrower ('minor') basin. Importantly, the figure indicates that the initial states are separated from the maximally adsorbed states by a small barrier. Interestingly, the broad basin shows that the variation in S_D is markedly greater than the variation in S_{D-NT} . We find that that S_{D-NT} is largely confined to values much lower than 1800 \AA^2 , indicating that the total dimeric adsorption never exceeds twice the mean monomer-SWCNT contact area.³³ Thus, while the SWCNT surface can induce destabilization in pre-formed $A\beta$ dimers, it cannot fully compensate for the enthalpic factors that bind the monomeric units.

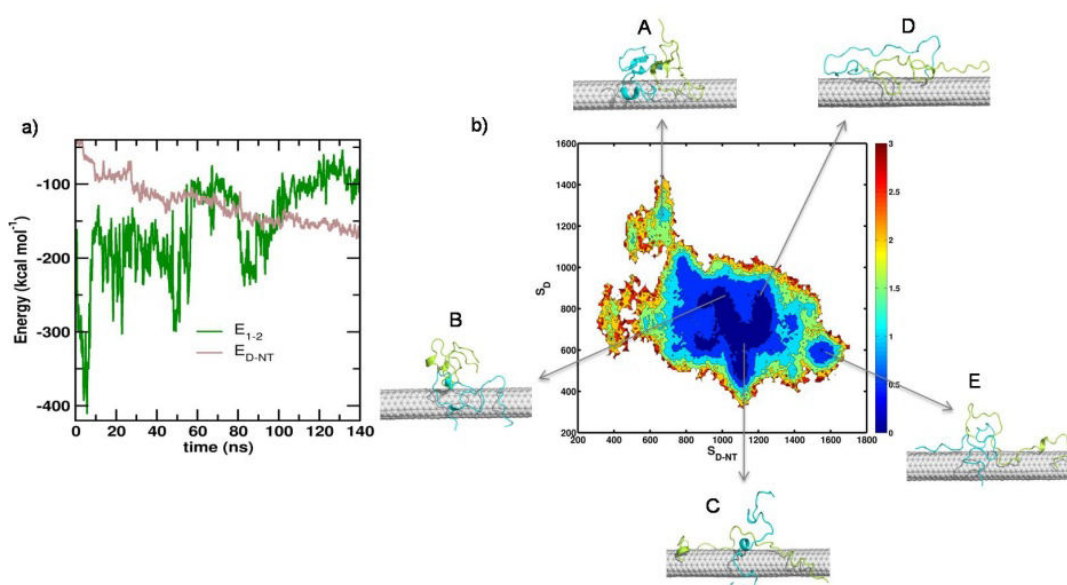


Figure 5.3. a) Time evolution of E_{1-2} and E_{D-NT} (see main text), from a representative simulation of surface bound dimeric system; b) Free energy landscape as function of inter-protein contact area (S_D , in \AA^2) and nanotube-protein contact area (S_{D-NT} , in \AA^2) for surface bound dimeric complexes. Representative snapshots in the free energy landscape are depicted are labeled as 'A', 'B', 'C', 'D' and 'E' (see main text). Units of free energy kcal mol⁻¹.

We investigated the effect of the surface on the structural integrity of the dimeric complex by evaluating the 'asphericity', α , of the pure and surface adsorbed complexes. The asphericity is defined as $\alpha = 1 - (I_{\min}/I_{\max})$, where I_{\min} and I_{\max} , the minimum and maximum

values, respectively, of the principle moments of inertia. I_{\min} and I_{\max} are equal in a perfectly spherical compact object leading to $\alpha = 0$; higher α indicate a lowering of the compactness. The α distributions are compared in Figure 5.4a. The mean of α for the free and the surface adsorbed dimers are $0.4 (\pm 0.2)$ and $1.7 (\pm 0.9)$, respectively, showing that the surface reduces the overall compactness of the dimeric state, in addition to the enhanced structural fluctuation evident earlier from S_{D-NT} . We further evaluated the inter-monomer residue-residue contact probability map for the free and surface dimers, presented in Figure 5.4b and c. As in earlier studies,⁶⁵ a pair of residues has been considered to form a contact if the separating distance of their side-chains does not exceed 7 Å. The reduction in the total number of inter-monomer contacts due to the interaction with the surface is evident from the comparison; the average number of inter-residue contacts decreases from 34 in the free dimeric ensemble to 19 in the dimer-SWCNT ensemble, corresponding to a 44.1% reduction. The reduction in the inter-monomer contact is pronounced in the region of the central hydrophobic core, L₁₇VFFA₂₁, and in the C-terminal region, G₂₉AIIGLMVGGV_{VIA}₄₂ region.

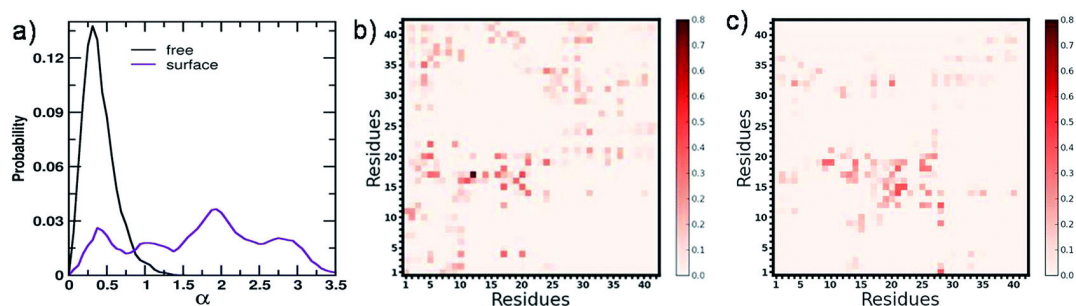


Figure 5.4. a) Probability distributions of the asphericity α for free and surface bound dimers. Inter-monomer residue-wise contact probabilities for the b) free, c) surface bound dimeric ensembles.

5.3.3 Growth Potential of Oligomers Immobilized on the Nanosurface

Free A β monomers are found to be in equilibrium with small oligomeric states in aqueous medium.²² In order to understand how binding to the nanotube may shift the monomer-oligomer equilibrium, we compared growth potentials of a representative surface adsorbed dimeric state ('C' in the major basin of Fig 5.3b) with that of a free dimer (from C1 of Fig 5.2b). The ABF procedure, as described in Methods, was used to evaluate the potential of mean force (PMF) as a function of the incoming distance (d_{in}), of the center of mass of a third monomer (M_I) from a pre-adsorbed monomer of the dimeric complex. In the case of the free dimer, d_{in} was the center of mass distance between the incoming monomer and the closer,

facing monomer of the dimeric complex. The resultant free energy profiles are compared in Figure 5.5. The most favorable approach distances in the two scenarios are close, reflected in similar positions of the free energy minimum obtained at 9.25 and 10 Å for the free and surface adsorbed complexes, respectively. However, unlike in the case of the free complex where the incoming monomer pays a small free energy cost to approach the existing dimer to within 6 Å, the corresponding penalty for the surface adsorbed complex is about three times higher. The PMF profile further shows that for the surface adsorbed complex, the thermodynamic cost for separating M_I far away from the existing complex ($d_{in} \sim 24$ Å) is about half the corresponding cost in the free complex. Thus, the free energy analysis shows that assembly and growth are possible for the surface adsorbed small $A\beta$ complexes, but the resultant complexes are less compact and relatively more vulnerable to disassembly. This indicates that the nanotube surface is likely to cause subtle shifts in the equilibrium between the peptide's monomeric and small oligomeric states.

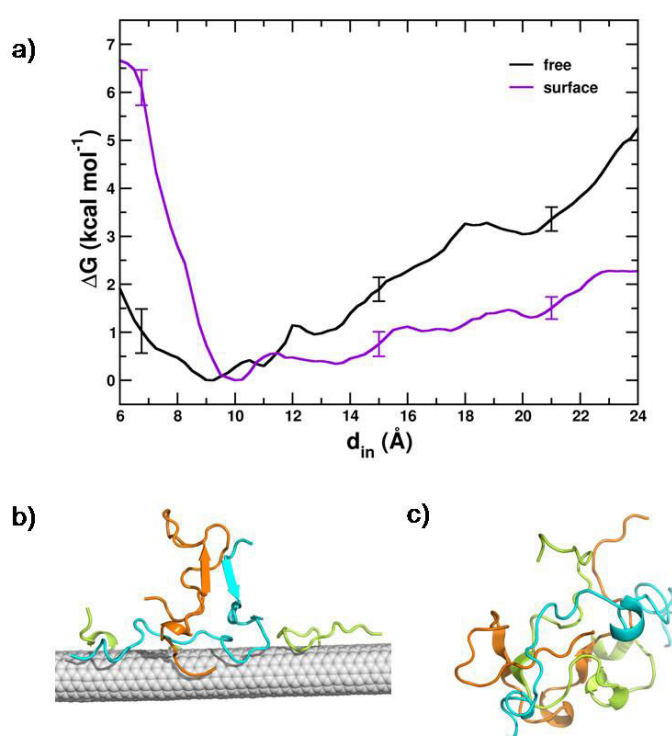


Figure 5.5. a) ABF based free energy profiles as a function of distance (d_{in}) of an incoming third monomer to a pre-existing free and surface adsorbed dimeric complex. Snapshots corresponding to the free energy minimum are shown for b) surface adsorbed, and c) free complexes.

We have further generated multiple unbiased simulation trajectories (totaling 900 ns) started with an incoming monomer placed in the vicinity of initial dimer-SWCNT complexes selected from ‘B’, ‘C’ and ‘D’ of Fig 5.3. The mean inter-peptide (E_T) and the trimer-

SWCNT (E_{T-NT}) interaction strengths over the last 10 ns were $-222.0 (\pm 79.6)$ and $-271.6 (\pm 30.0)$ kcal mol⁻¹, respectively, and the corresponding mean contact area of the SWCNT with the resulting trimeric complex was $1886.2 (\pm 128.2)$ Å². As in dimeric adsorption, we find that the adsorption is not proportional to the oligomeric number. Probability distribution of the inter-protein contact area (S_T) vs. the SWCNT contact area with the trimeric complex (S_{T-NT}) converted to a free energy landscape is provided in Figure 5.6; the initial 20 ns of the trajectories are not considered. Two predominant (S_{T-NT} , S_T) free energy basins centered at ‘A’, or (1700, 1700), and ‘B’, or (2100, 1700), are found to be in equilibrium. Thus, relative strengthening of the trimer-nanotube contacts occurs at the expense of the inter-monomer contacts, and vice-versa. Although the population centered at ‘B’ is slightly broader, the barrier separating the two distributions (~ 1 kcal mol⁻¹) can be accessed at physiological temperatures.

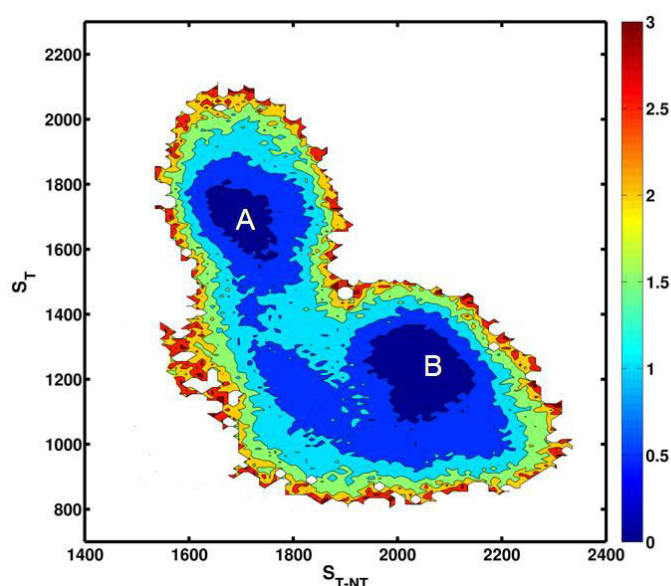


Figure 5.6. Free energy landscape as function of inter-protein contact area (S_T , in Å²) and nanotube-protein contact area (S_{T-NT} , in Å²) for surface bound trimeric complexes. Units for free energy are kcal mol⁻¹.

5.4 Summary and Conclusion

In summary, this work establishes the competitive nature of A β self-assembly and its adsorption propensity on the SWCNT surface. Although A β dimers have a marked weakening upon surface adsorption on the SWCNT, they are capable of growing into trimeric assemblies. Free energy calculations demonstrate that only a small shift in the dimer-trimer equilibrium in solution should occur in the surface adsorbed states over the free oligomeric

states. The results provide a basis for the development of carbon nanomaterial based therapeutics aimed at preventing A β self-assembly in aqueous media, and possibly in biological fluids. It is noteworthy that suitably functionalized CNTs offer a number of advantages, such as increased solubility and chemical functionality over pristine CNTs.^{66, 67} We will therefore seek to understand how suitable physico-chemical alterations to the SWCNT characteristics may influence the adsorption process and strategies to leverage those findings in the design of new potential therapeutics for AD treatment.

Before concluding, we remark that A β is just one member of a family of IDPs whose small oligomers and amyloid assemblies are associated with a debilitating disease.⁶ Different IDPs exhibit marked differences in self-assembly kinetics and are likely to trigger diseases onset at different stages during the assembly pathway. Interestingly, emerging research indicates overlapping etiologies for several of neurodegenerative proteopathies arising from co-assembly of IDPs associated with individual disorders.^{68, 69} It may therefore be worthwhile to investigate how other IDPs aggregate and adsorb on surfaces, the equilibrium of the adsorbed states with the monomers present in aqueous solution.

5.5 References

1. M. Mahmoudi, H. R. Kalhor, S. Laurent and I. Lynch, *Nanoscale*, 2013, **5**, 2570-2588.
2. C. Li and R. Mezzenga, *Nanoscale*, 2013, **5**, 6207-6218.
3. Y. D. Álvarez, J. A. Fauerbach, J. V. Pellegrotti, T. M. Jovin, E. A. Jares-Erijman and F. D. Stefani, *Nano Lett.*, 2013, **13**, 6156-6163.
4. P. Tompa, *Trends Biochem. Sci.*, 2012, **37**, 509-516.
5. F. U. Hartl, A. Bracher and M. Hayer-Hartl, *Nature*, 2011, **475**, 324-332.
6. F. Chiti and C. M. Dobson, *Annu. Rev. Biochem.*, 2006, **75**, 333-366.
7. S. L. Bernstein, T. Wyttenbach, A. Baumketner, J.-E. Shea, G. Bitan, D. B. Teplow and M. T. Bowers, *J. Am. Chem. Soc.*, 2005, **127**, 2075-2084.
8. S. Gnanakaran, R. Nussinov and A. E. Garcia, *J. Am. Chem. Soc.*, 2006, **128**, 2158-2159.
9. R. Pellarin, E. Guarnera and A. Caflisch, *J. Mol. Biol.*, 2007, **374**, 917-924.
10. M. G. Krone, L. Hua, P. Soto, R. Zhou, B. J. Berne and J.-E. Shea, *J. Am. Chem. Soc.*,

- 2008, **130**, 11066-11072.
11. Y. Miller, B. Ma and R. Nussinov, *Proc. Natl. Acad. Sci.*, 2010, **107**, 9490-9495.
 12. R. Krishnan, J. L. Goodman, S. Mukhopadhyay, C. D. Pacheco, E. A. Lemke, A. A. Deniz and S. Lindquist, *Proc. Natl. Acad. Sci.*, 2012, **109**, 11172-11177.
 13. D. Thirumalai, G. Reddy and J. E. Straub, *Acc. Chem. Res.*, 2012, **45**, 83-92.
 14. M. Varshney, P. S. Waggoner, C. P. Tan, K. Aubin, R. A. Montagna and H. G. Craighead, *Anal. Chem.*, 2008, **80**, 2141-2148.
 15. C. Cabaleiro-Lago, I. Lynch, K. A. Dawson and S. Linse, *Langmuir*, 2009, **26**, 3453-3461.
 16. J. A. Yang, W. Lin, W. S. Woods, J. M. George and C. J. Murphy, *J. Phys. Chem. B*, 2014, **118**, 3559-3571.
 17. Y. Miller, B. Ma and R. Nussinov, *Chem. Rev.*, 2010, **110**, 4820-4838.
 18. M. M. Pallitto and R. M. Murphy, *Biophys. J.*, 2001, **81**, 1805-1822.
 19. J. E. Straub and D. Thirumalai, *Annu. Rev. Phys. Chem.*, 2011, **62**, 437-463.
 20. C. Haass and D. J. Selkoe, *Nat. Rev. Mol. Cell Biol.*, 2007, **8**, 101-112.
 21. S. L. Bernstein, N. F. Dupuis, N. D. Lazo, T. Wyttenbach, M. M. Condrón, G. Bitan, D. B. Teplow, J.-E. Shea, B. T. Ruotolo, C. V. Robinson and M. T. Bowers, *Nat. Chem.*, 2009, **1**, 326-331.
 22. S. Nag, B. Sarkar, A. Bandyopadhyay, B. Sahoo, V. K. A. Sreenivasan, M. Kombrabail, C. Muralidharan and S. Maiti, *J. Biol. Chem.*, 2011, **286**, 13827-13833.
 23. G. Bitan, M. D. Kirkitadze, A. Lomakin, S. S. Vollers, G. B. Benedek and D. B. Teplow, *Proc. Natl. Acad. Sci.*, 2003, **100**, 330-335.
 24. J. T. Jarrett, E. P. Berger and P. T. Lansbury, *Biochemistry*, 1993, **32**, 4693-4697.
 25. L. Hou, H. Shao, Y. Zhang, H. Li, N. K. Menon, E. B. Neuhaus, J. M. Brewer, I.-J. L. Byeon, D. G. Ray, M. P. Vitek, T. Iwashita, R. A. Makula, A. B. Przybyla and M. G. Zagorski, *J. Am. Chem. Soc.*, 2004, **126**, 1992-2005.
 26. T. Lührs, C. Ritter, M. Adrian, D. Riek-Loher, B. Bohrmann, H. Döbeli, D. Schubert and R. Riek, *Proc. Natl. Acad. Sci. U.S.A.*, 2005, **102**, 17342-17347.
 27. J. Khandogin and C. L. Brooks, *Proc. Natl. Acad. Sci.*, 2007, **104**, 16880-16885.
 28. F. Massi and J. E. Straub, *Proteins: Struct., Funct., and Bioinf.*, 2001, **42**, 217-229.
 29. C. Cabaleiro-Lago, F. Quinlan-Pluck, I. Lynch, K. A. Dawson and S. Linse, *ACS*

- Chem. Neurosci.*, 2010, **1**, 279-287.
30. D. Brambilla, R. Verpillot, B. Le Droumaguet, J. Nicolas, M. Taverna, J. Kóňa, B. Lettiero, S. H. Hashemi, L. De Kimpe, M. Canovi, M. Gobbi, V. r. Nicolas, W. Scheper, S. M. Moghimi, I. Tvaroška, P. Couvreur and K. Andrieux, *ACS Nano*, 2012, **6**, 5897-5908.
 31. Q. Ma, G. Wei and X. Yang, *Nanoscale*, 2013, **5**, 10397-10403.
 32. W.-h. Wu, X. Sun, Y.-p. Yu, J. Hu, L. Zhao, Q. Liu, Y.-f. Zhao and Y.-m. Li, *Biochem. Biophys. Res. Commun.*, 2008, **373**, 315-318.
 33. A. K. Jana and N. Sengupta, *Biophys. J.*, 2012, **102**, 1889-1896.
 34. A. K. Jana, J. C. Jose and N. Sengupta, *Phys. Chem. Chem. Phys.*, 2013, **15**, 837-844.
 35. H. Li, Y. Luo, P. Derreumaux and G. Wei, *Biophys. J.*, 2011, **101**, 2267-2276.
 36. S. A. Andujar, F. Lugli, S. Hofinger, R. D. Enriz and F. Zerbetto, *Phys. Chem. Chem. Phys.*, 2012, **14**, 8599-8607.
 37. Q. Li, L. Liu, S. Zhang, M. Xu, X. Wang, C. Wang, F. Besenbacher and M. Dong, *Chem. – Eur. J.*, 2014, **20**, 7236-7240.
 38. J. E. Kim and M. Lee, *Biochem. Biophys. Res. Commun.*, 2003, **303**, 576-579.
 39. M. Mahmoudi, O. Akhavan, M. Ghavami, F. Rezaee and S. M. A. Ghiasi, *Nanoscale*, 2012, **4**, 7322-7325.
 40. A. K. Jana and N. Sengupta, *Biophys. Chem.*, 2013, **184**, 108-115.
 41. A. E. Conicella and N. L. Fawzi, *Biochemistry*, 2014, **53**, 3095-3105.
 42. M. Q. Liao, Y. J. Tzeng, L. Y. X. Chang, H. B. Huang, T. H. Lin, C. L. Chyan and Y. C. Chen, *FEBS Lett.*, 2007, **581**, 1161-1165.
 43. X. Zhu, R. P. Bora, A. Barman, R. Singh and R. Prabhakar, *J. Phys. Chem. B*, 2012, **116**, 4405-4416.
 44. S.-H. Chong and S. Ham, *Proc. Natl. Acad. Sci.*, 2012, **109**, 7636-7641.
 45. L. KalÈ, R. Skeel, M. Bhandarkar, R. Brunner, A. Gursoy, N. Krawetz, J. Phillips, A. Shinozaki, K. Varadarajan and K. Schulten, *J. Comput. Phys.*, 1999, **151**, 283-312.
 46. A. D. Mackerell, M. Feig and C. L. Brooks, *J. Comput. Chem.*, 2004, **25**, 1400-1415.
 47. A. D. MacKerell, D. Bashford, Bellott, R. L. Dunbrack, J. D. Evanseck, M. J. Field, S. Fischer, J. Gao, H. Guo, S. Ha, D. Joseph-McCarthy, L. Kuchnir, K. Kuczera, F. T. K. Lau, C. Mattos, S. Michnick, T. Ngo, D. T. Nguyen, B. Prodhom, W. E. Reiher, B. Roux, M. Schlenkrich, J. C. Smith, R. Stote, J. Straub, M. Watanabe, J. Wiórkiewicz-

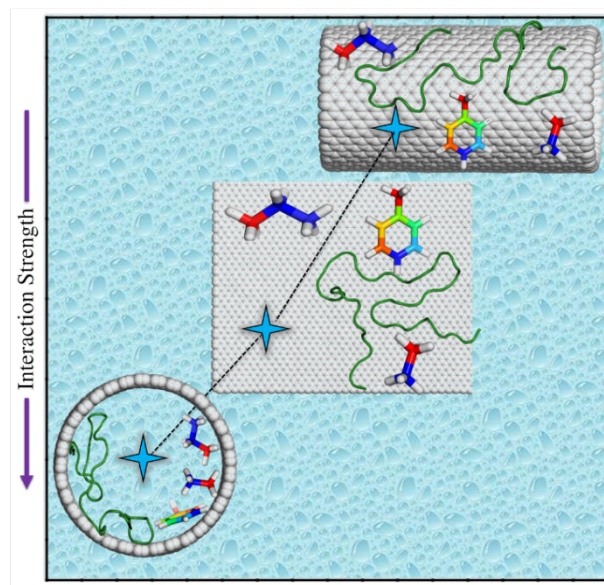
- Kuczera, D. Yin and M. Karplus, *J. Phys. Chem. B*, 1998, **102**, 3586-3616.
48. W. L. Jorgensen, J. Chandrasekhar, J. D. Madura, R. W. Impey and M. L. Klein, *J. Chem. Phys.*, 1983, **79**, 926-935.
49. G. J. Martyna, D. J. Tobias and M. L. Klein, *J. Chem. Phys.*, 1994, **101**, 4177-4189.
50. S. E. Feller, Y. Zhang, R. W. Pastor and B. R. Brooks, *J. Chem. Phys.*, 1995, **103**, 4613-4621.
51. U. Essmann, L. Perera, M. L. Berkowitz, T. Darden, H. Lee and L. G. Pedersen, *J. Chem. Phys.*, 1995, **103**, 8577-8593.
52. J.-P. Ryckaert, G. Ciccotti and H. J. C. Berendsen, *J. Comput. Phys.*, 1977, **23**, 327-341.
53. G. Wei, A. I. Jewett and J.-E. Shea, *Phys. Chem. Chem. Phys.*, 2010, **12**, 3622-3629.
54. K. Tai, T. Shen, U. Börjesson, M. Philippopoulos and J. A. McCammon, *Biophys. J.*, 2001, **81**, 715-724.
55. N. M. Glykos, *J. Comput. Chem.*, 2006, **27**, 1765-1768.
56. T. Simona, E. Veronica, V. Paolo, A. J. v. N. Nico, M. J. J. B. Alexandre, G. Remo, T. Teodorico, A. T. Piero and P. Delia, *ChemBioChem*, 2006, **7**, 257-267.
57. Y.-S. Lin, G. R. Bowman, K. A. Beauchamp and V. S. Pande, *Biophys. J.*, 2012, **102**, 315-324.
58. N. G. Sgourakis, Y. Yan, S. A. McCallum, C. Wang and A. E. Garcia, *J. Mol. Biol.*, 2007, **368**, 1448-1457.
59. K. Osapay and D. A. Case, *J. Am. Chem. Soc.*, 1991, **113**, 9436-9444.
60. E. Darve, D. Rodriguez-Gomez and A. Pohorille, *J. Chem. Phys.*, 2008, **128**, 144120-144113.
61. J. Hénin, G. Fiorin, C. Chipot and M. L. Klein, *J. Chem. Theory Comput.*, 2009, **6**, 35-47.
62. D. Rodriguez-Gomez, E. Darve and A. Pohorille, *J. Chem. Phys.*, 2004, **120**, 3563-3578.
63. J. Hénin and C. Chipot, *J. Chem. Phys.*, 2004, **121**, 2904-2914.
64. C.-c. Chiu, G. R. Dieckmann and S. O. Nielsen, *J. Phys. Chem. B*, 2008, **112**, 16326-16333.
65. C. Lee and S. Ham, *J. Comput. Chem.*, 2010, **32**, 349-355.

66. C. A. Dyke and J. M. Tour, *Chem. – A Eur. J.*, 2004, **10**, 812-817.
67. Y. Liu, C. Chipot, X. Shao and W. Cai, *J. Phys. Chem. C*, 2011, **115**, 1851-1856.
68. E. Masliah, E. Rockenstein, I. Veinbergs, Y. Sagara, M. Mallory, M. Hashimoto and L. Mucke, *Proc. Natl. Acad. Sci.*, 2001, **98**, 12245-12250.
69. D. J. Irwin, V. M. Y. Lee and J. Q. Trojanowski, *Nat. Rev. Neurosci*, 2013, **14**, 626-636.

Chapter - 6

**Unravelling Origins of the Heterogeneous Curvature Dependence
of Polypeptide Interactions with Carbon Nanostructures**

Abstract



Emerging nanotechnology has rapidly broadened interfacial prospects of biological molecules with carbon nanomaterials (CN). A prerequisite for effectively harnessing such hybrid materials is a multi-faceted understanding of their complex interfacial interactions as functions of the physico-chemical characteristics and the surface topography of the individual components. In this article, we address the origins of the curvature dependence of polypeptide adsorption on CN surfaces (CNS), a phenomenon bearing acute influence upon the behavior and activity of CN-protein conjugates. Our benchmark molecular dynamics (MD) simulations with the amphiphilic full-length amyloid beta ($A\beta$) peptide demonstrate that protein adsorption is strongest on the concave (inner) CN surface, weakest on the convex (outer) surface, and intermediary on the planar surface, in agreement with recent experimental reports. The curvature effects, however, are found to manifest non-uniformly between the amino acid subtypes. To understand the underlying interplay of the chemical nature of the amino acids and surface topography of the CN, we performed higher-level quantum chemical (QM) calculations with amino acid analogs (AAA) representing their five prominent classes, and convex, concave and planar CN fragments. Molecular electrostatic potential maps reveal pronounced curvature dependence in the mixing of electron densities, and a resulting variance in the stabilization of the non-covalently bound molecular complexes. Interestingly, our study revealed that the interaction trends of the high-level QM calculations were captured well by the empirical force field. The findings in this study have important bearings upon the design of carbon based bio-nanomaterials, and additionally, provide valuable insights on the accuracy of various computational techniques for probing non-bonded interfacial interactions.

6.1 Introduction

The large overlap between the length scales of functional nanomaterials and biological systems, coupled with rapid advances in the design of the former, has fueled emerging interest in the “nano-bio” interface.^{1,2} It has been realized that the influence exerted by nanosurfaces on biomolecular behavior could be leveraged in therapeutic, diagnostic, drug delivery and biomolecular recognition applications.³⁻⁷ Further, biopolymers or biomolecular assemblies can be used advantageously to solubilize or functionalize nanomaterials, and generate useful hybrids or nanocomposites with versatile functionalities.⁸ However, such prospects first necessitate detailed, molecular level understanding of the physico-chemical interactions between various nanomaterials and biomolecular complexes.

The uniqueness and versatility of the “nano-allotropes” of carbon, often referred to as carbon nanomaterials (CN), including graphene and single- and multi-walled carbon nanotubes, make them one of the most viable materials for nanotechnological applications.⁹ Composed entirely of sp^2 or quasi- sp^2 hybridized carbon atoms, and owing to their unique atomic arrangements and resulting characteristics, these materials have recently shown to be promising in diverse applications.¹⁰⁻¹³ Importantly, these materials also have profound influences on biological systems, and consequently, have found increasing relevance in biomedical applications;¹⁴ usages include the design of sensors for enzymatic activity¹⁵, protein nanotoxicity¹⁶, peptide oligomerization¹⁷, and nanopores for nucleic acid sequencing.¹⁸ These materials have further been noted to induce marked conformational changes and alter self-assembly thermodynamics and kinetics in proteins.¹⁹ Interestingly, despite lingering concerns related to their toxicity, their usage in nanomedicine has been under consideration for some time.^{14,20}

With the rapidly increasing prospects of interfacial interactions between CN and proteins, it is imperative to obtain a *de novo* characterization of the interactions and the plausible outcomes resulting from their superpositions. We first note that biological polymers, especially proteins, possess high chemical heterogeneity along their molecular chain, and the complex interplay of various long and short ranged non-bonded forces result in their uniqueness in terms of folding, functionality, self-assembly, etc. Thus, the observed modulation of protein behavior by carbon nanomaterials must result from a perturbation of these inherent forces. A protein side chain interacts with the carbon structures through weak non-covalent interactions broadly recognized as XH- π (X = O, N, C), π - π , anion- π , and

cation- π . A perusal of the naturally occurring amino acids suggests that except for non-polar aliphatic amino acids, all residues can be involved in multiple types of interactions with the CN; for instance, a phenylalanine residue can be involved in π - π and CH- π interactions simultaneously.

Recent spectroscopic studies show that CN curvature influences their intrinsic properties.²¹ Further, several recent experimental reports and computer simulations show that their interactions with proteins, leading to adsorption, encapsulation and influence over enzymatic activity, is deeply affected by CN surface topography. For the outer (convex) surfaces, protein-CN interaction strength is observed to increase with decreasing curvature, and attain a maximum at the planar (graphene) surface.²² However, concerns have been raised about the loss in activity of protein on adsorption. Efforts have been invested to maintain the protein structure on adsorption by modulating the curvature of the surface.^{23, 24} Experimental and theoretical studies have shown that protein adsorbed onto the highly curved outer surface of a carbon nanotube (CNT) is more stable compared to the planar graphene surface.²⁵⁻²⁷ Another theoretical study describes that the loss of native protein contacts upon adsorption on the inner CNT surface is smaller compared to graphene and the outer CNT surface.²⁸ Simultaneously, biomolecular encapsulation has facilitated exciting opportunities for biological and biomedical applications due to the intercellular delivery of these molecules via cell-penetrating transporters.^{29,30} However, adsorption characteristics and mechanisms as a function of CNS curvature remain largely unexplored till date.

In this work, we seek to address the origins of the long- and the short-ranged influences of carbon nanomaterials on protein adsorption behavior, with a focus on how these interactions depend on the geometry of the surface. We first investigated the adsorption propensities of the 42-residue peptide, Amyloid beta ($A\beta$) on carbon nanostructures of varying surface geometry using MD simulations. Several recent reports using molecular dynamics (MD) simulation demonstrate that the structure and organization of amyloid fibrils are markedly disrupted in the presence of carbon nanostructures.³¹⁻³³ Recent work from our group has shown that the strong competition between $A\beta$ adsorption on a CNT surface and its inherent propensity to self-assemble affects the thermodynamics of small oligomeric growth.^{17, 34-36} It is noteworthy that previous report has shown that the overall trends of complex non-bonded interactions between molecular entities are captured well by current generation empirical force fields used in MD simulations.³⁷ Our present simulation results reveal a strong dependence of the protein-surface interactions on the surface curvature, with

the inner (concave) surface of the CNT adsorbing the peptide most strongly and efficiently, followed by the planar (graphene) surface, and the outer (convex) surface. Interestingly, while the trends are maintained, the influence of curvature is non-uniform over amino acids of varying chemical nature.

Atomistic MD simulations implementing standard nonpolarizable (fixed-charge) force fields, in which the carbon atoms of the CN are modeled as uncharged Lennard-Jones particles that do not include electrostatics in protein-CN interactions. However, recent literature indicate that the non-covalent interactions can also include contributions from electrostatics and polarization.³⁸ For a better revelation of the nature of interaction and interaction energies, we resort to high-level quantum chemical calculations using density functional theory (DFT), using dispersion corrected density functionals. A set of analogs that suitably represent the various classes of naturally occurring amino acids were used in conjunction with CN fragments of varying curvature. The trends in interaction energies obtained from the quantum chemical calculations, mirroring those obtained from the MD simulations, reveal the causative factors contributing to surface topology dependence of the protein-CN interactions. Molecular electrostatic potential maps reflect the differential mixing of electron density between amino acid analogs and CN, consolidating the role of curvature in the stabilization of non-covalently bound molecular complexes.

6.2 Methods

6.2.1 MD Simulations

Coordinates of the carbon nanosurfaces were generated with the VMD utility.³⁹ An armchair (24,24) single-walled carbon nanotube (SWCNT) of length 70 Å, radius 16.3 Å, containing 2784 carbon atoms used was used to model protein adsorption on the outer (convex) and inner (concave) surfaces. The planar surface was modeled as a single graphene sheet of dimension s 84.7 Å × 83.7 Å. The SWCNT axes coincided with the x-axis in the systems with curved surfaces, while the graphene sheet was coincident with the x-y plane in the system with the planar surface. The convex and planar systems were set up such that there was a minimum distance of 15 Å between any pairs of surface and protein atoms. In the case of the radially symmetric concave system, the protein center of mass was situated on the SWCNT axis. Snapshots of different starting conformations of peptide-nanosurface complexes are shown in Figure 6.1. Rectangular simulation boxes were set up such that there

was a minimum distance of 13 Å between any protein atom and a box edge. Three sodium ions were added to neutralize each system. Each system was then solvated using the TIP3P⁴⁰ water model, resulting in 8.5 waters per carbon atom in the concave system, and an average of 10.6 and 11.2 water molecules per carbon atom in the planar and convex systems, respectively. The nanosurfaces were constrained at the setup position with a harmonic force of force constant 2.0 kcal mol⁻¹ Å⁻². Details of the full-length Aβ monomeric structure generation are found in our previous study.¹⁷ The CHARMM22 force field with the CMAP^{41,42} correction was used for the simulations, which were performed with the NAMD2.9 simulation package.⁴³ Bonds between hydrogen atoms were constrained using SHAKE algorithm.⁴⁴ The systems were first energy minimized for 10 000 steps with the conjugate gradient method, followed by simulations in the isothermal–isobaric ensemble. A temperature of 310 K temperature was maintained using Langevin dynamics with a collision frequency of 1 ps⁻¹, and a 1 atmosphere pressure was maintained with the Langevin piston Nosé–Hoover algorithm.⁴⁵ Timesteps of 2 fs were used to integrate the equation of motion and orthorhombic periodic boundary conditions were applied in three directions. The electrostatic interactions were calculated using particle mesh Ewald method⁴⁶ with a non-bonded cutoff of 12 Å with smoothing starting at 10.5 Å. Three independent trajectories, amounting to a total simulation time of 0.6 μs were generated for each system.

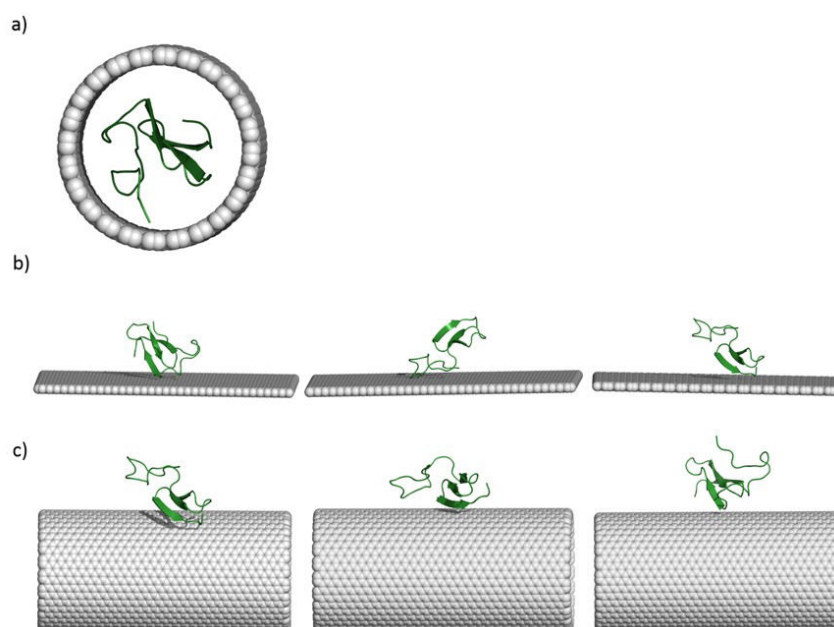


Figure 6.1. Snapshots of starting conformations of peptide nanosurface MD simulations, for peptide on the a) concave surface; b) planar surface; c) convex surface. The water molecules are not shown for clarity.

6.2.2 Trajectory Analyses

The peptide's contact area, $S_{contact}$, with the nanosurface was determined as,³⁴

$$S_{contact} = \frac{1}{2} [SASA_{peptide} + SASA_{CNS} - (SASA_{complex})] \quad (6.1)$$

Here, $SASA_{peptide}$, $SASA_{CNS}$ and $SASA_{complex}$ represent the solvent accessible surface area of the isolated peptide, of the isolated nanosurface, and of the peptide-nanosurface complex, respectively. The solvent accessible surface area is calculated with the VMD package using a probe diameter of 1.8 Å.

The interaction strengths of the concave, convex and planar carbon nanosurfaces with the full protein, and with the different classes of amino acids, are calculated with the NAMD Energy plugin available with the NAMD package.

The binding free energies of the full protein with the surfaces were obtained using the Molecular Mechanics-Generalized Born Surface Area (or MM-GBSA) method, as implemented in the NAMD package.^{47, 48} The calculation was performed on each protein-nanosurface complex, and separately on its subsets, namely the protein and the nanosurface. For each component, the total free energy of the system is,

$$G_{total} = H_{MM} + G_{solv-pol} + G_{solv-np} - TS_{config} \quad (6.2)$$

Here, H_{MM} , $G_{solv-pol}$, $G_{solv-np}$, and S_{config} represent, respectively, the total internal energy; the polar solvation free energy; the non-polar solvation free energy; and the configurational entropy. The term H_{MM} comprised of the bond, angle, dihedral, improper, electrostatic and van der Waals energies, and $G_{solv-pol}$ was calculated with the solvent dielectric constant of water at 310 K.⁴⁹ The non-polar solvation free energy is estimated as the product of the surface tension of water ($\gamma = 0.0072$) and the solvent accessible surface area (SASA) of the solute. The binding free energy is estimated as the difference,

$$\Delta G_{binding} = G_{total(complex)} - G_{total(nanosurface)} - G_{total(protein)} \quad (6.3)$$

As in many recent studies,^{47, 48, 50} the entropic changes were ignored to obtain,

$$\Delta G_{binding} = \Delta H_{MM} + \Delta G_{solv-pol} + \Delta G_{solv-np}$$

$$= (\Delta E_{electrostatic} + \Delta E_{vdW} + \Delta E_{internal}) + \Delta G_{solv-pol} + \Delta G_{solv-np} \quad (6.4)$$

$\Delta E_{electrostatic}$, ΔE_{vdW} and $\Delta E_{internal}$ are the changes in the electrostatic, van der Waals and the bonded energies, respectively.

6.2.3 DFT Methods

Current literature suggests that DFT methods can be employed to study the adsorption of small organic and inorganic molecules,⁵¹ such as amino acid side chains, on carbon nanostructures.^{52, 53} Recently, the M06 functional has been recognized to provide an improved treatment of non-covalent interactions.⁵⁴⁻⁵⁶ Thus, all the geometries reported in this study were first fully optimized at the M062X/6-31G** level of theory (L₁) using the Gaussian 09 suite of quantum-chemical programs.⁵⁷ This level of theory has recently been employed to account for the weak non-covalent interactions.⁵⁸ The CNT considered in the DFT study was an armchair single walled carbon nanotube (SWCNT). All the dangling bonds in carbon nanostructures (both CNT and graphene) were linked to the individual hydrogen atoms to compensate the unsatisfied valency of terminal carbon atoms. The lengths of the SWCNT and graphene structures were kept fixed in the entire study for the comparison of interaction energies. All the assessment of interaction energies is based on only the electronic energies. The interaction energy (E_i) between AAA and CNS was calculated as,

$$E_i = E_{AAA-CNS} - (E_{AAA} + E_{CNS}) \quad (6.5)$$

where, $E_{AAA-CNS}$ is the energy of the amino acid analogue and carbon nanostructure complex; E_{AAA} and E_{CNS} are the energies of amino acid analogue and carbon nanostructure, respectively, obtained from a single point energy calculation to the structures isolated from a optimized AAA-carbon nanostructure complex respectively.

To compare the effect of the functional on geometries and interaction energies, a full geometry optimization was performed at the dispersion-corrected B3LYP-D2 functional with the 6-31G** basis set (or L₂) for the geometries obtained at L₁. An evaluation of the energies of toluene-CNS complex obtained after the full geometry optimization at the M062X/6-311G** level of theory (L₃) and single point energy calculation at L₃ to the structures obtained at L₁ indicates that the structure obtained at the L₁ and L₃ are nearly same, as well as the interaction energies obtained by two methods were also obtained to be almost same. Therefore, to further evaluate the effect of the basis set on interaction energies for all molecular geometries, a single point energy calculation was performed at the M062X/6-

311G** level of theory (L_3) for the geometries obtained at L_1 . All the values reported at L_3 in this paper are single point energies for the structures obtained at L_1 . All the values reported in the manuscript for general description are at the L_1 level of theory, until unless mentioned specifically.

Previous studies indicate that the π - π and XH- π interactions of amino acid analogues (AAA) with convex surface of SWCNT and graphene complexes are dominated by dispersion.^{52, 59, 60} Therefore, for insights into the relative contribution of dispersive interactions, a full geometry optimization was carried out at the B3LYP/6-31G** level of theory in gas phase (L_7) for the AAA-CNS molecular complexes at all the three surfaces.

A protein contains both hydrophobic and hydrophilic side chains, and differential solvation in bulk solvent and in the vicinity of hydrophobic environment (for instance CN), can provide impetus for CN-amino acid interactions and eventually protein adsorption on the surfaces. Therefore, it is extremely important to consider the effect of solvent on interaction energies. The electrostatic effect of the water dielectric through bulk solvation on the interaction energies of different chemical pairs was determined by full geometry optimizations at the M062X/6-31G** (L_4 ; CPCM/M062X/6-31G**) and B3LYP-D2/6-31G** (L_5 ; CPCM/B3LYP-D2/6-31G**) level of theories in the dielectric continuum of water using the Conductor like Polarization Continuum Model (CPCM).^{61, 62} A single point energy calculation was performed at the CPCM/M062X/6-311G** level of theory (L_6) to the structures obtained at the L_4 .

In general, interactions of AAAs with concave surface of SWCNT can happen from three walls of concave surface of SWCNT. For example, adsorption of toluene on concave wall of SWCNT results from the composite effect of π - π interaction with lower wall and CH- π interactions with both lower as well as both the side walls of SWCNT. Contrary to this, the interaction of AAAs with side walls of SWCNT is not a case in convex surface of SWCNT, whereas there is clearly no possibility of existence of any such interactions with graphene, as graphene is a planar structure. Therefore, for a more meaningful comparison, the interactions obtained only due to a single wall, the lower wall in concave surface of SWCNT (in connection with the similarity of interactions on all the three surfaces) appear to be a better way of comparison. For a case of example, for an approximate estimation of interaction energies resulting due to lower concave wall and side concave walls of SWCNT, a fragmentation analysis procedure was implemented for both toluene-SWCNT and benzene-SWCNT complexes obtained in gas phase at the L_1 as shown in Figure 6.2 and 6.3.

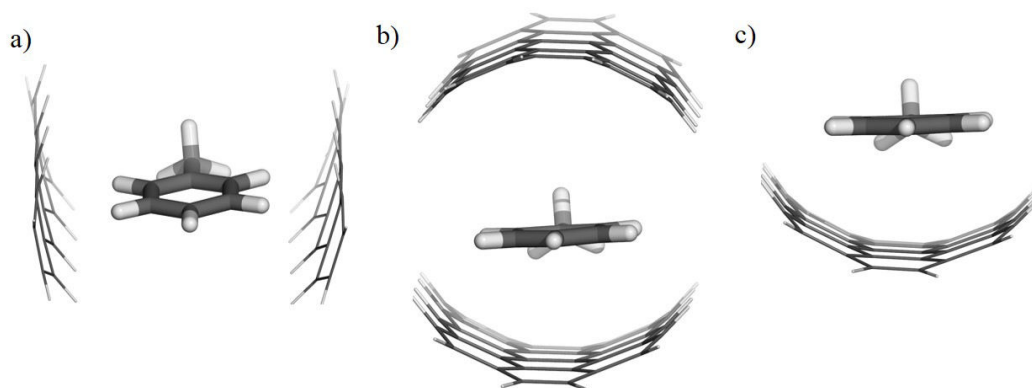


Figure 6.2. A schematic representation of interaction of a) toluene with the sidewalls of concave surface of SWCNT where hydrogens of phenyl ring and methyl group are interacting through CH- π , b) toluene with lower and upper wall and c) toluene with lower wall of concave surface of SWCNT through π - π of phenyl ring and CH- π of hydrogens of methyl substituent. Atom Colors: grey-carbon and white-hydrogen.

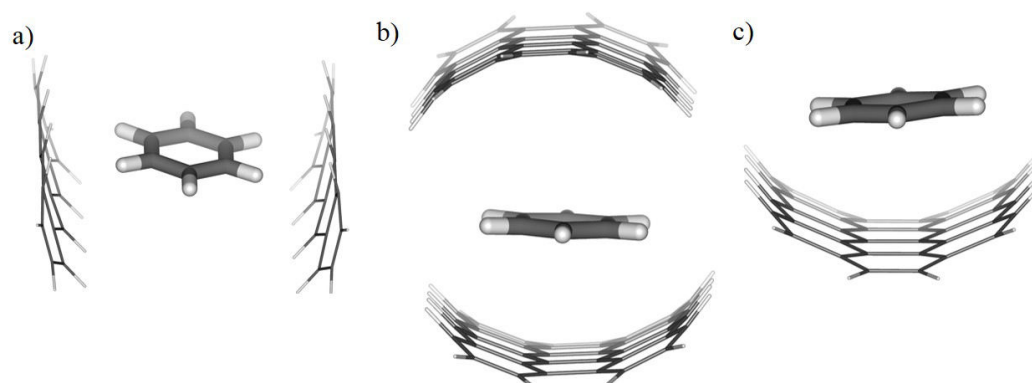


Figure 6.3. A schematic representation of interaction of a) benzene with the sidewalls of concave surface of SWCNT where hydrogens of phenyl ring are interacting through CH- π , b) benzene with lower and upper wall and c) benzene with lower wall of concave surface of SWCNT through π - π of phenyl ring. Atom Colors: grey-carbon and white-hydrogen.

6.3 Results

6.3.1 Surface Curvature Dependence of Protein Adsorption

We begin by comparing the adsorption characteristics of A β on the planar graphene surface, and the concave and convex surfaces of the (24, 24) SWCNT using MD simulations as described in *Methods*. We have earlier shown that the full-length peptide rapidly adsorbed on the outer surface of a (6, 6) SWCNT within the nanosecond timescales, with complete adsorption are initiated by the central hydrophobic core (L₁₇VFFA₂₁) and precipitated by the charged N-terminal domain (D₁AEFRHDSGYEVHHQK₁₆).³⁴ The magnitude of contact area

with the surface was found to be reflective of the strength of interactions leading to the adsorption. In Figure 6.4, we plot the total peptide-nanosurface contact area ($S_{A\beta-CNS}$) and interaction strengths ($E_{A\beta-CNS}$) for the three surfaces as a function of simulation time. The plots have been averaged over three individual trajectories. In the concave systems, on the average, the adsorption attains saturation within 20 ns, with $S_{A\beta-CNS}$ of attaining stable values of $1372.8 (\pm 27.0) \text{ \AA}^2$ and $E_{A\beta-CNS}$ reaching $-221.0 (\pm 12.0) \text{ kcal mol}^{-1}$. In contrast, on average, the adsorption attains saturation in the planar and the convex surfaces at about 100 ns and 80 ns, respectively. Further, the saturation values of $S_{A\beta-CNS}$ for the planar and convex surfaces are $1157.5 (\pm 24.5)$ and $910.8 (\pm 27.5) \text{ \AA}^2$ respectively, while those of $E_{A\beta-CNS}$ are $-175.4 (\pm 10.0)$ and $-139.5 (\pm 11.0) \text{ kcal mol}^{-1}$, respectively. This pattern establishes that the peptide's adsorption is strongest on the concave (inner) SWCNT surface, followed by the graphene (planar) and the convex (outer) SWCNT surface. In Figure 6.5, we present representative snapshots of the peptide-surface complexes along the representative trajectories at 0 ns, 100 ns and 200 ns.

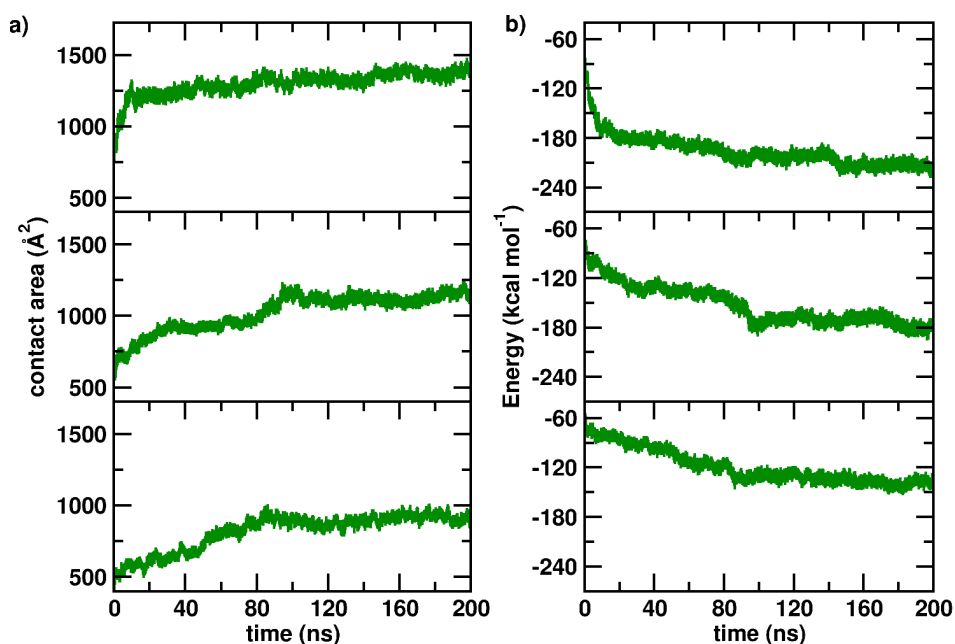


Figure 6.4. Time evolution of a) total peptide-SWCNT contact area and b) total peptide-SWCNT interaction energy, averaged over three independent trajectories for each system. The upper, middle and lower panels represent peptide-carbon nanosurface interactions on the concave, planar and convex surfaces, respectively.

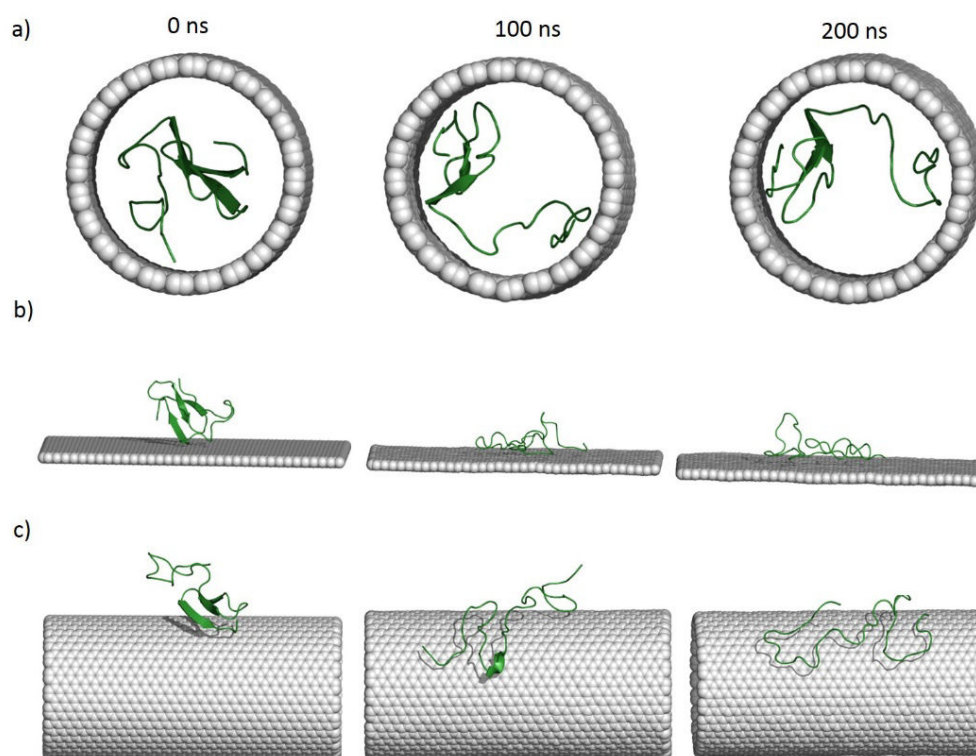


Figure 6.5. Representative snapshots of peptide adsorbed on a) concave surface of SWCNT, b) graphene and c) convex surface of SWCNT. The water molecules are not shown for clarity.

Despite the large number of hydrophobic residues in its sequence, the A β peptide is amphiphilic with polar and charged residues in the N-terminal domain and turn regions. In order to gain a better understanding of the interplay between curvature and chemical nature of the residues, we estimated from the simulation trajectories, the interaction strengths per residue belonging to the five different classes of amino acids, namely, aliphatic, aromatic, polar, acidic and basic. In Figure 6.6, we depict distributions of these interactions obtained from snapshots of the simulation trajectories taken after last 40 ns of three independent trajectories. It is clear from these distributions that all interactions show surface curvature dependence, although the influence is non-uniform for the different subtypes. The distributions corresponding to the three different curvatures are most distinct (have the least overlap) for the aliphatic residues, where the median interaction strength for the convex, planar and concave surfaces are -2.8, -3.6 and -4.8 kcal mol⁻¹, respectively. While a similar trend is observed in the case of the aromatic residues, the interactions per residue are significantly stronger, and there are greater degrees of overlap between the three distributions. The median interactions for the convex, planar and concave surfaces in this case are -9.6, -11.0 and -12.6 kcal mol⁻¹, respectively. Compared to aromatic residues, the

median interaction strengths of the basic residues are relatively weaker, being -4.5 , -7.3 and -9.0 kcal mol⁻¹ for the convex, planar and concave surfaces, respectively. These interactions are further weakened when the polar and acidic residues are considered. For polar residues, the median interactions for the convex, planar and concave residues are -2.1 , -4.1 and -5.6 kcal mol⁻¹, respectively, and -1.7 , -1.2 and -2.8 kcal mol⁻¹, respectively for the acidic residues. The markedly bimodal interaction distribution of the acidic residues with the convex surface arises from the variability in the interactions obtained from the independently simulated trajectories.

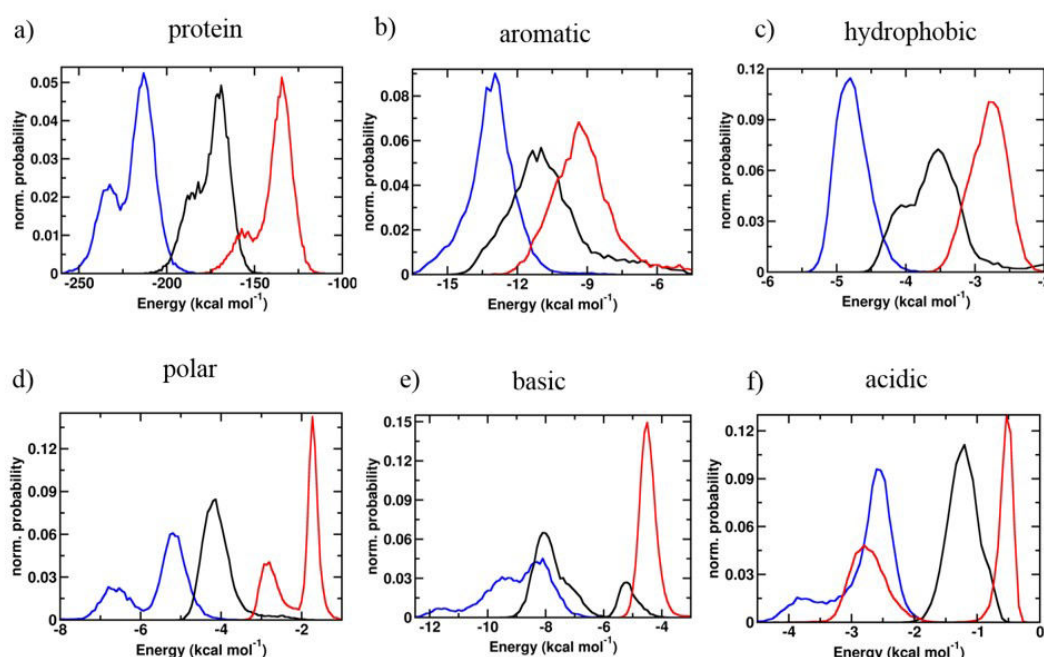


Figure 6.6. Normalized distributions of interaction energy of the full protein, and the five classes of amino acids with the CN surfaces. The interaction energy of full protein and amino acids with concave surface of SWCNT is in blue; with graphene in black; with convex surface of SWCNT in red. See text for details.

6.3.2 Curvature Dependence of Binding Free Energy

We have calculated the binding free energy of the A β peptide with the three surfaces using the MM-GBSA protocol as described in *Methods*. This method has been used recently in other studies to obtain protein surface binding free energies of similar systems. The mean and standard deviations of the quantities that constitute the total binding free energy are presented in Table 6.1; these data were obtained using the last 40 ns of the three independent trajectories, or a cumulative simulation time of 120 ns for each system. As seen from the trends in the values of $\Delta G_{binding}$, the binding is most favorable in the concave surface,

followed by the planar, and by the convex surface. On the other hand, the trends in $\Delta G_{solvation}$ indicate that the overall solvation is most unfavorable in the concave surface, followed by the planar and the convex surfaces. In each case, this is found to arise primarily due to the large positive value of $\Delta G_{solv-pol}$. The negative values of $\Delta G_{solv-np}$ indicate overall favorable associations of apolar domains of the protein with the carbon nanosurfaces. Interestingly, as the surface geometry changes from concave to planar and convex, $\Delta G_{solv-np}$ is found to increase while $\Delta G_{solv-pol}$ is found to decrease. Importantly, this analysis shows that ΔH_{MM} constitutes nearly 80% of the binding free energy, thereby establishing that, regardless of surface curvature, binding of the A β protein to the carbon nanosurface is primarily driven by the strong interactions between the protein and surface.

Contribution	Concave	Planar	Convex
$\Delta G_{binding}$	-174.4 (\pm 8.2)	-142.6 (\pm 8.7)	-115.4 (\pm 8.9)
ΔH_{MM}	-222.4 (\pm 11.3)	-176.1 (\pm 10.0)	-140.0 (\pm 10.9)
$\Delta E_{electrostatic}$	0.0	0.0	0.0
ΔE_{vdW}	-222.4 (\pm 11.3)	-176.1 (\pm 10.0)	-140.0 (\pm 10.9)
$\Delta E_{internal}$	0.0	0.0	0.0
$\Delta G_{solvation}$	48.0 (\pm 6.3)	33.5 (\pm 5.5)	24.6 (\pm 3.4)
$\Delta G_{solv-np}$	-20.5 (\pm 1.6)	-15.4 (\pm 1.6)	-13.2 (\pm 1.4)
$\Delta G_{solv-pol}$	68.5 (\pm 7.8)	48.9 (\pm 6.8)	37.9 (\pm 4.5)

Table 6.1. Individual components of the peptide-nanosurface binding free energies, on the concave, planar and convex surface (in kcal mol⁻¹). See text for details. Standard deviations are provided within braces.

6.3.3 Insights from DFT Calculations

The MD based analyses demonstrate that peptide interactions with carbon nanosurfaces have a complex dependence on surface curvature, with overall interactions being strongest with the inner, concave surface, and weakest with the outer, convex surface. Further, this dependence appears to be stronger in the aliphatic and the aromatic residues, and we find some ambiguity in the way interactions attributed to the acidic residues respond to changes in curvature. However, these results are based on empirical force fields, and the interaction trends that emerge could be qualitative in nature. Further, in a peptide chain, obtaining isolated interactions of various residues from contributions of neighboring residues is nearly

impossible. For the sake of a more general, sequence independent understanding, we systematically investigate the effect of curvature of the carbon nanosurface on the various interaction subtypes with high level QM calculations involving five amino acid analogs, each representative of one class of amino acids.

The interaction of proteins with carbon nanostructures can be attributed to the chemical diversity of the amino acid sequence in a typical protein. The twenty naturally occurring amino acids can be categorized into five major classes based on the functional groups *i.e.*, the most significant moiety associated to each side chain: aromatic, non-polar aliphatic, polar, acidic and basic. To fundamentally understand the nature and efficacy of interaction of amino acid residues in a protein with carbon nanostructures and the effect of CN surface curvature, representative side chain analogs corresponding to functional groups of side chains from each class of amino acids have been chosen for the present DFT studies (refer Table 6.2). Following subsections are intended towards the comprehensive DFT investigation considering all plausible heterogeneous interactions that can affect adsorption process of protein on CNSs, with additional emphasis given to adsorption on concave surface of SWCNT (in relation with convex surface of SWCNT and graphene).

Class	Representative amino acid	Representative amino acid analogue
Non-polar aromatic	Phenylalanine	Toluene
Non-polar aliphatic	Alanine, Valine, Leucine	Ethane
Polar aliphatic	Glutamine	Propanamide
Acidic	Glutamic acid	Propanoate
Basic	Lysine	Ethylammonium

Table 6.2. The name and structure of amino acid analogues chosen for the DFT studies

6.3.4 Interaction of Aromatic Residues with CNS

π - π stacking interactions between carbon nanostructures and the aromatic amino acids (Phe, Tyr, Trp) of protein are believed to be the major driving force for protein adsorption onto the carbon nanosurface.^{63, 64} Further, the stronger adsorption of protein on the graphene surface compared to convex surface of SWCNT could be attributable to stronger interactions of aromatic substrates with the graphene surfaces than the convex surface of SWCNTs.^{27, 52, 53, 65} Herein, in order to capture the comparative adsorption of proteins on the inner wall of the

carbon nanotube with regard to the graphene and convex surface of SWCNT, we report a detailed DFT study on interaction of structural and functional analogs of aromatic amino acids, the toluene and the benzene with CNSs; see Figure 6.7 for the optimized geometries. The interaction energy of toluene with the convex surface of nanotube is lower than that with the grapheme (Table 6.3), which is in accordance with previous reports.⁵³ It is interesting to note that, at the concave surface of SWCNT, interaction of the toluene is stronger by 7.8 kcal mol⁻¹ (Table 6.3) compared to the interaction on graphene, indicating adsorption of a protein should be strongest at the inner wall, as observed in our MD simulations.

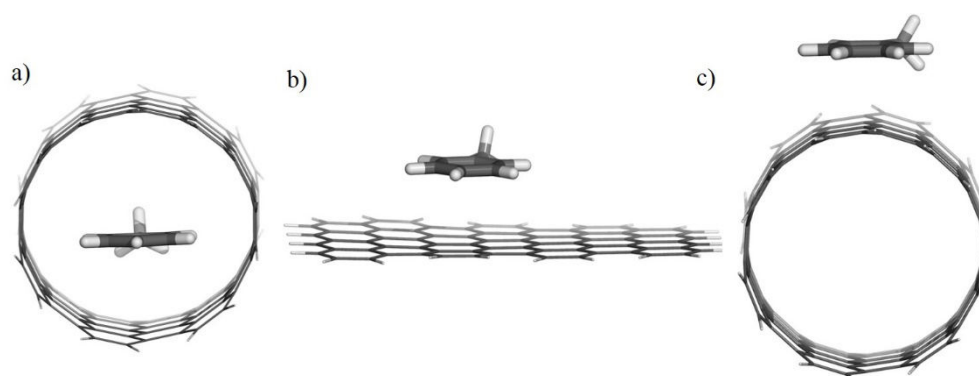


Figure 6.7. The gas phase optimized geometries of toluene with a) concave surface of SWCNT, b) graphene and c) convex surface of SWCNT at the M062X/6-31G** level of theory. Atom Colors: grey-carbon and white-hydrogen.

E_i	Toluene			Benzene		
	Concave	Planar	Convex	Concave	Planar	Convex
L_1	-19.7	-11.9	-9.2	-16.2	-9.5	-7.5
L_2	-30.0	-15.6	-12.3	-25.0	-12.6	-9.6
L_3	-24.0	-14.1	-10.9	-19.9	-11.4	-8.8
L_4	-18.5	-10.5	-8.3	-15.2	-8.2	-6.6
L_5	-29.3	-14.5	-11.5	-24.4	-11.6	-8.9
L_6	-22.7	-12.7	-9.8	-18.8	-10.0	-7.8

Table 6.3. Interaction energies of toluene and benzene with carbon nanostructures in kcal mol⁻¹. L_1 , L_2 , L_3 , L_4 , L_5 and L_6 correspond the values at the gas/M062X/6-31G**, gas/B3LYP-D2/6-31G**, gas/M062X/6-311G**, CPCM/M062X/6-31G**, CPCM/B3LYP-D2/6-31G** and CPCM/M062X/6-311G** level of theories.

An examination of the optimized geometry of concave surface of SWCNT and the toluene complex suggests that the H atoms of the phenyl ring and the methyl substituent are

involved in the CH- π interactions with the concave surface of SWCNT along three walls of SWCNT, the lower and the two side walls. To understand the interaction of toluene with the concave surface of SWCNT in more detail, a fragmentation analysis procedure was employed (as shown in Figure 6.2) to split the interaction energies obtained due to the π - π and CH- π interactions for toluene with the lower wall and CH- π interactions with the side-walls of concave surface of SWCNT. A fragmentation analysis of concave surface of SWCNT in the concave surface of SWCNT-toluene optimized complex was done by considering the molecule in two fragments: (i) toluene and the part of concave surface of SWCNT (the side walls) where the hydrogens of the phenyl ring and toluene are interacting through CH- π , and (ii) the toluene and a part of the concave surface of SWCNT, where the phenyl ring is interacting mainly through π - π and partially via the CH- π as well. We point out that the methyl group of toluene remains involved in CH- π interactions with concave surface of SWCNT in case (ii); see Figure 6.2. The single point energy calculations were done to the fragments obtained after fragmentation to get the interaction energies of fragments with the toluene. The interaction energy of toluene with concave surface of SWCNT is $-19.7 \text{ kcal mol}^{-1}$ (Table 6.3). Our calculations depict that the interaction energy of toluene with the lower wall of SWCNT (predominantly π - π in nature) is $-12.0 \text{ kcal mol}^{-1}$, which is just marginally stronger than the interaction energy of toluene with the graphene surface ($-11.9 \text{ kcal mol}^{-1}$); the additional $-5.4 \text{ kcal mol}^{-1}$ interaction energy comes from the interaction of the hydrogens of the toluene with the sidewalls of SWCNT. Only a marginal decrease in interaction energies on removal of upper surface of CNT (see column 2 and 3 in Table 6.4) suggest that the interactions of toluene with the upper surface of concave surface of SWCNT is very nominal.

E_i	total ^a	Lower wall ^b	(Lower + upper) walls ^c	Side-walls ^d	Sum ^e
Toluene	-19.7	-12.0	-12.2	-5.4	-17.4
Benzene	-16.2	-8.9	-9.3	-7.0	-15.9

Table 6.4. The interaction energies in kcal mol^{-1} of toluene and benzene with different walls of concave surface of SWCNT at the M062X/6-31G** level of theory in gas phase.

- Net interaction energy arises due to all the surfaces of concave surface of SWCNT
- Interaction energy only due to lower wall of SWCNT
- Interaction energy due to upper and lower walls of SWCNT
- Interaction energy due to both the side walls of SWCNT
- Sum of interaction energies with lower and two side walls of concave surface of SWCNT

To distinguish the affinity of the lone aromatic phenyl ring of toluene with carbon nanostructures, we separately optimized benzene-CNS complexes on all three surfaces. The results are shown in Table 6.3. Only a small weakening of the interactions of benzene in comparison to the toluene at all three surfaces further suggests that the major interaction of toluene with CNSs is π - π in nature. Fragmentation analysis for gas phase geometry of benzene-concave surface of SWCNT complex was also implemented, as illustrated in Figure 6.3. The energies are provided in Table 6.4. The values suggest that interaction energy of benzene with only lower wall of concave surface of SWCNT ($-8.9 \text{ kcal mol}^{-1}$, Table 6.4) is nearly close to the interaction energy of benzene with graphene ($-9.5 \text{ kcal mol}^{-1}$, Table 6.3). However, net interaction of benzene at the inner wall of CNT is fairly strong with the interaction energy being $-16.2 \text{ kcal mol}^{-1}$.

The role of solvent has totally been ignored in computing interaction of amino acids or their analogs with the CNS in all the QM studies reported so far.^{52, 53} However, several theoretical and experimental studies demonstrates that the solvent water plays an important part in protein adsorption on CNS.⁶⁶⁻⁶⁸ Dewetting of amino acids is essential condition for protein adsorption on CNS.^{35, 69} Therefore, to introduce the effect of bulk solvation, we performed, for the first time, full geometry optimizations of all AAA-CNS complexes in a dielectric continuum of water (dielectric constant, $\epsilon = 78.3553$) using implicit CPCM solvent model. Interestingly, the trend in E_i of toluene and benzene for the different surfaces obtained in the solvent phase is the same as that obtained in the gas phase (Table 6.3), but the values at individual surfaces are decreased by a small amount ranging from 0.7 to 1.4 kcal mol^{-1} (Table 6.3) indicating a small but non-negligible effect of solvation on interaction energies.

6.3.5 Interaction of Non-polar Aliphatic Residues with CNS

It is apparent from the experimental observations that the aliphatic amino acids (both polar as well as non-polar) are also found near the surfaces of carbon nanostructures.^{70, 71} Further, our atomistic MD simulations also illustrate that aliphatic amino acids strongly adsorb on carbon nanosurfaces (Figure 6.6). To further understand the details of the CH- π interactions, we performed DFT calculations to obtain the interactions of methane and ethane with carbon allotropes on all the three surfaces. The DFT optimized geometries are shown in Figure 6.8. The obtained trend in interaction strengths is similar to that obtained for the π - π interactions: concave surface of SWCNT > graphene > convex surface of SWCNT (shown in Table 6.5). Figure 6.9 and Figure 6.10 demonstrate the C-H covalent bond distances in optimized

geometries of ethane, methane and their respective complexes with carbon nanosurfaces. As expected, the C-H bonds that are pointed towards the surface are slightly longer in comparison to the C-H bonds that are directed away from the surface. An identical dependence (with E_i) of C-H bond lengths (that are pointed towards the surface) on nature of curvature of CNS has been observed for both methane- and ethane-CNS complexes. On the other hand, the C-H bonds that are directed away from the surface are unchanged regardless of the curvature of the surface. For the case of ethane, the number of C-H bonds that are pointed towards the surface changes depending upon the extent of curvature. For the most curved (towards the AAA) concave surface, four C-H bonds are directly pointed towards the surface. This number was found to be three and two for the graphene and the convex surface of SWCNT respectively. However, in all the methane-carbon nanostructure complexes, three C-H bonds are directed towards the surface, but the extent of bond lengthening increases from the convex to the planar to the concave surface (see Figure 6.10).

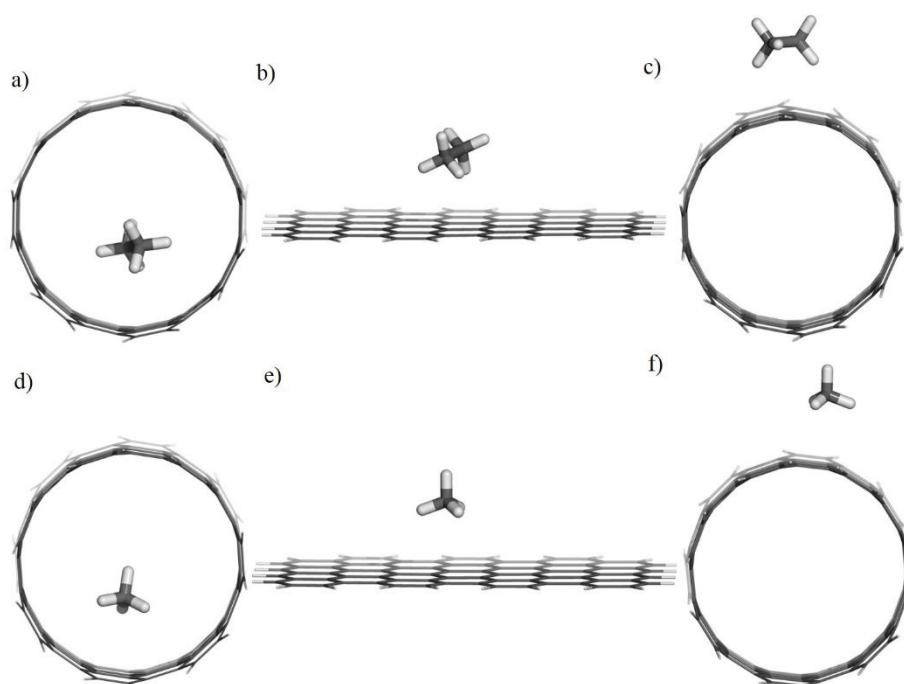


Figure 6.8. The gas phase optimized geometries of ethane and methane with concave surface of SWCNT, graphene and convex surface of SWCNT at the M062X/6-31G** level of theory. The 1st and 2nd columns correspond to the optimized complexes of ethane and methane respectively. Atom Colors: grey-carbon and white-hydrogen.

E_i	Ethane			Methane		
	Concave	Planar	Convex	Concave	Planar	Convex
L_1	-8.2	-4.3	-3.5	-5.6	-3.0	-2.3
L_2	-12.9	-6.4	-5.4	-7.9	-4.0	-3.3
L_3	-10.1	-5.0	-3.9	-6.8	-3.5	-2.6
L_4	-8.2	-4.3	-3.6	-5.6	-2.9	-2.3
L_5	-13.0	-6.4	-5.3	-7.9	-3.9	-3.3
L_6	-10.2	-5.0	-4.0	-6.8	-3.4	-2.5

Table 6.5. Interaction energy of ethane and methane with carbon nanostructures in kcal mol⁻¹. L_1 , L_2 , L_3 , L_4 , L_5 and L_6 correspond the values at the gas/M062X/6-31G**, gas/B3LYP-D2/6-31G**, gas/M062X/6-311G**, CPCM/M062X/6-31G**, CPCM/B3LYP-D2/6-31G** and CPCM/M062X/6-311G** level of theories.

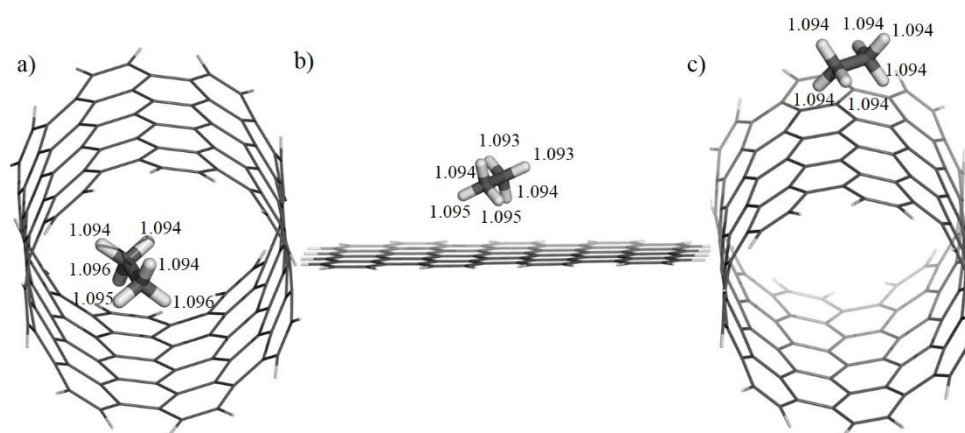


Figure 6.9. The gas phase optimized geometries of ethane with concave surface of SWCNT, graphene and convex surface of SWCNT at the M062X/6-31G** level of theory. The values correspond to the C-H bond distances of ethane. All the values are in Å. Atom Colors: grey-carbon and white-hydrogen.

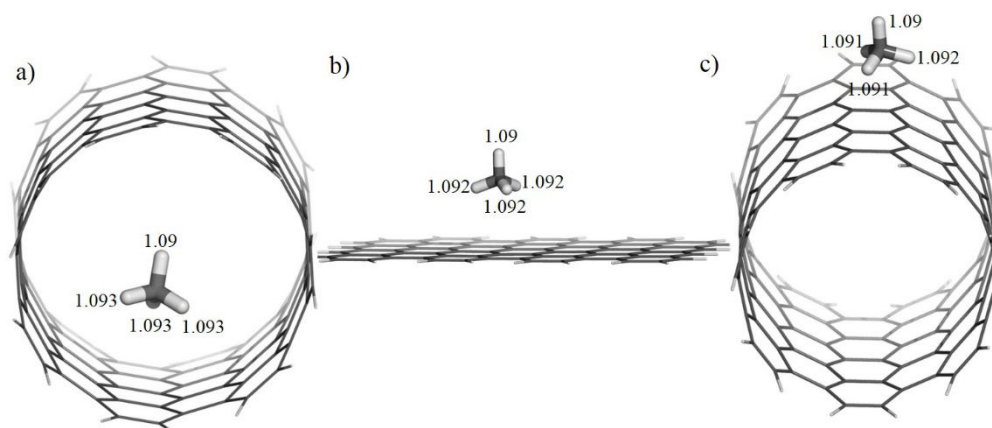


Figure 6.10. The gas phase optimized geometries of methane with concave surface of SWCNT, graphene and convex surface of SWCNT at the M062X/6-31G** level of theory. The values correspond to the C-H bond distances of methane. All the values are in Å. Atom Colors: grey-carbon and white-hydrogen.

The interactions of ethane and methane with CNSs in the solvent phase are almost the same as their corresponding values in the gas phase (Table 6.5). This result is ascribed to the non-polar nature of the solutes, ethane and methane. This is because the loss in solvation enthalpy, in the absence of explicit water molecules, is negligible when the exposure of the non-polar solute to the polar solvent (water, $\epsilon=78.3553$) is limited by the presence of carbon allotropes in its vicinity, in the AAA-CNS complex.

6.3.6 Interaction of Polar Residues with CNS

The interactions of polar but neutral amino acids with the CNS have been modeled with propanamide and propanoic acid. The interaction energy trends are found to be the same as CH- π and π - π interactions (Table 6.6). The amido and carboxylic groups in the optimized geometries of propanamide and propanoic acid complexes, respectively, are oriented almost parallel to the nanosurfaces (see Figure 6.11), which indicates the possibility of occurrence of a π - π type of stacking interactions of the CNS with the planar conjugated amido or acidic groups. To further confirm and quantify the existence of such π - π interactions, the interaction of formic acid (HCOOH) with the CNS has been examined. The alignment of formic acid parallel to all surfaces is a manifestation of the presence of the π - π interactions as an important component in total interaction strength arising from the polar amino acids; the corresponding interaction energy values display similar dependence on curvature effect (Table 6.6). We note that the number of CH- π interactions in methane is closer to that

exhibited by propanoic acid (three for methane on all surfaces; and two and three for propanoic acid in convex surface of SWCNT and graphene, respectively).

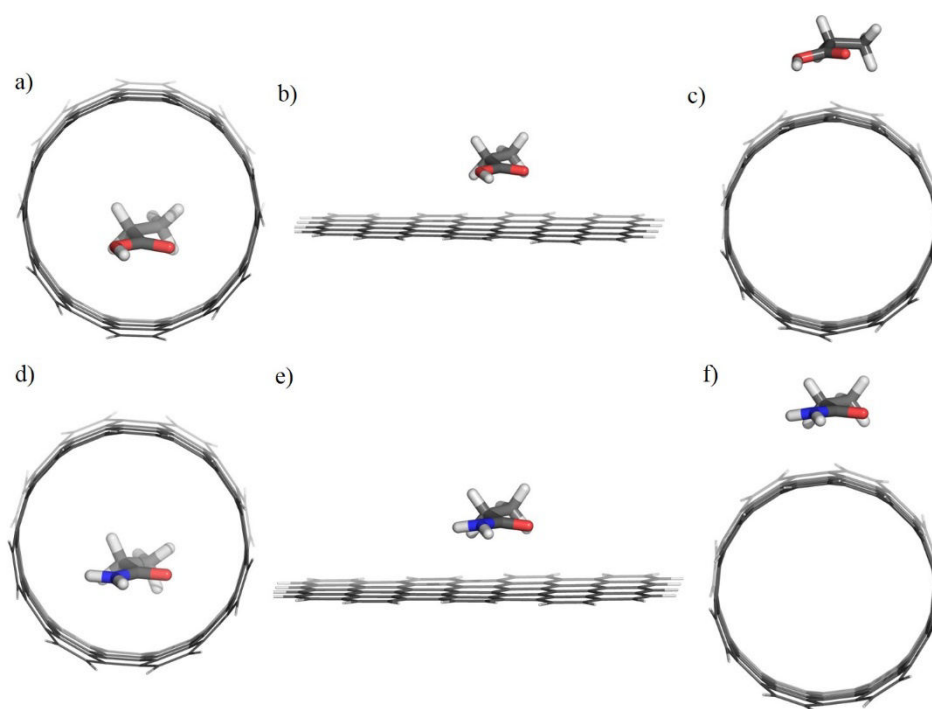


Figure 6.11. The gas Phase optimized geometries of propanoic acid and propanamide with concave surface of SWCNT, graphene and convex surface of SWCNT at the M062X/6-31G** level of theory. The 1st and 2nd columns correspond to the propanoic acid and propanamide respectively. Atom Colors: grey-carbon, white-hydrogen, red-oxygen and blue-nitrogen.

E _i	Propanoic Acid			Propanamide			Formic Acid		
	Concave	Planar	Convex	Concave	Planar	Convex	Concave	Planar	Convex
L ₁	-15.1	-9.4	-8.2	-17.1	-10.5	-8.4	-10.2	-5.9	-4.4
L ₂	-21.9	-12.9	-10.3	-26.4	-14.3	-11.6	-13.8	-7.8	-6.8
L ₃	-18.3	-10.7	-8.9	-20.5	-10.6	-9.4	-11.6	-6.6	-5.0
L ₄	-12.7	-8.5	-7.5	-13.1	-8.7	-7.3	-8.5	-5.0	-3.7
L ₅	-20.0	-12.0	-9.5	-22.9	-12.7	-10.4	-12.3	-6.5	-5.7
L ₆	-15.7	-9.8	-8.2	-16.2	-10.1	-8.3	-9.8	-5.7	-4.1

Table 6.6. Interaction energies of propanoic acid, propanamide and formic acid with carbon nanostructures in kcal mol⁻¹. L₁, L₂, L₃, L₄, L₅ and L₆ correspond the values at the gas/M062X/6-31G**, gas/B3LYP-D2/6-31G**, gas/M062X/6-311G**, CPCM/M062X/6-31G**, CPCM/B3LYP-D2/6-31G** and CPCM/M062X/6-311G** level of theories.

It is assumed here that orientation of CH group has a minimal effect on CH- π interaction. A comparison of interaction energies obtained for propanoic acid and formic acid

and their further comparison with interaction energies of methane on respective surfaces indicates that the π - π stacking interaction is more pronounced than the CH- π interaction in propanoic acid (see Table 6.5 and 6.6), and similarly in the propanamide, a structural and functional analog of the amino acids asparagine and glutamine. Propanoic acid is being taken as an analog of aspartic acid and glutamic acid, as it is being understood that at lower (acidic) pH these amino acids exist in protonated, the acidic form. The same energetic trend, but with smaller magnitudes in energies, is obtained in the solvent phase (Table 6.6), and the trend over the surface is further observed in the reduction in the interaction strength (Table 6.6). The obtained decrease for propanoic acid are -2.9, -0.9, -0.7 kcal mol⁻¹ for concave surface of SWCNT, graphene, convex surface of SWCNT respectively. The greater reduction in interaction strengths for propanamide (-4.0, -1.8 and -1.1 kcal mol⁻¹ on concave surface of SWCNT, graphene and convex surface of SWCNT, respectively) in the solvent phase with respect to their gas phase values is plausibly due to the more polar nature of amido moiety in propanamide compared to the carboxylic moiety of propanoic acid, which comes from the better conjugation of lone pair of electron on nitrogen (of amino group in propanamide; N being a better electron donor than O) than the lone pair of oxygen (of hydroxyl group) atom in the case of propanoic acid. It is well understood that molecules with higher polarity get better solvated in water ($\epsilon = 78.3553$), and any hindrance in solvation by entities such as CNS should cause a reduction in the stabilization energy.

6.3.7 Interaction of Acidic and Basic Residues with CNS

Charged amino acids such as Glutamic acid (Glu), Aspartic acid (Asp), Lysine (Lys), Arginine (Arg) exist mainly in the ionic form in aqueous solution at neutral pH. In a protein at neutral pH, the negatively charged amino acids (Glu, Asp) exist in monoanionic (carboxylate) form whereas the positively charged amino acids (Lys, Arg) exist in monocationic (ammonium or guanidinium) forms. Importantly, it has been shown that the charged amino acids also get adsorbed on the carbon nanosurfaces.^{4, 72, 73} The same is observed in our MD simulation study as well. A full QM geometry optimization of respective charged AAA-CNS complexes in water using the CPCM solvent model implies that trends in interaction energies for cation- π and anion- π interactions are in the same order as was in the cases of π - π stacking and XH- π interactions, *i.e.*, concave surface of SWCNT > graphene > convex surface of SWCNT (Table 6.7).

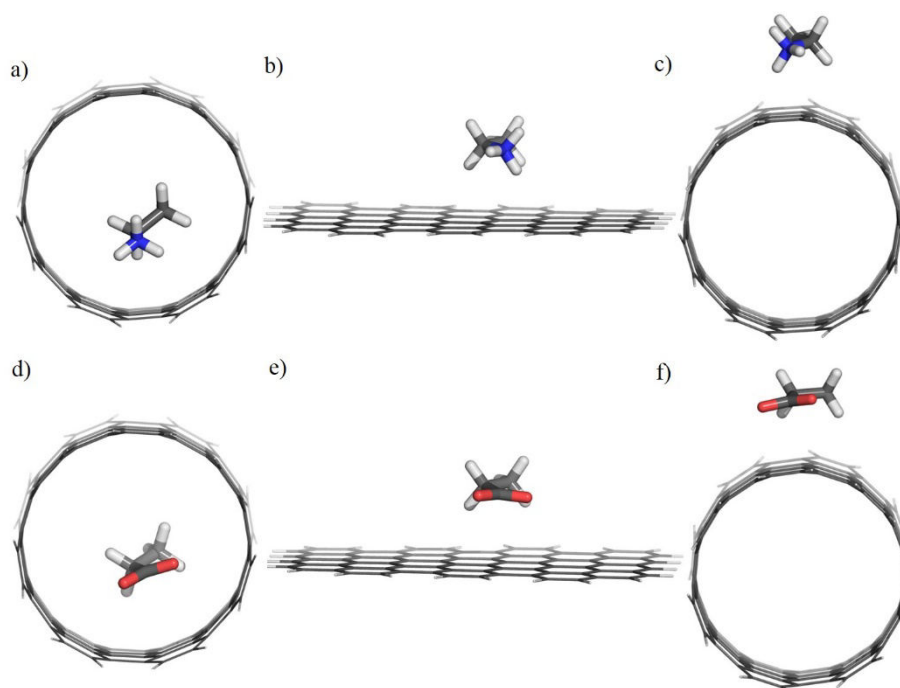


Figure 6.12. The gas phase optimized geometries of ethylammonium and propanoate with concave surface of SWCNT, graphene and convex surface of SWCNT at the CPCM/M062X/6-31G** level of theory. The 1st and 2nd columns correspond to the ethyl ammonium and propanoate respectively. Atom Colors: grey-carbon, white-hydrogen, red-oxygen, and blue-nitrogen.

E_i	Propanoate			Ethylammonium			Ammonium		
	Concave	Planar	Convex	Concave	Planar	Convex	Concave	Planar	Convex
L ₄	-9.1	-5.8	-5.4	-9.1	-5.9	-4.9	-2.9	-1.8	-1.6
L ₅	-17.7	-8.6	-8.2	-18.6	-10.7	-9.5	-7.9	-5.0	-4.4
L ₆	-13.9	-7.9	-6.6	-10.1	-6.4	-5.2	-3.1	-2.0	-1.6

Table 6.7. Interaction energies of propanoate, Ethylammonium and ammonium with carbon nanostructures in kcal mol⁻¹. L₄, L₅, and L₆ correspond the values at the CPCM/M062X/6-31G**, CPCM/B3LYP-D2/6-31G** and CPCM/M062X/6-311G**level of theories.

The optimized geometries are provided in Figure 6.12, a closer inspection of which suggests that the N-H bonds pointing towards the surface get lengthened, as was observed in the case of XH- π interactions. This suggests that the contribution of NH- π interaction in the net stabilization is due to the cation- π interaction. In the ethylammonium-CNS complexes, multiple C-H groups are found directed towards the CNS in interacting fashion. To extricate the interaction caused due to cationic -NH₃⁺ group, we studied independently the interaction of the NH₄⁺ ion with the CNS in water. From the interaction energy table (Table 6.7), we conclude that the cationic NH- π interaction is quite weaker in this complex. At the

CPCM/M062X/6-31G** (L₄) level of theory, the interaction energy of concave surface of SWCNT-NH₄⁺ complex is -2.9 kcal mol⁻¹, whereas the interaction energies with the graphene and the convex surface of SWCNT complex are -1.8 kcal mol⁻¹ and -1.6 kcal mol⁻¹, respectively. NH₄⁺ ion gets more stability (through solvation) when its solvation is not limited by the presence on non-polar materials. Greater restriction (in order of concave > planar > convex) in solvation resulted into greater loss in interaction energies, thus showing that the major contributor in interaction of cationic amino acids with CNSs in a protein is CH- π interactions. Interaction energies of propanoate, an anionic analog of charged amino acids, with CNSs is found to be very close to that of ethylammonium. In all the optimized propanoate-CNS complexes it has been seen that the negatively charged carboxylate group of propanoate is repelled away by the π -electron cloud of nanosurfaces, but by a slightly different magnitude.

6.4 Discussion

6.4.1 Dispersion

The degree and significance of dispersion on interaction of AAA with convex surface of SWCNT and graphene through XH- π and π - π interactions has been established.^{44, 51, 52} To further examine the impact of dispersive forces on interaction of AAA at the inner concave surface of the SWCNT, a geometry optimization of some selected examples of AAA-CNS complexes were also carried out at the B3LYP/6-31G** level of theory in gas phase (or L₇). A comparison of structures and interaction energies obtained at L₇ to those obtained at the dispersion corrected L₂ was performed to understand the impact of dispersion on overall interaction involving the concave surface of SWCNT, in comparison to graphene and convex surface of SWCNT. The E_i obtained at the L₇ are very small as compared to those obtained at the L₂ level of theory (Table 6.8), reflected in the larger AAA-CNS distance at L₇ (see Figure 6.13). This establishes that the dispersion is the prime source of interaction even within the inner surface of SWCNT. A recent Atomic Force Microscopy study at the concave surface of nanostructure support this result.⁷⁴

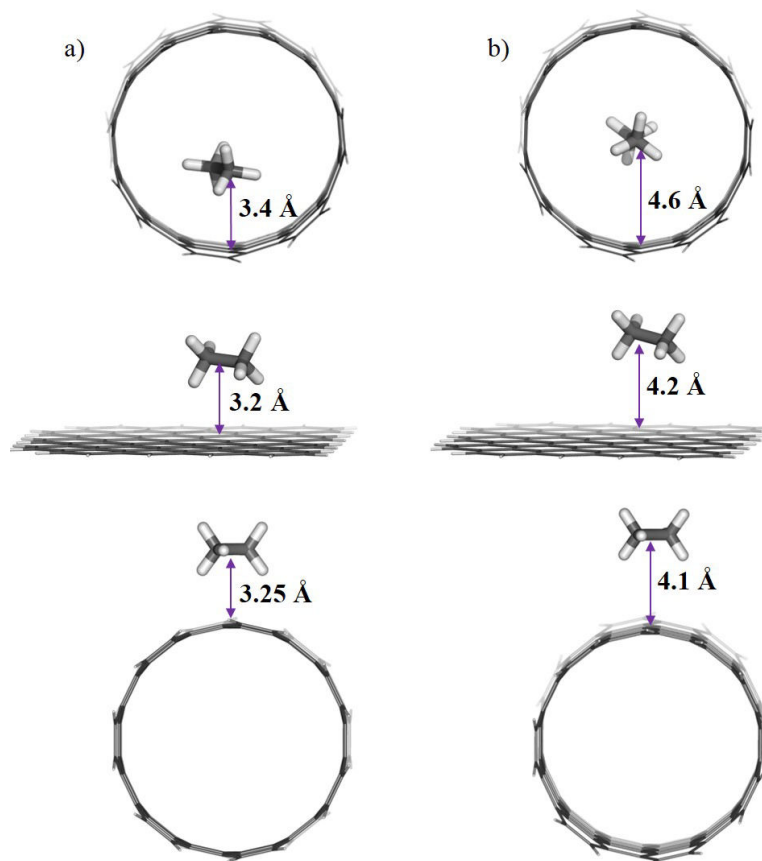


Figure 6.13. The gas phase optimized geometries of toluene with concave surface of SWCNT, graphene and convex surface of SWCNT at the a) dispersion corrected B3LYP-D2/6-31G** and b) B3LYP/6-31G** level of theories. The distances (Å) are calculated normal to the CNSs from the geometrical centers of toluene. Atom Colors: grey-carbon and white-hydrogen.

E_i	Toluene			Ethane			Propanamide		
	Concave	Planar	Convex	Concave	Planar	Convex	Concave	Planar	Convex
L_2	-30.0	-15.6	-12.3	-12.9	-6.4	-5.4	-26.4	-14.3	-11.6
L_7	2.6	0.0	0.0	0.1	-0.1	-0.2	-2.0	-1.1	-1.6

Table 6.8. The interaction energies in kcal mol⁻¹ of toluene, ethane and propanamide with the different CNSs. L_2 and L_7 correspond the values at the gas/B3LYP-D2/6-31G** and gas/B3LYP/6-31G** level of theories.

6.4.2 Molecular Orbital Picture

Highest Occupied Molecular Orbitals (HOMOs) and Lowest Unoccupied Molecular Orbitals (LUMOs) of AAA-CNS complexes are compared with the HOMOs and LUMOs of bare

CNS (see Table 6.9). The HOMO-LUMO gap was found to be unaffected due to the interactions, irrespective of the CNS surface, structure of the amino acid analogs and level of theory used, showing that the adsorption of all type of AAA on all the surfaces of CNS is basically physisorption. This result is in agreement with the prior reports available for the adsorption of AAA on convex surface of SWCNT and graphene.^{45,75, 76}

	Concave	Planar	Convex
Toluene	0.1 (0.2)	-0.1 (-0.1)	0.1 (0.1)
Ethane	0.1 (0.1)	0.0 (0.1)	0.0 (0.1)
Propanamide	0.1 (0.3)	0.0 (0.1)	0.0 (0.0)
Ethylammonium	0.2	0.0	0.2
Propanoate	0.3	0.1	-0.1

Table 6.9. The difference in HOMO-LUMO energy gap in kcal mol⁻¹ of optimized geometries of AAA-CNS complexes and the HOMO-LUMO energy gap of corresponding bare CNSs at the M062X/6-31G** level of theory. Values outside the parenthesis are solvent phase and values inside the parenthesis are gas phase values. Propanaminium-CNS and propanoate-CNS complexes are optimized only in solvent phase.

6.4.3 Molecular Electrostatic Potential Map

Molecular electrostatic potential maps (MESP) illustrate the three-dimensional charge distribution of a molecule. They are generated through values of electron density and visualized through mapping those values on the surface and subsequently defining the molecular boundaries. This method has recently been exploited as an efficient tool to describe the intermolecular interaction in noncovalently bonded molecular complexes.^{77,78} The MESP shown in Figure 6.14 and 6.15 were generated for an isosurface of electron density of AAA and carbon nanostructure complexes using the GaussView software at the M062X/6-31G** (or L₁) and CPCM/M062X/6-31G** (or L₄) level of theories.

The dependence of the interaction energy on the nature of the nanosurface can be attributed to differential π -electron densities originated due to the differential hybridization of the carbon atoms in the graphene (sp^2) and in the carbon nanotube (quasi- sp^2 to sp^3) and available spaces near the surfaces.^{79, 80} Due to the radially directed conjugated π -orbitals, the convex surface experiences a weaker, and the concave surface a higher π -electron density as

compared to the planar graphene surface. It is evident from Figure 6.14 and Figure 6.15 that the mixing of electron density between AAA and CNS are distinctly dependent on the surface curvature. Greater mixing of electron density results in a bigger potential surface, greater molecular volume and higher interaction strength. As the concave surface has the highest mixing of electron density between the interacting fragments (in all the cases), the magnitude of the interaction energy is highest in this case. The subsequent lower mixing of electron density between the interacting fragments on the planar and the convex surfaces results in weaker interactions. The smallest mixing of electron density on the outer surface is manifested in the weakest interaction (smallest magnitude of interaction energy), as revealed in Table 6.3, 6.5, 6.6 and 6.7.

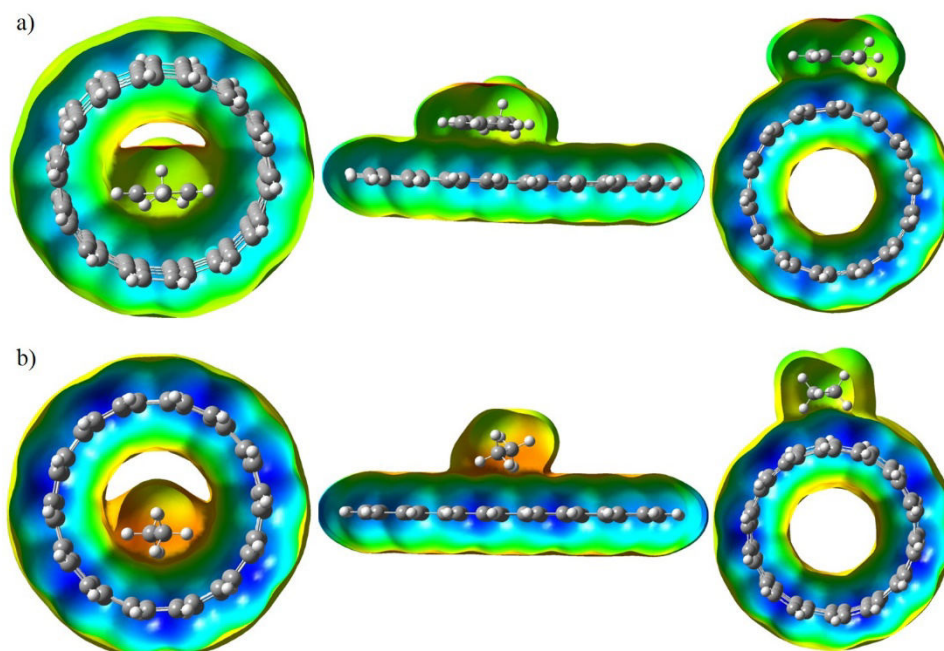


Figure 6.14. Molecular electrostatic potential isosurfaces of a) toluene and b) ethane at the M062X/6-31G** level of theory while in interaction with concave surface of SWCNT, graphene and convex surface of SWCNT respectively from left to right. The blue color indicates large positive potential, the red color indicates large negative potential, whereas yellow and green colors indicate intermediate values.

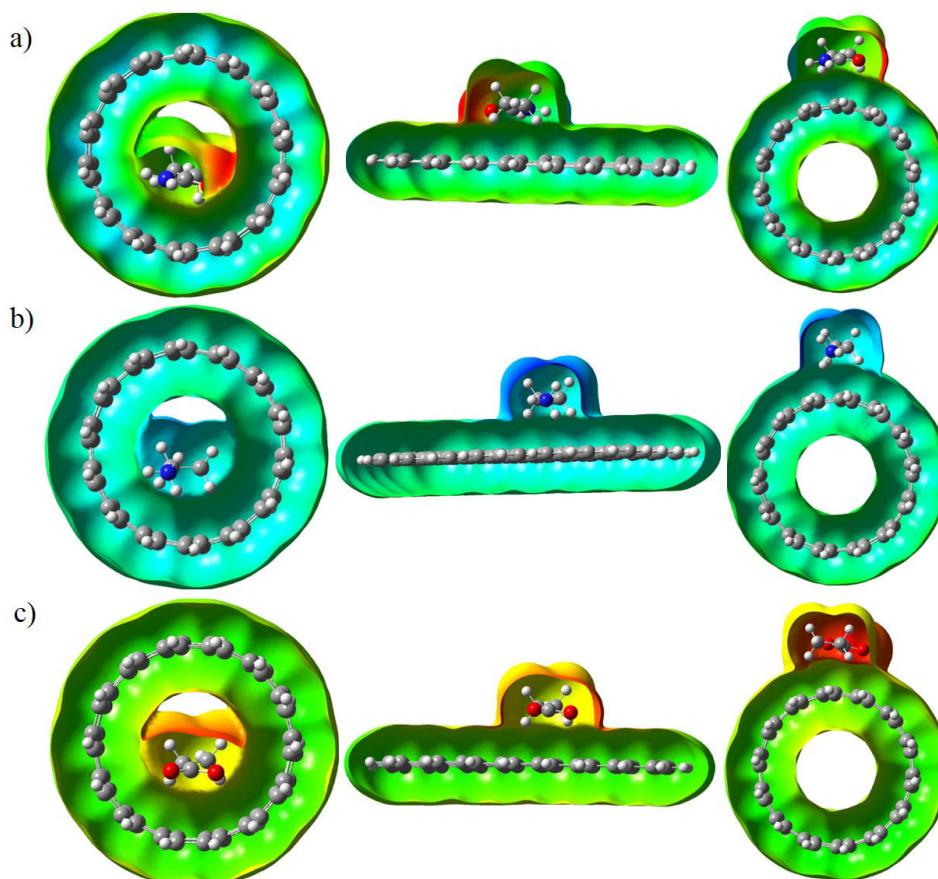


Figure 6.15. Molecular electrostatic potential isosurfaces of a) propanamide, at the M062X/6-31G** level of theory and b) ethylammonium and c) propanoate at the CPCM/M062X/6-31G** level of theory while in interaction with in-SWCNT, graphene and out-SWCNT respectively from left to right at the M062X/6-31G** level of theory. The blue color indicates large positive potential, the red color indicates large negative potential, whereas yellow and green colors indicate intermediate values.

6.5 Summary and Conclusions

In order to gain topographic control of emerging nano-biotechnological materials, it is imperative to develop a detailed understanding of how surface geometry of nanomaterials affect their interactions with biological molecules. Recent studies have shown that the degree of interaction and adsorption of proteins on carbon nanostructures is critically dependent on the surface curvature of these nanomaterials. Using empirical force field based computer simulations, we find that the inner (concave) surface adsorbs a representative amphiphilic peptide most strongly and efficiently, followed by the planar, and the outer (convex) surfaces, in agreement with the findings of recent reports. Representing the chemical space of the naturally occurring amino acids with five structural and functional analogs, we have elucidated the mechanistic underpinnings of the curvature dependence of the interactions with carbon nanostructures with high-level DFT calculations using various levels of theories.

The adsorption of the residues is purely physisorption, and the interaction trends revealed at the different theoretical levels are in excellent agreement with each other, and interestingly, with the trends obtained from atomistic MD simulations. This, and a similar observation reported previously, indicates that the primary interactions between the protein residues and the carbon nanostructures are dispersive in nature. The interactions, found to be strongest at the inner (concave) surface, followed by the planar, and the outer (convex) surfaces, are reflected in the hierarchy of electron density mixing in the molecular electrostatic potential maps.

The present study opens up several key issues pertinent to biomolecular interactions with carbon nanostructures. Firstly, it is established that the overall protein–nanosurface interaction strength should be distinctly curvature dependent, with the strongest interaction on the concave surface, followed by the planar and convex surfaces. Furthermore, this interaction is expected to be the predominant contribution to the overall binding free energy ($\Delta G_{\text{binding}}$), and thereby results in an identical curvature dependence of the latter. Interestingly, the solvation free energy change due to adsorption is found to follow an overall curvature dependent trend that is opposite to that of the peptide–surface interaction, mainly due to the unfavorable solvation free energy change of the polar groups.

The microscopic factors giving rise to these trends; the extent to which these trends are followed by other proteins of dissimilar sizes and sequences; and their association with the curvature dependence of protein structural distortion and are under active investigations in our laboratory. In addition, it would be worthwhile to investigate how suitable functionalizations could be used to alter individual components of the binding free energy, and thereby tune the curvature dependence of protein adsorption on these nanosurfaces. Future studies on these lines are expected to further contribute in the conception and design of tunable bio-nanomaterials for targeted use.

6.6 References

1. G. M. Whitesides, *Nat. biotechnol.*, 2003, **21**, 1161-1165.
2. A. E. Nel, L. Madler, D. Velegol, T. Xia, E. M. V. Hoek, P. Somasundaran, F. Klaessig, V. Castranova and M. Thompson, *Nat. Mater.*, 2009, **8**, 543-557.
3. M. Fakruddin, Z. Hossain and H. Afroz, *J. Nanobiotechnol.*, 2012, **10**, 31.
4. F. De Leo, A. Magistrato and D. Bonifazi, *Chem. Soc. Rev.*, 2015, **44**, 6916-6953.

5. Z. Tang, J. P. Palafox-Hernandez, W.-C. Law, Z. E. Hughes, M. T. Swihart, P. N. Prasad, M. R. Knecht and T. R. Walsh, *ACS Nano*, 2013, **7**, 9632-9646.
6. M. Calvaresi and F. Zerbetto, *Acc. Chem. Res.*, 2013, **46**, 2454-2463.
7. S. Marchesan and M. Prato, *Chem. Commun.*, 2015, **51**, 4347-4359.
8. R. Haggemueller, S. S. Rahatekar, J. A. Fagan, J. Chun, M. L. Becker, R. R. Naik, T. Krauss, L. Carlson, J. F. Kadla, P. C. Trulove, D. F. Fox, H. C. DeLong, Z. Fang, S. O. Kelley and J. W. Gilman, *Langmuir*, 2008, **24**, 5070-5078.
9. C. Merlet, B. Rotenberg, P. A. Madden, P.-L. Taberna, P. Simon, Y. Gogotsi and M. Salanne, *Nat. Mater.*, 2012, **11**, 306-310.
10. K. R. S. Chandrakumar, K. Srinivasu and S. K. Ghosh, *J. Phys. Chem. C*, 2008, **112**, 15670-15679.
11. D. G. A. Smith and K. Patkowski, *J. Phys. Chem. C*, 2014, **118**, 544-550.
12. D. G. A. Smith and K. Patkowski, *J. Phys. Chem. C*, 2015, **119**, 4934-4948.
13. Y. Liu, V. I. Artyukhov, M. Liu, A. R. Harutyunyan and B. I. Yakobson, *J. Phys. Chem. Lett.*, 2013, **4**, 1737-1742.
14. C. Cha, S. R. Shin, N. Annabi, M. R. Dokmeci and A. Khademhosseini, *ACS Nano*, 2013, **7**, 2891-2897.
15. K. Besteman, J.-O. Lee, F. G. M. Wiertz, H. A. Heering and C. Dekker, *Nano Lett.*, 2003, **3**, 727-730.
16. B. Luan and R. Zhou, *J. Phys. Chem. Lett.*, 2012, **3**, 2337-2341.
17. A. K. Jana and N. Sengupta, *Soft Matter*, 2015, **11**, 269-279.
18. C. Sathe, X. Zou, J.-P. Leburton and K. Schulten, *ACS Nano*, 2011, **5**, 8842-8851.
19. C. Li and R. Mezzenga, *Nanoscale*, 2013, **5**, 6207-6218.
20. B. Luan, T. Huynh, L. Zhao and R. Zhou, *ACS Nano*, 2015, **9**, 663-669.
21. M. S. Dresselhaus, A. Jorio, M. Hofmann, G. Dresselhaus and R. Saito, *Nano Lett.*, 2010, **10**, 751-758.
22. Z. Gu, Z. Yang, Y. Chong, C. Ge, J. K. Weber, D. R. Bell and R. Zhou, *Sci. Rep.*, 2015, **5**, 10886.
23. R. S. Kane and A. D. Stroock, *Biotechnol. Prog.*, 2007, **23**, 316-319.
24. A. A. Shemetov, I. Nabiev and A. Sukhanova, *ACS Nano*, 2012, **6**, 4585-4602.
25. P. Asuri, S. S. Karajanagi, H. Yang, T.-J. Yim, R. S. Kane and J. S. Dordick, *Langmuir*, 2006, **22**, 5833-5836.
26. A. S. Campbell, C. Dong, F. Meng, J. Hardinger, G. Perhinschi, N. Wu and C. Z. Dinu, *ACS Appl. Mater. Interf.*, 2014, **6**, 5393-5403.

27. K. Balamurugan, E. R. A. Singam and V. Subramanian, *J. Phys. Chem. C*, 2011, **115**, 8886-8892.
28. M. Radhakrishna and S. K. Kumar, *Langmuir*, 2014, **30**, 3507-3512.
29. N. W. Shi Kam, T. C. Jessop, P. A. Wender and H. Dai, *J. Am. Chem. Soc.*, 2004, **126**, 6850-6851.
30. R. Singhal, Z. Orynbayeva, R. V. Kalyana Sundaram, J. J. Niu, S. Bhattacharyya, E. A. Vitol, M. G. Schrlau, E. S. Papazoglou, G. Friedman and Y. Gogotsi, *Nat. Nano*, 2011, **6**, 57-64.
31. S. A. Andujar, F. Lugli, S. Hofinger, R. D. Enriz and F. Zerbetto, *Phys. Chem. Chem. Phys.*, 2012, **14**, 8599-8607.
32. Z. Fu, Y. Luo, P. Derreumaux and G. Wei, *Biophys. J.*, 2009, **97**, 1795-1803.
33. R. Vácha, S. Linse and M. Lund, *J. Am. Chem. Soc.*, 2014, **136**, 11776-11782.
34. A. K. Jana and N. Sengupta, *Biophys. J.*, 2012, **102**, 1889-1896.
35. A. K. Jana, J. C. Jose and N. Sengupta, *Phys. Chem. Chem. Phys.*, 2013, **15**, 837-844.
36. A. K. Jana and N. Sengupta, *Biophys. Chem.*, 2013, **184**, 108-115.
37. Z. Yang, Z. Wang, X. Tian, P. Xiu and R. Zhou, *J. Chem. Phys.*, 2012, **136**, 025103-025110.
38. N. Thellamurege and H. Hirao, *Molecules*, 2013, **18**, 6782-6791.
39. W. Humphrey, A. Dalke and K. Schulten, *J. Mol. Graphics*, 1996, **14**, 33-38.
40. W. L. Jorgensen, J. Chandrasekhar, J. D. Madura, R. W. Impey and M. L. Klein, *J. Chem. Phys.*, 1983, **79**, 926-935.
41. A. D. MacKerell, D. Bashford, Bellott, R. L. Dunbrack, J. D. Evanseck, M. J. Field, S. Fischer, J. Gao, H. Guo, S. Ha, D. Joseph-McCarthy, L. Kuchnir, K. Kuczera, F. T. K. Lau, C. Mattos, S. Michnick, T. Ngo, D. T. Nguyen, B. Prodhom, W. E. Reiher, B. Roux, M. Schlenkrich, J. C. Smith, R. Stote, J. Straub, M. Watanabe, J. Wiórkiewicz-Kuczera, D. Yin and M. Karplus, *J. Phys. Chem. B*, 1998, **102**, 3586-3616.
42. A. D. Mackerell Jr., M. Feig and C. L. Brooks, *J. Comput. Chem.*, 2004, **25**, 1400-1415.
43. L. KalÈ, R. Skeel, M. Bhandarkar, R. Brunner, A. Gursoy, N. Krawetz, J. Phillips, A. Shinozaki, K. Varadarajan and K. Schulten, *J. Comput. Phys.*, 1999, **151**, 283-312.
44. J.-P. Ryckaert, G. Ciccotti and H. J. C. Berendsen, *J. Comput. Phys.*, 1977, **23**, 327-341.
45. S. E. Feller, Y. Zhang, R. W. Pastor and B. R. Brooks, *J. Chem. Phys.*, 1995, **103**, 4613-4621.
46. U. Essmann, L. Perera, M. L. Berkowitz, T. Darden, H. Lee and L. G. Pedersen, *J. Chem. Phys.*, 1995, **103**, 8577-8593.
47. A. Vergara-Jaque, J. Comer, L. Monsalve, F. D. González-Nilo and C. Sandoval, *J. Phys. Chem. B*, 2013, **117**, 6801-6813.
48. R. D. Gorham, W. Rodriguez and D. Morikis, *Biophys. J.*, 2014, **106**, 1164-1173.

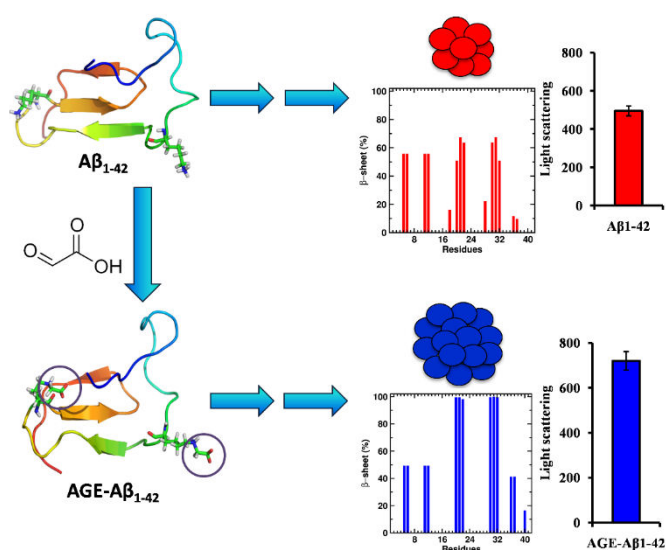
49. D. P. Fernández, Y. Mulev, A. Goodwin and J. L. Sengers, *J. Phys. Chem. Ref. Data*, 1995, **24**, 33-70.
50. L. Zhang, X. Xiao, Y. Yuan, Y. Guo, M. Li and X. Pu, *Sci. Rep.*, 2015, **5**, 9297.
51. D. Umadevi and G. N. Sastry, *J. Phys. Chem. C*, 2011, **115**, 9656-9667.
52. C. Rajesh, C. Majumder, H. Mizuseki and Y. Kawazoe, *J. Chem. Phys.*, 2009, **130**, 124911-124916.
53. D. Umadevi and G. N. Sastry, *Chem. Phys. Chem.*, 2013, **14**, 2570-2578.
54. Y. Zhao and D. G. Truhlar, *J. Phys. Chem. A*, 2006, **110**, 13126-13130.
55. Y. Zhao and D. G. Truhlar, *J. Chem. Physics*, 2006, **125**, 194101.
56. Y. Zhao and D. G. Truhlar, *Theor. Chem. Acc.*, 2008, **120**, 215-241.
57. M. Frisch, G. Trucks, H. Schlegel, G. Scuseria, M. Robb, J. Cheeseman, G. Scalmani, V. Barone, B. Mennucci and G. Petersson, *Gaussian Inc., Wallingford, CT*, 2009, **270**, 271.
58. G. Jindal and R. B. Sunoj, *Angew. Chem. Int. Ed.*, 2014, **126**, 4521-4525.
59. S. Tsuzuki and A. Fujii, *Phys. Chem. Chem. Phys.*, 2008, **10**, 2584-2594.
60. C. A. Hunter and J. K. M. Sanders, *J. Am. Chem. Soc.*, 1990, **112**, 5525-5534.
61. V. Barone and M. Cossi, *J. Phys. Chem. A*, 1998, **102**, 1995-2001.
62. M. Cossi, N. Rega, G. Scalmani and V. Barone, *J. Comput. Chem.*, 2003, **24**, 669-681.
63. X. Li, W. Chen, Q. Zhan, L. Dai, L. Sowards, M. Pender and R. R. Naik, *J. Phys. Chem. B*, 2006, **110**, 12621-12625.
64. G. R. Dieckmann, A. B. Dalton, P. A. Johnson, J. Razal, J. Chen, G. M. Giordano, E. Muñoz, I. H. Musselman, R. H. Baughman and R. K. Draper, *J. Am. Chem. Soc.*, 2003, **125**, 1770-1777.
65. G. Raffaini and F. Ganazzoli, *Langmuir*, 2013, **29**, 4883-4893.
66. J. Anversa and P. Piquini, *Chem. Phys. Lett.*, 2011, **518**, 81-86.
67. L. Piao, Q. Liu and Y. Li, *J. Phys. Chem. C*, 2012, **116**, 1724-1731.
68. L. Piao, Q. Liu, Y. Li and C. Wang, *J. Phys. Chem. C*, 2008, **112**, 2857-2863.
69. D. Zhao, C. Peng and J. Zhou, *Phys. Chem. Chem. Phys.*, 2015, **17**, 840-850.
70. L. Guo, A. Von Dem Bussche, M. Buechner, A. Yan, A. B. Kane and R. H. Hurt, *Small*, 2008, **4**, 721-727.
71. N. M. B. Cogan, C. J. Bowerman, L. J. Nogaj, B. L. Nilsson and T. D. Krauss, *J. Phys. Chem. C*, 2014, **118**, 5935-5944.
72. Z. He and J. Zhou, *Carbon*, 2014, **78**, 500-509.

-
73. E. Wu, M.-O. Coppens and S. Garde, *Langmuir*, 2015, **31**, 1683-1692.
 74. P. Elter, R. Lange and U. Beck, *Colloids Surf., B*, 2012, **89**, 139-146.
 75. C. Wang, S. Li, R. Zhang and Z. Lin, *Nanoscale*, 2012, **4**, 1146-1153.
 76. D. Umadevi, S. Panigrahi and G. N. Sastry, *Acc. Chem. Res.*, 2014, **47**, 2574-2581.
 77. Y. Zhao and D. G. Truhlar, *J. Am. Chem. Soc.*, 2007, **129**, 8440-8442.
 78. R. M. Kumar, M. Elango and V. Subramanian, *J. Phys. Chem. A*, 2010, **114**, 4313-4324.
 79. T. W. Odom, J.-L. Huang, P. Kim and C. M. Lieber, *J. Phys. Chem. B*, 2000, **104**, 2794-2809.
 80. M. Ouyang, J.-L. Huang and C. M. Lieber, *Acc. Chem. Res.*, 2002, **35**, 1018-1025.

Chapter – 7

**Glycation Induces Conformational Changes in Amyloid- β Peptide
and Enhances its Aggregation Propensity: Molecular Insights**

Abstract



Cytotoxicity of the Amyloid beta ($A\beta$) peptide, implicated in pathogenesis of Alzheimer's disease (AD), can be enhanced by its post-translational, non-enzymatic reactions with reducing sugars. However, little is known about underlying mechanisms that potentially enhance cytotoxicity of advanced glycation modified $A\beta$ (or AGE- $A\beta$). In this work, the behavior of suitably glycosylated $A\beta$, benchmarked *in vitro*

against the unglycosylated variety, clearly shows that glycation decreases the lag phase of $A\beta$ nucleation and accelerates fibril formation, while enhancing the overall beta-sheet content and aggregate size. Fully atomistic molecular dynamics (MD) simulations are exploited to obtain direct molecular insights into the process of early $A\beta$ self-assembly in the presence and absence of glycosylated Lysine residues. Analyses of data exceeding cumulative timescales of 1 microsecond for each system reveal that glycation results in stronger enthalpy of association between $A\beta$ monomers, lower conformational entropy in addition to sharp overall increase in the beta-sheet content. Further analyses reveal that the enhanced interactions originate, in large part, due to markedly stronger, as well as new, inter-monomer salt bridging propensities in the glycosylated variety. Interestingly, these conformational and energetic effects are broadly reflected in preformed protofibrillar forms of $A\beta$ small oligomers modified with glycation. Our combined results imply that post-translational glycation modification consolidates $A\beta$ self-assembly regardless of its point of occurrence in the pathway. They provide a basis for further mechanistic studies and therapeutic endeavors that could potentially result in novel ways of combating AGE related AD progression.

7.1 Introduction

Alzheimer's disease (AD) is a progressive neurodegenerative disorder accounting for more than 60% of the dementia cases worldwide.¹ The disease is pathologically characterized by formation of extracellular senile plaques and intracellular neurofibrillary tangles of hyperphosphorylated tau. Senile plaques are mainly composed of amyloid beta ($A\beta$) peptide aggregates which are associated with cell death and dementia. The $A\beta$ peptide is produced by a proteolytic cleavage of a large transmembrane protein, amyloid precursor protein (APP), involving a sequential cleavage by β and γ -secretases.²⁻⁴ However, the presence of effective clearance mechanisms in the normal brain ensures that the concentration of $A\beta$ remains physiologically low.

The $A\beta$ peptide belongs to a class of intrinsically disordered proteins (IDPs) that, unlike globular proteins, do not adopt an unambiguous stable native state under physiological conditions.^{5, 6} The absence of a global native state in IDPs is associated with their higher propensity of self-assembly and their ability to form ordered amyloid fibrils.⁵⁻⁷ The process of $A\beta$ aggregation is highly complex, and is generally considered to involve a nucleated polymerization mechanism.⁸ The aggregates of $A\beta$ may affect a wide range of cellular responses that lead to neuronal insult.⁹ Interestingly, emerging research suggests that the soluble and disordered small oligomeric $A\beta$ species are more neurotoxic than the insoluble fibrils.¹⁰ However, eliciting the structural details of the monomeric and oligomeric species of $A\beta$ are challenging due to their large conformational heterogeneity and high aggregation propensity in aqueous media.^{11, 12} Solution NMR experiments indicate β -strand propensities in the central hydrophobic core ($L_{17}VFFA_{21}$), C-terminal region ($I_{31}IGLMV_{36}$) and ($V_{39}VI_{41}$) in $A\beta_{1-42}$.¹³ Further, stabilization of the turn region is associated with the formation of salt-bridges and result in the most optimal packing of the hydrophobic regions.¹⁴⁻¹⁶ In addition, several research groups have turned to computer simulations to elicit the structural properties of $A\beta$ monomers and smaller oligomers.¹⁷⁻²⁰ Simulation studies using different force fields and sampling protocols indicate that the $A\beta$ monomer is mostly disordered in aqueous media, but with a preference for a hairpin like conformation.^{17, 21} This structure consists of a hydrophilic turn region flanked by hydrophobic β -sheet forming segments comprised of the CHC and the C-terminal regions at either end. Interestingly, recent studies show that chemically constraining the side chains of salt bridge forming residues accelerates $A\beta$ aggregation by stabilizing the β -hairpin structure.¹⁴ Thus, this β -hairpin structure may act as a

seed for further growth of aggregates and reduce the lag phase for fibril formation. We note here that the importance of β -hairpin structures has also been reported in the self-assembly processes of other disease-associated IDPs.^{22, 23}

It has been known for some time that post translational modifications can have profound impact on $A\beta$ neurotoxicity and AD pathogenesis.^{24, 25} Of the several post translational modifications possible, the process of nonenzymatic glycation wherein free amino acid residues especially N- ϵ -amino group of lysine and arginine react with the carbonyl groups of reducing sugars or reactive dicarbonyls like methyl glyoxal or glyoxal, and result in the production of Advanced Glycation End products (or AGEs)²⁶, is emerging to be an important pathway capable of modulating $A\beta$ self-assembly and fibrillogenesis.²⁷ Recent studies suggest that glycated $A\beta$ is significantly more neurotoxic than the unglycated, and may lead to faster AD progression.^{27, 28} This aspect is further important in light of the identification of diabetes as major risk factors for AD.²⁹⁻³¹ The AD brain shows elevated levels of AGEs and Receptors for Advanced Glycation End products (RAGE) that are similar to those found in diabetics. AGE formation leads to several types of cellular damage including altered protein structure and activity, increased protein aggregation and fibril formation, and RAGE activation.³²⁻³⁵ RAGEs can potentially interact with AGEs, $A\beta$ and AGE- $A\beta$ complexes leading to activation of signal transduction pathways associated with progression of AD.³² Further, AGE- $A\beta$ formation may increase the protease resistance of $A\beta$ that may potentially lead to its accumulation and hence advancement of AD.

Despite its emerging relevance in AD progression, to the best of our knowledge, currently there are no studies at the molecular level aimed at understanding the effects of glycation modifications on the structural, self-assembly and aggregation propensities of the $A\beta$ peptide. In the present study, we have first performed benchmark *in vitro* studies with ThioflavinT (ThT) binding fluorescence studies, circular dichroism (CD) and light scattering to evaluate the effects of $A\beta_{1-42}$ glycation on the peptide's structure and fibrillogenesis propensities. These studies revealed that the peptide's glycation resulted in distinctly faster rates of fibril formation along with greater beta-sheet propensities and larger aggregate sizes. For direct mechanistic insights, we evaluated the early self-assembly propensity as well as protofibrillar stability of partially carboxymethylated $A\beta_{1-42}$ peptide, with extensive, fully atomistic molecular dynamics (MD) simulations. Here, we point out that carboxymethylation, a predominant glycation modification *in vivo*,³⁶ was used to evaluate the influence of

glycation on the A β ₁₋₄₂ aggregation propensity. Hence lysine residue of A β was carboxymethylated and MD simulations were carried out.

Our simulations reveal that dimerization occurs more rapidly and with stronger interactions in the presence of a glycosylated A β ₁₋₄₂ peptide. Further, trimerization resulting from the addition of a second glycosylated peptide results in more strongly bound assemblies with a significantly larger number of inter-peptide contacts and clear enhancement in β -sheet propensities. It is found that charged interactions play a major role in the increased stabilities, with inter-peptide salt bridges involving (E²²-K²⁸), (D²³-K²⁸), (E¹¹-K¹⁶), (R⁵-D⁷) and (R⁵-E²²) getting significantly strengthened. Interestingly, we also observed a clear emergence of salt bridging propensity between (R⁵-K¹⁶), which is precluded in the unglycosylated system. Finally, we found marked similarities between these observations and those found in the case of a partially glycosylated protofibrillar construct of the A β ₁₋₄₀ peptide. Our results provide important insights into the mechanisms via which glycation can affect key elements along the A β amyloidogenesis pathways, and thereby the AD progression.

7.2 Methods

7.2.1 Experimental Methods

Materials. Thioflavin-T, A β ₁₋₄₂ peptide, sodium cyanoborohydride, ammonium hydroxide, glyoxylic acid, and phosphate buffer components were procured from Sigma-Aldrich. 3 kD cut-off filters were purchased from Millipore (Millipore, India). Water used in experiments was purified by Millipore purification system (Millipore, India).

Preparation of AGE-A β ₁₋₄₂. Modified method of Korwar *et.al.* was adopted to synthesize AGE-A β ₁₋₄₂.³⁷ A β ₁₋₄₂ was dissolved in ammonium hydroxide and briefly sonicated. AGE modified A β ₁₋₄₂ (AGE-A β ₁₋₄₂) was synthesized by incubating A β ₁₋₄₂ (22 μ M) with sodium cyanoborohydride (0.150 M) and glyoxylic acid (0.045 M) in sodium phosphate buffer (0.2 M, pH 7.4). The solution was incubated in dark for 24 h at 37°C and washed extensively to remove sodium cyanoborohydride and glyoxylic acid.

AGE Fluorescence Assay. AGE associated fluorescence was measured using Varioskan plate reader (Thermo Scientific, Finland) at 37°C. A β ₁₋₄₂ and AGE-A β ₁₋₄₂ samples were added to 96 well plate (black with flat bottom, corning) and fluorescence intensity was measured with excitation of 370 nm and emission was scanned from 400 nm to 540 nm.

Incubation Assays. A β_{1-42} and AGE-A β_{1-42} solution was sonicated briefly and centrifuged at 20,000g for 10 min to remove large insoluble aggregates. The supernatant containing monomeric A β_{1-42} and AGE-A β_{1-42} was then diluted in PBS to 22 μ M. These samples were then incubated at 37 °C for 48 h to perform CD spectroscopy and Static light scattering assays.

Thioflavin-T Fluorescence Assay. A β aggregation was monitored by Thioflavin T fluorescence assay. 50 μ l (22 μ M) of A β_{1-42} or AGE-A β_{1-42} sample was mixed with 150 μ l of Thioflavin T (ThT) solution (50 μ M ThT in PBS pH 7.0) in 96 well plate (black with flat bottom, Cornings). Fluorescence was recorded subsequently at excitation and emission wavelengths of 440 and 485 nm, respectively, using Varioskan plate reader (Thermo Scientific, Finland)

Circular Dichroism (CD) Spectroscopy. The CD spectra of A β_{1-42} and AGE-A β_{1-42} (50 μ g/ml) were recorded in wavelength range of 190-250 nm on a Jasco-J815 spectropolarimeter at room temperature. Each CD spectrum was accumulated from three scans at 50 nm/min with cell path length of 0.1 cm. CD signals from buffer were subtracted from the sample spectra and converted to mean residual ellipticity (MRE) in deg cm² dmol⁻¹ defined as,

$$MRE = \frac{M\theta_{\lambda}}{10dcr}$$

Here, M is the molecular weight of the protein, θ_{λ} is CD in millidegree, d is the path length in cm, c is the protein concentration in mg/ml and r is the number of amino acid residues in the protein.

Light Scattering Analysis. A β_{1-42} and AGE-A β_{1-42} aggregates were detected by static light scattering method using a Perkin-Elmer Luminescence spectrometer LS50B. Samples were diluted to 10 μ M in Milli Q water and spectra were acquired. Both excitation and emission wavelengths were set at 400 nm, excitation and emission slit width was set to 8 nm and 2.5 nm, respectively and scattering was recorded for 60 sec with the interval of 0.1 sec.

7.2.2 Computational Methods

Unglycated and Glycated A β Conformations

Details of full-length A β_{1-42} monomer structure generation with extensive MD simulations were reported in our previous study.³⁸ The calculated mean ¹⁵N and ¹³C $_{\alpha}$ chemical shifts using

the SHIFTS program³⁹ were compared with corresponding experimental data.¹³ Our higher β -strand content at the CHC and C-terminal domains are consistent with previously reported experimental and simulation data.^{13, 40-42} The dimerization data presented here corresponds to the self-assembling propensity of this highly probable conformation. A glycosylated and an unglycosylated monomer were placed at a center of mass distance of 33 Å at varying relative orientations to obtain a cumulative simulation data of 0.6 μ s. As in the previous work³⁸, a dimeric cluster selected *via* Cartesian principal component analysis (PCA) was allowed to associate with a second glycosylated monomer at varying relative orientations; a cumulative data of 1.0 μ s was obtained for these trimerization simulations. In addition, we have obtained a trimeric form of A β ₁₋₄₀ from the PDB structure 2M4J, obtained from the brain tissues of AD patients using solid-state nuclear magnetic resonance (ssNMR) and electron microscopy.⁴³ In this fibrillar model, a twist in residues F19-D23, a kink at G33, and a bend at G37-G38 facilitate contact between the peptide units. For generating glycosylated A β oligomers in this system, we have modified the K¹⁶ and K²⁸ of the two edge peptides in the trimer to N(6)-carboxymethyllysine; a cumulative data of 1.0 μ s was obtained for these systems.

MD Simulation Protocol

Molecular dynamics (MD) simulations with the NAMD simulation package,⁴⁴ using the CHARMM22 force field with the CMAP correction^{45, 46} for the protein, and the TIP3P water model⁴⁷ for the solvent. The force field parameters for the glycosylated residues were obtained by using the SwissPARAM webserver⁴⁸, which generates parameters that are consistent with the CHARMM force field. The partial charges were further refined by density functional theory (DFT) calculations using the Gaussian09 package. This strategy has recently been employed in several studies.^{49, 50} Each system was placed in a simulation box such that the minimum distance between a protein atom and a box edge was 15 Å. Requisite counter ions were added to neutralize the system, and three-dimensional orthorhombic periodic boundary conditions were applied. Each system was first energy minimized for 10 000 steps with the conjugate gradient method, followed by simulations in the isothermal-isobaric (NPT) ensemble at constant temperature, using a timestep of 2 fs. Langevin dynamics was used to maintain a constant temperature of 310 K using a collision frequency of 1 ps⁻¹, and a 1 atm pressure was maintained with the Nose-Hoover method.^{51, 52} SHAKE⁵³ was used to constrain bonds involving hydrogen atoms, and electrostatic interactions calculated with the particle-mesh

Ewald technique.⁵⁴ The non-bonded interactions were cut off at 12 Å, with smoothing starting at 10.5 Å.

Analyses of Simulation Data

Principle Component Analysis. Cartesian principle component analysis (cPCA), as implemented in the CARMA package⁵⁵, was used to cluster the data obtained from the cumulative MD data generated for each system. The first 100 ns of simulated data were not considered, and the translation and rotational degrees of freedom were first removed before this analysis. The ensembles were then projected onto the first (PC1) and the second (PC2) principal components, using an RMSD cutoff of 2.4 Å for the C_α atoms. The most populated cluster on this landscape was used for further analyses.

Secondary Structure. Structural propensities for individual residues were obtained with the STRIDE algorithm⁵⁶ as implemented in the VMD package⁵⁷.

Amino Acid Contacts and Salt Bridges. Two residues were considered to make contact if their terminal heavy atoms were within 7 Å in a given conformation. Inter-monomer contact probability maps were thus constructed for the dimeric and trimeric systems. A pair of positively and negatively charged residues was considered to make salt bridges if the hydrogen attached to the donor atom approached the acceptor atom 5 Å.

Solvent Accessible Surface Area (SASA). The SASA is calculated within the VMD package with a spherical probe of diameter 1.8 Å.

Energetics. Interaction energies between the peptide units, and its constituents, were calculated with the NAMD Energy plugin.

Configurational Entropy. The configurational entropy of the peptide units, after removal of the translational and rotational degrees of freedom, is calculated with the Schlitter's method⁵⁸ as implemented in the CARMA package.⁵⁵ According to this method, the absolute configurational entropy can be approximated as,

$$S_{abs} < S = \frac{1}{2} k_b \ln \det \left[1 + \frac{k_b T e^2}{h^2} M^{1/2} \sigma M^{1/2} \right]$$

Here, k_b is the Boltzmann's constant; T the temperature in absolute units; e is the Euler's number; h is Planck's constant divided by 2π , M is the $3N$ dimensional mass matrix containing N atomic masses of the system considered; and σ is the covariance matrix whose elements are calculated as,

$$\sigma_{ij} = \left\langle \left(x_i - \langle x_i \rangle \right) \left(x_j - \langle x_j \rangle \right) \right\rangle$$

7.3 Results and Discussion

7.3.1 Glycation Promotes A β Aggregation.

We first synthesized glycosylated A β_{1-42} by incubating it with the glycosylating agent, glyoxylic acid. Glyoxylic acid modifies basic amino acid residues like lysine mainly resulting in the formation of carboxymethyl lysine (CML)³⁷, a predominant glycation modification³⁶ in living system. Glycosylated proteins show characteristic emission at 440 nm upon excitation at 370 nm.⁵⁹ glycosylated A β_{1-42} spectrum shows increase in AGE specific fluorescence with λ_{max} emission at 440 nm which confirms the formation of AGEs, whereas there is no AGE associated fluorescence in the unglycosylated A β_{1-42} sample (Figure 7.1A).

To study A β aggregation, Thioflavin T binding assay was performed. Thioflavin T is known to bind hydrophobic regions of A β aggregates, resulting in enhanced fluorescence emission.⁶⁰ Both A β_{1-42} and glycosylated A β_{1-42} samples showed time dependent increase in ThT fluorescence signifying incubation dependent increase in aggregation (Figure 7.1B). However, glycosylated A β_{1-42} shows significantly higher ThT fluorescence than A β_{1-42} suggesting increased propensity of glycosylated A β_{1-42} to aggregate than A β_{1-42} only. To further gain an insight about change in secondary structure of A β_{1-42} and glycosylated A β_{1-42} , CD spectroscopy was performed. CD spectra evidently demonstrated decrease in the minima at 220 nm in glycosylated A β_{1-42} representing higher β sheet formation upon glycation (Figure 7.1C). These results were further corroborated with static light scattering assay. Light scattering is directly proportional to size of aggregates⁶¹, as expected the scattering was found to be more in glycosylated A β_{1-42} sample than only A β_{1-42} signifying larger A β aggregates in glycosylated A β_{1-42} (Figure 7.1D). These *in vitro* observations lead us to infer that glycation promotes β -sheet formation and increases A β_{1-42} aggregation propensity eventually leading to larger A β_{1-42}

aggregates. In the following sections, we report our MD simulations based mechanistic investigations of the potential underlying factors responsible for the enhanced self-assembly and aggregation of the partially glycosylated A β peptide and its complexes.

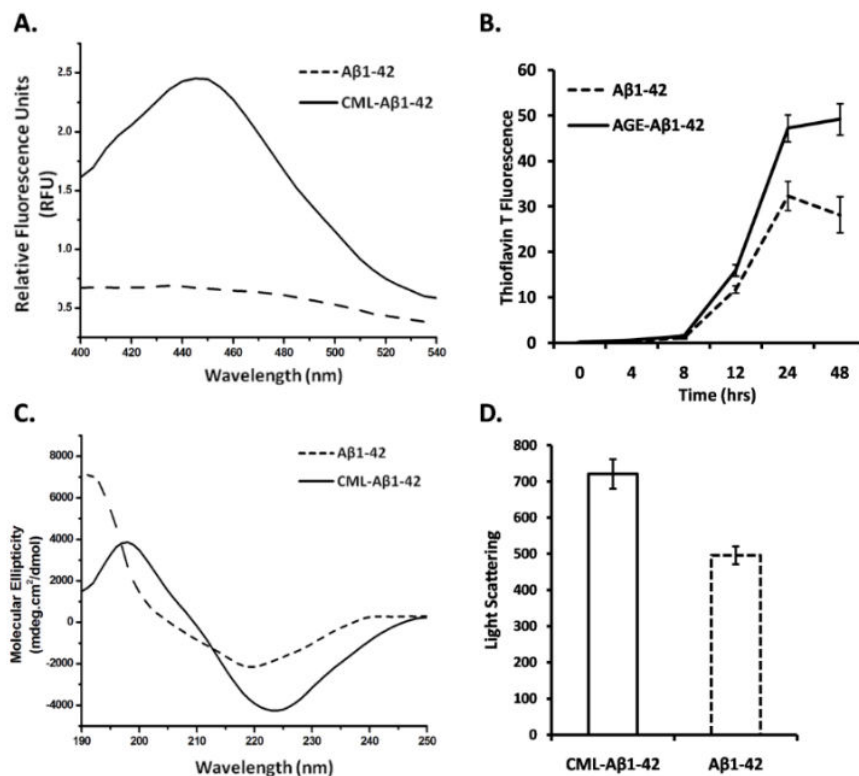


Figure 7.1. A) Fluorescence emission of A β (dotted line) and glycosylated A β (solid line) with excitation at 370 nm and emission scan from 400 to 540 nm. B) Kinetics of A β ₁₋₄₂ (dotted line) and glycosylated A β ₁₋₄₂ (solid line) aggregation by Thioflavin T assay. C) CD spectra depicting the mean residual ellipticity of A β ₁₋₄₂ (dotted line) and glycosylated A β ₁₋₄₂ (solid line). D) A bar graph representing scattering of light due to A β ₁₋₄₂ (dotted line) and glycosylated A β ₁₋₄₂ (solid line) aggregates.

7.3.2 Early Oligomerization.

In our *in silico* studies, we begin first by comparing the spontaneity of early oligomerisation of the full length A β with that of the glycosylated A β . The glycosylated monomer (see Figure 7.2) was generated by modifying the Lysine residues at positions 16 and 28 to N(6)-carboxymethyllysine. In Figure 7.3a and b, we present the temporal evolution of the total inter-monomer interactions (E_{1-2}) for the unglycosylated and glycosylated dimer averaged over multiple simulation trajectories. The mean values of E_{1-2} for the unglycosylated and glycosylated dimer over the last 40 ns of the simulation trajectories are $-193.7 (\pm 45.1)$ and $-276.1 (\pm 50.1)$ kcal mol⁻¹, respectively. Highly populated structural ensembles of unglycosylated and glycosylated

dimer were selected *via* Cartesian principal component analysis (cPCA), and the trimeric structural ensemble was obtained by placing a third monomer at center of mass distances of 33 Å from the resultant dimer at varying orientations. Figure 7.3c and d depict the temporal evolution of the total inter-monomer interactions (E_{1-2-3}) for the unglycated and glycated trimer averaged over multiple simulation trajectories. Here we point out that A β assembly is characterized by large degrees of structural and interaction heterogeneity, and PCA has been broadly accepted for determining the important conformations and interaction modes of such systems via simulation data.¹⁸ In Figure 7.4 we present snapshots of the representative conformations of the highly populated structural ensembles of unglycated and glycated A β trimer.

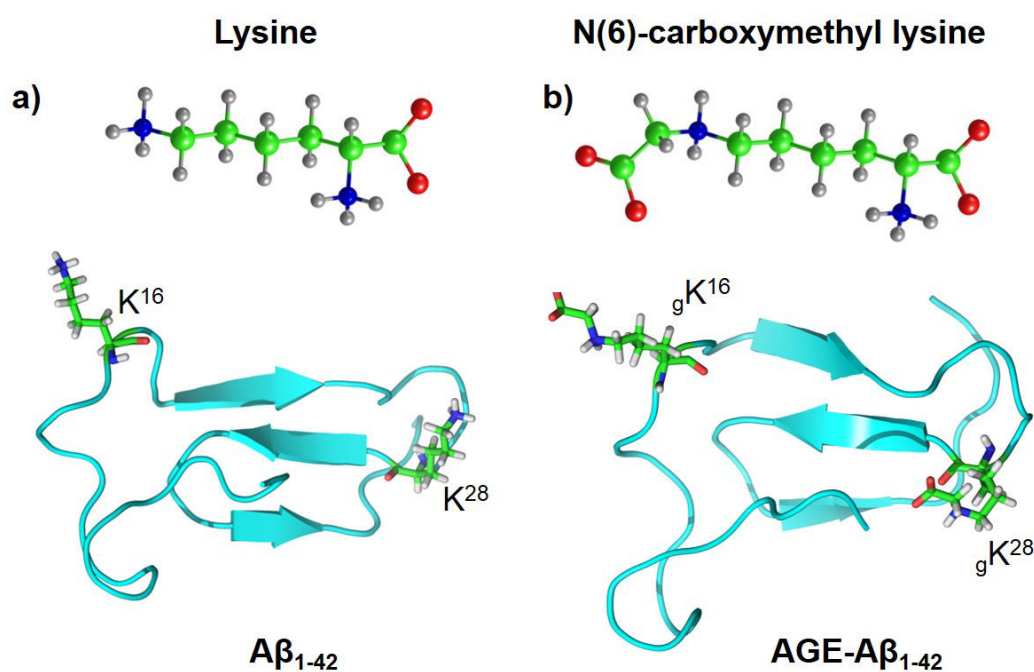


Figure 7.2. Initial structures of (a) unglycated and (b) glycated (AGE-A β ₁₋₄₂) A β monomer. K¹⁶ and K²⁸ residues were glycated (carboxymethylated) and are shown in stick representation. Side chain of lysine (K) and N(6)-carboxymethyl lysine (_gK) are also shown.

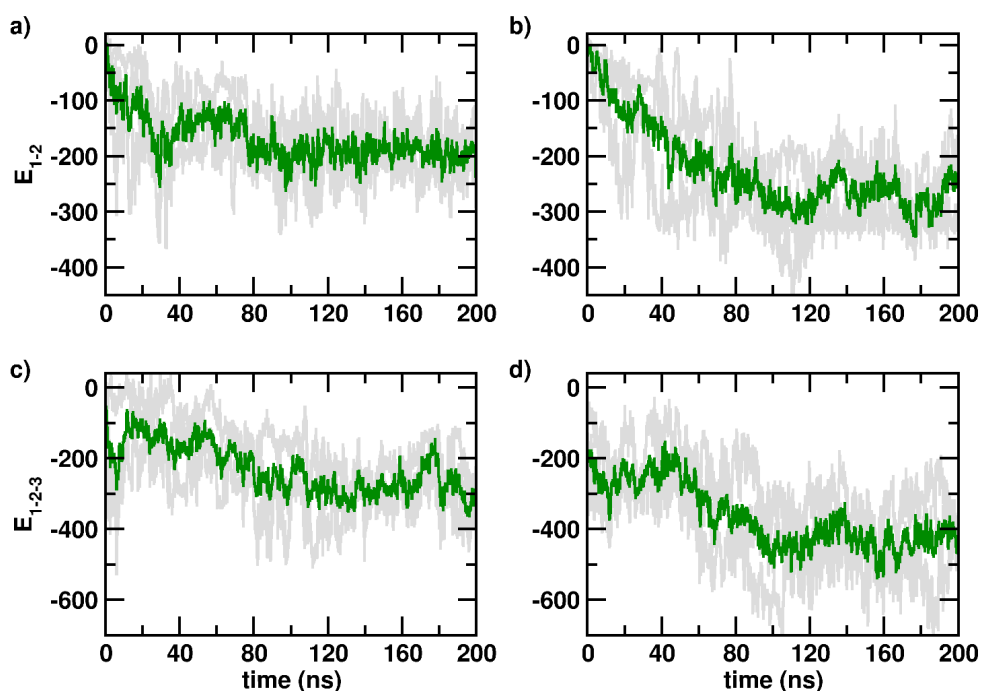


Figure 7.3. Time evolution of the total inter-monomer interaction energies in dimerizing (E_{1-2}) and trimerizing ($E_{1-2,3}$) simulations for unglycated (left column) and glycated (right column) A β trimer. Energies are in units of kcal mol⁻¹. Evolutions over individual trajectories are depicted in gray, and their averages are depicted in green.

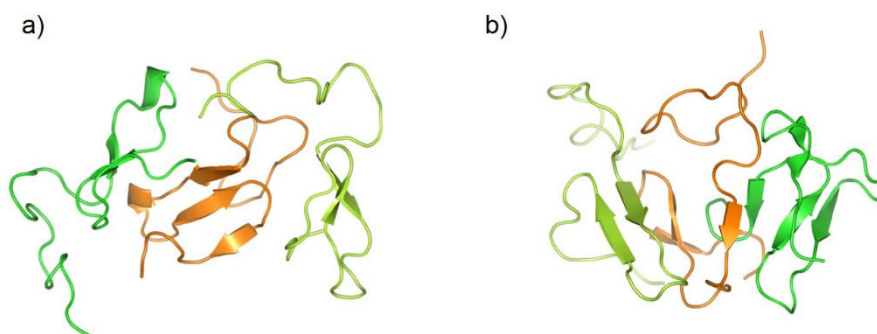


Figure 7.4. Representative snapshots of the highly populated structural ensembles of a) unglycated and b) glycated A β trimer.

We next analyzed the secondary and tertiary structures of the dominant conformations of the unglycated and glycated trimer. Residue-wise secondary structural propensities were calculated using STRIDE algorithm.⁵⁶ Tertiary structures are analyzed from the network of backbone and side chain contacts. In Figure 7.5a, we represent the residue-wise β -sheet percentage of unglycated and glycated systems. The β -strands are mostly localized in three regions: the N-terminal region (residues 5–6 and 11–12), CHC-turn region (residues 20–22) and the C-terminal (residues 30–32 and 36–37) region. Notably, the β -strand propensities of

the glycated system is significantly higher at the CHC-turn and C-terminal region and marginally lower in the N-terminal region compared to the unglycated system. The increase of β -sheet at the CHC and the C-terminal regions indicate that glycation decreases the initial lag phase for aggregation. Overall, the β -sheet percentages in the unglycated and glycated systems are 15.0 and 21.2 % respectively, in qualitative agreement with CD and ThT binding fluorescence assay, showing that glycation results in increased β -sheet propensity of small oligomers.

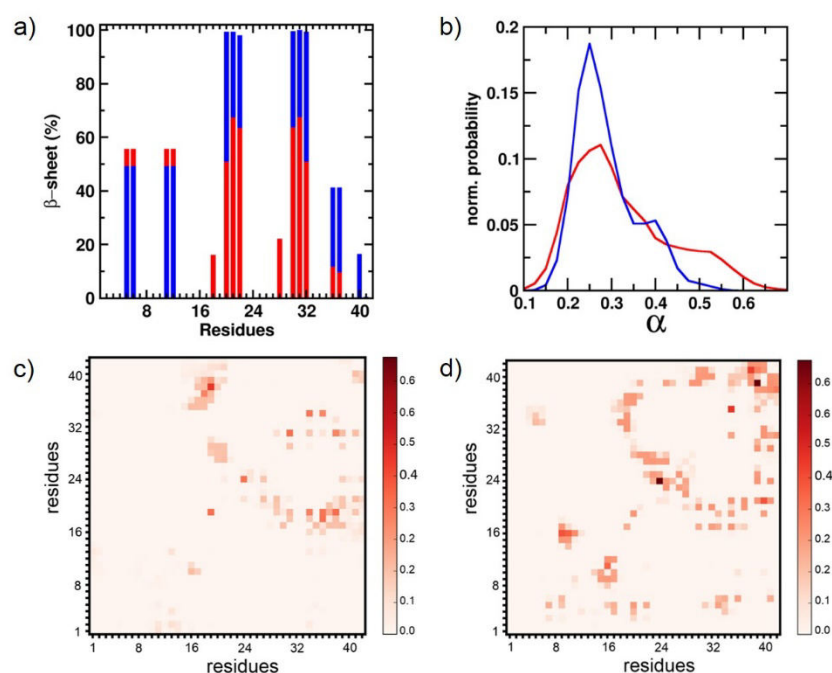


Figure 7.5. a) Residue-wise β -sheet (%) and b) distributions of asphericity (α) for unglycated (in red) and glycated (in blue) $A\beta$ trimer. Residue-residue contact probabilities for c) unglycated and d) glycated systems. In the contact maps, lower triangles display probabilities of inter-residue sidechain-sidechain contacts, while the upper triangles display probabilities of inter-residue backbone-backbone contacts.

We have investigated the effect of glycation on the size or compactness of the unglycated and glycated $A\beta_{1-42}$ systems by evaluating the ‘asphericity’ α , defined as $\alpha = 1 - (I_{min}/I_{max})$, where I_{max} and I_{min} , are the maximum and minimum values, respectively, of the principal moments of inertia of the system. When $I_{max} = I_{min}$ and $\alpha = 0$, the system is a perfect sphere, whereas increasing α indicates lowering of the compactness. We have shown α distributions for the unglycated and glycated system in Figure 7.5b. The mean values of α for the unglycated and glycated system are $0.3 (\pm 0.1)$ and $0.2 (\pm 0.07)$ respectively, showing that the glycation had a minimal effect on the size of the oligomer.

In order to evaluate the effects of glycation on the inter-monomer associations, we compare the inter-residue contact probabilities for the unglycated and glycated systems in Figure 7.5c and d. The lower triangles of the contact maps display probabilities of inter-residue sidechain-sidechain contacts, while the upper triangles display probabilities of inter-residue backbone-backbone contacts. The region with the highest contact density for the glycated system is the CHC/C-terminal (residues 17–20/30–41) and C-terminal/C-terminal (residues 35–42/35–42). The CHC/CHC (residues 19–20/19–20) regions also display high contact density. In comparison, these contacts are significantly weaker in unglycated A β oligomer system. The emergence of N-terminal/N-terminal, N-terminal/CHC and N-terminal/C-terminal contacts are additionally observed in the glycated system, but are absent in the unglycated A β oligomer.

To compare the conformational rigidity, we estimated the cumulative configurational entropy per C_{α} atom of the unglycated and glycated system using Schlitter's method described earlier. The results are shown in Figure 7.6. The mean configurational entropy per C_{α} atom for the unglycated and the glycated systems, averaged over the last 2 ns, is 39.3 and 38.3 J K $^{-1}$ mol $^{-1}$, respectively. The configurational entropy per C_{α} atom was higher for unglycated system compared to the glycated system. It is observed that the glycated system has relatively high number of inter-residue contact and stronger inter-protein interaction compared to the unglycated system; this is reflected in the lower configurational entropy.

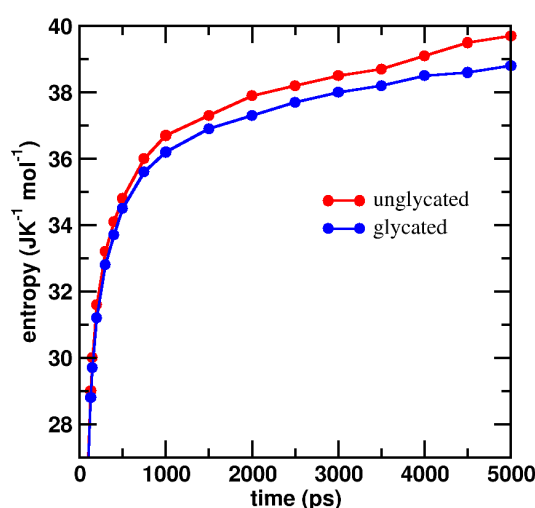


Figure 7.6. Cumulative configurational entropy per C_{α} atom of the unglycated and glycated A β trimer.

7.3.3 Glycation Strengthens Inter-Protein Association.

We present the normalized distribution of total inter-monomer interactions and their electrostatic and van der Waal components for the unglycated and glycated trimeric A β systems in Figure 7.7a, b and c; in Table 7.1, we have reported mean values of each and the corresponding difference in energy between the glycated and the unglycated systems. In both the unglycated and the glycated systems, the interactions are dominated by electrostatic interactions, which accounts for about 63% of the energy difference between the two systems. While the van der Waal component is significantly weaker, we note that this interaction is also ~ 46 kcal mol $^{-1}$ stronger in the glycated trimeric system compared to the unglycated trimer.

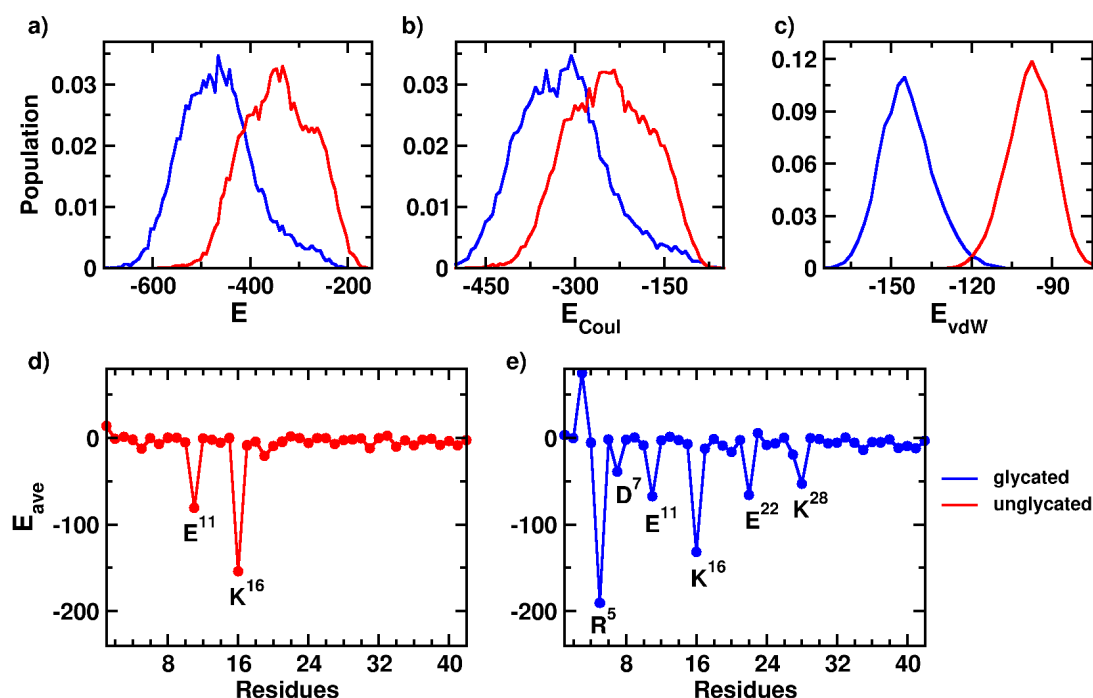


Figure 7.7. Distributions of inter-monomer a) non-bonded (E); b) electrostatic (E_{Coul}); and c) van der Waal (E_{vdW}) interaction energies for the unglycated and glycated A β trimer. Residue-wise average nonbonded interaction energy (E_{ave}) for d) unglycated, and e) glycated systems. Energies are in units of kcal mol $^{-1}$. The residues with strong interactions are denoted with one letter code of respective amino acids.

	E_u	E_g	ΔE
nonbonded	-344.7 (\pm 70.3)	-468.2 (\pm 76.5)	-123.5
electrostatic	-245.2 (\pm 69.0)	-322.8 (\pm 75.4)	-77.6
van der Waal	-99.5 (\pm 8.5)	-145.3 (\pm 9.8)	-45.8

Table 7.1. Mean values of inter-monomer non-bonded, electrostatic and van der Waal interaction energies for unglycated (E_u) and glycated (E_g) A β trimer, and corresponding difference in energy (ΔE) between the unglycated and glycated systems. Energies are in units of kcal mol⁻¹. Standard deviations are provided within braces.

To identify the key interacting residues, we provide an average residue-wise breakdown of the total inter-peptide interaction energy in Figures 7.7d and e. Interestingly, we found that in both unglycated and glycated A β small oligomeric assemblies, the charged residues exhibit significantly stronger interactions compared to the hydrophobic and polar residues. This was further corroborated when we considered inter-protein residue wise contact energy map corresponding to the maximum interaction energy (shown in Figure 7.8), and its electrostatic and the van der Waals components (shown in Figure 7.9). It was noteworthy here that interactions arising from the salt-bridge forming residues in the turn and the N-terminus regions gave rise to the strongest interactions in the glycated A β systems, compared to the unglycated A β systems.

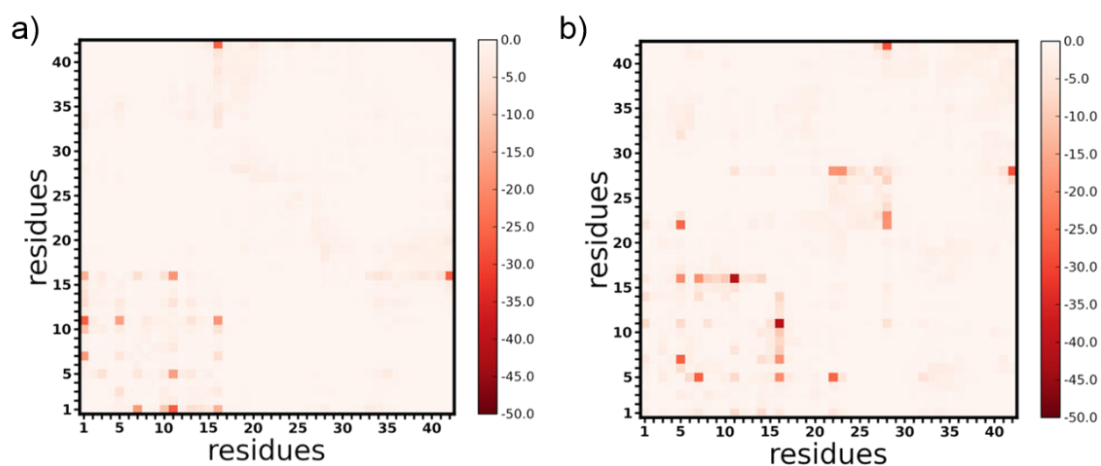


Figure 7.8. Residue specific inter-monomer maximum nonbonded interaction energies (in kcal mol⁻¹) of unglycated (left column) and glycated (right column) A β trimer.

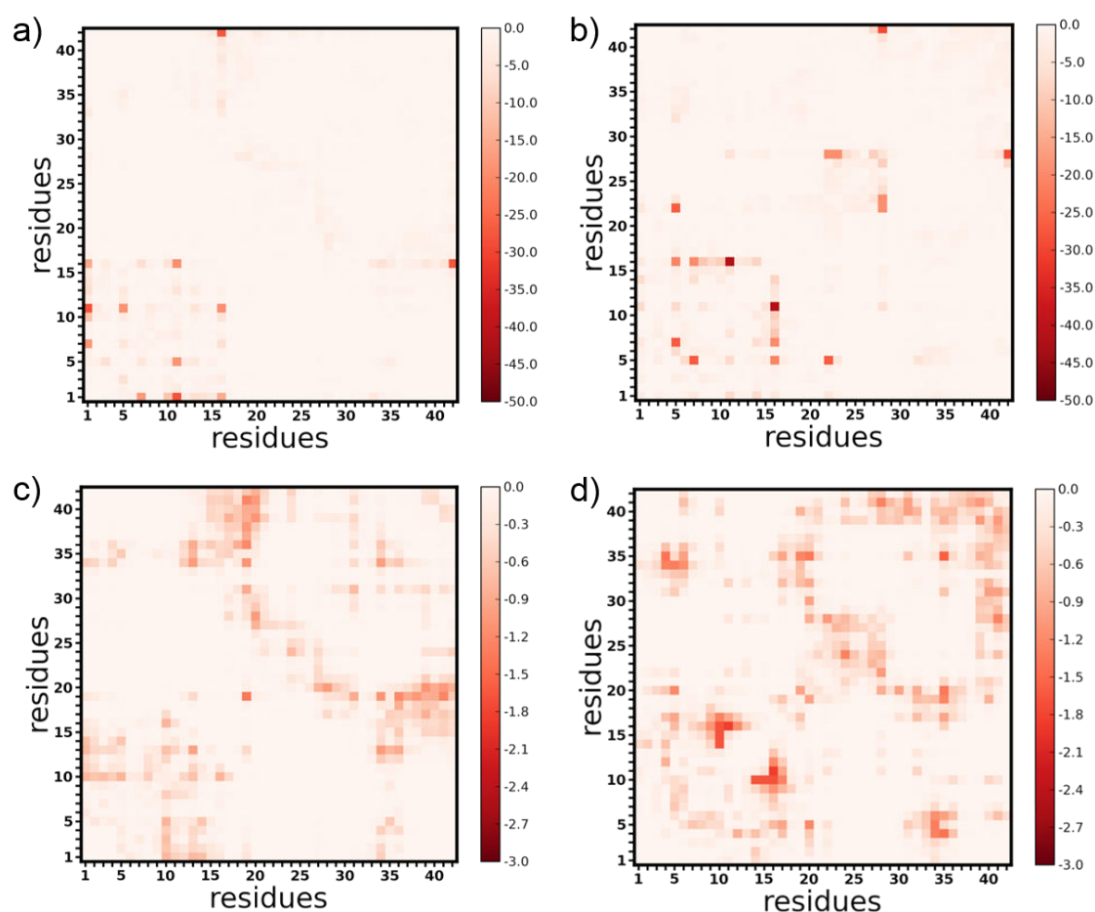


Figure 7.9. Residue specific inter-monomer maximum electrostatic interaction energies (in kcal mol^{-1}) of a) unglycated and b) glycated A β trimer. Residue specific inter-monomer maximum van der Waal interaction energies (in kcal mol^{-1}) of c) unglycated and d) glycated A β trimer.

7.3.4 Intra- and Intermolecular Salt Bridging Propensities.

The significant role of electrostatic interactions in the unglycated and glycated A β assembly lead us to investigate the possible role of salt bridges in stabilizing the inter-protein interaction. At neutral pH, A β_{1-42} has six negatively charged residues (D¹, E³, D⁷, E¹¹, E²² and D²³) and three positively charged residues (R⁵, K¹⁶ and K²⁸). Experimental and theoretical evidences indicate that the intramolecular and intermolecular salt bridges in turn region play an important roles in oligomer stability and fibril formation.¹⁴⁻¹⁶ In glycated A β , the modification of the Lysine residues to N(6)-carboxymethyllysine can potentially enhance the salt-bridging interactions due to increase in the number of charged sites (see Figure 7.2). We have compared the intra and inter-molecular salt bridge between K²⁸ and E²² or D²³ in the unglycated and glycated oligomers by calculating the center of mass distance between the C ^{γ} and N ^{ζ} atoms of the salt-bridging residues within the same peptide unit, and between

associating units. These intramolecular (d_{intra}) and intermolecular (d_{inter}) distance distributions are shown in Figures 7.10.

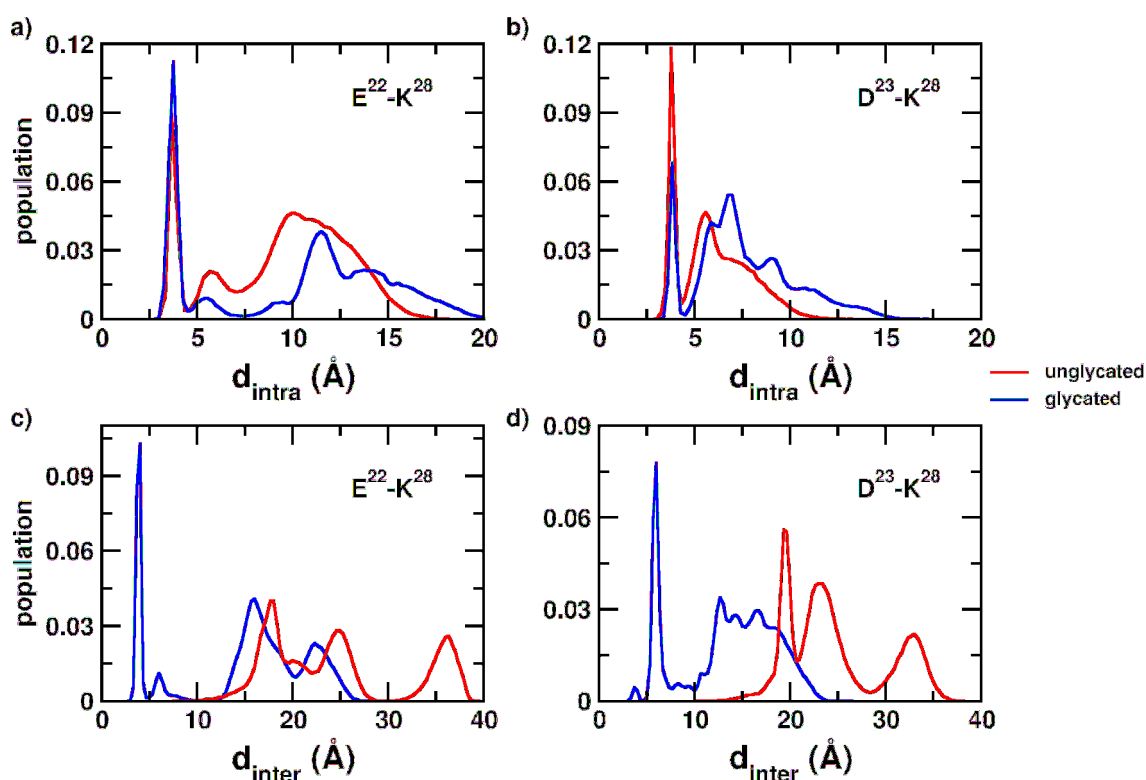


Figure 7.10. Distributions of intra-peptide distance (d_{intra}) and inter-peptide distance (d_{inter}) between the salt-bridge forming pairs in the turn region of the unglycated and glycated A β trimers.

As observed in Figures 7.10a and b, the intramolecular salt bridge propensities between E²²-K²⁸ and D²³-K²⁸ are nearly identical in the unglycated and the glycated oligomeric systems, indicating that the stabilities of the intramolecular turn regions remain unaltered due to glycation. However, more interesting differences can be elicited from inspection of the intermolecular salt bridging propensities. In Figures 7.10c and d, the d_{inter} distributions between E²²-K²⁸ and D²³-K²⁸ in the glycated oligomeric systems are characterized by the presence of a sharp peak at about 3.7 Å and 5.5 Å respectively, indicating high propensities of inter-monomer salt bridging propensities. Notably, however, this peak is entirely absent in the case of the unglycated system indicative of a lack of salt bridging propensities between the disordered oligomers.

It is noteworthy that the N-terminal region encompassing residues 1 to 16 are primarily disordered in the monomeric and fibrillar states of A β . However, recent experimental and theoretical studies suggest that some residues in the N-terminal region

could play important roles in fibril stability and amyloid toxicity.^{43, 62-65} In Figures 7.11, we compare the d_{inter} distributions between the pairs E¹¹-K¹⁶, R⁵-D⁷, R⁵-K¹⁶ and R⁵-E²² in the unglycated and glycated oligomeric systems.

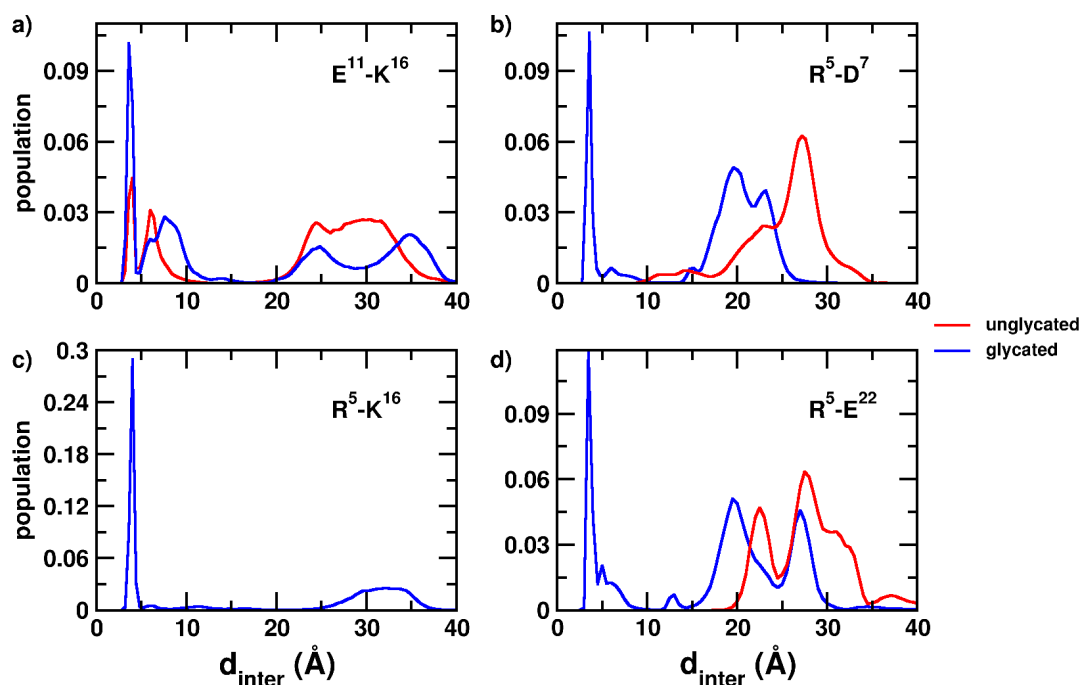


Figure 7.11. Distribution of inter-peptide distances (d_{inter}) between the salt-bridge forming pairs in the N-terminal region of the unglycated and glycated A β trimers.

As seen in Figure 7.11a, while the E¹¹-K¹⁶ salt bridge is present in both systems, its propensity is noticeably enhanced in the glycated system compared to the unglycated system. It is noteworthy here that the importance of R⁵ has been demonstrated recently *via* mutation studies, wherein replacement of this N-terminal residue with Alanine is found to result in the decreased tendency towards A β aggregate formation.^{62, 63} Inspection of the d_{inter} distributions involving R⁵, in Figures 7.11b, c and d, shows that this residue does not participate in salt bridges within the small oligomers in the unglycated form. However, clear salt bridging propensities emerge in the glycated oligomers, with sharp first peaks in the values at 3.5, 4.0 and 3.5 Å, respectively, for the R⁵-D⁷, R⁵-K¹⁶ and R⁵-E²² pairs. In fact, while the R⁵ and K¹⁶ residues do not even approach each other in the unglycated system, but show a very strong propensity to form salt bridges upon glycation.

7.3.5 Effect of Glycation on Preformed Protofibrils.

The simulations and analyses presented thus far clearly demonstrate that chemical modifications resulting from glycation of key residues in the A β peptide have important

effects in A β self-assembly, particularly in small oligomeric stability, secondary structural content, structural disorder, and propensities of inter-peptide salt bridges. These effects are expected to have major consequences in terms of higher ordered assembly, as is indeed corroborated by the experimental data presented earlier.

In order to gain a deeper understanding, we further studied the effect of glycation on the stabilities of pre-formed protofibrillar species. We performed extensive MD simulations of the peptide's trimeric state extracted from its protofibrillar structure⁴³, both in the unglycated and the glycated forms (see Methods for details). As done previously, the most populated cluster was elicited with cPCA and in Figure 7.12 we present snapshots of the representative conformations of the most populated cluster of pre-formed protofibrillar species. In Figure 7.13a, b and c, we compare the normalized distributions of the total inter-protein interactions, along with its electrostatic and van der Waals components, between the unglycated and the glycated assemblies; the mean interaction values are reported in Table 7.2. For the ordered protofibrils, the mean inter-peptide interaction is strengthened by ~ 244 kcal mol⁻¹ due to glycation of the Lysine residues. Interestingly, this strengthening is found to arise purely due to enhanced electrostatic interactions; the van der Waals component of the interaction remains nearly unchanged between the unglycated and the glycated assemblies. Inspecting the residue-wise breakup of the mean interaction strengths, presented in Figure 7.13d and e, we again find that the enhancement in the interactions can be predominantly attributed to R⁵, D⁷, K¹⁶, D²³ and K²⁸. These interactions are therefore reminiscent of the interactions observed earlier in the case of the disordered small oligomers.

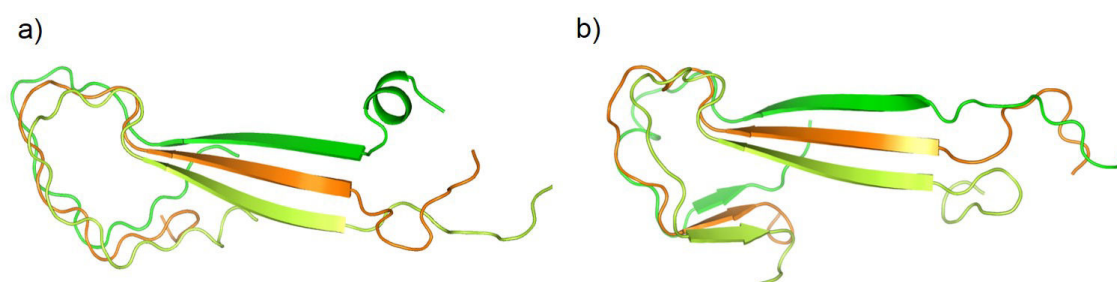


Figure 7.12. Representative snapshots of the highly populated structural ensembles of a) unglycated and b) glycated A β protofibrillar structure.

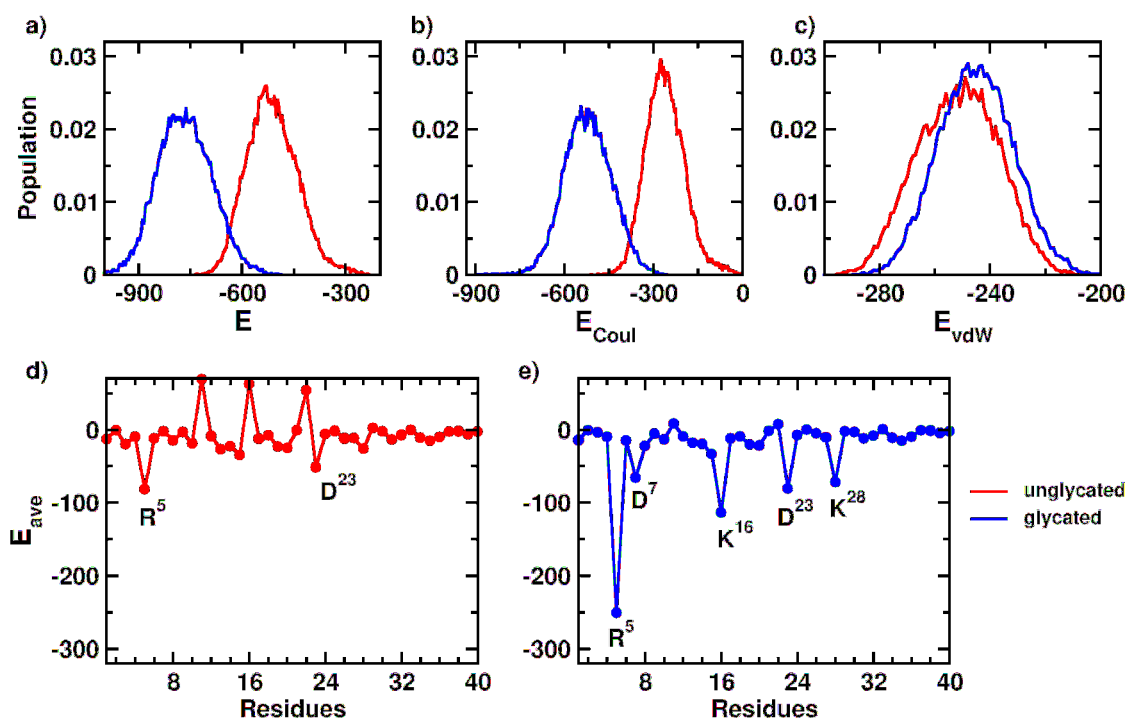


Figure 7.13. Distribution of inter-monomer a) nonbonded (E) b) electrostatic (E_{Coul}) and c) van der Waal (E_{vdW}) interaction energy for unglycated and glycated A β protofibrillar structure. Residue-wise average nonbonded interaction energy (E_{ave}) for unglycated and glycated system. Energies are in kcal mol $^{-1}$ unit. The residues with strong interactions are denoted with one letter code of respective amino acids.

	E_u^f	E_g^f	ΔE
nonbonded	-525.2 (\pm 72.1)	-769.3 (\pm 80.6)	-244.1
electrostatic	-272.1 (\pm 66.1)	-523.7 (\pm 80.8)	-251.6
van der Waal	-253.1 (\pm 13.8)	-245.6 (\pm 13.5)	7.5

Table 7.2. Mean values of inter-monomer non-bonded, electrostatic and van der Waal interaction energies for unglycated (E_u^f) and glycated (E_g^f) A β protofibrillar structures, and corresponding difference in energy (ΔE) between the unglycated and glycated systems. Energies are units of in kcal mol $^{-1}$. Standard deviations are provided within braces.

We further inspected the salt bridging propensities of the charged residues (see Figures 7.14 and 7.15) and found broad similarities with those arising due to glycation in the disordered oligomers. First, glycation is found to bring about a sharp increase in the stability of the intramolecular D 23 -K 28 salt bridge, as reflected in the height of the first peak in the d_{intra} distribution (shown in Figure 7.14). In addition, the inter-molecular propensity of this salt bridge is strengthened to a significant degree in the glycated system (see in Figure 7.14). At the N terminus in the glycated A β protofibrils, R 5 form inter-chain salt bridges with D 7 ,

which is not observed in unglycated A β assembly (in Figure 7.15a). The R⁵-E¹¹ intermolecular salt bridge, also observed in the unglycated A β protofibrils, is stabilized significantly in the glycated protofibril (shown in Figure 7.15b). Interestingly, unlike the disordered oligomeric system, the COO⁻ group of the glycated K¹⁶ is found to form salt bridges with NH₃⁺ group of unglycated K¹⁶ (shown in Figure 7.15c).

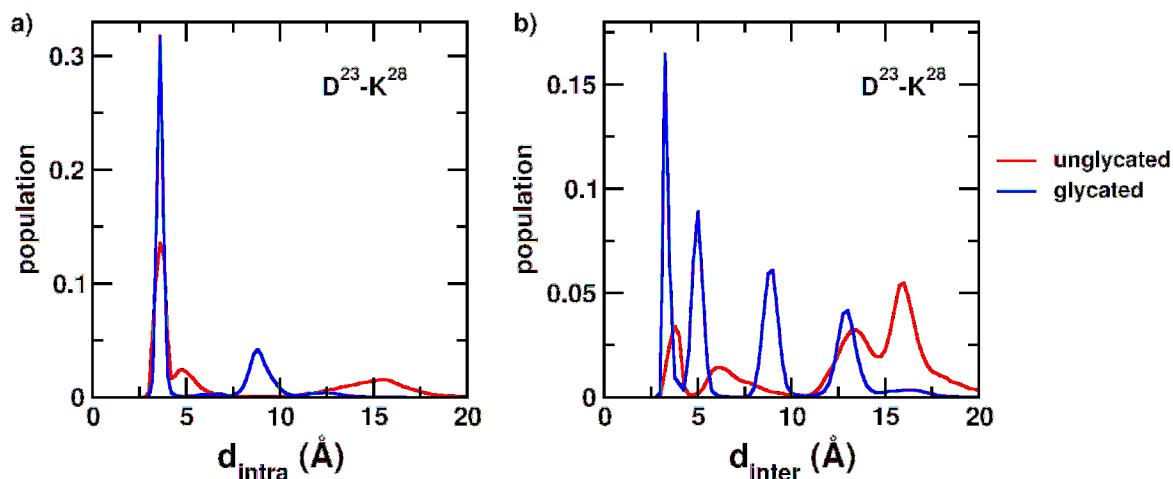


Figure 7.14. Distribution of intra (d_{intra}) and inter-residue (d_{inter}) distances between the salt-bridge forming pairs in turn region of unglycated and glycated A β protofibrillar structure.

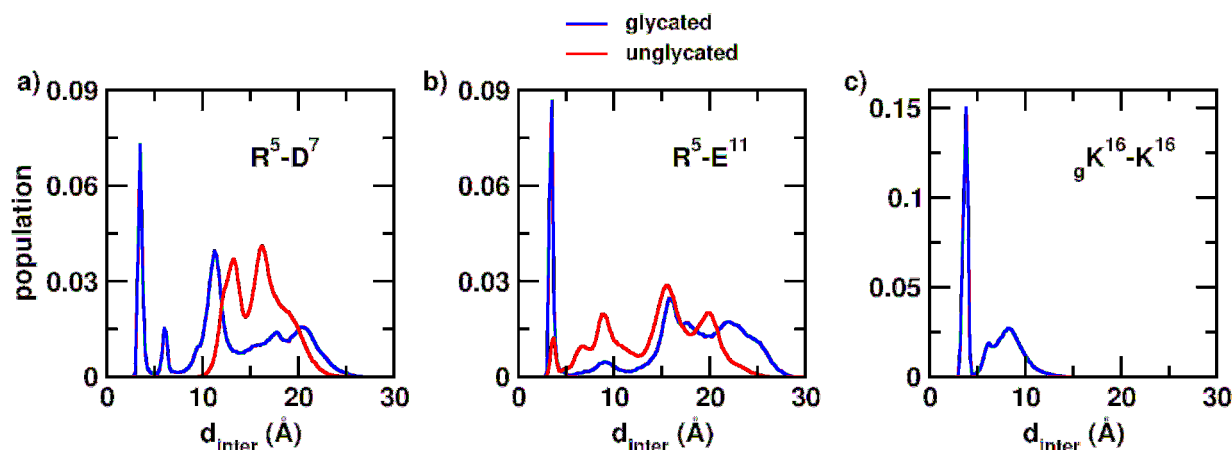


Figure 7.15. Distribution of inter-residue (d_{inter}) distances between the salt-bridge forming pairs in N-terminal region of unglycated and glycated A β protofibrillar structure.

Finally, we analyzed the structural propensities content of the unglycated and glycated protofibrils; comparisons of the mean residue-wise beta-sheet content are presented in Figure 7.16. While the N-terminal domain, CHC and the turn regions show large similarities in the beta sheet content, we find a significant enhancement in the C-terminal regions. Particularly, the beta-sheet content of C-terminal residues Ala³⁰, Ile³¹, Ile³², Leu³⁴, Met³⁵ and Val³⁶

increased substantially. These analyses collectively demonstrate that even partial glycation of preformed ordered oligomers can induce thermodynamic favorability of the aggregates and make them structurally more aggregation prone.

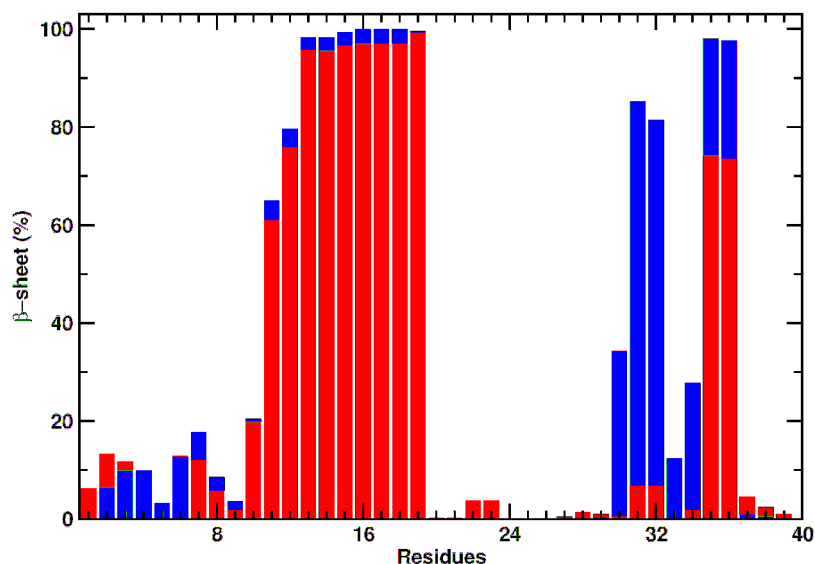


Figure 7.16. Residue-wise β -sheet (%) of unglycated (in red) and glycated (in blue) A β protofibrillar structure.

7.4 Conclusions

Recent studies establish that post-translation modifications of the A β peptide, particularly the processes of glycation resulting in the production of Advanced Glycation End products (AGEs), can accelerate its rates of self-assembly, fibrillation and therefore neurotoxicity. Further, in view of the identification of hyperglycemia as a major risk factor for Alzheimer's disease (AD), it is imperative to understand, at the molecular level, how glycation influences the structural and self-assembly propensities of the A β peptide.

In the present study, we have combined key *in vitro* studies with extensive computer simulations to establish a basis for explaining the mechanisms *via* which glycation of the Lysine residues influences the stability, structure and self-assembly characteristics of the A β peptide. Our ThT binding, CD and light scattering evidences provide strong indication that glycation enhances the overall beta sheet content and reduces the lag time for A β nucleation. Our extensive self-assembly simulations for the dimeric and trimeric forms of A β showed that the resultant small oligomers are bound much more strongly and with a significantly larger number of inter-monomer contacts when the peptide is glycated. The origins of the stronger enthalpy of binding were found to be predominantly electrostatic in nature, although

dispersion interactions also made significant contributions. The electrostatic interactions were attributed to sharp enhancement in the salt bridging interactions between the aggregating monomers. The resultant rigidification of the assemblies were accompanied by markedly greater propensities for beta-sheet component in the residues, indicating that glycation resulted in structural modifications of key self-assembling entities and plausibly making them more aggregation prone.

Interestingly, glycation was found to have major stabilizing effects also on putative pre-formed protofibrillar structures corresponding to those found in brains of AD patients. The overall beta sheet content, high in the protofibrillar aggregates, was further enhanced in the C-terminal region due to glycation. However, the higher energetic stabilization of the partially glycosylated protofibrils were attributed solely to electrostatic interactions arising due to enhancement in inter-peptide salt bridging, with dispersion interactions playing no significant roles. The broad similarities between the observed effect of glycation on the early oligomerizing systems as well the protofibrillar structures suggest that this post-translational modification is capable of enhancing self-assembly kinetics regardless of its point of occurrence.

The current results pave the way for further mechanistic studies into how glycation may affect the nucleation mechanisms of A β assembly and the formation and stabilities of highly ordered aggregates. We further point out here that an important mode of A β neurotoxicity is related to their ability to porate and damage cellular membrane.⁶⁶ Since AGE modifications are associated with higher neurotoxicity, it could be worthwhile to benchmark the neurotoxicities of variously glycosylated A β assemblies *via* their interactions with membrane bilayers. Such systematic studies involving synchronized computer simulations and detailed experimental investigations are expected to further aid in the development of suitable therapeutics for halting or preventing the progression of AGE related AD complications.

7.5 References

1. I. W. Hamley, *Chem. Rev.*, 2012, **112**, 5147-5192.
2. R. P. Friedrich, K. Tepper, R. Röncke, M. Soom, M. Westermann, K. Reymann, C. Kaether and M. Fändrich, *Proc. Natl. Acad. Sci.*, 2010, **107**, 1942-1947.
3. R. J. O'Brien and P. C. Wong, *Ann. Rev. Neurosci.*, 2011, **34**, 185.
4. R. M. Nisbet, J.-C. Polanco, L. M. Ittner and J. Götz, *Acta Neuropathol.*, 2015, **129**,

- 207-220.
5. H. J. Dyson and P. E. Wright, *Nat. Rev. Mol. Cell Biol.*, 2005, **6**, 197-208.
 6. V. N. Uversky, *Front. Aging Neurosci.*, 2015, **7**, 18.
 7. M. M. Babu, R. van der Lee, N. S. de Groot and J. Gsponer, *Curr. Opin. Struct. Biol.*, 2011, **21**, 432-440.
 8. A. Šarić, Y. C. Chebaro, T. P. Knowles and D. Frenkel, *Proc. Natl. Acad. Sci.*, 2014, **111**, 17869-17874.
 9. H. Akiyama, S. Barger, S. Barnum, B. Bradt, J. Bauer, G. M. Cole, N. R. Cooper, P. Eikelenboom, M. Emmerling and B. L. Fiebich, *Neurobiol. Aging*, 2000, **21**, 383-421.
 10. C. Haass and D. J. Selkoe, *Nat. Rev. Mol. Cell Biol.*, 2007, **8**, 101-112.
 11. R. Tycko and R. B. Wickner, *Acc. Chem. Res.*, 2013, **46**, 1487-1496.
 12. W. Qiang, K. Kelley and R. Tycko, *J. Am. Chem. Soc.*, 2013, **135**, 6860-6871.
 13. L. Hou, H. Shao, Y. Zhang, H. Li, N. K. Menon, E. B. Neuhaus, J. M. Brewer, I.-J. L. Byeon, D. G. Ray, M. P. Vitek, T. Iwashita, R. A. Makula, A. B. Przybyla and M. G. Zagorski, *J. Am. Chem. Soc.*, 2004, **126**, 1992-2005.
 14. G. Reddy, J. E. Straub and D. Thirumalai, *J. Phys. Chem. B*, 2009, **113**, 1162-1172.
 15. M. Chandrakesan, D. Bhowmik, B. Sarkar, R. Abhyankar, H. Singh, M. Kallianpur, S. P. Dandekar, P. K. Madhu, S. Maiti and V. S. Mithu, *J. Biol. Chem.*, 2015, **290**, 30099-30107.
 16. M. A. Grant, N. D. Lazo, A. Lomakin, M. M. Condrón, H. Arai, G. Yamin, A. C. Rigby and D. B. Teplow, *Proc. Natl. Acad. Sci.*, 2007, **104**, 16522-16527.
 17. D. J. Rosenman, C. R. Connors, W. Chen, C. Wang and A. E. García, *J. Mol. Biol.*, 2013, **425**, 3338-3359.
 18. Y.-S. Lin, G. R. Bowman, K. A. Beauchamp and V. S. Pande, *Biophys. J.*, 2012, **102**, 315-324.
 19. B. Ma and R. Nussinov, *Proc. Natl. Acad. Sci.*, 2002, **99**, 14126-14131.
 20. A. Baumketner and J.-E. Shea, *J. Mol. Biol.*, 2007, **366**, 275-285.
 21. D. J. Rosenman, C. Wang and A. E. García, *J. Phys. Chem. B*, 2015, **120**, 259-277.
 22. M. Grabenauer, C. Wu, P. Soto, J.-E. Shea and M. T. Bowers, *J. Am. Chem. Soc.*, 2010, **132**, 532-539.
 23. Q. Qiao, G. R. Bowman and X. Huang, *J. Am. Chem. Soc.*, 2013, **135**, 16092-16101.

24. D. J. Selkoe, *J. Biol. Chem.*, 1996, **271**, 18295-18298.
25. C. S. Atwood, R. N. Martins, M. A. Smith and G. Perry, *Peptides*, 2002, **23**, 1343-1350.
26. A. Lapolla, D. Fedele and P. Traldi, *Clin. Chim. Acta*, 2005, **357**, 236-250.
27. X. Li, L. Du, X. Cheng, X. Jiang, Y. Zhang, B. Lv, R. Liu, J. Wang and X. Zhou, *Cell Death Dis.*, 2013, **4**, e673.
28. C. Chen, X.-H. Li, Y. Tu, H.-T. Sun, H.-Q. Liang, S.-X. Cheng and S. Zhang, *Neuroscience*, 2014, **257**, 1-10.
29. M. Barbagallo and L. J. Dominguez, *World J Diabetes*, 2014, **5**, 889-893.
30. B. Kim, C. Backus, S. Oh and E. L. Feldman, *J. Alzheimer's Dis.*, 2013, **34**, 727-739.
31. M. Baram, Y. Atsmon-Raz, B. Ma, R. Nussinov and Y. Miller, *Phys. Chem. Chem. Phys.*, 2016, **18**, 2330-2338.
32. K. B. Batkulwar, S. B. Bansode, G. V. Patil, R. K. Godbole, R. S. Kazi, S. Chinnathambi, D. Shanmugam and M. J. Kulkarni, *Proteomics*, 2015, **15**, 245-259.
33. B.-R. Choi, W.-H. Cho, J. Kim, H. J. Lee, C. Chung, W. K. Jeon and J.-S. Han, *Exp. Mol. Med.*, 2014, **46**, e75.
34. S. Lovestone and U. Smith, *Proc. Natl. Acad. Sci.*, 2014, **111**, 4743-4744.
35. S. B. Bansode, A. D. Chougale, R. S. Joshi, A. P. Giri, S. L. Bodhankar, A. M. Harsulkar and M. J. Kulkarni, *Mol. Cell. Proteomics*, 2013, **12**, 228-236.
36. S. Reddy, J. Bichler, K. J. Wells-Knecht, S. R. Thorpe and J. W. Baynes, *Biochemistry*, 1995, **34**, 10872-10878.
37. A. M. Korwar, G. Vannuruswamy, M. G. Jagadeeshaprasad, R. H. Jayaramaiah, S. Bhat, B. S. Regin, S. Ramaswamy, A. P. Giri, V. Mohan and M. Balasubramanyam, *Mol. Cell. Proteomics*, 2015, **14**, 2150-2159.
38. A. K. Jana and N. Sengupta, *Soft Matter*, 2015, **11**, 269-279.
39. K. Osapay and D. A. Case, *J. Am. Chem. Soc.*, 1991, **113**, 9436-9444.
40. N. G. Sgourakis, Y. Yan, S. A. McCallum, C. Wang and A. E. Garcia, *J. Mol. Biol.*, 2007, **368**, 1448-1457.
41. S. Côté, P. Derreumaux and N. Mousseau, *J. Chem. Theory Comput.*, 2011, **7**, 2584-2592.
42. Y. Yan, S. A. McCallum and C. Wang, *J. Am. Chem. Soc.*, 2008, **130**, 5394-5395.

43. J.-X. Lu, W. Qiang, W.-M. Yau, C. D. Schwieters, S. C. Meredith and R. Tycko, *Cell*, 2013, **154**, 1257-1268.
44. L. KalÈ, R. Skeel, M. Bhandarkar, R. Brunner, A. Gursoy, N. Krawetz, J. Phillips, A. Shinozaki, K. Varadarajan and K. Schulten, *J. Comput. Phys.*, 1999, **151**, 283-312.
45. A. D. MacKerell, D. Bashford, Bellott, R. L. Dunbrack, J. D. Evanseck, M. J. Field, S. Fischer, J. Gao, H. Guo, S. Ha, D. Joseph-McCarthy, L. Kuchnir, K. Kuczera, F. T. K. Lau, C. Mattos, S. Michnick, T. Ngo, D. T. Nguyen, B. Prodhom, W. E. Reiher, B. Roux, M. Schlenkrich, J. C. Smith, R. Stote, J. Straub, M. Watanabe, J. Wiórkiewicz-Kuczera, D. Yin and M. Karplus, *J. Phys. Chem. B*, 1998, **102**, 3586-3616.
46. A. D. Mackerell, M. Feig and C. L. Brooks, *J. Comput. Chem.*, 2004, **25**, 1400-1415.
47. W. L. Jorgensen, J. Chandrasekhar, J. D. Madura, R. W. Impey and M. L. Klein, *J. Chem. Phys.*, 1983, **79**, 926-935.
48. V. Zoete, M. A. Cuendet, A. Grosdidier and O. Michielin, *J. Comput. Chem.*, 2011, **32**, 2359-2368.
49. E. H. Hill, K. Stratton, D. G. Whitten and D. G. Evans, *Langmuir*, 2012, **28**, 14849-14854.
50. M. F. Mabanglo, A. W. R. Serohijos and C. D. Poulter, *Biochemistry*, 2012, **51**, 917-925.
51. G. J. Martyna, D. J. Tobias and M. L. Klein, *J. Chem. Phys.*, 1994, **101**, 4177-4189.
52. S. E. Feller, Y. Zhang, R. W. Pastor and B. R. Brooks, *J. Chem. Phys.*, 1995, **103**, 4613-4621.
53. J.-P. Ryckaert, G. Ciccotti and H. J. C. Berendsen, *J. Comput. Phys.*, 1977, **23**, 327-341.
54. U. Essmann, L. Perera, M. L. Berkowitz, T. Darden, H. Lee and L. G. Pedersen, *J. Chem. Phys.*, 1995, **103**, 8577-8593.
55. N. M. Glykos, *J. Comput. Chem.*, 2006, **27**, 1765-1768.
56. M. Heinig and D. Frishman, *Nucleic Acids Res.*, 2004, **32**, W500-W502.
57. W. Humphrey, A. Dalke and K. Schulten, *J. Mol. Graph.*, 1996, **14**, 33-38.
58. J. Schlitter, *Chem. Phys. Lett.*, 1993, **215**, 617-621.
59. K. Nomoto, M. Yagi, U. Hamada, J. Naito and Y. Yonei, *Anti-Aging Med.*, 2013, **10**, 92-100.
60. R. Khurana, C. Coleman, C. Ionescu-Zanetti, S. A. Carter, V. Krishna, R. K. Grover, R. Roy and S. Singh, *J. Struct. Biol.*, 2005, **151**, 229-238.

61. A. A. Sahasrabudde, S. M. Gaikwad, M. Krishnasastry and M. I. Khan, *Protein Sci.*, 2004, **13**, 3264-3273.
62. Y. Yoshiike, T. Akagi and A. Takashima, *Biochemistry*, 2007, **46**, 9805-9812.
63. O. Coskuner and O. Wise-Scira, *ACS Chem. Neurosci.*, 2013, **4**, 1549-1558.
64. I. Bertini, L. Gonnelli, C. Luchinat, J. Mao and A. Nesi, *J. Am. Chem. Soc.*, 2011, **133**, 16013-16022.
65. M. H. Viet, P. H. Nguyen, P. Derreumaux and M. S. Li, *ACS Chem. Neurosci.*, 2014, **5**, 646-657.
66. R. D. Johnson, D. G. Steel and A. Gafni, *Protein Sci.*, 2014, **23**, 869-883.



Copyrights and Permissions

**OXFORD UNIVERSITY PRESS LICENSE
TERMS AND CONDITIONS**

Apr 28, 2016

This is a License Agreement between Asis K. Jana ("You") and Oxford University Press ("Oxford University Press") provided by Copyright Clearance Center ("CCC"). The license consists of your order details, the terms and conditions provided by Oxford University Press, and the payment terms and conditions.

All payments must be made in full to CCC. For payment instructions, please see information listed at the bottom of this form.

License Number	3846330291792
License date	Apr 12, 2016
Licensed content publisher	Oxford University Press
Licensed content publication	Cardiovascular Research
Licensed content title	Advanced glycation end products and vascular inflammation: implications for accelerated atherosclerosis in diabetes
Licensed content author	Giuseppina Basta,Ann Marie Schmidt,Raffaele De Caterina
Licensed content date	2004-09-01
Type of Use	Thesis/Dissertation
Institution name	None
Title of your work	Modulation of Self-Assembly Pathways of the Alzheimer's Amyloid Beta Peptide with Carbon Based Nanomaterials and Chemical Modifications
Publisher of your work	n/a
Expected publication date	Apr 2016
Permissions cost	0.00 USD
Value added tax	0.00 USD
Total	0.00 USD
Total	0.00 USD
Terms and Conditions	

**STANDARD TERMS AND CONDITIONS FOR REPRODUCTION OF MATERIAL
FROM AN OXFORD UNIVERSITY PRESS JOURNAL**

1. Use of the material is restricted to the type of use specified in your order details.
2. This permission covers the use of the material in the English language in the following territory: world. If you have requested additional permission to translate this material, the terms and conditions of this reuse will be set out in clause 12.
3. This permission is limited to the particular use authorized in (1) above and does not allow you to sanction its use elsewhere in any other format other than specified above, nor does it apply to quotations, images, artistic works etc that have been reproduced from other sources which may be part of the material to be used.
4. No alteration, omission or addition is made to the material without our written consent.

Permission must be re-cleared with Oxford University Press if/when you decide to reprint.

5. The following credit line appears wherever the material is used: author, title, journal, year, volume, issue number, pagination, by permission of Oxford University Press or the sponsoring society if the journal is a society journal. Where a journal is being published on behalf of a learned society, the details of that society must be included in the credit line.

6. For the reproduction of a full article from an Oxford University Press journal for whatever purpose, the corresponding author of the material concerned should be informed of the proposed use. Contact details for the corresponding authors of all Oxford University Press journal contact can be found alongside either the abstract or full text of the article concerned, accessible from www.oxfordjournals.org Should there be a problem clearing these rights, please contact journals.permissions@oup.com

7. If the credit line or acknowledgement in our publication indicates that any of the figures, images or photos was reproduced, drawn or modified from an earlier source it will be necessary for you to clear this permission with the original publisher as well. If this permission has not been obtained, please note that this material cannot be included in your publication/photocopies.

8. While you may exercise the rights licensed immediately upon issuance of the license at the end of the licensing process for the transaction, provided that you have disclosed complete and accurate details of your proposed use, no license is finally effective unless and until full payment is received from you (either by Oxford University Press or by Copyright Clearance Center (CCC)) as provided in CCC's Billing and Payment terms and conditions. If full payment is not received on a timely basis, then any license preliminarily granted shall be deemed automatically revoked and shall be void as if never granted. Further, in the event that you breach any of these terms and conditions or any of CCC's Billing and Payment terms and conditions, the license is automatically revoked and shall be void as if never granted. Use of materials as described in a revoked license, as well as any use of the materials beyond the scope of an unrevoked license, may constitute copyright infringement and Oxford University Press reserves the right to take any and all action to protect its copyright in the materials.

9. This license is personal to you and may not be sublicensed, assigned or transferred by you to any other person without Oxford University Press's written permission.

10. Oxford University Press reserves all rights not specifically granted in the combination of (i) the license details provided by you and accepted in the course of this licensing transaction, (ii) these terms and conditions and (iii) CCC's Billing and Payment terms and conditions.

11. You hereby indemnify and agree to hold harmless Oxford University Press and CCC, and their respective officers, directors, employs and agents, from and against any and all claims arising out of your use of the licensed material other than as specifically authorized pursuant to this license.

12. Other Terms and Conditions:

v1.4

Questions? customer-care@copyright.com or +1-855-239-3415 (toll free in the US) or +1-978-646-2777.